Imperial College London
Department of Civil and Environmental Engineering

Phase Field-Based Electro-Chemo-Mechanical Models for Predicting Interface Degradation in Solid-State Batteries

Runzi Wang

Submitted in part fulfilment of the requirements
for the degree of Doctor of Philosophy at
Imperial College London
June, 2024

I hereby declare that this thesis titled "Phase Field-Based Electro-Chemo-Mechanical Models for Predicting Interface Degradation in Solid-State Batteries" is my own work. All sources and materials used have been properly acknowledged and cited according to academic standards. I confirm that this thesis has not been submitted for any other degree or professional qualification and is not currently being considered by another examination board. All research was conducted in accordance with the ethical guidelines and regulations of Imperial College London.

Runzi Wang



Phase Field-Based Electro-Chemo-Mechanical Models for Predicting Interface Degradation in Solid-State Batteries © 2024 by Runzi Wang is licensed under CC BY-NC-ND 4.0

The copyright of this thesis rests with the author. Unless otherwise indicated, its contents are licensed under a Creative Commons Attribution-Non Commercial-No Derivatives 4.0 International Licence (CC BY-NC-ND). Under this licence, you may copy and redistribute the material in any medium or format on the condition that; you credit the author, do not use it for commercial purposes and do not distribute modified versions of the work. When reusing or sharing this work, ensure you make the licence terms clear to others by naming the licence and linking to the licence text. Please seek permission from the copyright holder for uses of this work that are not included in this licence or permitted under UK Copyright Law.

Abstract

All-solid-state lithium metal batteries (ASSLBs) are considered the next-generation electrochemical energy storage solution, potentially replacing conventional liquid-state lithium-ion batteries (LSLBs) due to their theoretically higher energy and power densities, as well as their enhanced safety. However, challenges such as low electrolyte ionic conductivity and dendrite formation still hinder their widespread application. While significant breakthroughs have been achieved in enhancing solid electrolyte materials, limited efforts have been dedicated to developing finite-element models that address these challenges through multi-physics couplings. This research aims to propose a mechanistic theory for predicting interface stability in ASSLBs involving the evolution of voids in Li metal electrodes during charging and discharging. A phase-field formulation is developed to allow a dynamic tracking of the evolution of the void-lithium interface, coupled with a viscoplastic description of Li deformation that captures creep effects and incorporates mass transfer. The model also accounts for the interaction between the electrode and the solid electrolyte, predicting current distributions and local current 'hot spots' that precede dendrite formation. The evolution of voids and current hot spots is successfully predicted as a function of applied pressure, material properties, and dis/charge history. Key experimental observations are captured, including current density distribution in electrolyte and void morphology, sensitivity to applied current, the role of pressure in enhancing electrolyte-electrolyte contact, and the dominant role of creep on void diffusion. The results demonstrated the capability of the model to correctly predict the dynamic evolution of the interface morphology during battery cycles. However, through quantitative analysis, its limitations in high-pressure-related simulation are acknowledged. Despite these challenges, this model constitutes a novel contribution to this research field and offers insightful understandings for researchers through qualitative analysis.

Acknowledgements

First and foremost, I would like to express my deepest gratitude to my supervisors, Prof. Emilio Martínez-Pañeda, Prof. Ying Zhao, and Dr. Billy Wu, for their invaluable guidance, patience, and encouragement throughout my PhD journey. Their insights and expertise have been fundamental to the success of this project.

I extend my heartfelt thanks to the members of my thesis committee, Dr. Anna Hankin and Prof. Laurence Brassart, for their constructive feedback, suggestions, and for generously sharing their knowledge.

I am also grateful to my colleagues and friends in the Mechanics of Materials Lab, whose camaraderie, collaboration, and stimulating discussions have greatly enriched my academic experience.

Additionally, I appreciate the administrative support from the Department of Civil and Environmental Engineering at Imperial College London, which ensured the smooth progression of my studies.

To my family and my girlfriend, thank you for your unwavering love, patience, and encouragement. Your belief in me has been a constant source of strength and motivation.

Thank you all for your support and belief in me. This accomplishment would not have been possible without each and every one of you.

Contents

Abstract i

Acknowledgements ii

1 Introduction 1

1.1 Background . . . 1

1.2 Research Aim and Thesis Overview . . . 6

2 Development of SSB Technology: An Overview 8

2.1 State-of-the-Art Materials and Cutting-Edge Technology . . . 8

2.1.1 SSE Materials . . . 8

2.1.2 Approaches to Improve Performance of SSBs . . . 14

2.2 Modelling Attempts . . . 20

2.2.1 Continuum Mechanics Models . . . 21

2.2.2 Phase Field Models for SSBs . . . 27

2.3 Summary . . . 29

3 Theory Fundamentals 31

3.1 Theory of Electrochemical Systems . . . 31

3.1.1 Basic Concepts of an Electrochemical System . . . 31

3.1.2 The Electrode Kinetics . . . 40

3.1.3 Charge and Mass Transfer . . . 43

3.1.4 Essential Parameters to Quantify Battery Performance . . . 46

3.2 Theory of Mechanics of Continua . . . 49

3.2.1 Mathematical Description of Kinematics and Strain Tensors . . . 50

3.2.2 Forces and Stress Tensors . . . 56

3.2.3 Conservation Laws . . . 58
3.2.4 Principle of Virtual Work . . . 58
3.2.5 Constitutive Equations for Materials . . . 59
3.3 Phase Field Method . . . 62
3.3.1 Kinetic Equations . . . 63
3.3.2 Free Energy Functional . . . 64
3.4 Summary . . . 65

4 A Phase Field-Based Electro-Chemo-Mechanical Formulation for Interface Degradation Prediction in SSBs 66
4.1 Theory of the Model . . . 66
4.1.1 Preliminaries . . . 67
4.1.2 Free Energy and Chemical Potential of the Lithium Metal Electrode . . . 69
4.1.3 Phase Field Formulation of the Helmholtz Free Energy of a Lithium Electrode with Voids . . . 72
4.1.4 Kinematic and Constitutive Equations . . . 73
4.1.5 Governing Equations . . . 76
4.2 Numerical Implementation . . . 79
4.2.1 Interface Velocity . . . 80
4.2.2 Interfacial Energy and Thickness Based on the Phase Field Model . . . 81
4.3 Summary . . . 83

5 Insights into Voiding at Li/SE Interface 85
5.1 Model Configuration . . . 86
5.1.1 Boundary Conditions . . . 86
5.1.2 Initial Conditions . . . 88
5.1.3 Coupling with the Electro-Mechanical Behaviour of the Solid Electrolyte . . . 88
5.2 Material Model Calibration and Parameter Selection . . . 91
5.3 Single Void Analysis . . . 93
5.3.1 Void Evolution in the Electrode under Stripping and Plating . . . 95
5.3.2 Influence of the Applied Current and the Phase Field Kinetic Coefficient . . . 98
5.3.3 Investigating the Competing Role of Creep Deformation and Li Diffusion . . . 102
5.4 Cyclic Charging of A Solid-State Cell with Multiple Interface Defects . . . 104

5.5 Summary . . . 108

6 Understanding the Accelerated Short-Circuiting Mechanism of Anode-Free SSBs 110

6.1 Experimental Insight . . . 111

6.1.1 In Situ Li Deposition Behaviour at the Current Collector Surface . . . 111

6.1.2 Cycling Performance of the Anode-free SSBs . . . 113

6.1.3 Inferred Mechanisms for Accelerated Short-Circuit Phenomena . . . 114

6.2 Phase-Field Decipher of the Impact of Local Li Depletion . . . 116

6.2.1 Governing Equations . . . 116

6.2.2 Boundary Conditions and Initial Conditions . . . 117

6.2.3 Results and Discussion . . . 122

6.3 Summary . . . 123

7 Towards Quantitative SSB Predictions 124

7.1 Boundary Conditions and Initial Conditions . . . 125

7.2 Quantitative analysis of Interface Contact Loss During Stripping . . . 127

7.2.1 Results Considering Creep Deformation of the Li Metal Anode . . . 127

7.2.2 Results Considering Elastic Deformation of the Li Metal Anode . . . 130

7.3 Summary . . . 134

8 Concluding Remarks and Future Works 136

List of Tables

2.1 Summary of typical SSE materials and their electrochemical properties 12

3.1 Standard electrode potentials with respect to SHE 40

5.1 Phase field and material parameters for a Li anode - LLZO electrolyte system 91

5.2 Viscoplastic material parameters for lithium metal 93

6.1 Reported material properties 121

7.1 Selected values of the phase field interface kinetics coefficient L for different i_{app} . . . 131

List of Figures

1.1 Comparative Analysis of Battery Technologies: Gravimetric ($\mathrm{Wh\,kg^{-1}}$) and Volumetric Energy Densities ($\mathrm{Wh\,l^{-1}}$) [1]. Lead-acid, known for its cost-effectiveness and recyclability, serves as a primary choice for car ignition and uninterruptible power supplies (UPS). Ni-Cd batteries, limited by memory effects and environmental concerns, are increasingly replaced by Li-ion alternatives. Nickel-metal hydride (Ni-MH) batteries, while being supplanted by Li-ion, still find niche applications, such as in security system backups. Li-polymer (PLiON), Li-ion, and Li metal batteries represent the forefront of ongoing research and development in energy storage technologies. 2

1.2 Global EV stock (in million) and EV electricity demand (in GWh): historical data and future predictions (years with *). EVs include Battery Electric vehicles (BEVs) and Plug-in Hybrid Electric Vehicles (PHEVs). The prediction data are evaluated under the Stated Policies Scenario (STEPS). All data come from the 'Global EV outlook 2023' by the IEA [2]. 3

1.3 Number of publications containing 'solid state battery*' from the year 2000 to 2023, data collected from Web of Science in January 2024. 4

1.4 Sketch of the typical structures of the state-of-the-art batteries, including a) a liquid-state Li-ion battery, which is usually composed of current collectors (CC), a ternary material cathode such as NCM, a graphite anode (GA), a separator and liquid electrolyte (LE), and b) a solid-state Li-ion battery, which is different from an LSB with solid electrolyte (SE) and lithium metal anode (LMA). 5

1.5 Main challenges confronting the practicality and commercialization of SSBs, including interface-related issues: void formation, high charge transfer resistance, dendrite nucleation and growth, solid electrolyte interphase (SEI) formation and fracture, and coating fracture and delamination of cathode particles; non-interface issues: cathode tortuosity, cracks and defects in the SE, SE's ionic conductivity, and electrode volume changes during battery cycles. 6

2.1 The advancement of key SSE materials and SSB technologies from 1920s to 2016 [3]. . 9

2.2 The major issues faced by SSBs and the corresponding solutions. 14

2.3 a) Configuration of an integrated SSB with LLZO nanowire upgraded PEO/LITFSI composite SSE fused with $LiFePO_4$ cathode (left) and voltage-time figure to illustrate the improvement in electrochemical stability of Li/PLLN/Li symmetric cell compared with Li/PL/Li and Li/PLLM/Li cells (right) [4]. b) A better interfacial wettability and lower interface resistance achieved by SSE surface conditioning [5]. c) Surface engineering by introducing a Li alloyed buffer layer. The insets are SEM images from the work of Kato et al. [6]. d) An experimental setup to apply pressure to the Li symmetric cell (left) and the normalized voltage-time figure of the cell under different stack pressures. Short circuits happen before cycling begins when the cell is under 75 MPa [7]. 19

2.4 a) Variation of the stability parameter $\Delta\mu$ with the ratio of shear moduli between the electrolyte (G^s) and the electrode (G^e) [8]. b) Sketch of the model for dendrite growth initiation as climbing dislocations [9]. c) Direct optical observation of dendrite growth in a transparent LLZTO SSE under applied currents of 0.1 mA for ① - ③ in the first row, and 0.5 mA for ① - ③ in the second row [10]. d) Operando X-ray computed tomography (XCT) cross-sections of a $Li/Li_6PS_5Cl/Li$ symmetric cell during lithium plating, showing dendrite initiation at a pristine interface and subsequent crack propagation in the SSE [11]. e) Setup for void initiation prediction at an interface with a pre-existed impurity (left), and the distribution of normalized Von Mises stress σ/σ_0 in the electrode and normalized current density $-j_z/j_\infty$ in the electrolyte (right) [12]. 26

2.5 a) Different Li dendritic patterns were predicted with different initial dendrite nuclei and applied voltage [13]. b) Cracking of a cathode particle [14]. c) Illustration of the model setup and predictions of dendrite growth in the ceramic SSE employing a multi-coupling phase field model [15]. d) Depiction of the proposed mechanism of the phase field-damage model, where d denotes the damage variable and ξ denotes the electrodeposition reaction coordinate (top row), and the prediction of the crack propagation coupled with Li deposition (bottom row) [16]. 29

3.1 Simple illustrations of two different electrochemical systems. 34

3.2 The reaction Gibbs energy $\Delta_r\mathcal{G}$ is defined as the slope of the Gibbs energy change $\Delta\mathcal{G}$ against the change of the extent of reaction ζ [17]. E_{cell} is the cell potential. Reaction is spontaneous in the forward direction when $\Delta_r\mathcal{G} < 0$ or $E_{\text{cell}} > 0$ and in the reverse direction when $\Delta_r\mathcal{G} > 0$ or $E_{\text{cell}} < 0$. 35

3.3 Typical OCV-SoC curves under different temperatures for a Li-ion battery [18]. 48

3.4 Formation of dead Li caused by the formation and rupture of solid electrolyte interface (SEI) 49

3.5 Deformation of a closed body region $\mathcal{B}$ after time t in an Euclidean space. 50

3.6 Deformation of a closed body region $\mathcal{B}$ to a final state $\mathcal{B}_t$ involving an intermediate deformation step $\mathcal{B}_{t'}$. 51

3.7 Surface traction and body force. 56

3.8 Components of Cauchy stress tensor. 57

3.9 a) The conventional sharp interface method, and b) the phase-field method, in problems involving crack Γ, Γ_d and phase transformation ($\mathcal{B} \Leftrightarrow \Omega$). The subscript d denotes a diffuse interface, and ℓ_k is the thickness of the corresponding diffuse interfaces. 63

4.1 Interplay between voiding and dendrite formation: SEM images and sketches of the process of voiding and dendrite formation during plating and stripping cycles. The presence of voids generates local current 'hot spots' at the locations where the void meets the Li anode and the solid electrolyte. Li deposition will be exacerbated in these regions and lead to the nucleation of dendrites, which grow until causing the short circuit of the cell. The SEM images are based on the work by Spencer Jolly et al. [19] using Na anodes but are representative of what is observed in other all-solid-state battery systems, including Li-based. 67

4.2 Schematic of the physical mechanisms governing voiding at the anode-electrolyte interface of all-solid-state batteries: (a) initial stripping stage, with vacancy diffusion and Li dissolution; (b) advanced stripping stage, with voiding, Li dissolution and both adatom and vacancy diffusion; (c) mechanical interactions relevant to both stripping and plating - vacancy diffusion distorts the lattice while creep due to an applied pressure closes the voids; (d) initial plating stage, with Li deposition reversing void growth; and (e) advanced plating stage, with void occlusion being observed due to further Li deposition. 68

4.3 Illustration of the sites in a volume V of lithium metal. The shaded area denotes the network of lithium lattice sites and takes over a volume V^{m}. Thus, the voids occupy a volume of $V^{\mathrm{v}} = V - V^{\mathrm{m}}$. In V^{m}, there are $N^{\mathrm{m}}_{\mathrm{Li}}$ lattice sites occupied by lithium atoms, leaving $N^{\mathrm{m}}_{\mathrm{v}}$ lattice sites vacant. 70

4.4 Illustration of different domains, boundaries and interfaces of the problem. 77

4.5 Phase field interface thickness: comparison between the theoretical estimate ($\ell = 1$ µm, for $\kappa = 4.5 \times 10^{-7}\,\mathrm{N}$ and $w = 3.5 \times 10^{6}\,\mathrm{N\,m^{-2}}$) and the numerical prediction. The distance along the interface is normalised by the void radius (R = 10 µm). For consistency, the interface thickness is determined by drawing a line tangent to the ξ distribution predicted at $\xi = 0.5$. 83

5.1 Complete electro-chemo-mechanical model, coupling the deformation-diffusion-phase field behaviour of the Li metal electrode with the electro-mechanical behaviour of the solid electrolyte. 88

5.2 Uniaxial stress σ versus strain ε curves for lithium metal at $T = 298$ K and different strain rates ($\dot{\varepsilon}$). Comparison between the experiments by LePage et al. [20] (symbols) and numerical predictions of the model (lines) for the parameters listed in Table 5.2. . 92

5.3 Single void boundary value problem: dimensions, configuration and boundary conditions. The initial conditions and governing equations for the electrolyte and electrode domain are also included. 94

5.4 Numerical experiments on a single void model: voiding and local current hot spots under stripping, as characterised by the evolution of the phase field order parameter in the electrode and the current density distribution in the electrolyte. 95

5.5 Numerical experiments on a single void model: voiding and local current hot spots under plating, as characterised by the evolution of the phase field order parameter in the electrode and the current density distribution in the electrolyte. 96

5.6 Numerical experiments on a single void model: quantifying changes in void shape for (a) stripping and (b) plating. The results are shown relative to a Cartesian coordinate system (x_1, x_2) whose origin is located in the centre of the circle containing the semi-circular void, with x_2 being perpendicular to the electrode-electrolyte interface. 97

5.7 Numerical experiments on a single void model: quantifying the role of the applied current i_{app} for (a) stripping and (b) plating. Results are shown for a time of 1 h and relative to a Cartesian coordinate system (x_1, x_2) whose origin is located in the centre of the circle containing the semi-circular void, with x_2 being perpendicular to the electrode-electrolyte interface. 99

5.8 Numerical experiments on a single void model: quantifying the role of the phase field kinetic parameter L for (a) stripping and (b) plating. Results are shown for a time of 1 h and relative to a Cartesian coordinate system (x_1, x_2) whose origin is located in the centre of the circle containing the semi-circular void, with x_2 being perpendicular to the electrode-electrolyte interface. 101

5.9 Numerical experiments on a single void model: quantifying the competition between Li diffusion and creep; (a) void shape evolution relative to a Cartesian coordinate system (x_1, x_2) whose origin is located in the centre of the circle containing the semi-circular void, with x_2 being perpendicular to the electrode-electrolyte interface, and (b) percentage change in void radius versus time. 103

5.10 Solid-state cell with multiple interface defects: dimensions, configuration and boundary conditions. Initial and boundary conditions are also provided. Six voids of different radii are introduced to induce an uneven current distribution; as quantified in the schematic, these voids are placed at arbitrary locations along the electrode-electrolyte interface. . 105

5.11 Numerical experiments on a Li metal anode - LLZO electrolyte system under realistic conditions: predictions of void evolution and current distribution for several stripping and plating cycles. 106

5.12 Numerical experiments on a Li metal anode - LLZO electrolyte system under realistic conditions: influence of the applied pressure p in the void evolution and current distribution. A complete charge-discharge cycle over 2.5 h is simulated, starting with a 1.25 h stripping half cycle. The figures display the results obtained after 30% of the stripping ($t = 22.5$ min.) and plating ($t = 97.5$ min.) half cycles. 107

6.1 a) Cells forgoing the active anode material (right) could effectively reduce the stack volume by approximately 15% compared with Li-excess SSBs (left). b) to d) Illustrate the cell voltage fluctuations during Li deposition onto copper foil at current densities of 0.5, 1, and 1.5 mA cm^{-2}, under a stack pressure of 15 MPa. e) Presents a synchrotron X-ray tomography cross-section of the anode-free SSB after depositing 5.5 mAh cm^{-2} Li at 0.5 mA cm^{-2}, featuring a close-up to highlight thickness variations. f) Depicts a mapping of Li layer thickness over an area of 800 um by 800 um, where brighter colours signify thicker Li layers, as indicated by the legend bar on the right [21]. 111

6.2 Cycling performance of anode-free SSBs: a) Demonstrates the Cu/LPSC/Li half-cell cycling at 0.5 mA cm^{-2}, featuring an in-situ deposited capacity of 3 mAh cm^{-2}. b) Showcases the Cu/LSPC/NMC full-cell cycling at the same current density, with the NMC cathode initially holding a capacity of 3 mAh cm^{-2}. c) Compares these results with a Li-excess full-cell (Li/LPSC/NMC) cycled under identical conditions, where the NMC cathode has a 3 mAh cm^{-2} capacity, supplemented by a pre-existing Li metal anode measuring 0.3 mm [21]. 113

6.3 A diagram illustrating the material and morphological changes at the interface between the copper substrate and the SSE in an anode-free SSB: a) Initial state of the interface immediately following the first in-situ lithium deposition. b) Morphology of the interface approaching the completion of lithium stripping, with current constrictions present but not yet reaching the critical threshold for void formation. c) As stripping continues, current constrictions intensify, causing localized current densities to exceed the critical level for void formation, leading to the emergence of voids at the Li/SSE interface. d) During the plating half-cycle succeeding c), current constrictions elevate local current densities significantly above the overall current density, surpassing the critical threshold for lithium filament growth and facilitating its development. 115

6.4 Sketch of the simulated domain, including the Li metal anode and the SSE, with the associated governing equations of the model. The initial and boundary conditions are also provided. 119

6.5 Mechanistic numerical predictions of stripping behaviour (as characterized by the phase field parameter ξ within the lithium metal) and normalized current in the SSE i_l/i_{app}, where i_{app} is the globally applied current of 0.25 $\text{mA}\,\text{cm}^{-2}$. a) Initial geometry and conditions shortly after stripping begins ($t = 0+$), with a small lithium bulge introduced to mimic the result of uneven plating/stripping. b) Later in the stripping process ($t = 3300$s), showing some voiding and current localization at the lithium bulge. c) Snapshot after the surrounding flat lithium area has been fully stripped ($t = 3800$s), revealing localized voiding and significant localization of current at the bulge. 122

7.1 Model setup for quantitative studies. 125

7.2 Numerical results of the final moment before complete interfacial contact loss happens under different stripping current densities and constant pressure of $p = 0.005$ MPa. The viscoplastic material model is adopted for the Li metal anode. $t = 0^+$ is the communal initial state for all current density cases. 127

7.3 Results of the numerical experiments showing a) The precise locations of the void interface that is shown in Fig. 7.2 (represented by $\xi = 0.5$) for different applied current densities. (x_1, x_2) is a Cartesian coordinate system with its origin located at the centre of the void and x_2 in the perpendicular direction of the Li/SE interface. The coordinate system is normalized by the initial radius of the void R_0, and b) the magnitude of ξ and i/i_{app} along the Li/SE interface under $i_{\text{app}} = 0.1$ $\text{mA}\,\text{cm}^{-2}$ at different stripping moment t. 128

7.4 Evolution of the cell voltage versus time during stripping considering the creep deformation of the Li metal anode. The FE predictions are depicted by solid lines, with different stripping current densities represented by distinct colours. The circles represent experimental data reported by Lee et al. [22]. 129

7.5 An illustration of the power-law fit between L and $i_{\text{app}}/i_{\text{r}}$. 131

7.6 Evolution of the cell voltage versus time during stripping considering the elastic deformation of the Li metal anode. The FE predictions are depicted by solid lines, with different stripping current densities represented by distinct colours. The circles represent experimental data reported by Lee et al. [22]. 132

7.7 a) Numerical contours of the final moment before complete interfacial contact loss happen under different stripping current densities and constant pressure of $p = 5.6$ MPa. A linear elastic material model is adopted for the Li metal anode. $t = 0^+$ is the communal initial state for all current density cases. b) The precise locations of the void interface (represented by $\xi = 0.5$) for those shown in a). c) and d) SEM images and sketch (top right illustration) of the Cu substrate, Li anode, and the LLZO after stripping at current densities of 0.1 and 0.4 mA cm^{-2}, respectively [22]. 133

7.8 The reduction of the active area ratio of the interface as stripping proceeds for different current densities under an applied pressure of 5 MPa. The solid lines are the simulation outputs, and the circles are experimental data reported by Lu et al. [23]. 134

Chapter 1

Introduction

In an era of rapid technological advancement, the quest for an efficient, reliable, safe, and environmentally friendly energy storage solution has never been more critical. And batteries constitute the core of this quest - the powerhouses that drive our society forward and make it run efficiently. In the past decades, batteries featuring intercalating lithium ions and organic solution electrolytes have gained considerable progression and thus led to a revolution in portable devices and electric vehicles (EVs). While the improvements are multifaceted and remarkable, specifically in energy density and safety, they are reaching a development plateau where further advancements become extremely difficult [24]. Changing the lane becomes a better choice. In this context, various alternatives have been raised. Among all these routes to the future, solid-state batteries (SSBs) have emerged as a beacon of hope, promising to revolutionize energy storage with their superior safety guarantees, higher energy densities and wider working condition windows compared to liquid-based Li-ion batteries [24]. However, just as all newly developing technologies, SSBs are facing significant commercial realization hurdles that significantly undermine battery performance and longevity and bring unacceptable safety risks for public daily utilization. Hence, understanding and addressing the mechanisms behind this issue and tackling the corresponding challenges is not just about answering a scientific inquiry but more importantly, a crucial step towards a realizable electrified society of the future that relies on sustainable energy.

1.1 Background

The journey of lithium batteries, a cornerstone of modern energy storage technologies, began with the discovery of lithium in 1817 by Swedish chemist *Johan August Arfwedson*. The position of lithium as a prime candidate for energy storage is attributed to its low mass density ($0.534\ \mathrm{g\,cm^{-3}}$), high

theoretical specific energy density (3860 $mAh\,g^{-1}$, or approximately 350 $Wh\,l^{-1}$, as shown in Fig. 1.1), and favourable electrode potential with respect to standard hydrogen electrode (−3.04 V) [25]. Early explorations in the 1970s demonstrated lithium metal's utility in primary cells, offering high capacity and variable discharge rates [1]. However, lithium's high reactivity with liquid electrolytes and the consequent dendritic growth led to its gradual abandonment in favour of safer alternatives. The shift was marked by the identification of intercalation compounds as viable alternatives to substitute metallic Li, laying the groundwork for the lithium-ion battery (LIB) concept [26, 27]. Since lithium existed as an ion instead of a metallic state in LIB, the dendrite problem was solved. The commercial breakthrough came in 1991 with Sony's launch of the first lithium-ion battery, characterized by lithium cobalt oxide ($LiCoO_2$) cathode, hard carbon anode [28], and liquid-state electrolyte composed of a mixture of organic solvent and Li salt, setting the stage for the extensive adoption and development of lithium-ion technology.

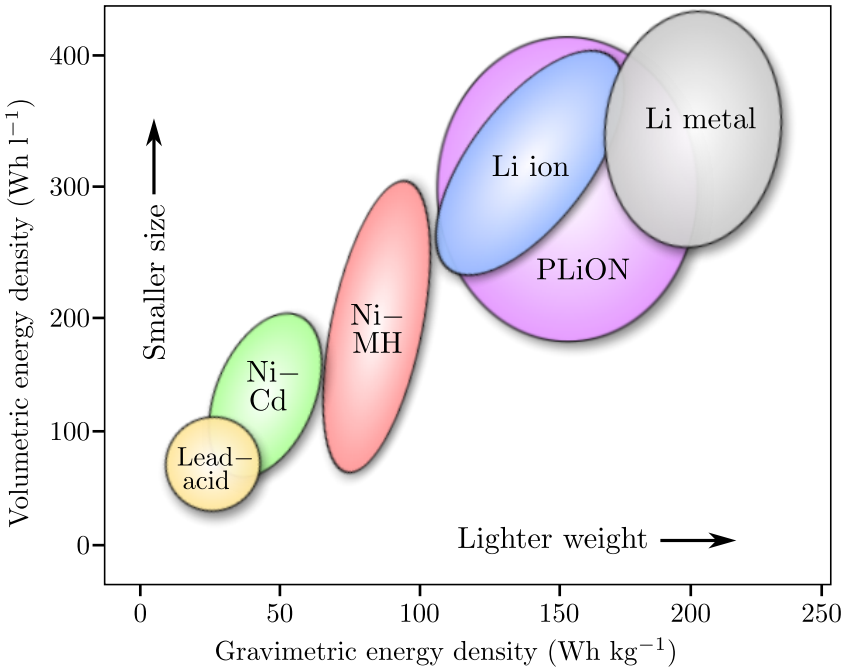


Figure 1.1: Comparative Analysis of Battery Technologies: Gravimetric ($Wh\,kg^{-1}$) and Volumetric Energy Densities ($Wh\,l^{-1}$) [1]. Lead-acid, known for its cost-effectiveness and recyclability, serves as a primary choice for car ignition and uninterruptible power supplies (UPS). Ni-Cd batteries, limited by memory effects and environmental concerns, are increasingly replaced by Li-ion alternatives. Nickel-metal hydride (Ni-MH) batteries, while being supplanted by Li-ion, still find niche applications, such as in security system backups. Li-polymer (PLiON), Li-ion, and Li metal batteries represent the forefront of ongoing research and development in energy storage technologies.

Over the years, significant advancements have been made. The cutting-edge liquid-based LIBs have shifted to ternary cathode material, for example, $LiNi_{1-x-y}Co_xMn_yO_2$ (NCM), for higher energy densities and improved safety features [28], reflecting an enduring pursuit of more efficient, reliable,

and safer energy storage solutions. Governments globally also increasingly recognise the advent of a new era powered by electrification. In 2010, the Electric Vehicles Initiative (EVI) was launched by the International Energy Agency (IEA), marking the establishment of a collaborative policy forum involving multiple governments. This initiative spurred a decade of intensified research and production of electric vehicles across various nations. Over ten years later, the outcome of this campaign is remarkable. From 2018 to 2022, the total number of EVs in circulation increased more than five-fold, with over 26 million EVs now operating on the roads worldwide (see Fig. 1.2). In the meantime, the development of EVs will inevitably lead to an increasing demand for EV batteries. According to the IEA predictions, global EV stock and the corresponding demand for electricity will expand nearly tenfold in the next ten years.

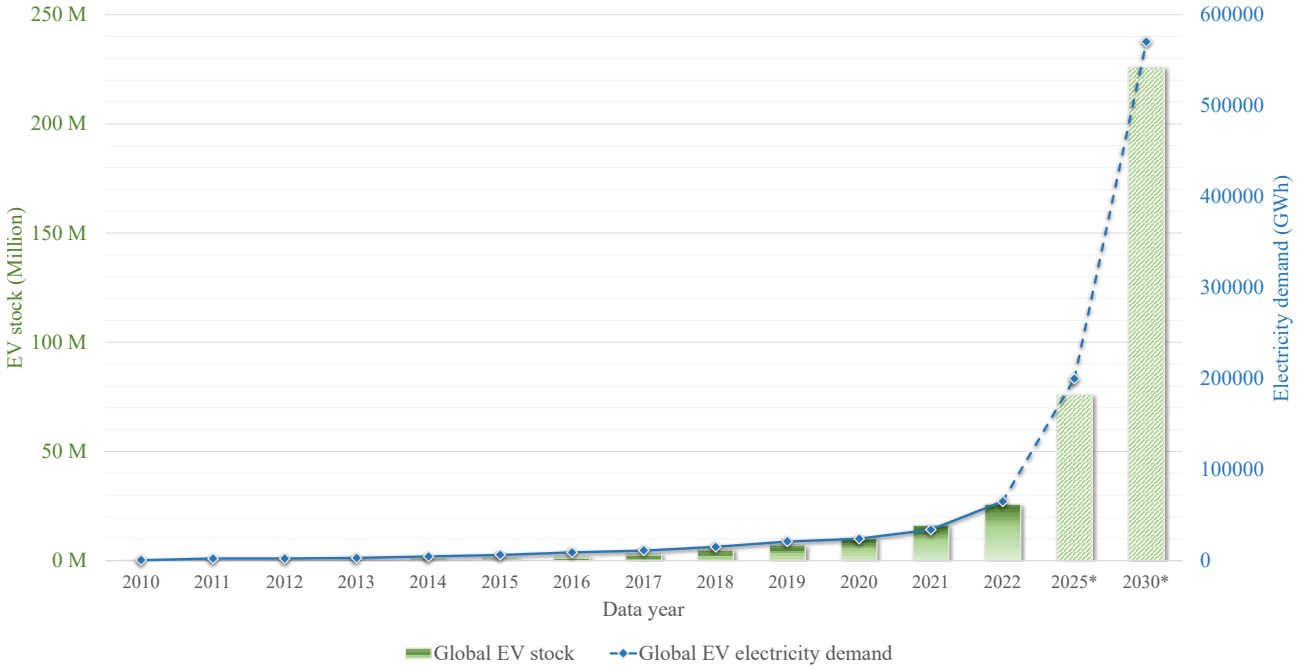


Figure 1.2: Global EV stock (in million) and EV electricity demand (in GWh): historical data and future predictions (years with *). EVs include Battery Electric vehicles (BEVs) and Plug-in Hybrid Electric Vehicles (PHEVs). The prediction data are evaluated under the Stated Policies Scenario (STEPS). All data come from the 'Global EV outlook 2023' by the IEA [2].

Despite the flourishing of the new EV market and the great progress made in the traditional liquid-based LIBs, range anxiety on EVs has never gone away, and batteries are still struggling to reach the expectations of a fully electrified society. The underlying cause behind this reality is insufficient specific energy density. Janek and Zeier predicted both in their early comment article in 2016 and the most recent review article in 2023 that the performance of the liquid-based LIBs will inevitably reach a physicochemical limit and a follow-up revolutionary technology is in urgent need [24, 29]. For the new generation of batteries to gain market acceptance and achieve success, it is essential to simultaneously

possess the following characteristics: high energy density, high power density, high energy efficiency, high capacity retention, a broader range of operating conditions, and most importantly, utmost safety [30]. Solid-state batteries, which emerged as the most potential and realistic alternative to liquid-state batteries (LSBs), have drawn tremendous research attention throughout the past decades. The number of relevant publications has grown almost exponentially from the year 2011 to 2022 (see Fig. 1.3 for the growth of the number of publications related to the keyword 'solid state battery*' on Web of Science for the past 20 years). 2011 can be regarded as the first year of the solid-state battery research explosion, which is when Kamaya et al. [31] discovered the lithium superionic conductor $Li_{10}GeP_2S_{12}$ that featured comparable Li-ion conductivity (1.2 $S\,m^{-1}$ at room temperature) against its organic liquid competitor, which not only solved the fundamental difficulties that have hindered the development of solid-state battery for many years but more importantly, reignited the research craze for it.

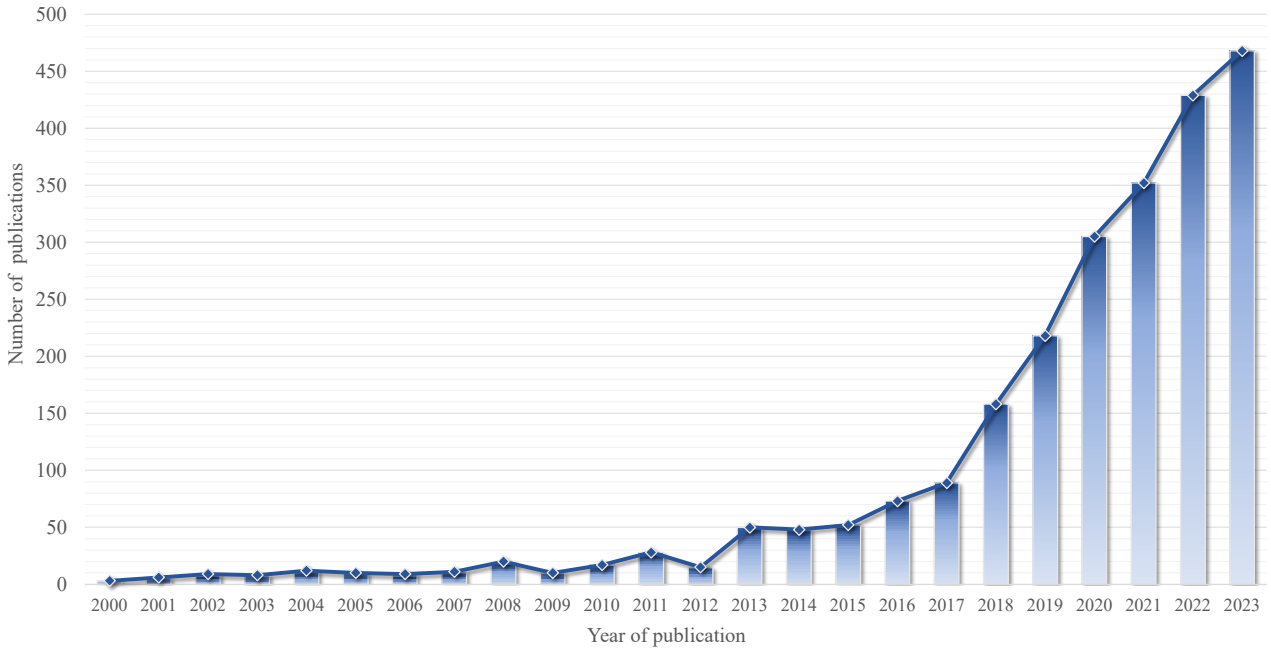


Figure 1.3: Number of publications containing 'solid state battery*' from the year 2000 to 2023, data collected from Web of Science in January 2024.

An SSB presents a significant advancement over LSBs by substituting the liquid electrolyte with a solid counterpart. This seemingly simple modification yields a host of exciting new features for batteries. Among these benefits are a substantially higher specific energy density, rapid charging and discharging capabilities, enhanced thermal stability providing increased safety, and a wider range of application scenarios [24, 32]. Fig. 1.4 illustrates typical structures of an LSB and an SSB. State-of-the-art LSBs commonly adopt a solution of ethylene carbonate (EC) and diethyl carbonate (DEC) solvent and $LiPF_6$ solute, while dominant electrolyte materials of SSBs include sulfides-, halides-, polymers- and

oxides-based solid ion conductors [3]. The introduction of a solid ion-conductor revolutionizes battery design by enabling the employment of a pure metallic lithium anode, a strategy not feasible in LSBs due to lithium's high reactivity with liquid electrolytes and uncontrollable Li dendrite growth. The primary attractive benefit of a Li metal anode lies in its substantial enhancement of energy storage efficiency. For a tangible illustration, an SSB equipped with NCA ($LiNi_{0.8}Co_{0.15}Al_{0.05}O_2$) cathode could potentially elevate the specific energy to 393 $Wh\,kg^{-1}$ and the energy density to 1143 $Wh\,L^{-1}$. In contrast, an LSB with the same NCA cathode achieves 264 $Wh\,kg^{-1}$ and 635 $Wh\,L^{-1}$ according to Betz et al. [33]. This indicates a respective improvement of at least 50% and 80% by introducing Li metal anode.

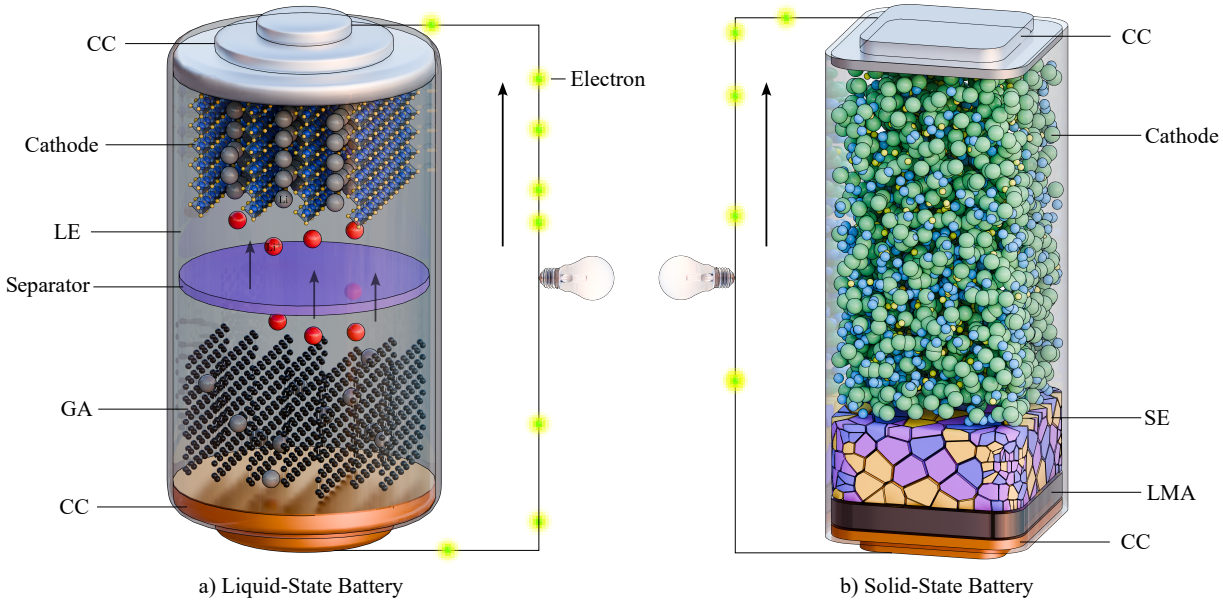


Figure 1.4: Sketch of the typical structures of the state-of-the-art batteries, including a) a liquid-state Li-ion battery, which is usually composed of current collectors (CC), a ternary material cathode such as NCM, a graphite anode (GA), a separator and liquid electrolyte (LE), and b) a solid-state Li-ion battery, which is different from an LSB with solid electrolyte (SE) and lithium metal anode (LMA).

However, research and development (R&D) efforts for SSBs have faced considerable challenges over the past decades, with several critical issues impeding their path to practicality and commercialization. These hurdles are predominantly interface-related, affecting the anode-solid electrolyte (SE), cathode-SE, and electrode-current collector (CC) interfaces, as identified in Fig. 1.5. Interface stability is vital for SSBs' long-term cycling performance, directly influencing their economic viability and energy storage efficiency [29]. Addressing these challenges requires a nuanced approach that not only stabilizes and maintains effective contact at solid-solid interfaces within the electrochemical environment but also considers the energy density, battery safety and production cost. A solution that significantly increases

the mass and volume of inactive materials, leading to lower energy efficiency than LSBs, or exhibits higher safety risks would not be deemed successful. Despite the myriad of obstacles, the good news is that they can be largely consolidated into a primary focus on interface stabilization. Coping with this central focus enables targeted advancements in overcoming the principal barriers to the development of SSBs.

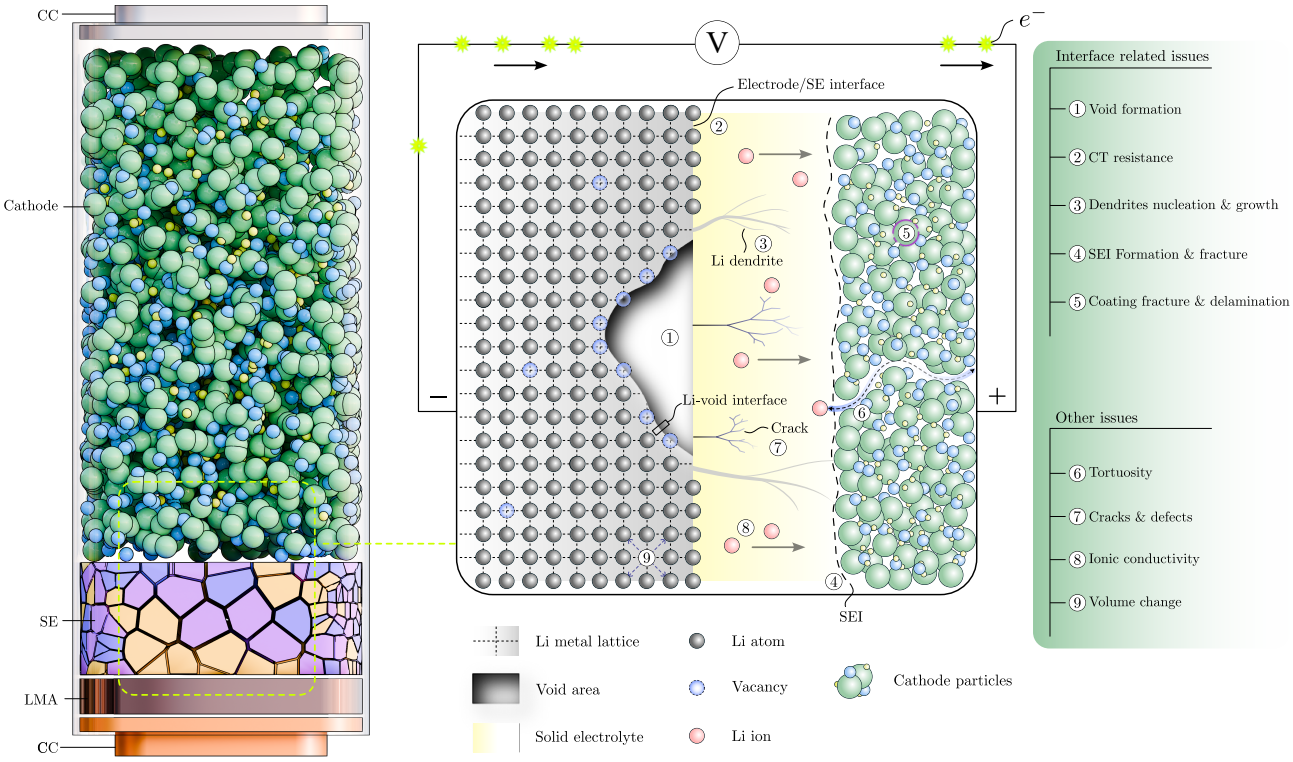


Figure 1.5: Main challenges confronting the practicality and commercialization of SSBs, including interface-related issues: void formation, high charge transfer resistance, dendrite nucleation and growth, solid electrolyte interphase (SEI) formation and fracture, and coating fracture and delamination of cathode particles; non-interface issues: cathode tortuosity, cracks and defects in the SE, SE's ionic conductivity, and electrode volume changes during battery cycles.

1.2 Research Aim and Thesis Overview

The overarching aim of this research is to develop a comprehensive theoretical framework aimed at overcoming the most formidable challenges encountered by SSBs, with a particular focus on interface-related issues. This framework endeavours to integrate multiple disciplines, encompassing electrochemistry, solid mechanics, and thermodynamics, to capture the complex behaviour of SSBs during operation in an accurate way. Central to this thesis is addressing the critical question: What causes the deterioration of the contact integrity during battery cycling, and what could be done to mitigate or even reverse this process?

To answer this critical question and establish a model for systematic analysis, knowledge of the continuum mechanics of solids and electrochemical systems is required. An in-depth understanding of phase field methods and numerical modelling approaches is also necessary. With the foundation of the theory established and firmly grasped, the derivation of the model can be presented. To document this process in a clear and unambiguous way, the thesis is arranged as follows:

- Chapter 1 (this chapter) provides the necessary background information and the motivation underpinning this research project.
- Chapter 2 is a comprehensive review of the development of the SSBs and modelling attempts in recent years. In this chapter, the key challenges hindering the commercialization of SSBs and the technical gap that necessitates research investigations are identified.
- Chapter 3 lists all the necessary theory fundamentals for the establishment of the multi-coupling model that is presented in this work.
- Chapter 4 provides detailed derivation for the establishment of the model and remarks on numerical implementations.
- Chapters 5 and 6 verify the model's effectiveness in qualitative predictions through several case studies, including collaborative work with our laboratory colleagues.
- Chapter 7 presents quantitative analysis utilizing this model. However, critical limitations are identified, and the influence of the limitations is discussed.
- Chapter 8 is the end of the journey. The insights gained throughout this research are discussed, and potential future directions are suggested.

Chapter 2

Development of SSB Technology: An Overview

This chapter aims to provide a coherent and comprehensive overview of the major advances in experimental research and theoretical modelling that underpin the development of SSBs. The chapter is structured as follows: Section 2.1 lists landmark laboratory discoveries in SSE materials, as well as techniques exploited in recent years to realize practical SSBs. Section 2.2 summarizes representative modelling attempts that are targeted at providing insights and deepening our understanding of the key challenges facing SSBs. By reviewing these advances, we aim to show how the research community has progressively addressed key challenges, such as enhancing interfacial stability, improving ionic conductivity, and mitigating mechanical degradation. This dual perspective not only celebrates the achievements to date but also identifies key avenues for future research, thus paving the way for the next leap in SSB technology.

2.1 State-of-the-Art Materials and Cutting-Edge Technology

2.1.1 SSE Materials

The identification of lithium metal's exceptional energy storage capabilities catalyzed a sustained pursuit to exploit lithium metal as the most ideal material for advanced battery technologies. However, the inherent high chemical reactivity of alkali metals rendered the combination of lithium metal with aqueous lithium-ion conductor electrolytes for battery fabrication impracticable. This realization necessitated a shift towards SSE as a viable alternative. In their comprehensive review, Chen et al. [3]

amply documented the evolution and discovery of critical SSE materials pivotal to the advancement of SSB technology, encapsulating the cumulative technological progress achieved over the preceding century and up until 2016 (Fig. 2.1).

The quest for an ideal SSE demands a material to exhibit high ionic conductivity akin to liquid electrolytes while maintaining electrochemical stability across a wide voltage window, possess mechanical robustness to resist dendrite penetration and meanwhile offer good mechanical compatibility with electrodes, and is cost-effective [34]. Over the past decades, considerable efforts have been devoted to exploring and testing material combinations to meet these stringent standards. These materials are broadly categorized into inorganic SSEs (further divided into oxides, sulphides, and halides) and polymer SSEs [3].

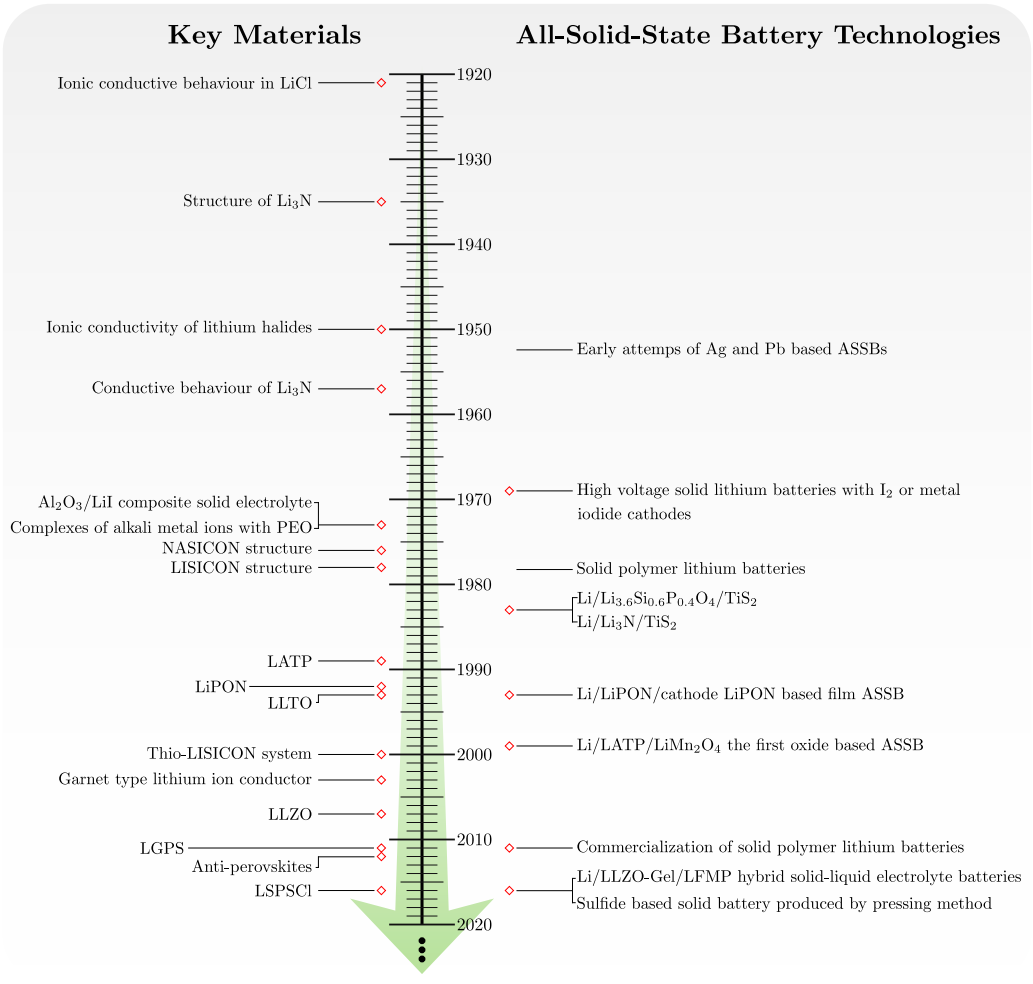


Figure 2.1: The advancement of key SSE materials and SSB technologies from 1920s to 2016 [3].

Inorganic SSEs

Progress was stalled prior to the 1970s, but a few promising SSE materials existed that could conduct ions, such as lithium chloride (LiCl) or lithium nitride (Li_3N). However, with their relatively low ionic conductivity and properties such as poor cycle life, they didn't get picked up for application or use. By the 1970s and 1980s, SSE materials exhibiting high ionic conductivity began to emerge. Among the notable advances, sodium superionic conductors (NASICON) with the structured framework $Na_{1+x}Zr_2P_{3-x}Si_xO_{12}$ were reported by Goodenough et al. [35] in 1976. This was closely followed by the introduction of lithium superionic conductors (LISICON), $Li_{2+2x}Zn_{1-x}GeO_4$, by Bruce and West [36] in 1983, showcasing conductivity levels around 10^{-7} S cm^{-1} at room temperature. These materials represented a significant leap in ionic conductivity over earlier lithium halide (e.g., LiI) and lithium nitride (e.g., Li_3N) based electrolytes, marking a pivotal moment in SSB development [37]. The 1990s heralded a new era with the advent of inorganic oxide materials as SSEs. A breakthrough came in 1993 when Inaguma et al. [38] identified chalcocite $Li_{0.34}La_{0.51}TiO_{2.94}$ (LLTO), achieving an ionic conductivity of 2×10^{-5} S cm^{-1}. The garnet-type solid electrolyte $Li_7La_3Zr_2O_{12}$ (LLZO), reported by Murugan et al. [39] in 2007, was characterized by its remarkable ionic conductivity and mechanical robustness and recognized as a promising candidate for SSB applications. A groundbreaking milestone was reached in 2011 with the discovery of $Li_{10}GeP_2S_{12}$ (LGPS) by Kamaya et al. [31]. The compound exhibited the highest ionic conductivity known at the time for SSE materials, achieving 1.2×10^{-2} S cm^{-1} at room temperature. This conductivity not only surpassed that of some traditional liquid electrolytes at that time but also marked a turning point in the commercial feasibility of SSBs. The pursuit of safer energy storage solutions with higher energy density, coupled with concerns over thermal runaway risks in conventional liquid electrolytes, reignited interest in SSB research–a field that had seen diminished activity following the widespread commercial success of liquid lithium-ion batteries in the 1990s. In 2016, the research community witnessed yet another breakthrough when Kato et al. [40] reported a chlorine-doped silicon-based compound, $Li_{9.54}Si_{1.74}P_{1.44}S_{11.7}Cl_{0.3}$ (LSPSCl), setting a new benchmark for ionic conductivity at 2.5×10^{-2} S cm^{-1} at room temperature. Following this, in 2018, Kraft et al. [41] delved into the impacts of germanium substitution in lithium argyrodites, $Li_{6+x}P_{1-x}Ge_xS_5I$, on the SSE overall performance. Their research demonstrated that, by applying cold pressing and hot sintering techniques, these materials could achieve an ionic conductivity of up to 2.11×10^{-2} S cm^{-1}, further affirming the viability of SSBs as a formidable option for next-generation energy storage solutions. Such advancements reinforce the notion that diverse material compositions

are capable of attaining, and even exceeding, the ionic conductivity thresholds deemed essential for commercial success, typically to be over 1×10^{-3} S cm^{-1} at room temperature [4, 34, 42]. This revelation underscores a crucial opportunity: with strategic and considered material engineering, the possibility to develop SSEs that not only achieve superior electrochemical performance but also maintain excellent mechanical synergy with electrodes exists.

Beyond oxide and sulfide SSEs, the exploration of solid-state halide electrolytes has not stood still. Despite the challenges faced by halide SSEs, such as suboptimal ion transport efficiency and vulnerability to moisture, their unique attributes have kept them in the realm of consideration. These include straightforward synthesis processes, the elimination of high-temperature treatments, and a degree of flexibility conducive to mechanical synergy with electrodes. In 2018, Asano et al. [43] introduced two new halide SSEs, Li_3YCl_6 (LYC) and Li_3YBr_6 (LYB), which demonstrated lithium-ion conductivities of 5.1×10^{-4} S cm^{-1} and 1.7×10^{-3} S cm^{-1}, respectively, with the latter meeting the threshold for commercial application. The year 2019 saw further advancements with Li et al. [44] reporting on Li_3InCl_6, produced through mechanical and annealing approaches, reaching a conductivity of 1.49×10^{-3} S cm^{-1} at room temperature. Enhancements to the synthesis of Li_3InCl_6 were achieved later in the same year by the same team [45]. They employed a water-mediated route, simplifying the preparation process and boosting the conductivity to 2.04×10^{-3} S cm^{-1}.

Polymer SSEs

Polymer SSEs are typically more flexible, with enhanced interfacial contact with electrodes compared to the more rigid inorganic SSEs, thereby exhibiting reduced interfacial resistance. However, their widespread adoption has been hampered by challenges such as low Li-ion conductivity and limited electrochemical window. In response, the development of hybrid inorganic-polymer composite SSEs has emerged as an alternative research avenue in recent years. These composites aim to merge the high ionic conductivity of inorganic SSEs with the advantageous deformability of polymers, thereby improving the overall performance of polymer SSEs. In this innovative field, the team led by John B. Goodenough has made significant strides. In 2020, they introduced a polymer-composite SSE by integrating two lithium-insulating oxides known for their high oxygen vacancy concentration–fluorite $Gd_{0.1}Ce_{0.9}O_{1.95}$ and perovskite $La_{0.8}Sr_{0.2}Ga_{0.8}Mg_{0.2}O_{2.55}$–with poly(ethylene oxide) (PEO) [46]. This composite demonstrated an ionic conductivity surpassing 10^{-4} S cm^{-1} at 30°C, marking a substantial improvement nearly two orders of magnitude greater than that of PEO alone, which is around 10^{-6} S cm^{-1}. Continuing their efforts to enhance the electrochemical performance and mechanical strength

of polymer SSEs, in 2021, Fang et al. [47] from Goodenough's group further innovated by incorporating Li_2S_6 into the PEO matrix. This addition achieved an ionic conductivity of 1.7×10^{-4} S cm^{-1} at 40°C, slightly above room temperature.

Table 2.1 presented below provides a comprehensive overview of the SSEs that are currently the focus of significant attention within the research community. This summary includes their chemical compositions, ionic conductivities, and the years they were reported, distinguishing them based on their classification into inorganic and polymer categories. The oxide, sulfide, and halide SSEs all belong to the inorganic category, while the polymer SSEs are described in terms of the polymer matrices used and the specific inorganic components they are combined with.

Table 2.1: Summary of typical SSE materials and their electrochemical properties

Category	Material	[1]σ_{Li^+} [S cm^{-1}] @ T_{mea} [°C]	Year	Ref
Inorganic	Li_3PS_4	3×10^{-7} @ RT	1984	TACHEZ et al. [48]
	$Li_{0.34}La_{0.51}TiO_{2.94}$	2×10^{-5} @ RT	1993	Inaguma et al. [38]
	$Li_7La_3Zr_2O_{12}$	3×10^{-4} @ RT	2007	Murugan et al. [39]
	$Li_{10}GeP_2S_{12}$	1.2×10^{-2} @ RT	2011	Kamaya et al. [31]
	$Li_{9.54}Si_{1.74}P_{1.44}S_{11.7}Cl_{0.3}$	2.5×10^{-2} @ RT	2016	Kato et al. [40]
	$Li_{6+x}P_{1-x}Ge_xS_5I$	2.11×10^{-2} @ RT	2018	Kraft et al. [41]
	Li_3YCl_6	5.1×10^{-4} @ RT	2018	Asano et al. [43]
	Li_3YBr_6	1.7×10^{-3} @ RT	2018	Asano et al. [43]
	Li_3InCl_6	$1.49 \times 10^{-3} \sim 2.04 \times 10^{-3}$ @ RT	2019	Li et al. [44, 45]
Polymer	PEO – $Gd_{0.1}Ce_{0.9}O_{1.95}$ – $La_{0.8}Sr_{0.2}Ga_{0.8}Mg_{0.2}O_{2.55}$	$\sim 10^{-4}$ @ 30	2020	Wu et al. [46]
	PEO – Li_2S_6	1.7×10^{-4} @ 40	2021	Fang et al. [47]

[1] σ_{Li^+} denotes the ionic conductivity, T_{mea} is the temperature at which the conductivity is measured.

The Dilemma of SSE Materials

The discussion thus far has centred on the advancements in SSEs with a focus on ion transfer efficiency—a critical property for SSBs. The efficiency of ionic transfer in SSEs is paramount, historically constituting a bottleneck in the advancement of SSBs. It is a feature that has a direct influence on the battery's charge and discharge rates, as well as its power density. Elevated ionic conductivity facilitates smoother

ion movement within the electrolyte, thereby enabling quicker charging and discharging processes. Decades of research have elevated the ionic conductivity of cutting-edge SSEs to levels on par with some commercially successful aqueous electrolytes, which is a notable achievement for SSB progress. Yet, meeting one single electrochemical requirement is insufficient for overcoming all the challenges SSBs face. Persistent issues, such as the growth and penetration of Li dendrites through the electrolyte, remain unresolved and continue to impede the commercial success of SSBs [29, 42, 49–51]. It was once hypothesized that SSEs with high mechanical strength could provide a definitive solution to dendrite challenges [8], positioning inorganic SSEs with superior mechanical moduli as particularly promising candidates. However, subsequent studies have indicated that, although these materials can mitigate the issue, they fail to eliminate it. Dendrite penetration still occurs and can trigger irreversible SSB failure after fewer charge/discharge cycles than required for commercial viability. This problem is often linked to inadequate interfacial contact between the inorganic SSE and the electrodes. Additionally, the manufacturing of inorganic SSEs typically involves complex, high-temperature treatments, adding to additional production costs. Furthermore, long-term atmospheric exposure can cause some inorganic SSEs to degrade or decompose (e.g., sulfide SSEs release toxic H_2S gas in humid conditions, and oxide SSEs can generate carbonate impurities at the electrode/SSE interface, causing interfacial resistance to increase [3]).

Polymer SSEs stand out for their distinct advantages in mechanical compatibility with electrodes, enabling them to form and sustain relatively robust interfacial contacts throughout battery cycles. They are also noted for their superior electrochemical stability and more straightforward manufacturing processes [3]. To address the challenges associated with their inherently low ionic conductivity and mechanical strength, significant advancements have been achieved by incorporating inorganic Li salts into the polymer system, thereby creating polymer-composite SSE materials that are both fast in ion conduction and flexible confronting interface contact degradation, which makes them highly anticipated candidates paddling the SSB technology revolution. Nevertheless, formidable challenges still exist; notably, their ionic conductivity often fails to meet the requisite levels for commercial deployment, with few material combinations reaching the necessary benchmarks [3, 52]. Furthermore, the limited electrochemical stability window of these composites compromises the batteries' performance at high voltages and limits compatibility with a range of electrode materials [3], undermining their potential to enhance battery energy density.

In summary, the SSE materials discussed in this section each present distinct advantages yet concurrently encounter numerous shortcomings and challenges. To date, no single material has

emerged that wholly satisfies the comprehensive spectrum of requirements encompassing chemistry, electrochemistry, mechanics, thermal stability, safety, and cost-effectiveness, presenting a formidable challenging task. Among the most critical issues to address is the growth and penetration of Li dendrites, a problem largely contingent on the ability to establish and maintain robust contact at the electrode/SSE interface and on the electrolyte's strength and internal microstructure to effectively keep dendrite proliferation outside its outer surface. Polymer composites emerge as a promising avenue for addressing this challenge, yet it is clear that success will necessitate meticulous material selection and strategic design. More importantly, a deeper understanding of the underlying mechanisms will be instrumental in devising effective strategies to overcome this issue.

2.1.2 Approaches to Improve Performance of SSBs

The inner circle of Fig. 2.2 summarized the critical challenges confronting SSBs, encapsulating issues such as low ionic conductivity, dendrite growth, material degradation, and the loss of contact at the electrode/SSE interface. Concurrently, the outer circle presents a compendium of the prevailing solutions devised to mitigate these concerns.

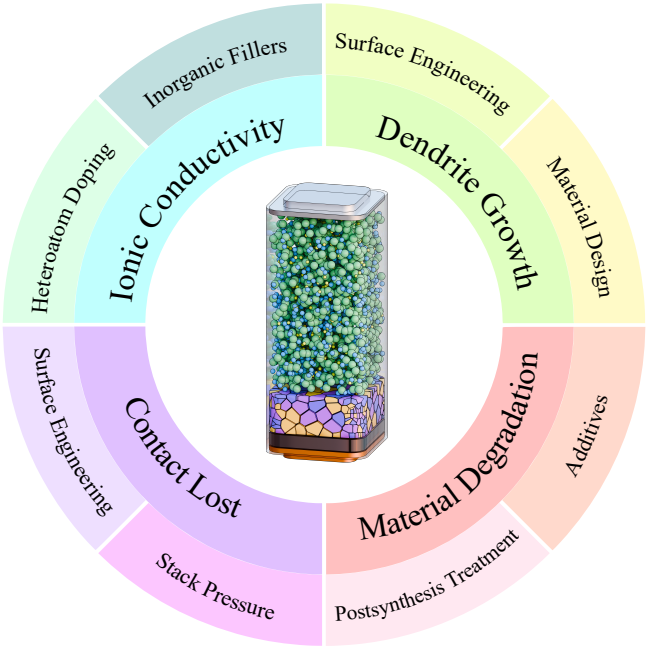


Figure 2.2: The major issues faced by SSBs and the corresponding solutions.

Approaches to Improve Ionic Conductivity

Heteroatom doping is a widely adopted strategy for enhancing the ionic conductivity of inorganic SSEs. The mechanisms include: i) The dopants introduce additional vacancies and defects in the crystal

structure of the electrolyte, providing additional transport channels for the ions. ii) The dopants can induce lattice distortions or phase transitions, potentially rendering the crystal structure more favourable to ion migration. iii) Through careful selection of type and quantity management of dopants, it's possible to diminish the energy barriers obstructing ion movement across the lattice, making it easier for ions to hop between the vacancies [53]. The effort made by Li et al. [54] to improve the electrochemical properties and minimize the release of H_2S gas of the sulfide-based SSE $Li_7P_3S_{11}$ by doping indium to form $Li_7P_{2.9}S_{10.9}In_{0.1}$, as well as LGPS and LSPSCl mentioned in the previous section are all representative examples. Furthermore, the doping technique has also enabled the development of a broad spectrum of oxide SSEs based on garnet-type LLZO. Thangadurai et al. [55] offered an extensive overview of these derivative materials in their review.

Inorganic fillers, on the other hand, are primarily utilized to rectify the inherent limitations of polymeric solid electrolytes, particularly their low ion transport efficiency. This approach was first reported by Skaarup et al. [56] in 1988, who demonstrated a remarkable increase in ionic conductivity—three orders of magnitude higher—of a new SSE created by blending $LiCF_3SO_3$ and Li_3N with PEO compared to pure PEO. More recently, an integrated SSB reported by Wan et al. [4] has garnered notable interest. This study utilized PEO/LITFSI (PL) as both the cathode binder and the composite electrolyte matrix, incorporating LLZO nanowires as the enhancing agent to create a ceramic-filled composite SSE (PLLN). The PLLN was then thermally fused with $LiFePO_4$ cathode to establish an integrated SSE-cathode configuration. The test outcomes highlighted a remarkable improvement in electrochemical performance compared to using solely PL or PL with LLZO microparticle enhancement (PLLM). And the ionic conductivity of this new setup reached $2.39 \times 10^{-4}\ \mathrm{S\,cm^{-1}}$ at room temperature.

Both heteroatom doping and inorganic filling have the potential to significantly enhance SSE materials' electrochemical performance. However, the journey is neither straightforward nor without its challenges. Factors such as the quantity of doping atoms, the complexity of synthesizing the resultant compounds, the physicochemical attributes of the dopants, and even their rarity must be carefully considered. Likewise, the amount, size, morphology, and distribution of inorganic fillers decisively influence the properties of the final polymer-composite materials. Consequently, thorough justification and precise calculations are imperative before finalizing the composition of new material to prevent undue resource expenditure and avert performance declines due to inappropriate combinations of materials.

Approaches to Mitigate Material Degradation

Material degradation is a critical concern related to the chemical stability of SSEs, which is linked to their intrinsic properties. Specifically, in humid environments, sulfide SSEs are susceptible to generating H_2S, whereas oxide SSEs tend to experience H^+/Li^+ exchange, leading to the formation of a Li_2CO_3 impurity layer. This layer significantly impairs the interface's wettability and causes the interface resistance to increase considerably. Both scenarios underscore the critical role of the intrinsic properties of SSE in chemical stability. As for the mitigation solutions, oxides possess the capability to absorb H_2S, hence can be incorporated as oxide additives into sulfide SSEs and markedly diminish H_2S emission [57]. Yet, this measure may inadvertently elevate the energy barrier for ion hopping, thereby reducing the SSE ionic conductivity [58]. The impurity layer formation on oxide SSE interfaces can be effectively mitigated through straightforward post-synthesis treatments, such as grinding and polishing in an inert atmosphere [5, 59]. Interestingly, these procedures, despite their simplicity, are very effective. Significant interfacial resistance drop to a level comparable to that of the solid-liquid interface of a conventional liquid battery ($\sim 2\ \Omega\,cm^{-2}$) can be achieved, as reported by Sharafi et al. [5].

Approaches to Enhance Interface Contact and Inhibit Dendrite Growth

Interfacial contact loss and dendrite growth are interrelated challenges, with numerous studies highlighting their intrinsic causality [11, 21–23, 60–64]. Loss of interfacial contact causes poor contact between the electrode and the SSE, leading to reduced charge transfer efficiency. Dendrite growth mainly occurs during battery cycling, especially during charging. Dendritic structures composed of electrode active materials form due to the uneven deposition triggered by high local current density at the electrode/SSE interface. The dendrite can intrude into and penetrate even the 'hardest' SSEs, such as ceramic LLZO [65], causing battery short circuits. The generally recognised mechanism of the mutual reinforcement effect between the two phenomena (using the anode/SSE interface as an example) is: i) initial interfacial inhomogeneity leading to uneven current density distribution, which, during discharge, results in a faster lithium dissolution rate in areas of high current density, exacerbating surface unevenness, reducing effective contact area (contact loss), and further unbalancing current density distribution; ii) during subsequent charging, the uneven distribution causes lithium deposition rates in high current density areas to significantly exceed the average, favouring dendrite nucleation and growth; iii) through ongoing battery cycling, these two processes reinforce each other, deteriorating

interface morphology, further diminishing effective contact area, and concentrating current densities at narrow points until dendritic failure becomes inevitable.

Building on the proposed mechanism, some researchers have identified interfacial engineering as a promising strategy to enhance interfacial contact and inhibit dendrite formation simultaneously. A common technique involves introducing an interlayer between the metal electrode and SSE (as shown in Fig. 2.3c). In their studies, Tsai et al. [66] polished an Al-contaminated, Ta-substituted LLZO surface and inserted a thin Au layer to bolster contact with the Li metal electrode. The results showed that the formation of dendrites was delayed. However, as the current densities in the galvanostatic cycling were increased, dendrites still emerged. Tsai et al. [66] attributed this outcome to the disparity in ionic conductivity between the grain and grain boundary of the ceramic SSE, leading to uneven lithium deposition over multiple high-current-density cycles. Similar conclusions were drawn by Krauskopf et al. [67] that the occurrence of dendrites is related to the microstructural characteristics of the LLZO. Notably, they also suggested that the introduction of a lithium alloy interlayer does not inherently alter the dynamics at the interface. Thus, for effective dendrite suppression, it is crucial that the lithium diffusivity of the alloy is sufficiently high. This ensures that the maximum lithium fluxes the interlayer can accommodate exceed those induced by the applied current densities. Otherwise, the existence of the interlayer may, on the contrary, compromise the SSB performance under high current density. Another noteworthy endeavour is the formation of a graphite interlayer between the Li metal electrode and the garnet-type $Li_{5.9}Al_{0.2}La_3Zr_{1.75}W_{0.25}O_{12}$ (LALZWO) ceramic electrolyte, as conducted by Shao et al. [68] through the simple technique of drawing a graphite layer onto the Li metal surface using a pencil. Given its good ductility and compressibility, it is reasonable to consider graphite as a good candidate to alleviate difficulties in forming effective contact between ceramic SSEs and metal electrodes. Meanwhile, graphite is found to be capable of spontaneously forming a LiC_6 layer with excellent ionic and electronic conductivity after a period of contact with lithium, thus facilitating stable and uniform ion transfer at the interface [68]. The experimental findings show the great potential of utilizing graphite as an interlayer, with the tested lithium-symmetric battery demonstrating remarkable cycling stability—over 500 cycles under galvanostatic conditions with an applied current density of 0.3 $mA\,cm^{-2}$ at room temperature and a total stable cycling duration exceeding 1000 hours. This achievement represents one of the most impressive cycling performance outcomes reported for SSBs to date.

Applying stack pressure is also recognized as an effective strategy to enhance contact at the electrode/SSE interface [7, 19, 62, 69–72]. This approach leverages the low-yield stress characteristic

of lithium, which, under applied pressure, will experience creep deformation and allow the voids at the interface to be refilled, thus improving interfacial contact and lowering interface resistance. Following the identification of the pressure-dependence of the interfacial resistance, higher and higher pressures have been applied to the systems of potential SSB candidates, ranging from a few megapascals [62] to tens and hundreds of megapascals [7, 73]. While the beneficial impact of pressure on interfacial contact is undoubted, overly high pressures are not expected either from the mechanical stability point of view or from the industrial feasibility. Doux et al. [7] documented an instance of immediate dendrite failure in SSBs attributed to the application of excessive pressure (75 MPa), where the lithium metal was compelled to intrude into the SSE's microscopic structures, forming 'artificial' dendrites before the battery cycles began. Consequently, recent investigations have shifted focus towards the exploration of strategies to prevent lithium dendrite formation under low or zero pressure conditions [74, 75].

Through material design, composite SSEs, which combine the high ionic conductivity advantage of inorganic SSEs and the superior mechanical compatibility of polymer SSEs, are also one of the solutions that have attracted much attention in recent years as a potential solution to simultaneously resolve the poor interfacial contact and dendrite growth issues. The details of this strategy have been elaborated in Section 2.1.1 and discussed in Section 2.1.1 and will not be reiterated here.

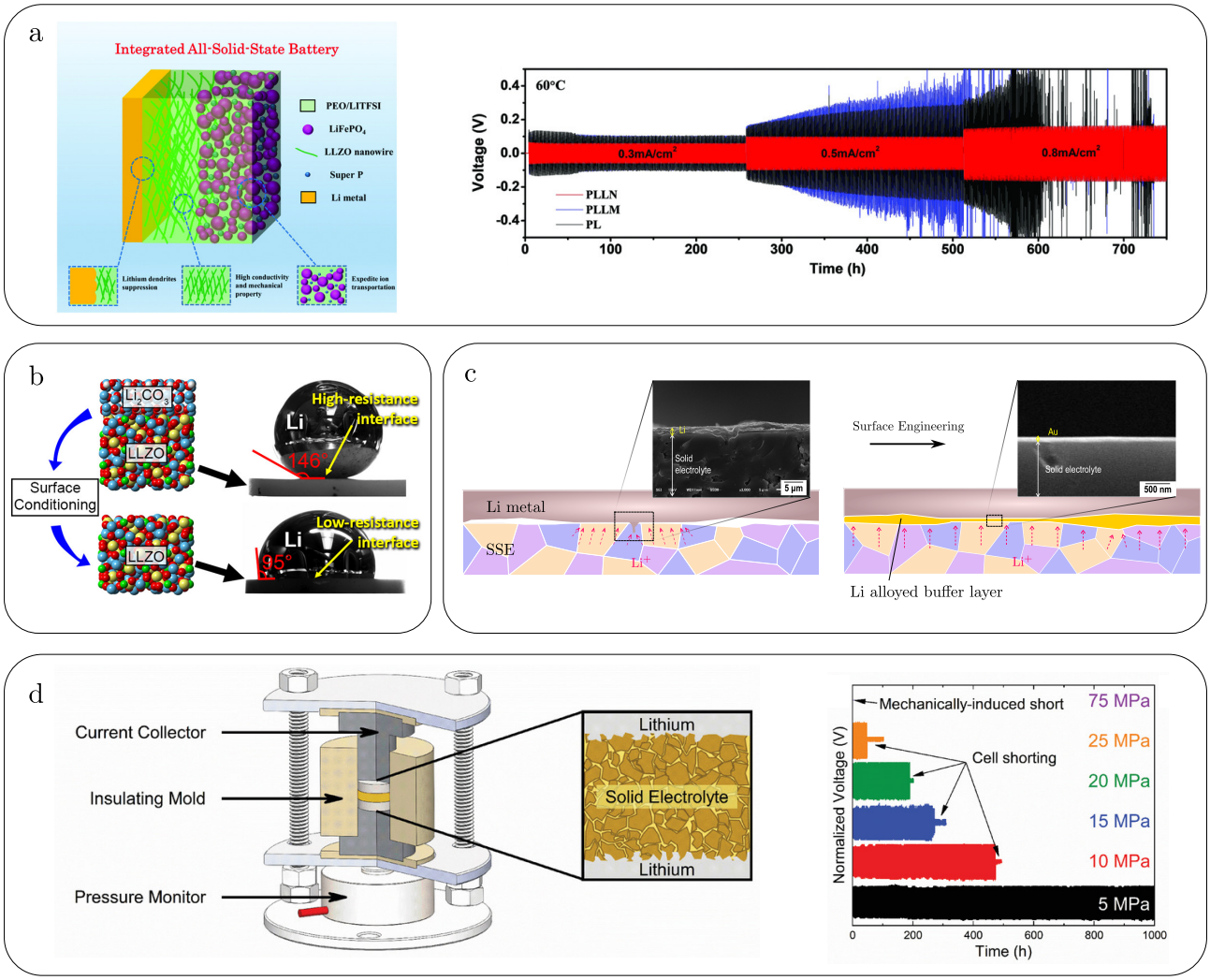


Figure 2.3: a) Configuration of an integrated SSB with LLZO nanowire upgraded PEO/LITFSI composite SSE fused with $LiFePO_4$ cathode (left) and voltage-time figure to illustrate the improvement in electrochemical stability of Li/PLLN/Li symmetric cell compared with Li/PL/Li and Li/PLLM/Li cells (right) [4]. b) A better interfacial wettability and lower interface resistance achieved by SSE surface conditioning [5]. c) Surface engineering by introducing a Li alloyed buffer layer. The insets are SEM images from the work of Kato et al. [6]. d) An experimental setup to apply pressure to the Li symmetric cell (left) and the normalized voltage-time figure of the cell under different stack pressures. Short circuits happen before cycling begins when the cell is under 75 MPa [7].

In conclusion, the journey toward commercializing SSBs is fraught with challenges, particularly those stemming from poor contact at the solid-solid interface. The research community has proposed a lot of solutions to address these issues. Some approaches are straightforward and effective, such as enhancing interfacial contact through grinding and polishing the SSE surface, improving wettability with a graphite interlayer, and reversing contact loss by applying moderate pressure and slight temperature increases. However, certain solutions lack practicality for commercial application, like exerting tens of megapascals of pressure on the battery pack or using rare metal (e.g., gold) alloys as interlayers. Others necessitate thorough evaluation and precise calculations prior to implementation, including

heteroatom doping and the incorporation of inorganic fillers into polymer matrices. Drawing parallels from the history of technological advancement, particularly the successful commercialization of liquid Li-ion batteries, it is clear that for SSBs to achieve commercial viability, they must not only surpass conventional liquid batteries in performance, longevity, and safety but also ensure the scalability of solutions to the highlighted challenges, considering the scarcity of materials used. Although formidable, overcoming these obstacles is imperative, as the potential for enhanced energy storage efficiency presents a compelling incentive for further in-depth research in this field.

2.2 Modelling Attempts

It can be seen from Section 2.1 that the major bottleneck that once held the development of SSBs back, i.e. the ionic conductivity, has been effectively addressed, and the corresponding research routes are now clear and robust. However, resolving the electrochemical and mechanical destabilization issues at the electrode/SSE interface, such as dendrite growth and interfacial losses, remains elusive. The primary barrier stems from a lack of in-depth understanding of the corresponding mechanisms involved. Describing and reproducing these phenomena through numerical modelling could be a crucial step towards enhancing our grasp of such mechanisms. Given the fundamental differences between the solid-solid interface in SSBs and the solid-liquid interface in traditional LSBs, models designed for LSBs fall short when applied to SSBs. Consequently, modifications and improvements are essential, particularly in terms of chemical-electrochemical-mechanical coupling and the boundary conditions at the solid-solid interface.

In recent years, there has been an increase in modelling efforts aimed at tackling the critical challenges faced by SSBs, with the hope of uncovering the underlying mechanisms through mathematical tools and offering a boost for laboratory research. Zhao et al. [76] delivered an exhaustive review of the electro-chemo-mechanical modelling of LIBs. The review is primarily on liquid-state batteries, spanning three size scales: particle, composite electrode, and cell. A dedicated section on SSB modelling attempts is also included. However, as the exploration of SSB modellings is still nascent, robust theories to explain the mechanisms of key challenges, such as lithium dendrite nucleation and evolution at SSB interfaces, are absent. While models developed for LSBs are suggested not to be directly applied to SSBs, general models, for instance, material fracture models based on degradation mechanisms (can be used to simulate dendrite-stimulated SSE cracking), can still serve as a fundamental framework for developing an SSB-dedicated theory. In a later mini-review, Tian et al. [77] offered supplementary

insights to the SSB modelling section in the work by Zhao et al. [76]. Their analysis primarily discussed the limitations of early models depicting lithium deposition on uneven solid-solid interfaces, highlighted by those proposed by Monroe and Newman [8, 78, 79], along with an evaluation of subsequent variants and efforts to enhance these models. The review article by Bistri et al. [80] delivers a detailed summary specifically tailored for SSB modelling. It concentrates on key areas such as the modelling of dendrite growth on lithium metal anodes, the fracture of SSEs, mechanical compatibility at the interface, and the chemo-mechanical modelling of composite electrode active particles. This comprehensive work offers a clear evolution process towards SSB modelling for researchers in this field.

The authors of these reviews consistently highlight the significance of mechanical behaviour in modelling SSBs, which indicates a distinct departure from the scenario with conventional LSBs. The fluidity of the electrolyte in LSBs provides a nearly infinite capacity to accommodate electrode deformation and changes in interface morphology, significantly mitigating the harmfulness of various issues, including particle intercalation-caused volume change and destabilization of the interface morphology due to uneven lithium deposition/dissolution. Such challenges, however, have proved to be fatal for SSBs.

The phase field method (PFM) has quickly become a powerful tool over the past decade, renowned for its ability to dynamically track interface movements and simulate the evolution of complex topological changes. This capability has been revolutionary in addressing challenges such as material corrosion [81, 82] and cracking [83, 84]. Given its potential, applying the phase-field method to monitor interfacial evolution and lithium dendrite growth in SSBs is a logical strategy. A lot of researchers have pursued this approach. However, there haven't been any review articles to summarize the specific application of the method in SSB modelling. Therefore, this section will be devoted to reviewing the utilization of the phase-field method, along with several vital formulations based on continuum mechanics to reflect the modelling progress made in recent years.

2.2.1 Continuum Mechanics Models

The electrochemo-mechanical model developed by Monroe and Newman [8] was among the earliest theoretical attempts to explain the dynamic processes occurring at the solid-solid interfaces in SSBs. Their 2D model simulated a lithium/polymer contact with their interface tuned following a cosine pattern, $x_2 = A\cos(\omega x_1)$, where x_1 and x_2 are the two perpendicular axes in a Cartesian coordinate system and the electrode surface is parallel to x_1, A is the amplitude and ω is the frequency, which is a rational simplification of the interface roughness. The core of the model is a modified Butler-Volmer

kinetic equation, which has the form

$$i_{\text{loc}} = i_0 \exp\left[\frac{(\alpha_m - \alpha_a)}{RT}\Delta\mu_{e^-}\right]\left[\exp\left(\frac{\alpha_a F}{RT}\eta\right) - \exp\left(-\frac{\alpha_c F}{RT}\eta\right)\right], \tag{2.1}$$

where i_{loc} is the local current density at the interface. $\Delta\mu_{e^-}$ represents the electrochemical potential change after taking into account the local stress status resulting from electrode deformation. i_0, R, T, F are exchange current density, gas constant, absolute temperature and Faraday's constant, respectively. α_a and α_c are anodic and cathodic transfer coefficients, respectively, which satisfy $\alpha_a + \alpha_c = 1$. α_m is the mechanical transfer coefficient, which represents the portion of deformation-induced electrochemical potential difference that contributes to the reaction activation energy; the author argues that this value should be 1 [79]. η is the overpotential. The derivation of Eq. (2.1) follows their earlier work [79] and assumes that the charge transfer resistance comes from the solution rather than from the electrode. In other words, the rate of the chemical reaction at the interface is restricted by the charge transfer process on the solution side, where it is primarily affected by the properties of the electrolyte involving its ionic conductivity, ion concentration distribution, and particle diffusivity.

Compared with the undeformed electrode, a modification term is introduced, i.e.,

$$\frac{i_{\text{loc}}^{\text{def}}}{i_{\text{loc}}^{\text{undef}}} = \exp\left[\frac{(1-\alpha_a)}{RT}\Delta\mu_{e^-}\right]. \tag{2.2}$$

For typical redox reaction with single charge transfer, $0 < 1 - \alpha_a < 1$, therefore, if $\Delta\mu_{e^-} > 0$, then $i_{\text{loc}}^{\text{def}} > i_{\text{loc}}^{\text{undef}}$, indicating an increased local current density at the deformed electrode interface and vice versa. Monroe and Newman [8] defined a stability parameter accordingly, which reads

$$\Delta\mu \equiv \frac{\Delta\mu_{e^-}}{A\cos(\omega x_1)}. \tag{2.3}$$

Eq. (2.3) reveals that when $\Delta\mu > 0$, namely when $\Delta\mu_{e^-}$ has the same sign as $A\cos(\omega x_1)$ (where $A\cos(\omega x_1) > 0$ corresponds to peak areas and $A\cos(\omega x_1) < 0$ to valley areas of the roughened interface), peak areas where there is inherently a higher current density will experience further increase in current density, while valley areas where there is inherently a lower current density will see a further reduction. This results in an amplification of interface roughness.

Analysis of the stability parameter demonstrates that when the shear modulus of the solid electrolyte surpasses twice that of the electrode, the value of $\Delta\mu$ can be reduced below 0. According to the theory of Monroe and Newman [8], this suggests a self-flattening tendency of the interface, thus inhibiting the

growth of dendrites.

However, this has been proven to be a false prediction that contradicts subsequent experimental studies [85]. This discrepancy occurs because the kinetic processes at the interface are oversimplified. The model assumes no local concentration changes in the vicinity of the interface and that the electrode and electrolyte are perfectly adherent. First of all, achieving such assumptions in reality is impractical. Second, these two assumptions combined imply an implicit condition that the material transfer rate within the electrode and the electrolyte is infinitely fast, meaning that the active materials at the electrode surface are immediately replenished regardless of how fast they dissolve. Experimental observations do not support this. Just as Kasemchainan et al. [62] have noted in their experiment-based hypothesis, the delayed replenishment of active materials at the interface causes the debonding between the electrode and electrolyte, facilitating the subsequent formation of lithium dendrites.

Shishvan et al. [9] presented an innovative modelling perspective by treating dendrites' initiation and growth in ceramic electrolytes as climbing dislocations. In their model, dendrite growth occurs with the cracking of the electrolyte at the dendrites' tip followed by the formation of an unoccupied volume space, after which Li ions from the electrolyte flow into the dendrites' tip at a constant chemical potential and reoccupy the void. The model culminated with a predictive equation for the critical current density (CCD) of dendrite growth and gives the prediction that it decreases with increasing initial dendrite length, electrode/electrolyte interface resistance, and interface void size, aligning well with experimental observations. Notably, the model introduces a Butler-Volmer kinetic equation between the electrode and electrolyte that encapsulates the effect of pressure, which renders

$$i_{\mathrm{loc}} = \hat{i}_0 \left\{ \exp\left[\frac{(1-\beta)F\eta + p_{\mathrm{m}}\Omega_{\mathrm{v}}}{RT} \right] - \exp\left[\frac{-\beta F\eta - p_{\mathrm{m}}(\Omega_{\mathrm{Li}} - \Omega_{\mathrm{v}})}{RT} \right] \right\}, \tag{2.4}$$

where $0 < \beta < 1$ is the symmetry factor, p_{m} is the pressure within the electrode, Ω_{Li} and Ω_{v} are the molar volumes of Li atoms and vacancies of the Li metal anode, respectively. Local exchange current density $\hat{i}_0$ is also linked with pressure p_{m} through

$$\hat{i}_0 = i_0 \left[\theta_{\mathrm{m}}^0 \exp\left(\frac{p_{\mathrm{m}}\Omega_{\mathrm{v}}}{RT} \right) + (1 - \theta_{\mathrm{m}}^0) \right]^{-1} \exp\left[\frac{(1-\beta)p_{\mathrm{m}}(\Omega_{\mathrm{Li}} - \Omega_{\mathrm{v}})}{RT} \right], \tag{2.5}$$

where i_0 is the reference exchange current density when there is no electrode deformation, and θ_{m}^0 denotes the Li occupancy rate under zero pressure (see Chapter 4 for detailed definition).

In their follow-up work, Shishvan et al. [86] extended their climbing dislocation model and derived

an expression to characterize the dendrite growth rate in ceramic electrolytes. Calculations show that the growth rate of dendrites increases linearly with the increase of the applied current density once it exceeds the CCD threshold for dendrite initiation. In addition, further simulations indicate that the growth of dendrites is reversible, and the dendrite dissolution process has no requirements on the magnitude of applied current densities.

However, the models of Shishvan et al. [9, 86] presuppose the presence of a segment of dendrite in the electrolyte before the start of simulations, which is inconsistent with common observations. In a more typical scenario, dendrites are seen to nucleate at a pristine Li/SSE interface, with battery cycles proceeding, cracking of the SSE is observed and the subsequent growth of dendrites within [11, 87]. This also means their model somewhat bypasses elucidating the dendrite's 'true initiation' mechanism, i.e., the electrochemo-mechanical processes that start from the nucleation at localized regions on the electrode surface and their subsequent penetration into the electrolyte. In addition, the assumption that Li^+ on the flank of the dendrite is always in equilibrium with those in the adjacent electrolyte raises questions. From an in situ optical microscopy observation of lithium dendrite growth in a transparent garnet-type SSE [10], it can be seen that the morphology of the dendrites varies considerably in the direction parallel to the electrode/electrolyte interface. It remains unclear how much this morphology change affects the electrolyte behaviour, especially whether it provides additional stimulation to the cracking of the electrolyte.

In view of this, Shishvan et al. [12] conducted further investigations on the prerequisites for dendrite growth, namely the onset conditions for the growth of interfacial voids. The model developed emphasizes the importance of the power-law creep of the lithium metal and the resulting dislocations. A modified Butler-Volmer equation accounting for creep-deformed electrodes is presented, which renders

$$i_{\mathrm{loc}} = i_0 \left[\frac{F\eta - T_{\mathrm{n}}\Omega_{\mathrm{Li}}}{RT}\right] \hat{\theta}_{\mathrm{v}}^{1-\beta} \exp\left[\frac{(1-\beta)h_{\mathrm{v}}}{RT}\right], \tag{2.6}$$

where T_{n} represents the surface traction acting on the electrode in the direction of the outer normal of the surface. h_{v} denotes the enthalpy of vacancy formation. The power-law creep in the Li electrode leads to an increase in dislocation density, followed by the emergence of additional volumes, which are considered by the authors as extra vacancies available for the transport of lithium atoms. Therefore, the effective vacancy rate $\hat{\theta}_{\mathrm{v}}$ inside the deformed lithium electrode is increased compared to that of the

lithium metal without creep (θ_{v}, the detailed definition can be found in Chapter 4), indicating

$$\hat{\theta}_{\mathrm{v}} = \theta_{\mathrm{v}} + \alpha \frac{(\rho_{\mathrm{d}} b^2)\Omega_{\mathrm{Li}}}{\Omega_{\mathrm{v}}}, \tag{2.7}$$

where α is a metal constant related to its crystal structure. ρ_{d} is the dislocation density and b is Burgers vector.

The model explores the initiation of the void in the vicinity of a hemispherical impurity particle located at the electrode/electrolyte interface that exhibits both electric and ionic insulation. Void growth is determined by the moment when the surface integral of the normal traction on the electrode surface that is in contact with the hemispherical impurity becomes a tensile force. The impurity/electrode interface is assumed not to be able to sustain tension, so tensile traction will result in the debonding of the interface, and hence voids begin to appear. The analytical results of the model are consistent with experimental observations, indicating that the applied stack pressure inhibits void formation and that higher applied current density necessitates higher pressure for effective void suppression.

However, as acknowledged by the authors, the initiation of the voids at the interface investigated in their model is attributed to the debonding between the impurity and electrode surfaces rather than due to insufficient replenishment of active materials from the bulk electrode to the interface, as suggested by Kasemchainan et al. [62]. These represent two distinct mechanisms. Furthermore, Shishvan et al. [12] modelled the lithium dissolution processes at the interface through a velocity boundary condition perpendicular to the electrode surface, which inevitably imposes additional unrealistic stresses on the electrode and also can not be directly equivalent to the interface morphology change caused by the electrochemical reaction. On the other hand, while researchers recognize the enhancing effect of lithium creep on its internal lithium transport [72], there hasn't been a comprehensive theoretical framework for quantification purposes. Shishvan et al. [12]'s attempt to quantify the impact of dislocations generated by lithium power-law creep on lithium transport as an increase of effective vacancy rate is an innovative way of conceptualization, but whether it has rationality needs further experimental verification.

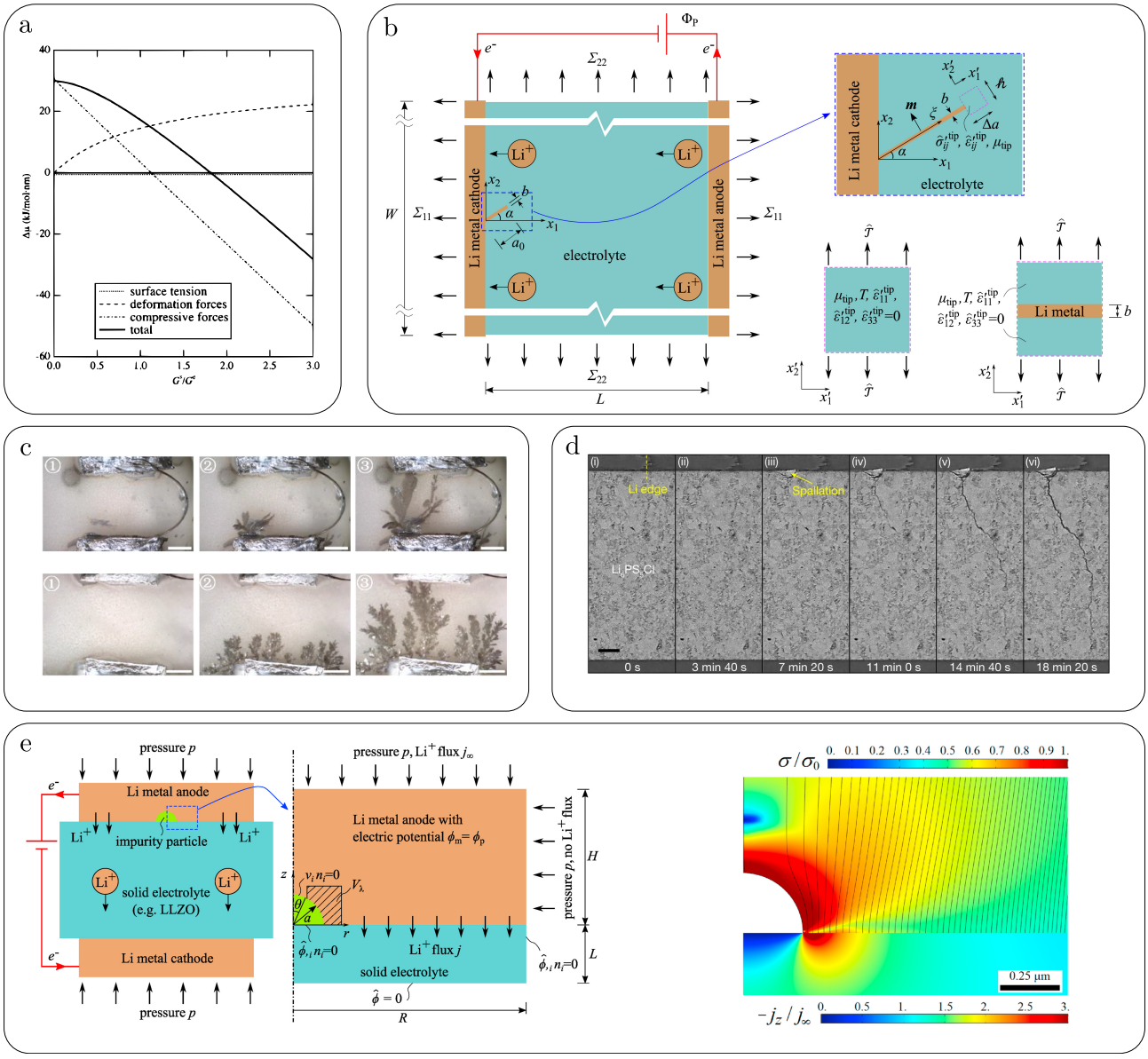


Figure 2.4: a) Variation of the stability parameter $\Delta\mu$ with the ratio of shear moduli between the electrolyte (G^s) and the electrode (G^e) [8]. b) Sketch of the model for dendrite growth initiation as climbing dislocations [9]. c) Direct optical observation of dendrite growth in a transparent LLZTO SSE under applied currents of 0.1 mA for ① - ③ in the first row, and 0.5 mA for ① - ③ in the second row [10]. d) Operando X-ray computed tomography (XCT) cross-sections of a Li/Li_6PS_5Cl/Li symmetric cell during lithium plating, showing dendrite initiation at a pristine interface and subsequent crack propagation in the SSE [11]. e) Setup for void initiation prediction at an interface with a pre-existed impurity (left), and the distribution of normalized Von Mises stress σ/σ_0 in the electrode and normalized current density $-j_z/j_\infty$ in the electrolyte (right) [12].

The above-mentioned models, rooted in pure continuum mechanics, share a common limitation: they fail to reproduce the temporal evolving interfacial contact states caused by dynamic changes in the morphology of the electrode/SSE interfaces, which are critical to SSBs. This limitation implies that a specialized model tailored for each representative interfacial contact state is required, which hinders the efficiency of research in this domain. The introduction of the PFM offers a potential pathway to address this dilemma.

2.2.2 Phase Field Models for SSBs

The PFM is a powerful tool that has gained sustained popularity in recent years. By leveraging an auxiliary order parameter, a continuous description of the free-energy functional across domains containing multiple phases can be constructed. Through solving the equilibrium or non-equilibrium dynamic interphase evolution of the system under varying external conditions employing the principle of free-energy minimization and describing the interface between phases as a continuous and smooth transition utilizing an interpolation function, challenges associated with tracking interfaces through the conventional sharp-interface methods can be effectively circumvented.

Early applications of the PFM in batteries were directed at understanding the stress-free growth of dendrites during electrodeposition and the fracturing of electrode particles due to the intercalation of active materials. Chen et al. [13] developed a non-linear phase field model to investigate the dendrite growth pattern in the electrolyte during non-uniform electrodeposition. Their model employed a single order parameter to distinguish between the electrode and the electrolyte, incorporating the thermodynamic driving force for the electrode reaction by taking into account the Butler-Volmer kinetics as a source term in the governing equations that regulate cation diffusion in the electrodeposition system. The model identified three distinct dendrite growth patterns by adjusting the applied voltage and the initial interface morphology and achieved good consistency with observations. Nevertheless, the model's framework did not consider the impact of electrolyte mechanical properties on dendrite growth; namely, the mechanical contribution is omitted when constructing the free-energy functional across the system. Miehe et al. [14] combined finite elastic strain theory with a phase-field fracture model to investigate the generation and propagation of internal cracks in electrode particles in conventional Li-ion batteries due to the lithiation and delithiation cycles. Although particle cracking models address issues generally faced by LSBs, its integrated multi-physics approach can offer enlightening insights for addressing dendrite growth-induced SSE cracking in SSBs.

In the last few years, a number of phase-field multiphysics coupling models that targeted specifically solving the unique challenges of SSBs have begun to emerge. Tian et al. [88] combined density-functional theory (DFT) and PFM to investigate the effects of internal defects, such as pores and cracks, on the growth of lithium dendrites across several different SSE materials. Their findings reveal that the surface band gap of LLZO is significantly lower than that in bulk, indicating that the surface regions (including the surface of internal defects, such as grain boundaries) possess a higher electronic conductivity than the bulk regions (e.g., the interior of the grains). This results in a higher tendency

to trap more electrons and accelerate the deposition of Li^+ in surface areas during battery cycling and promote a rapid spread of Li dendrites. Such conclusions are consistent with the understanding that high electronic conductivity in SSEs contributes to dendrite penetration, as highlighted in an experimental report published in *Nature Energy* by Han et al. [89]. It is worth noting that the free energy functional of their phase-field model incorporated the elastic strain energy density compared to the model of Chen et al. [13] to describe the deformation of the SSE and Li metal, giving the total energy of the system with the following form

$$\mathcal{G} = \int_V (f_{\text{ch}} + f_{\text{grad}} + f_{\text{elec}} + f_{\text{mech}})\, \mathrm{d}V, \tag{2.8}$$

where $\mathcal{G}$ is the total free energy of the system, V is the system volume, f_{ch}, f_{grad}, f_{elec}, f_{mech} denote chemical energy density, gradient energy density related to the interface, electrostatic energy density and mechanical energy density, respectively. The derivation of the expressions for f_{ch}, f_{grad}, f_{elec} share similarities with those presented by Chen et al. [13] and their conceptual foundations can be traced back to the earlier work of Guyer et al. [90]. In another related work, Yurkiv et al. [91] undertook a modelling work to study the effect of solid electrolyte interface (SEI) on dendrite growth. In their model, a noise term f_{ns} based on the Langevin noise method is introduced to the free energy functional to reflect the free energy change during stochastic lithium electrodeposition caused by the presence of SEI and employed anisotropic mobility for Li^+ to restrict ion diffusion in the direction fully covered by SEI. Yuan et al. [15] also developed a phase field model involving the propagation of dendrites in a polycrystalline SSE. Unlike the model presented by Tian et al. [88], Yuan et al. [15] focused on the propagation of dendrites as well as cracking within one grain harbouring a pre-existing defect and ignored the electron enrichment effect of the grain boundaries. Bistri and Di Leo [16] proposed a continuous electro-chemo-mechanical gradient theory that couples electrochemical reactions, mechanical deformation and damage. The theory elucidated the complex coupling when trying to capture the growth mechanism of lithium dendrites involving intra- and inter-crystalline crack propagation in SSE materials. That is, by introducing two phase-field order parameters to respectively characterize the Li electrodeposition and the solid damage process, their theoretical framework provides a holistic view of how mechanical stresses affect Li deposition kinetics (including electrodeposition within the damage region of SSE), as well as the influence of the electrodeposition-induced mechanical deformation and cracking of the solid material to the transport of Li^+.

However, these models mainly focus on dendrite formation and propagation in the SSE and

cannot predict the dynamic response of the electrode-electrolyte interface during cycling, especially the nucleation and evolution of voids in the Li metal anode, which is considered a fundamental phenomenon that needs deeper understanding to decipher the mechanism of dendrite penetration. In addition, it is still not clear how the interplay between pressure, Li creep, diffusion, electrochemical reaction and current density governs electrochemical instabilities in an SSB, specifically in a Li metal anode. Predicting voiding and the associated localisation of current requires resolving complicated non-linear coupling problems and computationally tracking the evolution and merging/division of voids of arbitrary shape - a formidable task.

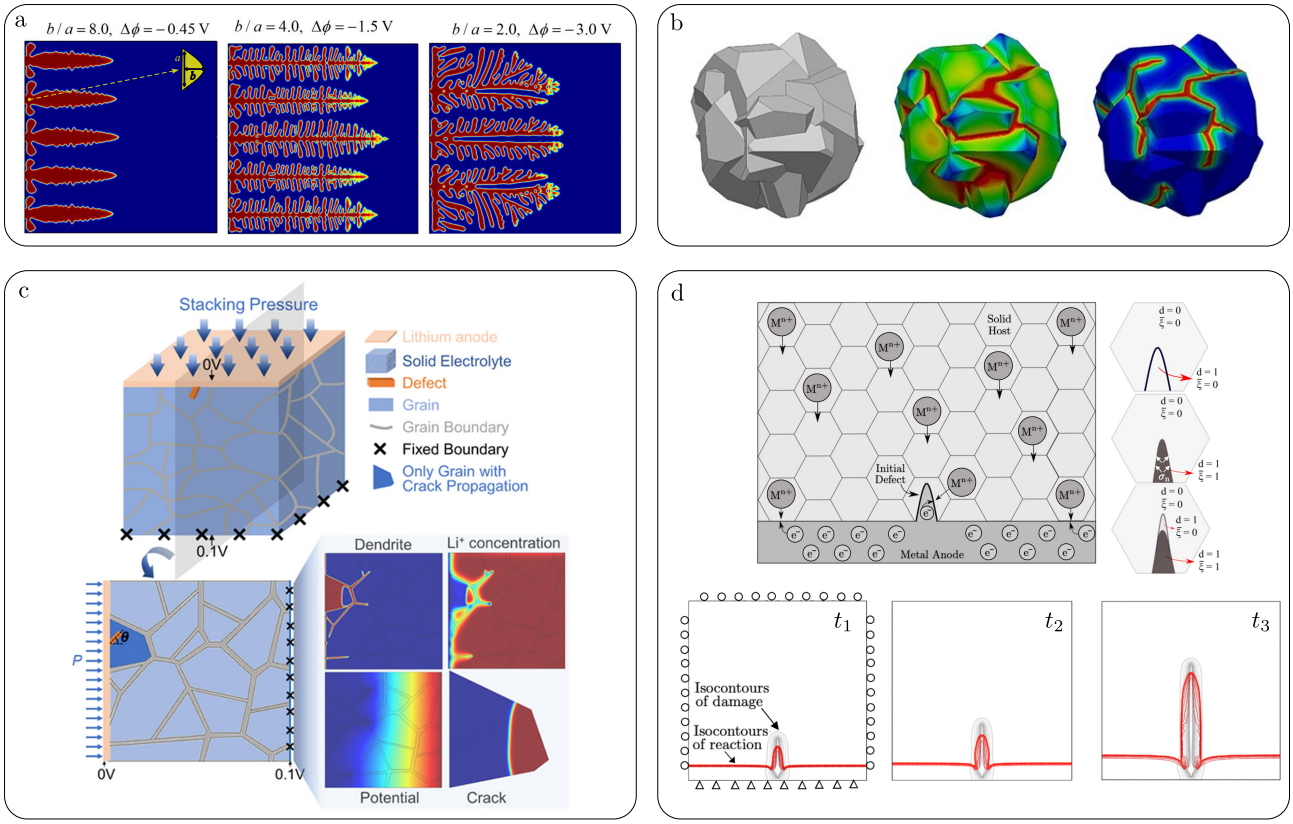


Figure 2.5: a) Different Li dendritic patterns were predicted with different initial dendrite nuclei and applied voltage [13]. b) Cracking of a cathode particle [14]. c) Illustration of the model setup and predictions of dendrite growth in the ceramic SSE employing a multi-coupling phase field model [15]. d) Depiction of the proposed mechanism of the phase field-damage model, where d denotes the damage variable and ξ denotes the electrodeposition reaction coordinate (top row), and the prediction of the crack propagation coupled with Li deposition (bottom row) [16].

2.3 Summary

In this chapter, a comprehensive overview of the SSB technology is provided, encompassing iterations of SSE materials, technical endeavours aimed at advancing the practical implementation of SSB technology, and various modelling attempts dedicated to gaining a deeper understanding of the mechanisms behind

the challenges confronting SSBs. A thorough discussion on the dilemmas hindering the realisation of SSBs is also presented, with particular emphasis on the most urgent issues to be coped with, namely the mechanical and electrochemical stability of interfacial between the metal anode and the SSE. In regard to the challenges, several strategies have been proposed, including the application of stack pressure to the electrodes, polishing the electrode/SSE interface, introducing an interlayer between the electrodes and the electrolyte, and developing new polymer-inorganic composite SSE material. Despite these efforts, dendrite formation and the resultant risk of short-circuit failure due to dendrite penetration persist under high-current and long-cycling conditions. The underlying reason for this situation highlights a lack of deep understanding of the electrochemical-mechanical coupling mechanism at play in the formation and growth of dendrites.

To fill this gap, researchers have developed many mathematical models, wishing to propose an explanation for this complex coupling phenomenon. Initial attempts were constructed with continuum mechanics theories. However, these early models often oversimplified the dynamic nature of interface geometry changes due to the lack of the ability to track the morphological evolution of interfaces, leading to discrepancies between model predictions and experimental observations. To overcome these limitations, the phase-field approach was introduced. Yet, the application of PFM in SSBs is still in its nascent stages, with most of the models focusing primarily on the qualitative reproduction of dendrite growth in the SSE. There is a noticeable deficiency in quantitative analyses and a lack of investigation into the root causes of dendrite formation, i.e., the electrochemical-mechanical coupling mechanisms that cause the loss of interfacial contact. This marks a crucial frontier for SSB development. Deciphering this mysterious process will help to propel the development of SSBs with a pivotal step forward.

To effectively address this issue and debunk the mechanism, several critical factors must be taken into account, including i) The creep deformation and substitution diffusion of lithium metal, ii) Modified electrode kinetics to encompass the effects of localised active material depletion, and iii) Dynamic tracking of the location of interfacial current density constriction phenomena. Each of these factors represents a significant aspect in terms of the interface stability issues that lack exhaustive discussion in the previous research. The following chapters will delve deeper into these aspects and exploit their implications for the battery's overall stability.

Chapter 3

Theory Fundamentals

3.1 Theory of Electrochemical Systems

An electrochemical system encompasses a broad array of setups capable of converting chemical energy into electrical energy and vice versa. The applications based on this system are commonly seen in our daily lives, such as batteries and electro-deposition. The most primitive models for these applications are galvanic cells and electrolytic cells, respectively. A galvanic cell harnesses chemical energy into electric energy by generating electric currents from spontaneous redox reactions. An electrolytic cell, in contrast, converts electric energy into chemical energy by accepting external input of currents or potential differences. Both of the two are composed of various chemical dynamics inside the cell, including the transport of charges, execution of half-cell reactions, and mass transport.

3.1.1 Basic Concepts of an Electrochemical System

An electrochemical system must contain at least three phases to function either as a galvanic cell or an electrolytic cell [92]. These essential components include two electrodes and one electrolyte that separates them. There must also be an outer circuit that connects them to enable the electrons to flow between the two electrodes.

Electrodes in electrochemical systems are typically composed of materials with high electron conductivity, such as metals, alloys, semiconducting materials, or other non-metallic substances like carbon. The commonality of these electrode materials is that they all allow for a relatively independent movement of electrons inside them, but the ions' mobility is limited. Therefore, in an electrochemical reaction, the charged species that flow through the electrode and form an electric current in the outer circuit are electrons. For a properly functioning cell, it is imperative that electrons should not be

allowed to enter the electrolyte. The conductivity of the electrons in an electrode depends mainly on the electronic structure of the material and the temperature (conductivity usually increases with decreasing temperature). Generally speaking, the order magnitude of the conductivity for typical electrode materials is usually about 10^2 to 10^7 $\mathrm{S\,cm^{-1}}$ [92].

An electrolyte is usually composed of salt solutions, molten salt mixtures or solid insulating materials such as ceramic complex [92]. The difference between an electrolyte material and an electrode material is that an electrolyte material only allows ions or molecules to move within their domain and blocks the transport of electrons. Here, the conductivity of the electrolyte is described by the ionic conductivity, which usually decreases with the increment of temperature and is of the order magnitude 10^{-4} to 10^{-1} $\mathrm{S\,cm^{-1}}$ [92].

Unlike a chemical reaction, in which the oxidation and reduction reaction happens at the same location, an electrochemical reaction usually has separated half-cell reactions. That is to say, the oxidation and the reduction reactions in an electrochemical system happen in different places – at the interfaces of the two electrodes. Therefore, a general chemical redox reaction in the form of

$$\mathrm{A} + \mathrm{B} \rightarrow \mathrm{C} + \mathrm{D}, \tag{3.1}$$

where A and B are reactants, C and D are products, can be split up and written in the form of a reversible half-cell reaction as

$$\mathrm{Ox}_i + z_i \mathrm{e}^- \underset{k_a}{\overset{k_c}{\rightleftharpoons}} \mathrm{Red}_i, \tag{3.2}$$

where the subscript i refers to the species present in the system, Ox_i denotes the oxidized form of species of i and Red_i represents the reduced form. z_i indicates the electron stoichiometry associated with species i, which essentially reflects the number of electrons involved in the oxidation or reduction of that species (e.g. for reaction $\mathrm{Cu}^{2+} + 2\mathrm{e}^- \rightarrow \mathrm{Cu}(s)$, $z_{\mathrm{Cu}} = +2$). k_c and k_a are the rate constants of the cathodic process (reduction reaction) and anodic process (oxidation reaction), respectively. They will be discussed in greater depth in the following sections.

As mentioned before, the current flows in different forms in the electrode and electrolyte. In the electrode, the primary charge carriers are electrons, resulting in what is known as electronic current. The corresponding charges in the electrolyte are predominantly carried by the ions and form an ionic current. Conventionally, the electronic current in the electrode is measured by current density i (in $\mathrm{A\,m^{-2}}$ or $\mathrm{C\,m^{-2}\,s^{-1}}$), which could be interpreted as the average amount of charge that goes through a

unit area per unit time. Meanwhile, the charge transfer process in the electrolyte could be measured by the ionic flux J_i (in $\mathrm{mol\,m^{-2}\,s^{-1}}$), where the subscript i refers to a specific species in the system. J_i could be interpreted as the amount of material that goes through a unit area per unit of time. These two quantities can be related through Faraday's law of electrolysis, which has the form

$$m_i = \frac{QM_i}{Fz_i}, \tag{3.3}$$

where m_i is the mass of the product of species i during one redox reaction, Q is the amount of charge, M_i is the molar mass of the species i, and F is Faraday's constant.

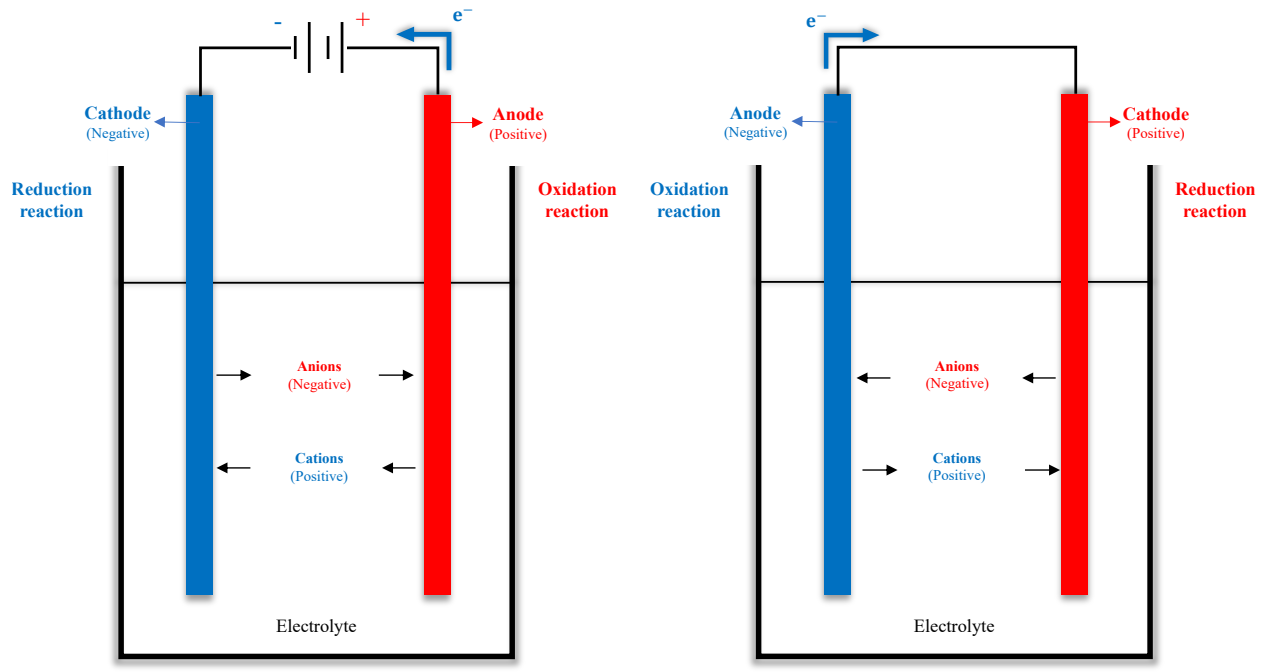
Rearranging Eq. (3.3) to change the product mass m_i and the current I into equivalent product flux and current density, Eq. (3.3) can then be rewritten as

$$i_n = z_i F J_i, \tag{3.4}$$

where i_n here refers to the cathodic current density i_c or anodic current density i_a, and J_i is the product flux of species i [17].

Galvanic Cells and Electrolytic Cells

Based on the direction of the energy conversion, electrochemical systems can be divided into two different types of cells: electrolytic cells (Fig. 3.1a) and galvanic cells (Fig. 3.1b). The galvanic cells can produce electric currents that could do work in the outer circuit, while electrolytic cells accept currents from the outer circuit and convert them into chemical energy. The rechargeable lithium-ion batteries commonly seen in cell phones and electric vehicles can be regarded as galvanic cells during discharging and electrolytic cells during charging, i.e., reversible cells.



(a) Electrolytic cell

(b) Galvanic cell

Figure 3.1: Simple illustrations of two different electrochemical systems.

In a galvanic cell, oxidation reactions take place on the surface of the negative electrode. The material particles on the surface of the negative electrode are oxidized and, therefore, lose their electrons to the electrode. Conversely, reduction reactions occur at the surface of the positive electrode. The cations (positively charged) in the electrolyte consume electrons in the positive electrode and are hence reduced. The electrons flow from the negative electrode to the positive electrode in the outer circuit. The cell process in an electrolytic cell is the opposite of a galvanic cell. Note that the terms 'anode' and 'cathode' refer to different electrodes in electrolytic cells and galvanic cells. Regardless of whether the cell is galvanic or electrolytic, the 'anode' is consistently defined as the electrode where oxidation takes place, and the 'cathode' is the electrode where reduction happens.

Reaction Gibbs Energy

As stated in thermodynamic theory, a spontaneous chemical reaction under constant temperature and pressure always has the direction towards a lower Gibbs free energy [17].

Consider a redox reaction with the form as Eq. (3.1). Assume the amount of the reactants and products before the reaction begins are n_{AB} and n_{CD}, respectively. After an infinitesimal amount of time, the redox reaction starts and proceeds with an extent of reaction of $\mathrm{d}\zeta$ (in moles, mol), which is a useful concept to track how far a reaction has proceeded. During this period of time, the amount

of the reactants changes from n_{AB} to $(n_{\mathrm{AB}} - \mathrm{d}\zeta)$, while the amount of products changes from n_{CD} to $(n_{\mathrm{CD}} + \mathrm{d}\zeta)$ correspondingly. The reaction Gibbs energy, $\Delta_r\mathcal{G}$, at any point of the reaction can be defined in terms of the extent of the reaction as

$$\Delta_r\mathcal{G} = \left(\frac{\partial\mathcal{G}}{\partial\zeta}\right)_{p,T}, \tag{3.5}$$

where $\mathcal{G}$ is the Gibbs free energy (see Fig. 3.2). p is pressure and T is absolute temperature. Since the reaction Gibbs free energy can also be interpreted as the chemical potential difference [17], it follows that

$$\Delta_r\mathcal{G} = \mu_{\mathrm{CD}} - \mu_{\mathrm{AB}}, \tag{3.6}$$

where μ_{CD} and μ_{AB} are chemical potentials of the products and reactants, respectively.

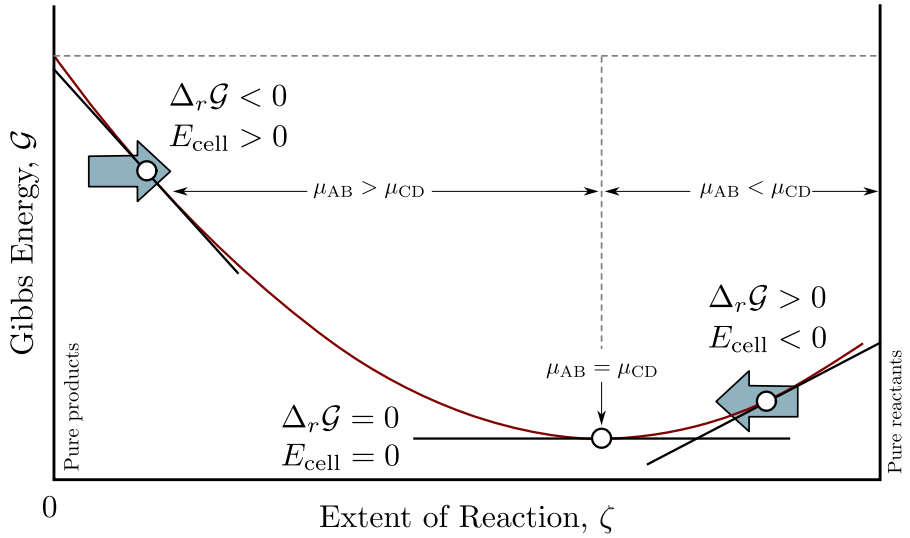


Figure 3.2: The reaction Gibbs energy $\Delta_r\mathcal{G}$ is defined as the slope of the Gibbs energy change $\Delta\mathcal{G}$ against the change of the extent of reaction ζ [17]. E_{cell} is the cell potential. Reaction is spontaneous in the forward direction when $\Delta_r\mathcal{G} < 0$ or $E_{\mathrm{cell}} > 0$ and in the reverse direction when $\Delta_r\mathcal{G} > 0$ or $E_{\mathrm{cell}} < 0$.

In an electrochemical reaction, the chemical potentials μ_i are expanded to electrochemical potentials, $\bar{\mu}_i$, to take into account the influence of electrostatic potentials, as the charged species (ions) in an electrochemical system will experience the effect of the electric field while the neutral species generated by chemical reactions will not. The electrochemical potential is measured in $\mathrm{J\,mol^{-1}}$, which can be interpreted as the amount of energy possessed per unit mole of electroactive materials. The relationship between the electrochemical potential and chemical potential then reads [92, 93]

$$\bar{\mu}_i = \mu_i + z_i F\phi, \tag{3.7}$$

where ϕ is the electrostatic potential.

For an arbitrary electrochemical reaction with the form

$$\mathrm{A} + 2\mathrm{B} \rightarrow 3\mathrm{C} + 4\mathrm{D}, \tag{3.8}$$

when the reaction proceeded for an infinitesimal extent of $\mathrm{d}\zeta$ mol, the amount of reactants and products changed by

$$\mathrm{d}n_i = s_i \mathrm{d}\zeta, \tag{3.9}$$

where the subscript i here represents reaction substances, and s_i denotes the stoichiometric numbers of the chemical equation. They are defined as negative integers for reactants and positive integers for products (e.g. for Eq. (3.8), $s_A = -1$, $s_B = -2$, $s_C = +3$, $s_D = +4$).

The variation in Gibbs free energy can be calculated through

$$\mathrm{d}\mathcal{G} = \sum_i \bar{\mu}_i \mathrm{d}n_i, \tag{3.10}$$

hence

$$\mathrm{d}\mathcal{G} = \sum_i \bar{\mu}_i s_i \mathrm{d}\zeta, \tag{3.11}$$

which leads to

$$\Delta_r \mathcal{G} = \left(\frac{\partial \mathcal{G}}{\partial \zeta}\right)_{p,T} = \sum_i s_i \bar{\mu}_i. \tag{3.12}$$

The electrochemical potential $\bar{\mu}_i$ is related to the species activity through

$$\bar{\mu}_i = \bar{\mu}_i^{\ominus} + RT \ln a_i \tag{3.13}$$

where $\bar{\mu}_i^{\ominus}$ stands for standard electrochemical potential, which is independent of concentration. R is the gas constant and T is the absolute temperature. a_i refers to the activity of the species.

In a typical liquid electrochemical system with the salt solution as an electrolyte, the species activity a_i can be expressed by the product of species molality m_i and activity coefficient γ_i.

$$a_i = m_i \gamma_i. \tag{3.14}$$

Substitute Eq. (3.13) to Eq. (3.12) yields

$$\Delta_r \mathcal{G} = \sum_i s_i \bar{\mu}_i^{\ominus} + RT \sum_i s_i \ln a_i = \Delta_r \mathcal{G}^{\ominus} + RT \ln \prod_i a_i^{s_i}, \tag{3.15}$$

where $\Delta_r \mathcal{G}^{\ominus}$ denotes the standard reaction Gibbs energy.

Define a new parameter $\mathcal{Q}$ as reaction quotient,

$$\mathcal{Q} = \prod_i a_i^{s_i}, \tag{3.16}$$

since the stoichiometric numbers s_i are negative for all the reactants and positive for the products, therefore, the reaction quotient $\mathcal{Q}$ has the physical meaning of

$$\mathcal{Q} = \frac{\text{Product Activities}}{\text{Reactant Activities}}. \tag{3.17}$$

Then the reaction Gibbs energy, also called the difference in electrochemical potential, can be rewritten as

$$\Delta_r \mathcal{G} = \Delta \bar{\mu}_i = \Delta_r \mathcal{G}^{\ominus} + RT \ln \mathcal{Q}. \tag{3.18}$$

When a reaction reaches equilibrium, it arrives at a state where the gradient of the Gibbs energy change, $\Delta_r \mathcal{G}$ becomes zero, which corresponds to the extreme point in Fig. 3.2. According to Eq. (3.18), a specific value of $\mathcal{Q}$ can be calculated. This value is a function of the activities (or concentrations for ideal solutions) of the reaction component under equilibrium. A new equilibrium constant, $\mathcal{K}$, can be defined as

$$\mathcal{K} = \left(\prod_i a_i^{s_i} \right)_{\text{equilibrium}}, \tag{3.19}$$

and it is related to the standard reaction Gibbs energy through

$$\Delta_r \mathcal{G}^{\ominus} = -RT \ln \mathcal{K}. \tag{3.20}$$

Cell Potentials

Newman's definition of cell potentials in the book [92] highlights their fundamental nature in electrochemistry, which says, "one must speak of the cell potential as the difference in the thermodynamic electrochemical potential of electrons between two leads of identical composition, temperature, and pressure" [92, pp. 28]. The cell potential, which is also referred to as the electromotive force (EMF)

on many formal occasions and acts as the driving force to the flow of electrons through the external circuit, can be related to the reaction Gibbs energy $\Delta_r\mathcal{G}$ through Faraday's constant F by

$$\Delta_r\mathcal{G} = -zFE_{\text{cell}}, \tag{3.21}$$

where z is the number of electrons involved in the reaction (also the valence of the corresponding ion) and E_{cell} is the cell potential. The negative sign indicates when a reaction is spontaneous, namely $\Delta_r\mathcal{G} < 0$, then the cell potential, also EMF, $E_{\text{cell}} > 0$, meaning that a thermodynamically favoured reaction possesses the ability to produce electric work (see Fig. 3.2).

Until now, three different kinds of potentials have been introduced, including the chemical potential, the electrochemical potential and the cell potential. The chemical potential μ and the electrochemical potential $\bar{\mu}$ are closely related concepts but are distinct in their definitions, which have been highlighted by Eq. (3.7). However, one may still be confused by the difference between the electrochemical potential and the cell potential. One way to distinguish them is to see through their units to identify their inner link. The electrochemical potentials $\bar{\mu}$ have the unit of joules per mole ($\mathrm{J\,mol^{-1}}$) while the cell potentials E_{cell}, however, are measured in volts (V), which can also be written as joules per coulomb ($\mathrm{J\,C^{-1}}$), and z is dimensionless. By dividing the reaction Gibbs energy by the product of Faraday's constant, which is expressed in coulombs per mole ($\mathrm{C\,mol^{-1}}$), and z, the resulting unit is $\mathrm{J\,C^{-1}}$, aligning with that of cell potential. This transformation reveals the physical significance of E_{cell} as the Gibbs energy change concerning the amount of electric charge transferred in the reaction.

Substitute Eq. (3.21) into Eq. (3.18) yields the expression for the cell potential in terms of the standard Gibbs energy and the reaction quotient

$$E_{\text{cell}} = -\frac{\Delta_r\mathcal{G}^{\ominus}}{zF} - \frac{RT}{zF}\ln\mathcal{Q}. \tag{3.22}$$

The first term on the right-hand side of Eq. (3.22) is a constant value for a given electrochemical system under standard conditions, known as the standard cell potential and can be represented by a new parameter $E^{\ominus}_{\text{cell}} = -\Delta_r\mathcal{G}^{\ominus}/zF$. Consequently, Eq. (3.22) can be concisely expressed as the **Nernst equation**

$$E_{\text{cell}} = E^{\ominus}_{\text{cell}} - \frac{RT}{zF}\ln\mathcal{Q}. \tag{3.23}$$

The Nernst equation reveals the interconnection between the cell potential and the component involved in the electrochemical reaction through the reaction quotient parameter $\mathcal{Q}$. When the cell

reaction reaches its equilibrium, the cell potential will become zero, and the reaction quotient $\mathcal{Q}$ becomes the equilibrium constant $\mathcal{K}$. Then, the standard cell potential can be calculated through this special case of the Nernst equation by

$$E_{\text{cell}}^{\ominus} = \frac{RT}{zF} \ln \mathcal{K}. \tag{3.24}$$

Eq. (3.24) can be used to determine the equilibrium constant $\mathcal{K}$ by measuring the open circuit voltage (OCV) U_{OCV}, namely the observed value of cell potential E_{cell}.

Electrode Potentials

The standard cell potential can be calculated through the standard electrode potential

$$E_{\text{cell}}^{\ominus} = E_R^{\ominus} - E_O^{\ominus}, \tag{3.25}$$

where the $E_R^{\ominus}$ and $E_O^{\ominus}$ refer to the standard electrode potentials of the electrodes experiencing reduction reaction and oxidation reaction, respectively.

Direct measurement of the absolute potential of a single electrode is a task that lacks physical feasibility [94]. Therefore, the standard electrode potential is typically expressed as a relative value with respect to a reference electrode, with the standard hydrogen electrode (SHE) being the most frequently utilized reference. The half-cell reaction of the SHE is

$$2\text{H}^+\,(\text{aq}) + 2\text{e}^- \rightarrow \text{H}_2\,(\text{g}), \tag{3.26}$$

where the letters in the parenthesis signify the state of the matter. (aq) refers to an aqueous solution, (g) refers to gas. Besides, (s) (see Table 3.1) denotes solid.

Reaction (3.26) occurs on a platinum electrode. To make it a reference electrode, its potential under standard conditions (pressure of the hydrogen is 1 bar, the activity of the hydrogen ion in the solution is 1) at a given temperature is conventionally assigned a value of zero.

The standard electrode potential of an arbitrary material M can then be defined as the cell potential when this M electrode is paired with a SHE and acts as a cathode. Table 3.1 shows the standard electrode potential of some frequently seen electrodes.

Table 3.1: Standard electrode potentials with respect to SHE

The reduction half-reaction	[1] $E^{\ominus}$ [V]
$Li^+ + e^- \rightarrow Li\,(s)$	-3.0401
$Na^+ + e^- \rightarrow Na\,(s)$	-2.71
$2H^+ + 2e^- \rightarrow H_2\,(g)$	0
$Pt^{2+} + 2e^- \rightarrow Pt\,(s)$	+1.188
$CoO_2\,(s) + 4H^+ + e^- \rightarrow Co^{3+} + 2H_2O$	+1.42

[1] $E^{\ominus}$ denotes the standard electrode potential.

The electrode potential of an arbitrary material M under non-standard conditions can be calculated through the Nernst equation (3.23).

$$E^{\mathrm{M}} = E^{\ominus} - \frac{RT}{zF} \ln \mathcal{Q}. \tag{3.27}$$

For a reversible electrode where the oxidation and reduction reaction proceed simultaneously, the Nernst equation can also be used to calculate the equilibrium electrode potential.

$$E_{\mathrm{eq}} = E^{\ominus} - \frac{RT}{zF} \ln \mathcal{K}. \tag{3.28}$$

3.1.2 The Electrode Kinetics

The Net Current Density and Overpotential

For a cell electrode, the oxidation reaction and reduction reaction occur concurrently. The oxidation reaction generates an anodic current density directed into the electrode from the interface, while the reduction reaction produces a cathodic current density moving through the electrode towards the interface. Denoting the anodic and cathodic current density as i_a and i_c, respectively, the net current density, i, is defined as

$$i = i_a - i_c. \tag{3.29}$$

The anodic and cathodic current densities are in a constant state of competition within an electrochemical cell. When $i_c > i_a$, the overall reaction is dominated by reduction, and the mobile electrons in the electrode will be consumed. Conversely, if $i_c < i_a$, oxidation reactions dominate, the electrons will accumulate near the electrode surface. Equilibrium is achieved when $i_c = i_a$ with net current density $i = 0$. At this state of equilibrium, the exchange current density i_{exc} is defined as either

the anodic current density or the cathodic current density.

The electrode overpotential, denoted as η, arises when the electrode is connected to an outer circuit and currents are flowing inside. It quantifies a deviation of the observed electrode potential from the equilibrium electrode potential when the cell is connected to an outer circuit and stands for the requirement for a given current density to flow through the electrode. The definition renders

$$\eta = E^{'} - E_{\text{eq}}, \tag{3.30}$$

where $E^{'}$ is the applied potential difference (e.g. battery during charging) or the potential difference under working conditions (e.g. battery during discharging). Denoting the potential difference between the bulk electrode (ϕ_s) and electrolyte (ϕ_l) as $\Delta\phi = \phi_s - \phi_l$. In the absence of an external circuit connection, $\Delta\phi = E_{\text{eq}}$. Once the electrodes are connected and currents start to flow, $\Delta\phi$ deviates from E_{eq} and hence $\Delta\phi = E^{'}$, and the overpotential can be rewritten as

$$\eta = \Delta\phi - E_{\text{eq}}. \tag{3.31}$$

In a galvanic cell, the presence of overpotential results in a reduction in the absolute values of electrode potentials. That is, the negative electrode becomes less negative while the positive electrode becomes less positive, as it is a form of energy dissipation.

The Butler-Volmer Equation

The relationship between the net current density and the overpotential for characterizing a certain electrochemical reaction at the electrode/electrolyte interface can be expressed by the **Butler-Volmer equation**

$$i_n = i_{\text{exc}} \left[\exp\left(\frac{\alpha_a F}{RT}\eta\right) - \exp\left(-\frac{\alpha_c F}{RT}\eta\right) \right], \tag{3.32}$$

where i_n is the net current density on the n electrode, i_{exc} is the exchange current density. α_a and α_c are the charge transfer coefficients of the anodic and cathodic processes, respectively.

When the overpotential (i.e., the difference between the actual electrode potential and the equilibrium electrode potential) is very small (usually within a few millivolts), it can be assumed that the electrochemical reaction is near equilibrium. At this point, the exponential terms in the Butler-Volmer equation can be linearized by Taylor expansion and retaining only the first-order terms, resulting in a

linearized expression:

$$i_n = i_{\text{exc}} \frac{(\alpha_a + \alpha_c)\, F}{RT} \eta. \tag{3.33}$$

On the contrary, if the overpotential is large, Eq. (3.32) can be simplified to a Tafel equation. Specifically, when the anodic overpotential is large, the cathodic process (reduction reaction) can be neglected, and conversely, when the cathodic overpotential is large, the anodic process (oxidation reaction) can be neglected. Hence Eq. (3.32) can be simplified to

$$\begin{cases} i_n = i_{\text{exc}} \exp\left(\dfrac{\alpha_a F}{RT}\eta\right) & \text{for } \alpha_a F\eta \gg RT, \\ i_n = -i_{\text{exc}} \exp\left(-\dfrac{\alpha_c F}{RT}\eta\right) & \text{for } \alpha_c F\eta \ll -RT. \end{cases} \tag{3.34}$$

The charge transfer coefficient α_i with the subscript $i = a$ or c is a dimensionless parameter that measures the favourable direction of an electrochemical reaction. It shows the fraction of the applied potential, which supports either the anodic process or the cathodic process [94]. The charge transfer coefficient can also be represented by a symmetry factor β [94]. On this occasion, β can be interpreted as

$$\beta = 1 - \frac{\alpha_a}{z} \quad \text{or} \quad \beta = \frac{\alpha_c}{z}. \tag{3.35}$$

The value of β varies from 0 to 1. It is usually defined as 0.5 before an experimental refinement is made.

The exchange current density i_{exc} is a parameter governed by the temperature, the property of the electrode material, and the electrolyte components adjacent to the electrode. For a reversible electrochemical reaction with the form of Eq. (3.2), the exchange current density can be expressed as

$$i_{\text{exc}} = zF k_a^{\alpha_c} k_c^{\alpha_a} c_{\text{Red}}^{\alpha_c} c_{\text{Ox}}^{\alpha_a}, \tag{3.36}$$

where c_{Red} and c_{Ox} are concentrations of the reduced species and oxidized species, respectively. k_a and k_c are anodic and cathodic reaction rate constants that depend on temperature through an Arrhenius relation

$$k = \Lambda \exp\left(-\frac{\mathcal{E}_a}{RT}\right), \tag{3.37}$$

where Λ is a pre-exponential factor that is related to the collision frequency of the reactant molecules,

$\mathcal{E}_a$ is the activation energy, namely the energy barrier to overcome for the reaction to commence.

3.1.3 Charge and Mass Transfer

Fick's Law

Fick's law describes the behaviour of a substance transported from a region of high concentration to a region of low concentration through diffusion driven by the presence of a concentration gradient. It was first proposed by the German physiologist Adolf Fick in 1855 and is one of the fundamental laws describing the phenomenon of diffusion.

Fick's first law provides a quantitative description of the diffusive flux under steady-state conditions, where the concentration distribution does not change over time. It states that the flux of a material through a unit area, namely the diffusive flux, is proportional to the concentration gradient at that location with its direction opposite to that of the concentration gradient, which is mathematically given by

$$\mathbf{J}_i = -D_i \nabla c_i, \tag{3.38}$$

where $\mathbf{J}_i$ (usually in $\mathrm{mol\,m^{-2}\,s^{-1}}$) is the material flux of species i, D_i (usually in $\mathrm{m^2\,s^{-1}}$) is the corresponding diffusion coefficient and c_i is the concentration.

Fick's second law describes the dynamics of how the concentration of a substance changes over time and space during a non-steady-state diffusion. It is built upon the first law and takes into account the conservation of mass, which is formulated as

$$\frac{\partial c_i}{\partial t} = \nabla \cdot (D_i \nabla c_i)\,, \tag{3.39}$$

and the mass balance is expressed as

$$\frac{\partial c_i}{\partial t} + \nabla \cdot \mathbf{J}_i = 0. \tag{3.40}$$

Diffusion, Migration and Convection

Charge transfer in the electrolyte is achieved by the transport of ions and is propelled by three primary mechanisms: diffusion, migration, and convection, and adheres to the principle of conservation. In ideally dilute solutions, the combined effect of the above processes can be mathematically articulated by

$$\mathbf{J}_i = \underbrace{-\nu_i u_i c_i F \nabla \Phi}_{\text{migration}} \underbrace{- D_i \nabla c_i}_{\text{diffusion}} + \underbrace{c_i \mathbf{v}}_{\text{convection}}, \tag{3.41}$$

where ν_i is the valence of the ion of species i. u_i ($\mathrm{m^2\,V^{-1}\,s^{-1}}$) is the mobility of the charged particles. u_i represents the average velocity of the ions under the influence of an electric field. $\nabla\Phi$ is the gradient of the electrostatic potential (The negative of the gradient of electric potential is the electric field vector $\mathbf{E} = -\nabla\Phi$). $\mathbf{v}$ is the velocity vector of the bulk movement of the solution. The three terms on the right hand of the equation represent the flux component of migration, diffusion and convection, respectively. This equation is also known as the **Nernst-Planck equation**.

The migration term in Eq. (3.41) is induced by the existence of charged species in an electric field. The mobility u_i, according to its definition, can be interpreted mathematically as

$$u = \frac{v_d}{E}, \tag{3.42}$$

where v_d ($\mathrm{m\,s^{-1}}$) is the drift velocity of the particles and E ($\mathrm{V\,m^{-1}}$) is the magnitude of the electric field. It can be related to the diffusivity through the Nernst-Einstein relation

$$u_i = \frac{D_i}{RT}. \tag{3.43}$$

The diffusion component arises from spatial variations in solution concentration. The direction of the diffusion flux can be different or even opposite the direction of migration. If the diffusion coefficient is non-uniform, necessary adjustment is needed accordingly. In the absence of the concentration gradient, the diffusion term is negligible and can be omitted from the overall transport equation.

The flux resulting from convection is caused by the bulk motion of the solution medium, which can be triggered by the gradient in density or by mechanical disturbance. While convection on its own in an electrochemical solution will not induce a current owing to electrical neutrality, it can significantly alter the concentration distribution, thereby affecting the transport process [92]. In SSB analysis, the convection term is typically disregarded since SSEs are assumed not to exhibit any bulk flow. Taking this into consideration and substituting Eq. (3.43) into Eq. (3.41), the Nernst-Planck equation reduces to

$$\mathbf{J}_i = \frac{-\nu_i c_i D_i F}{RT}\nabla\Phi - D_i\nabla c_i. \tag{3.44}$$

The Conservation Laws and Electric Neutrality

In an electrochemical system, there are three major conservation laws, including the conservation of charge, the conservation of mass, and the conservation of momentum.

Mass balance of a local volume element in an electrochemical system mandates that the rate of concentration change for a species i over time must equal the net sum of fluxes of species i into and out of the volume, plus any production of i [92], which gives

$$\frac{\partial c_i}{\partial t} + \nabla \cdot \mathbf{J_i} = R_i, \tag{3.45}$$

where R_i here refers to the production of the homogeneous chemical reactions that happened in bulk solution. For an electrochemical system where the dominant reaction is the heterogeneous reaction that happened on the electrode interface, R_i can be regarded as 0, and Eq. (3.45) reduces to Eq. (3.40).

Electric Neutrality is achieved naturally except for the electric double-layer area. In the bulk electrolyte, this requirement can be expressed as

$$\sum_i \nu_i c_i = 0. \tag{3.46}$$

The material flux can be coupled with the current density through **Faraday's Law**

$$\mathbf{i} = F \sum_i \nu_i \mathbf{J_i}. \tag{3.47}$$

The Conservation of Charge can be derived from the mass balance equation (Eq. (3.45)), given that all charges within an electrochemical system are carried by charged particles. By integrating the charge per mole $\nu_i F$ into Eq. (3.45) for each relevant species, and summing over all charged species involved in the reaction, equation (3.45) becomes

$$F \frac{\partial}{\partial t} \sum_i \nu_i c_i = -\nabla \cdot F \sum_i \nu_i \mathbf{J_i} + F \sum_i \nu_i R_i, \tag{3.48}$$

given the assumption of electric neutrality (Eq. (3.46)) and assuming no bulk chemical reactions occur in the solution, and combining Eq. (3.47), Eq. (3.48) reduces to

$$\nabla \cdot \mathbf{i} = 0. \tag{3.49}$$

Substituting Eq. (3.41) into Eq. (3.47) yields

$$\mathbf{i} = -F^2 \nabla \Phi \sum_i \nu_i^2 u_i c_i - F \sum_i \nu_i D_i \nabla c_i + F \mathbf{v} \sum_i \nu_i c_i, \tag{3.50}$$

where for the first term on the right-hand side of the Eq. (3.50), a conductivity of the solution (ionic conductivity), κ, can be defined as

$$\kappa = F^2 \sum_i \nu_i^2 u_i c_i. \tag{3.51}$$

Based on Eq. (3.50), the divergence of the current density vector renders

$$\nabla \cdot \mathbf{i} = -F^2 \nabla \cdot \left(\nabla \Phi \sum_i \nu_i^2 u_i c_i \right) - F \nabla \cdot \left(\sum_i \nu_i D_i \nabla c_i \right) + F \nabla \cdot \left(\mathbf{v} \sum_i \nu_i c_i \right). \tag{3.52}$$

Combining Eq. (3.51) with Eq. (3.52) and taking into account the assumption of electric neutrality and a uniform concentration distribution with no bulk reaction in the solution, Eq. (3.52) reduces to

$$0 = -\nabla \cdot (\kappa \nabla \Phi). \tag{3.53}$$

If the ionic conductivity can be assumed to be a constant, then equation (3.53) conforms to the **Laplace equation**

$$\nabla^2 \Phi = 0, \tag{3.54}$$

where (∇^2) is the Laplace operator, which can also be written as (Δ).

The Conservation of Mass can be written in a differential form of the continuity equation as

$$\frac{\partial \rho}{\partial t} + \nabla \cdot (\rho \mathbf{v}) = 0, \tag{3.55}$$

where ρ is the mass density, and $\mathbf{v}$ is the flow velocity.

The Conservation of Momentum for a steady-state system can be expressed as

$$\nabla \cdot \boldsymbol{\sigma} + \mathbf{b} = 0, \tag{3.56}$$

where $\boldsymbol{\sigma}$ is the stress tensor and $\mathbf{b}$ is the body force.

3.1.4 Essential Parameters to Quantify Battery Performance

Before delving deeper into the intricacies of modelling in SSBs, it is vital to clarify several key battery definitions to establish a foundational groundwork and avoid ambiguities.

Battery Capacity

Battery capacity refers to the total amount of electric energy that could be stored and released from the cell under a given condition (e.g. temperature, C-rate, voltage, etc.). It is usually quantified in ampere-hours (A h), representing the amount of continuous current that can be supplied by the battery over a period of one hour. It can be calculated by

$$C = \int_0^{t_{\text{cutoff}}} I(\tau)\,\mathrm{d}t, \tag{3.57}$$

where C is the battery capacity (in A h or mA h), $I(\tau)$ is the discharging current as a function of time τ. t_{cutoff} is the time point when the battery discharge stops.

Theoretical Capacity of Electrode Materials

The theoretical capacity of an electrode is the maximum amount of charge that can be stored by the electrode material under ideal conditions, which is typically measured in milliampere-hours per gram ($\text{mAh}\,\text{g}^{-1}$). Theoretical calculations of this quantity require consideration of the number of electrons transferred involved in the electrode reaction, the molar mass of the electrode material, and the Faraday constant, which renders

$$C_{\text{th}} = \frac{zF}{M}, \tag{3.58}$$

where C_{th} is the theoretical capacity and M is the molar mass of the material. Multiplying Eq. (3.58) with the mass density of the electrode material yields the theoretical volume capacity, while multiplying with average operation voltage yields the theoretical energy density.

State of Charge (SoC)

The battery state of charge refers to the ratio of the battery capacity at a random time with respect to its rated capacity [95]. It is usually denoted by percentage and varies from 0% to 100%. 0% means the battery has been depleted, and 100% means that the battery is at its full capacity. The battery SoC can be calculated through [96]

$$\text{SoC}_t = \text{SoC}_0 - \frac{\int_0^t I_d(\tau)\,\mathrm{d}t}{C_r}, \tag{3.59}$$

where SoC_t is the battery SoC at time point t, SoC_0 is the initial state of charge. $I_d(\tau)$ is the discharge current in terms of time. C_r is the rated battery capacity, which is usually measured and given by the manufacturer and represents the maximum amount of energy that should be possessed by the battery.

Note that the open circuit voltage (OCV) of a battery is closely related to its SoC, exhibiting a dynamic relationship wherein the OCV decreases as the SoC diminishes. This correlation is influenced by several key factors, including temperature and C-rates, and the relationship is typically nonlinear [97, 98]. The OCV-SoC curve can be determined empirically through experimental approaches. Although OCV-SoC curves show similarities for most Li-ion batteries, they are not exactly identical across different battery makers and models [97, 99].

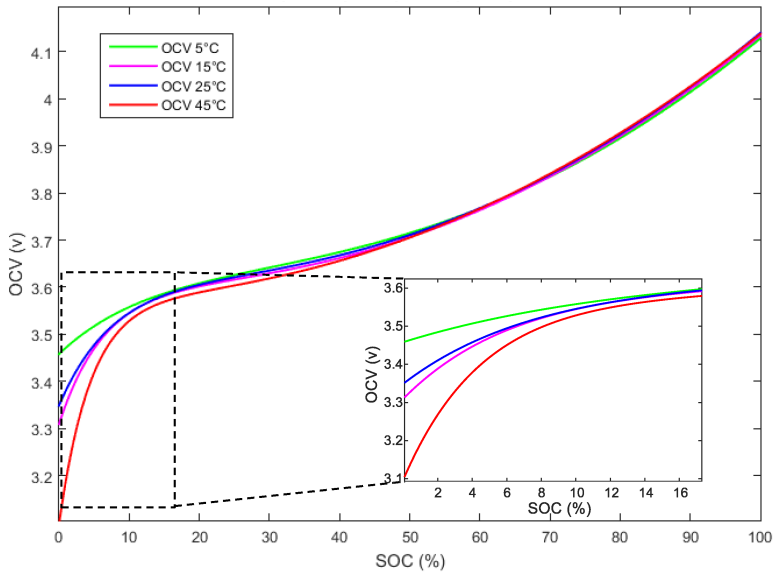


Figure 3.3: Typical OCV-SoC curves under different temperatures for a Li-ion battery [18].

Battery C-rate

The C-rate is a measure of the charge and discharge rate of a battery, indicating how fast the battery is being charged or discharged relative to its total capacity. It quantifies the proportionality of the dis-/charge current with respect to the battery's maximum capacity and is expressed in terms of xC (in h^{-1}), where x is a real number that scales the dis-/charge current in relation with the battery capacity. For instance, a battery with a rated capacity of 10 A h discharging with a current of 10 A operates at a discharge C-rate of 1C, meaning its total capacity will be exhausted in 1 hour. If it discharges at 2 A, then the discharge C-rate is denoted as 0.2C, and the depletion time is extended to 5 hours.

Coulombic Efficiency (CE)

Coulombic efficiency (CE) (or Faraday efficiency, current efficiency) refers to the ratio between the full capacity extracted during discharging and the full capacity that goes into the battery during charging

within one battery cycle. That is

$$\mathrm{CE} = \left(\frac{\text{Discharge Capacity}}{\text{Charge Capacity}} \right) \times 100\%. \tag{3.60}$$

CE is directly related to the cyclability of a battery, with its degradation implying a loss of mobile ions that should participate in the battery cycle, thus leading to a permanent reduction in the battery capacity [100]. In conventional LSBs, the advancement in technology has enabled most market-available batteries to achieve and sustain a CE of around 99% throughout their cycling life [100]. However, for SSBs featuring Li-metal anodes, low initial CE and the following CE drop during battery cycling remains a challenging issue. The primary cause of CE decline is attributed to the formation of inactive lithium. Fang et al. [100] emphasized that this issue is even more serious than the dendrite growth for Li-metal anode. Lu et al. [101] also conclude that before Li dendrites appear, significant battery capacity fading has already happened due to the combined effect of the excess inactive Li and the inward-growth porous structure in the bulk Li-metal electrode.

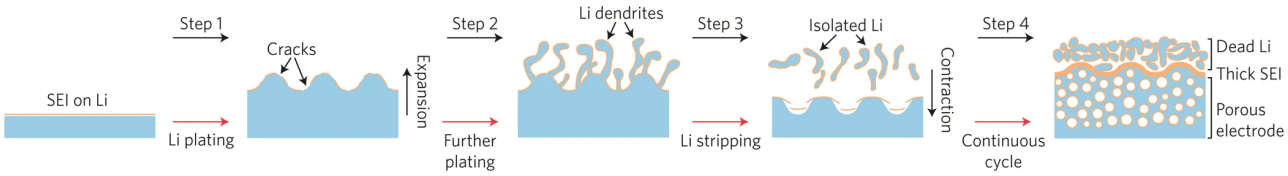


Figure 3.4: Formation of dead Li caused by the formation and rupture of solid electrolyte interface (SEI) leads to a reduction in battery CE [102].

3.2 Theory of Mechanics of Continua

In this section, we summarize the fundamental theories of the mechanics of continua that are related to our research, drawing on the books of Bower [103] and Gurtin et al. [104]. Throughout this section, tensor notations will be used for the majority of the equations, with boldface Latin and Greek letters representing the vectors and second-order tensors

$$\mathbf{A},\ \mathbf{B},\ \mathbf{C}, ...,\ \mathbf{a},\ \mathbf{b},\ \mathbf{c}, ...,\ \boldsymbol{\alpha},\ \boldsymbol{\beta},\ \boldsymbol{\gamma}, ..., \tag{3.61}$$

and blackboard bold Latin letters to denote fourth-order tensors

$$\mathbb{A},\ \mathbb{B},\ \mathbb{C}, ... \tag{3.62}$$

In some cases, index notation may also be employed for a compact description. In such a case, a vector $\mathbf{X}$, a second-order tensor $\mathbf{F}$, and a forth-order tensor $\mathbb{C}$ can be equivalently expressed as

$$\mathbf{X} \equiv X_i, \quad \mathbf{F} \equiv F_{ij}, \quad \mathbb{C} \equiv C_{ijkl}. \tag{3.63}$$

The Einstein summation convention is also adopted, hence the dot product of two vectors $\mathbf{a}$ and $\mathbf{b}$ in three-dimensional space can be written as

$$\mathbf{a} \cdot \mathbf{b} \equiv a_i b_i \equiv \sum_{i=1}^{3} a_i b_i = a_1 b_1 + a_2 b_2 + a_3 b_3. \tag{3.64}$$

3.2.1 Mathematical Description of Kinematics and Strain Tensors

Mathematical description of Kinematics

Consider a closed body region $\mathcal{B}$ in a three-dimensional Euclidean space $\mathfrak{R}^3$ with a Cartesian coordinate system characterized by orthogonal basis $\{\mathbf{e}_i\} = \{\mathbf{e}_1, \mathbf{e}_2, \mathbf{e}_3\}$.

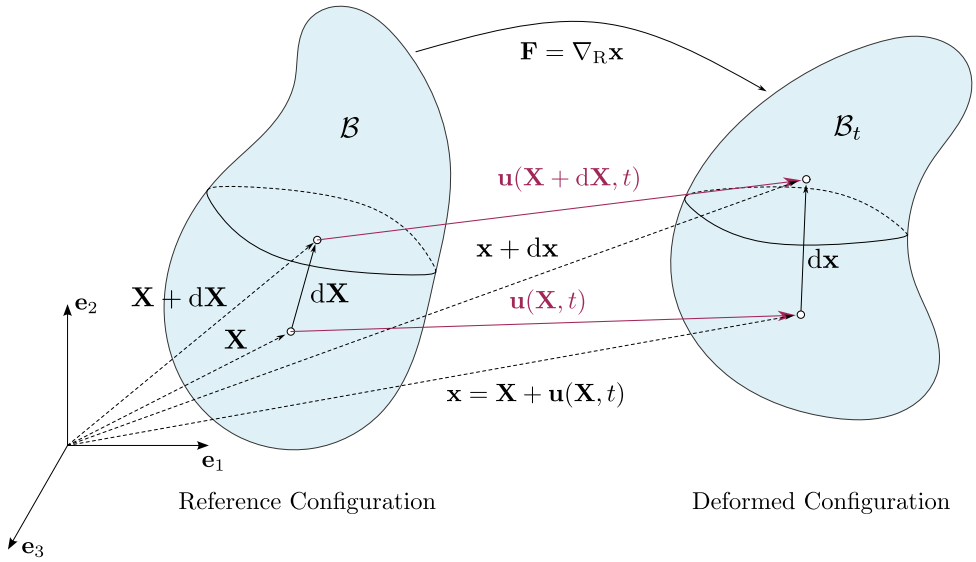


Figure 3.5: Deformation of a closed body region $\mathcal{B}$ after time t in an Euclidean space.

After a period of time t, body $\mathcal{B}$ deformed and moved to occupy a new space denoted by $\mathcal{B}_t$ (see Fig. 3.5). We choose the body $\mathcal{B}$ at $t = 0$ as a reference configuration and denote the state of $\mathcal{B}$ after deformation at time t as a deformed configuration. A material particle located at point $\mathbf{X}$ in the reference configuration $\mathcal{B}$ moved to a new position $\mathbf{x}$ in the deformed configuration $\mathcal{B}_t$ at time t, the

displacement vector $\mathbf{u}$ of this material particle can be defined as

$$\mathbf{u}(\mathbf{X}, t) = \mathbf{x} - \mathbf{X}. \tag{3.65}$$

Consequently, the velocity vector $\mathbf{v}$ and acceleration vector $\mathbf{a}$ of the material point $\mathbf{X}$ at time t can be calculated through

$$\mathbf{v} \equiv \dot{\mathbf{u}}(\mathbf{X}, t) = \frac{\partial \mathbf{u}(\mathbf{X}, t)}{\partial t} \quad \text{and} \quad \mathbf{a} \equiv \ddot{\mathbf{u}}(\mathbf{X}, t) = \frac{\partial^2 \mathbf{u}(\mathbf{X}, t)}{\partial t^2}. \tag{3.66}$$

The deformation gradient tensor $\mathbf{F}$ can be defined as

$$\mathbf{F} \equiv \nabla_{\mathbf{X}} \mathbf{x} = \mathbf{I} + \nabla_{\mathbf{X}} \mathbf{u}, \tag{3.67}$$

where $\nabla_{\mathbf{X}}(\cdot)$ is the gradient operator with respect to $\mathbf{X}$ in the reference configuration. $\mathbf{H} = \nabla_{\mathbf{X}} \mathbf{u}$ is the displacement gradient tensor.

An infinitesimal line segment $\mathrm{d}\mathbf{X}$ in the reference configuration deforms to $\mathrm{d}\mathbf{x}$ in the deformed configuration. They can be related by the deformation gradient tensor through

$$\mathrm{d}\mathbf{x} = \mathbf{F} \cdot \mathrm{d}\mathbf{X}. \tag{3.68}$$

For multiple deformation steps, such as two successive deformations, an intermediate configuration $\mathcal{B}_{t'}$ can be defined, as shown in Fig. 3.6.

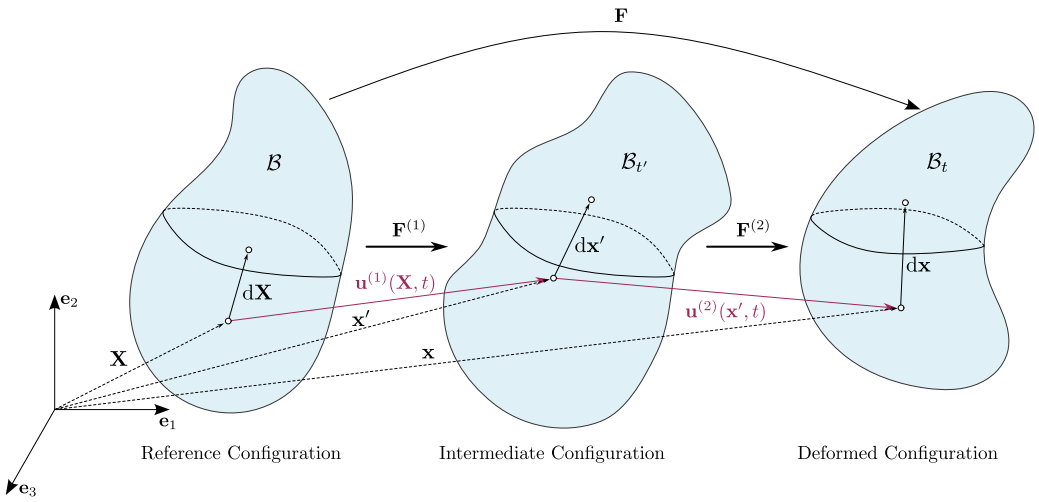


Figure 3.6: Deformation of a closed body region $\mathcal{B}$ to a final state $\mathcal{B}_t$ involving an intermediate deformation step $\mathcal{B}_{t'}$.

The deformation gradient tensors, which signify a mapping of the infinitesimal line segment from its initial state to a subsequent deformed state, can be written as

$$\mathbf{F}^{(1)} = \nabla_{\mathbf{X}}\mathbf{x}' \quad \text{and} \quad \mathbf{F}^{(2)} = \nabla_{\mathbf{x}'}\mathbf{x}, \tag{3.69}$$

where $\nabla_{\mathbf{x}'}(\cdot)$ denotes the gradient operator with respect to $\mathbf{x}'$ in the intermediate configuration. The relation between line segments is similar to Eq. (3.68) and renders

$$\mathrm{d}\mathbf{x}' = \mathbf{F}^{(1)} \cdot \mathrm{d}\mathbf{X}, \quad \mathrm{d}\mathbf{x} = \mathbf{F}^{(2)} \cdot \mathrm{d}\mathbf{x}'. \tag{3.70}$$

The deformation gradient tensor from the initial state $\mathcal{B}$ to its final state $\mathcal{B}_t$ follows

$$\mathrm{d}\mathbf{x} = \mathbf{F} \cdot \mathrm{d}\mathbf{X} \quad \text{with} \quad \mathbf{F} = \mathbf{F}^{(2)} \cdot \mathbf{F}^{(1)}. \tag{3.71}$$

This multiplicative decomposition principle presented in Eq. (3.71) can be used to calculate the total deformation characterized by contributions from different origins, such as a finite deformation consisting of both elastic deformation and inelastic deformation, which has the form

$$\mathbf{F} = \mathbf{F}^{\mathrm{e}} \cdot \mathbf{F}^{\mathrm{inel}}, \tag{3.72}$$

where $\mathbf{F}^{\mathrm{e}}$ represents the deformation gradient tensor attributed to elastic deformations, while $\mathbf{F}^{\mathrm{inel}}$ denotes the deformation gradient tensor associated with inelastic deformations. $\mathbf{F}^{\mathrm{inel}}$ can be decomposed into more specific contributions arising from different mechanisms, for instance, plasticity ($\mathbf{F}^{\mathrm{p}}$) and chemical reactions ($\mathbf{F}^{\mathrm{ch}}$), and follows

$$\mathbf{F} = \mathbf{F}^{\mathrm{e}} \cdot \mathbf{F}^{\mathrm{inel}} = \mathbf{F}^{\mathrm{e}} \cdot \mathbf{F}^{\mathrm{p}} \cdot \mathbf{F}^{\mathrm{ch}}. \tag{3.73}$$

Consequently, with the above definition of $\mathbf{F}$ (Eq. (3.73)), the Green-Lagrange strain tensor can be calculated through Eq. (3.80).

For geometrically linear or non-linear analysis characterized by small deformations (infinitesimal deformation), a more straightforward additive decomposition of the strain can be adopted, featuring with

$$\boldsymbol{\varepsilon} = \boldsymbol{\varepsilon}^{\mathrm{e}} + \boldsymbol{\varepsilon}^{\mathrm{inel}} = \boldsymbol{\varepsilon}^{\mathrm{e}} + \boldsymbol{\varepsilon}^{\mathrm{p}} + \boldsymbol{\varepsilon}^{\mathrm{ch}}, \tag{3.74}$$

where the superscripts have the same meaning as in Eq. (3.73). $\boldsymbol{\varepsilon}$ is the infinitesimal strain tensor, which is defined in detail later in Eq. (3.82). Note that the additive decomposition is not applicable for large deformations.

The Jacobian is defined as the determinant of the deformation gradient tensor

$$J = \det(\mathbf{F}), \tag{3.75}$$

which is a measurement of the ratio of volume change during deformation. If $J = 1$, then no volume change occurs during deformation, which is also a requirement that must be satisfied for an incompressible material. $J > 1$ indicates an increase in volume while $J < 1$ signify a volume shrinkage. Note that $J \leq 0$ is unacceptable for any physically admissible deformation as it indicates a negative volume and the deforming object has undergone an irrational 'flip', which is physically impossible and meaningless.

Several useful tensor quantities related to the deformation gradient tensor $\mathbf{F}$ include:

The right ($\mathbf{U}$) and left ($\mathbf{V}$) stretch tensors, which characterize the pure stretching effect of a body experienced during deformation with $\mathbf{U}$ denotes the stretching of the body with respect to the reference configuration and $\mathbf{V}$ represents the stretching with respect to the deformed configuration

$$\mathbf{U} = \sqrt{\mathbf{F}^T \cdot \mathbf{F}}, \quad \text{and} \quad \mathbf{V} = \sqrt{\mathbf{F} \cdot \mathbf{F}^T}. \tag{3.76}$$

The rotation tensor $\mathbf{R}$ is an orthogonal tensor which signifies the pure rotation effect of the body where it rotates as a whole with no distance variations between the material points within it.

The right ($\mathbf{C}$) and left ($\mathbf{B}$) Cauchy-Green deformation tensors, which are both symmetric and positive definite, are defined as

$$\mathbf{C} = \mathbf{F}^T \cdot \mathbf{F}, \quad \text{and} \quad \mathbf{B} = \mathbf{F} \cdot \mathbf{F}^T. \tag{3.77}$$

It is readily comprehensible that they are related to the right ($\mathbf{U}$) and left ($\mathbf{V}$) stretch tensor through

$$\mathbf{C} = \mathbf{U}^2, \quad \text{and} \quad \mathbf{B} = \mathbf{V}^2. \tag{3.78}$$

With the above definitions of Eqs. (3.76), the deformation gradient tensor $\mathbf{F}$ can be uniquely

decomposed through a multiplicative decomposition into a product of rotations and stretches:

$$\mathbf{F} = \mathbf{R} \cdot \mathbf{U}, \quad \text{and} \quad \mathbf{F} = \mathbf{V} \cdot \mathbf{R}, \tag{3.79}$$

which are also regarded as right polar decomposition ($\mathbf{F} = \mathbf{R} \cdot \mathbf{U}$) that considers the deformation as a stretching ($\mathbf{U}$) followed by a rotation ($\mathbf{R}$), and left polar decomposition ($\mathbf{F} = \mathbf{V} \cdot \mathbf{R}$) that considers the deformation as a rotation ($\mathbf{R}$) followed by a stretching ($\mathbf{V}$).

Measurement of Strains

The Green-Lagrange Strain Tensor (or Green-St. Venant Strain Tensor), which is a quantity used to describe the strain state of a continuum body during deformation relative to its undeformed (or reference) configuration, specifically for cases of large shape changes or non-linear deformation. It is defined as

$$\mathbf{E} = \frac{1}{2}\left(\mathbf{F}^T \cdot \mathbf{F} - \mathbf{I}\right), \tag{3.80}$$

or written in a form with displacement gradient tensor as

$$\mathbf{E} = \frac{1}{2}\left[(\nabla \mathbf{u})^T + \nabla \mathbf{u} + (\nabla \mathbf{u})^T \cdot \nabla \mathbf{u}\right], \tag{3.81}$$

where the superscript T denotes the transpose operation. Note that the subscript $\mathbf{X}$ for the gradient operator has been omitted for clarity. The usage of the gradient operator ∇ will, by default, refer to an operation with respect to the reference configuration in the subsequent context unless otherwise stated.

For small shape change assumptions where the displacement and its gradient are trivial relative to the size scale of the continuum body, the deformation can be considered linear, and an **Infinitesimal Strain Tensor** can be defined as

$$\boldsymbol{\varepsilon} = \frac{1}{2}\left[\nabla \mathbf{u} + (\nabla \mathbf{u})^T\right], \tag{3.82}$$

The infinitesimal strain tensor can be decomposed into a volumetric strain part (representing the expansion and compression of the volume of the deforming body) and a deviatoric strain part (pure shape changes with no volume variation) in accordance with specific engineering scenario requirements:

$$\boldsymbol{\varepsilon} = \boldsymbol{\varepsilon}_{\text{dev}} + \frac{1}{3}\text{tr}(\boldsymbol{\varepsilon})\mathbf{I}, \tag{3.83}$$

where $\boldsymbol{\varepsilon}_{\text{dev}}$ is the deviatoric strain and $\text{tr}(\boldsymbol{\varepsilon})$ denotes the volumetric strain. $\text{tr}(\boldsymbol{\varepsilon})$ is the summation of

the diagonal elements of $\boldsymbol{\varepsilon}$ that can be expanded as

$$\mathrm{tr}(\boldsymbol{\varepsilon}) \equiv \varepsilon_{kk} = \varepsilon_{11} + \varepsilon_{22} + \varepsilon_{33}. \tag{3.84}$$

Measurement of Rates

Similar to the way of defining the displacement gradient $\mathbf{H}$, the velocity gradient tensor can be defined as

$$\mathbf{L} = \nabla_{\mathbf{x}}\mathbf{v} = \dot{\mathbf{F}} \cdot \mathbf{F}^{-1}. \tag{3.85}$$

Note that the gradient operation to $\mathbf{v}$ is performed with respect to the deformed configuration as highlighted by $\nabla_{\mathbf{x}}(\cdot)$.

Likewise, a stretch rate tensor ($\mathbf{D}$) and a spin tensor ($\mathbf{W}$) can be defined as

$$\mathbf{D} = \frac{1}{2}(\mathbf{L} + \mathbf{L}^T) \quad \text{and} \quad \mathbf{W} = (\mathbf{L} - \mathbf{L}^T). \tag{3.86}$$

Consequently, the velocity gradient tensor can also be expressed as

$$\mathbf{L} = \mathbf{D} + \mathbf{W}. \tag{3.87}$$

The strain rate measured with Green-Lagrange strain tensor can be written as

$$\dot{\mathbf{E}} = \mathbf{F}^T \cdot \mathbf{D} \cdot \mathbf{F}. \tag{3.88}$$

Compatibility Equations for Strains

The compatibility equations are a set of mathematical equations that guarantee a given strain distribution arises from a continuous, single displacement field within a three-dimensional space. In other words, these equations ensure that observed strain distributions are physically realizable, meaning that they can result from genuine physical movements and deformations of actual materials rather than mere theoretical constructs.

The compatibility conditions require

$$\frac{\partial^2 \varepsilon_{ij}}{\partial X_k \partial X_l} + \frac{\partial^2 \varepsilon_{kl}}{\partial X_i \partial X_j} - \frac{\partial^2 \varepsilon_{il}}{\partial X_j \partial X_k} - \frac{\partial^2 \varepsilon_{jk}}{\partial X_i \partial X_l} = 0. \tag{3.89}$$

3.2.2 Forces and Stress Tensors

Surface Traction and Body Force

Surface traction, denoted as $\mathbf{T}$, refers to the force per unit area acting on the surfaces (e.g., the boundaries $\partial\mathcal{B}$ and $\partial\mathcal{B}_t$ illustrated in Fig. 3.7 or any imaginary cross-sectional surfaces within the body) of an object. It can be originated as a result of friction, pressure and adhesion. Surface traction is conceptually defined as

$$\mathbf{T}(\mathbf{n}) = \lim_{\mathrm{d}S\to 0} \frac{\mathrm{d}\mathbf{P}}{\mathrm{d}S}, \tag{3.90}$$

where $\mathbf{n}$ is the surface normal and $\mathbf{T}(\mathbf{n})$ emphasizes the surface dependency of the traction force $\mathbf{T}$. $\mathrm{d}\mathbf{P}$ is the force acting on the area $\mathrm{d}S$.

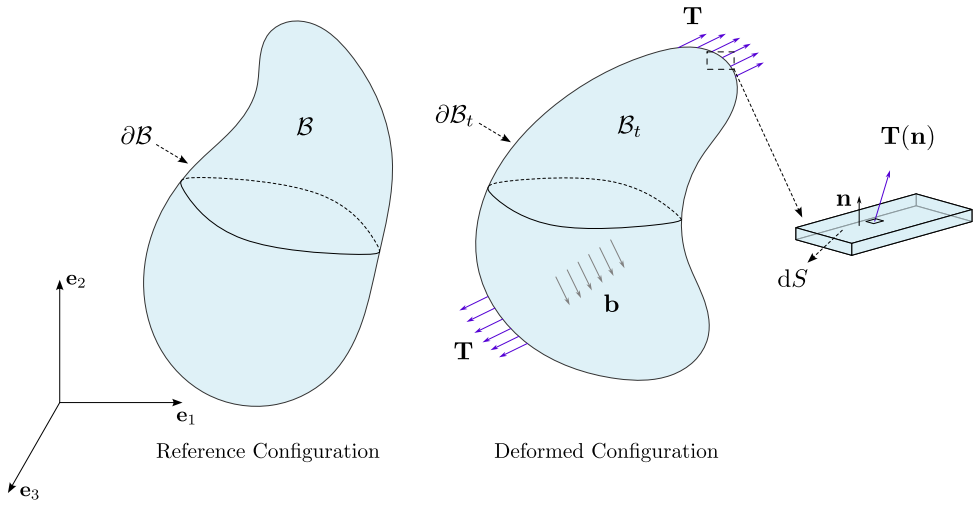


Figure 3.7: Surface traction and body force.

The body force, often characterized by the boldface symbol $\mathbf{b}$, is a type of force per unit mass acting inside an object. Representative examples of volumetric forces include gravity, electromagnetic forces, and inertial forces. Unlike surface traction, volumetric forces do not depend on the existence of an object's surface; they are distributed within the object. According to its definition, the body force can be expressed as

$$\mathbf{b} = \frac{1}{\rho} \lim_{\mathrm{d}V\to 0} \frac{\mathrm{d}\mathbf{P}}{\mathrm{d}V}, \tag{3.91}$$

where ρ is the mass density and $\mathrm{d}\mathbf{P}$ here refers to the force acting on an infinitesimal volume element $\mathrm{d}V$.

Consequently, the resultant force exerted on an object with volume V and surface area S can be

expressed as

$$\mathbf{P} = \int_S \mathbf{T}(\mathbf{n})\,\mathrm{d}S + \int_V \rho\mathbf{b}\,\mathrm{d}V. \tag{3.92}$$

Cauchy Stress Tensor

The Cauchy stress tensor, also known as the true stress tensor, is a second-order tensor that provides a complete mathematical description of the stress state of a material point inside a continuous medium, including normal and shear stresses. For a given surface element with its normal denoted as $\mathbf{n}$, the traction $\mathbf{T}(\mathbf{n})$ and the Cauchy stress tensor $\boldsymbol{\sigma}$ follows

$$\mathbf{T}(\mathbf{n}) = \mathbf{n} \cdot \boldsymbol{\sigma}. \tag{3.93}$$

Or in an index form as

$$T_i(\mathbf{n}) = n_j \sigma_{ji}, \tag{3.94}$$

where the subscript ji of the stress tensor indicates the ith component of traction acting on a surface with its normal in the direction of $\mathbf{e}_j$, as shown in Fig 3.8.

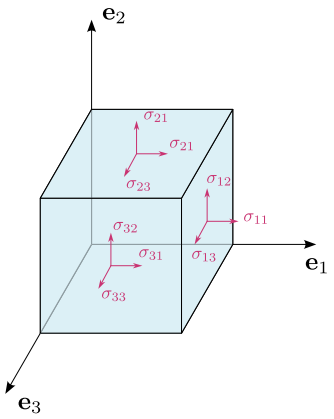


Figure 3.8: Components of Cauchy stress tensor.

Several useful stress definitions to address specific needs can be derived from the Cauchy stress tensor, including:

- **Hydrostatic stress**, which is associated with the uniform pressure applied in all directions, leading to pure volumetric change of the material without altering its shape:

$$\sigma_h = \frac{1}{3}\mathrm{tr}(\boldsymbol{\sigma}). \tag{3.95}$$

- **Deviatoric stress** is responsible for the pure shape distortion of a material with no volume alternation:

$$\boldsymbol{\sigma}_{\text{dev}} = \boldsymbol{\sigma} - \sigma_h \mathbf{I}. \tag{3.96}$$

- **Von Mises effective stress** is a scalar quantity that plays an important role in yield behaviour assessment of materials subjected to multi-axial stress states:

$$\sigma_e = \sqrt{\frac{2}{3}\boldsymbol{\sigma}_{\text{dev}} : \boldsymbol{\sigma}_{\text{dev}}}. \tag{3.97}$$

3.2.3 Conservation Laws

Conservation of Linear Momentum

Following Newton's second law of motion, which states that the force acting on an object is equal to the mass of the object multiplied by its acceleration, the conservation of linear momentum for an object subjected to a body force requires

$$\nabla_{\mathbf{x}} \cdot \boldsymbol{\sigma} + \rho \mathbf{b} = \rho \mathbf{a}. \tag{3.98}$$

where $\nabla_{\mathbf{x}}(\cdot)$ emphasizes that the gradient operation is performed with respect to the deformed configuration.

Conservation of Angular Momentum

The principle of conservation of angular momentum dictates that the Cauchy stress tensor must be symmetric, i.e.,

$$\boldsymbol{\sigma} = \boldsymbol{\sigma}^T. \tag{3.99}$$

3.2.4 Principle of Virtual Work

The principle of virtual work is the basis of finite element analysis. It states that for a system in equilibrium, the sum of the work done by all external forces (including both applied and constraining forces) and internal forces on any imaginary displacement of the system is zero. Here, "imaginary displacement" refers to the hypothetical, infinitesimal displacement of the material points in the system that is consistent with the constraints.

For dynamic analysis of a system subjected to body force and surface traction (as shown in Fig. 3.7) and experiencing infinitesimal motions, the principle of virtual work states

$$\delta W = \int_{\mathcal{B}} \boldsymbol{\sigma} : \delta\dot{\boldsymbol{\varepsilon}}\, \mathrm{d}V + \int_{\mathcal{B}} \rho_{\mathcal{B}}\mathbf{a} \cdot \delta\mathbf{v}\, \mathrm{d}V - \int_{\mathcal{B}} \rho_{\mathcal{B}}\mathbf{b} \cdot \delta\mathbf{v}\, \mathrm{d}V - \int_{\partial\mathcal{B}} \mathbf{T}(\mathbf{n}) \cdot \delta\mathbf{v}\, \mathrm{d}S = 0, \tag{3.100}$$

where the symbol δ indicates an infinitesimal variation of the variable. $\dot{\boldsymbol{\varepsilon}}$ denotes the strain rate, which is defined as $\dot{\boldsymbol{\varepsilon}} = 1/2\left[\nabla\mathbf{v} + (\nabla\mathbf{v})^T\right]$. $\rho_{\mathcal{B}}$ is the mass density when at the initial state. Note that the integration made in Eq. (3.100), highlighted by $\mathcal{B}$ and $\partial\mathcal{B}$, is based on the geometry of the reference configuration. Specifically, for a static or quasi-static analysis where $\mathbf{v} = 0$, Eq. (3.100) reduces to

$$\delta W_{\text{static}} = \int_{\mathcal{B}} \boldsymbol{\sigma} : \delta\boldsymbol{\varepsilon}\, \mathrm{d}V - \int_{\mathcal{B}} \rho_{\mathcal{B}}\mathbf{b} \cdot \delta\mathbf{u}\, \mathrm{d}V - \int_{\partial\mathcal{B}} \mathbf{T}(\mathbf{n}) \cdot \delta\mathbf{u}\, \mathrm{d}S = 0. \tag{3.101}$$

3.2.5 Constitutive Equations for Materials

Linear Elastic Materials

For a linear elastic material assumed to have isotropic material properties and experience small deformations, the relationship between its stress and strain can be expressed as

$$\boldsymbol{\varepsilon} = \frac{1+\nu}{E}\boldsymbol{\sigma} - \frac{\nu}{E}\mathrm{tr}(\boldsymbol{\sigma})\mathbf{I}, \quad \text{and inversely,} \quad \boldsymbol{\sigma} = \frac{E}{1+\nu}\boldsymbol{\varepsilon} + \frac{E\nu}{(1+\nu)(1-2\nu)}\mathrm{tr}(\boldsymbol{\varepsilon})\mathbf{I}, \tag{3.102}$$

where ν is poison's ratio, E is Young's modulus. Or, in a simpler form, employing a fourth-order elastic stiffness tensor $\mathbb{C}$ or an elastic compliance tensor $\mathbb{S}$ as

$$\boldsymbol{\sigma} = \mathbb{C} : \boldsymbol{\varepsilon}, \quad \text{and inversely,} \quad \boldsymbol{\varepsilon} = \mathbb{S} : \boldsymbol{\sigma}. \tag{3.103}$$

Index notation is often used for the stiffness and compliance tensors and hence renders Eqs. (3.103) to $\sigma_{ij} = C_{ijkl}\varepsilon_{kl}$ and $\varepsilon_{ij} = S_{ijkl}\sigma_{kl}$.

Note that the strain tensor used here (Eqs. (3.102) to Eqs. 3.103) is infinitesimal strain as defined in Eq. (3.82), and the stress tensor is Cauchy stress since all stress measurements are approximately equal in small deformation analysis.

Strain Energy Density for Linear Elastic Material

When the material is subjected to an external load and undergoes deformation, part of the work done by the external load is converted and stored as a reversible strain energy. For linear elastic materials,

the strain energy density ψ^{e} can be calculated through the stress and strain:

$$\psi^{\mathrm{e}} = \frac{1}{2}\boldsymbol{\sigma} : \boldsymbol{\varepsilon}^{\mathrm{e}} = \frac{1}{2}\sigma_{ij}\varepsilon^{\mathrm{e}}_{ij}, \tag{3.104}$$

where the superscript e indicates an elastic deformation-induced strain. Combining with Eqs. (3.102), the strain energy density can also be written as

$$\psi^{\mathrm{e}} = \frac{1+\nu}{2E}\boldsymbol{\sigma} : \boldsymbol{\sigma} - \frac{\nu}{2E}[\mathrm{tr}(\boldsymbol{\sigma})]^2 \quad \text{or} \quad \psi^{\mathrm{e}} = \frac{E}{2(1+\nu)}\boldsymbol{\varepsilon}^{\mathrm{e}} : \boldsymbol{\varepsilon}^{\mathrm{e}} + \frac{E\nu}{2(1+\nu)(1-2\nu)}[\mathrm{tr}(\varepsilon^{\mathrm{e}})]^2. \tag{3.105}$$

Rate-Dependent Deformations: Creep and Viscoplasticity

When a material's deformation behaviour changes in response to the rate at which loads are applied, it is categorized as rate-dependent deformation. Typical rate-dependent deformations include creep and viscoplasticity. Such phenomena are particularly evident in some metals, including lithium metal, especially when subjected to high pressure or at elevated temperatures.

Different from a linear elastic deformation, the constitutive relation involving rate-dependent deformations is characterized by several key concepts. With a small strain assumption (which means the strain and stress can be measured by infinitesimal strain and Cauchy stress, respectively) as an example of a straightforward elaboration, these concepts can be expressed as

- **Strain rate decomposition**: the total strain experienced by the material can be divided into elastic part and plastic part through an additive decomposition as

$$\dot{\boldsymbol{\varepsilon}} = \dot{\boldsymbol{\varepsilon}}^{\mathrm{e}} + \dot{\boldsymbol{\varepsilon}}^{\mathrm{p}}. \tag{3.106}$$

- **Rate constitutive equation for the elastic part** follows the linear elastic rules listed in Eqs. (3.103) and renders

$$\dot{\boldsymbol{\varepsilon}}^{\mathrm{e}} = \mathbb{S} : \dot{\boldsymbol{\sigma}}. \tag{3.107}$$

- **Plastic flow potential function**, which specifies the direction and governs the magnitude of the plastic strain rate, is dependent on the stress (often employ the von Mises effective stress σ_e) and material resistance to plastic flow (often characterized by material state variable σ_0) and has a general form as

$$\mathfrak{g} = \mathfrak{g}(\sigma_e, \sigma_0). \tag{3.108}$$

- **Plastic flow rule**, which is used to determine the direction and the magnitude of the strain increment resulting from a stress state based on the plastic flow potential function and has a general form expressed in

$$\dot{\boldsymbol{\varepsilon}}^{\mathrm{p}} = \dot{\lambda}\frac{\partial \mathfrak{g}}{\partial \boldsymbol{\sigma}}. \tag{3.109}$$

  where $\dot{\lambda} > 0$ is a plastic multiplier related to the hardening rule.

- **Strain hardening laws** provides a quantitative description of the hardening phenomenon when the material is plastically deforming and takes effect through the state variable σ_0 and encapsulates various mathematical forms.

Typical material models involving the above-mentioned general descriptions of rate-dependent deformations include **power law creep** and **Anand viscoplastic model** [105], which stand out in this research due to their applicability for non-linear deformation behaviour controls of lithium metal.

The plastic strain rate characterized by a power law relation, which is the most commonly used model to quantify the secondary creep and is suitable for small deformations, is expressed as

$$\dot{\boldsymbol{\varepsilon}}^{\mathrm{cr}} = A\exp\left(-\frac{Q}{RT}\right)\left(\frac{\sigma_e}{\sigma_{\mathrm{ref}}}\right)^n \frac{3}{2}\left(\frac{\boldsymbol{\sigma}_{\mathrm{dev}}}{\sigma_e}\right), \tag{3.110}$$

where A is a pre-exponential factor, Q is the activation energy, σ_{ref} is a reference stress and n is stress exponent.

Anand viscoplastic model is also a suitable choice, which is expressed as

$$\dot{\boldsymbol{\varepsilon}}^{\mathrm{v}} = \frac{3}{2}\left(\frac{\boldsymbol{\sigma}_{\mathrm{dev}}}{\sigma_e}\right)\dot{\bar{\epsilon}}^{\mathrm{v}} = A\exp\left(-\frac{Q}{RT}\right)\left(\frac{\sigma_e}{S}\right)^{\frac{1}{m}}\frac{3}{2}\left(\frac{\boldsymbol{\sigma}_{\mathrm{dev}}}{\sigma_e}\right), \tag{3.111}$$

where $\dot{\bar{\epsilon}}^{\mathrm{v}} = A\exp\left(-Q/RT\right)\left(\sigma_e/S\right)^{\frac{1}{m}}$ is the equivalent plastic shear strain-rate, m is the strain rate sensitivity exponent. S is the flow resistance with its rate defined as

$$\dot{S} = H_0\left|1-\frac{S}{S_{\mathrm{S}}}\right|^a \operatorname{sign}\left(1-\frac{S}{S_{\mathrm{S}}}\right)\dot{\bar{\epsilon}}^{\mathrm{v}} \quad \text{with} \quad S_{\mathrm{S}} = S_0\left[\frac{\dot{\bar{\epsilon}}^{\mathrm{v}}}{A\exp\left(-\frac{Q}{RT}\right)}\right]^n, \tag{3.112}$$

where S_{S} is the flow resistance saturation value and $\{H_0,\, S_0,\, a,\, n\}$ are strain hardening related parameters [105].

3.3 Phase Field Method

The phase field method stands out as a powerful mathematical framework in the past decades characterized by the introduction of continuous auxiliary field variables for both effective and straightforward descriptions of different states of materials in problems involving dynamic analysis, such as crack propagation prediction [83, 106, 107], corrosion [108], and phase transformation simulation [109, 110].

Before the advent of PFM, tackling intricate topological evolutions associated with free interfaces and phase transition processes posed significant challenges for researchers. Conventional approaches relied heavily on sharp interface models, as shown in Fig. 3.9a, which conceptualize the phase boundary between different material states or phases as a clear demarcation line. Although this approach is proven to be effective when dealing with interfaces with simple geometry and known locations, it falls short if faced with complicated geometrical interactions or when there is a need to account for the physicochemical properties of the interface itself. The PFM, on the other hand, replaced the discrete description near the interfaces in sharp interface models with a smooth transition with the help of a set of auxiliary field variables (often vary smoothly from 0 to 1 at the interface areas, such as the cracking problem shown in Fig. 3.9b). This enables a natural depiction of the successive variations in physical and chemical properties adjacent to and inside the interface areas. The dynamic behaviours of the interfaces, including migration, merging, and splitting, can also be readily captured by solving the space-time evolution equations for the phase field variables. The equations are usually constructed based on the principle of minimising the system's free energy, which often takes into account contributions from mechanical, chemical as well as interfacial energies. The comprehensive mathematical framework of the PFM, essential for an in-depth understanding of the energetics and dynamics of phase transitions and interface movements, will be elaborated in detail in this section.

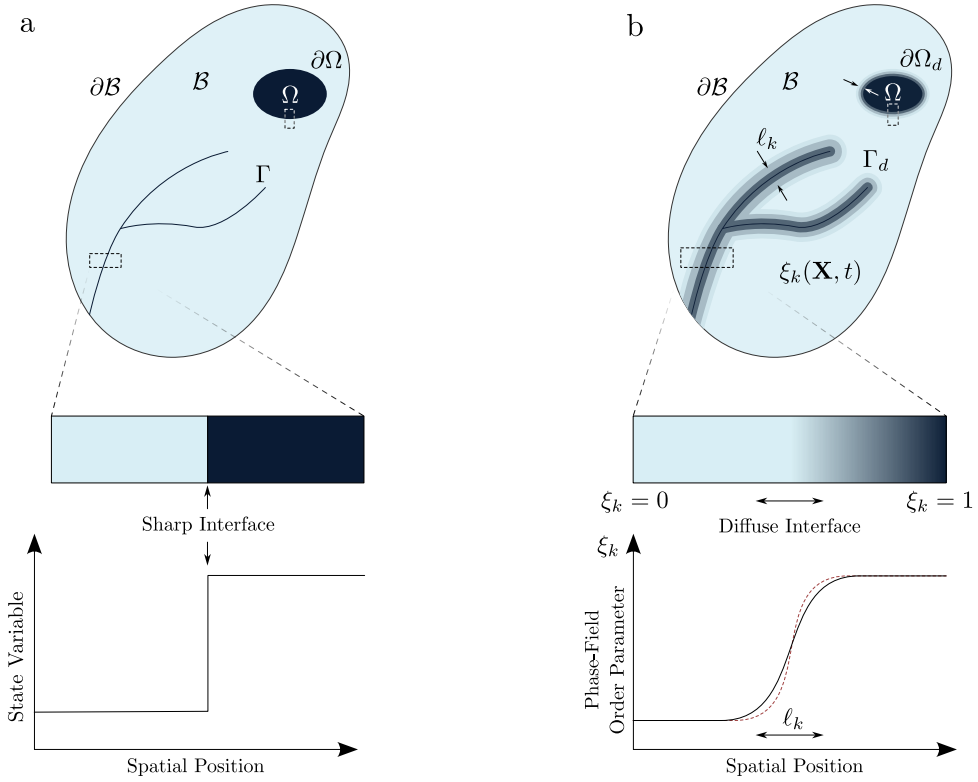


Figure 3.9: a) The conventional sharp interface method, and b) the phase-field method, in problems involving crack Γ, Γ_d and phase transformation ($\mathcal{B} \Leftrightarrow \Omega$). The subscript d denotes a diffuse interface, and ℓ_k is the thickness of the corresponding diffuse interfaces.

3.3.1 Kinetic Equations

The field variables that set the foundation of the PFM can be categorized into two primary types: conserved variables and non-conserved variables. Conserved variables pertain to physical quantities that maintain a constant amount within the system in the absence of external sources or sinks influencing material exchange. The dynamics of conserved variables are often encapsulated by equations featuring a diffusion term and following the framework of the Cahn-Hilliard type non-linear diffusion equation [111, 112]:

$$\frac{\partial \chi_i(\mathbf{X},t)}{\partial t} = \nabla \cdot M_i \nabla \frac{\delta \mathcal{F}}{\delta \chi_i(\mathbf{X},t)}, \tag{3.113}$$

where $\chi_i(\mathbf{X},t)$ is a conserved variable (e.g., the concentration of a component within a system) that is a function of spatial coordinates $\mathbf{X}$ and time t. M_i is a mobility coefficient. $\mathcal{F}$ is the free energy. The subscript $i = 1, 2, 3, ...$ indicates the possibility of multiple conserved variables interacting within the system.

In contrast, non-conserved variables refer to those quantities that do not necessarily comply with the conservation laws (e.g., the phase field order parameter). They are often governed by Allen-Cahn

type relaxation equations [113, 114]:

$$\frac{\partial \xi_k(\mathbf{X},t)}{\partial t} = -L_k \frac{\delta \mathcal{F}}{\delta \xi_k(\mathbf{X},t)}, \tag{3.114}$$

where $\xi_k(\mathbf{X},t)$ represents the phase field variables characterizing different phases within the system with the subscript $k = 1, 2, 3, ...$, and L_k is a kinetics parameter dictating the rate of phase transformations.

3.3.2 Free Energy Functional

The free energy functional $\mathcal{F}$ describes the system's thermodynamic energy state and serves as the driving force for phase evolution due to its natural tendency towards minimization. It quantifies the total free energy of the system $\mathcal{F}$ for a given multi-phase configuration considering contributions of various energy forms such as bulk energy $\mathcal{F}_{\text{bulk}}$, elastic energy $\mathcal{F}_{\text{e}}$, interfacial energy $\mathcal{F}_{\text{int}}$; and potentially other forms of energy specific to the particular challenges being addressed. The expression of $\mathcal{F}$ can thus be delivered as

$$\mathcal{F} = \mathcal{F}_{\text{bulk}} + \mathcal{F}_{\text{int}} + \mathcal{F}_{\text{e}} + ... \tag{3.115}$$

Eq. (3.115) is often expressed in energy density form such that

$$\begin{aligned}
\mathcal{F}(\chi_i, \xi_k, \nabla\chi_i, \nabla\xi_k, T, p, \boldsymbol{\varepsilon}, ...) &= \int_{\mathcal{B}} f(\chi_i, \xi_k, \nabla\chi_i, \nabla\xi_k, T, p, \boldsymbol{\varepsilon}, ...)\, \mathrm{d}V \\
&= \int_{\mathcal{B}} f_{\text{bulk}}(\chi_i, \xi_k, T, p) + f_{\text{int}}(\nabla\chi_i, \nabla\xi_k) + f_{\text{e}}(\boldsymbol{\varepsilon}) + ...\, \mathrm{d}V \\
&= \int_{\mathcal{B}} f_{\text{bulk}}(\chi_i, \xi_k, T, p) + \sum_i \frac{1}{2}\kappa_{\chi_i}|\nabla\chi_i|^2 + \sum_k \frac{1}{2}\kappa_{\xi_k}|\nabla\xi_k|^2 + f_{\text{e}}(\boldsymbol{\varepsilon}) + ...\, \mathrm{d}V,
\end{aligned} \tag{3.116}$$

where f denotes the local free energy density function, which is affected by several factors, including the phase field variables and their gradients. $f_{\text{bulk}}(\chi_i, \xi_k, T, p)$ refers to the portion of energy density associated with the volumetric properties of the material. It usually serves as an indicator of thermodynamic stability in a homogeneous region of the system where the phase field variables are held constant. The dependency of f_{bulk} is primarily on the phase field variable itself rather than its gradient or rate of change and is closely related to the chemical potential and thermodynamic regulators such as temperature T and pressure p. $f_{\text{int}}(\nabla\chi_i, \nabla\xi_k)$ is the energy density term responsible for the tuning of the diffuse interface and depends on the gradient of the phase field variables ($\frac{1}{2}\kappa_{\chi_i}|\nabla\chi_i|^2$ and $\frac{1}{2}\kappa_{\xi_k}|\nabla\xi_k|^2$) with κ_{χ_i} and κ_{ξ_k} denoting the gradient energy coefficients. $f_{\text{e}}(\boldsymbol{\varepsilon})$ is the elastic energy density.

An equilibrium of the system under some given constraint conditions (temperature, pressure, chemical components, etc.) can be achieved following the principle of minimizing the free energy and enforcing

$$\frac{\delta \mathcal{F}}{\delta \chi_i} = 0 \quad \text{and} \quad \frac{\delta \mathcal{F}}{\delta \xi_k} = 0, \tag{3.117}$$

for each conserved (χ_i) and non-conserved variable (ξ_k), providing guidance for the time evolution of these field variables in combination with the kinetic equations (3.113) and (3.114) and gives

$$\frac{\partial \chi_i(\mathbf{X}, t)}{\partial t} = \nabla \cdot M_i \nabla \frac{\delta \mathcal{F}}{\delta \chi_i(\mathbf{X}, t)} = \nabla \cdot M_i \nabla \left(\frac{\partial f_{\text{bulk}}}{\partial \chi_i} - \kappa_{\chi_i} \Delta \chi_i \right) \quad \text{with} \quad i = 1,\, 2,\, 3,\, ..., \tag{3.118}$$

and

$$\frac{\partial \xi_k(\mathbf{X}, t)}{\partial t} = -L_k \frac{\delta \mathcal{F}}{\delta \xi_k(\mathbf{X}, t)} = -L_k \left(\frac{\partial f_{\text{bulk}}}{\partial \xi_k} - \kappa_{\xi_k} \Delta \xi_k \right) \quad \text{with} \quad k = 1,\, 2,\, 3,\, ... \tag{3.119}$$

Note that the symbol $\Delta(\cdot) = \nabla^2(\cdot) = \nabla \cdot \nabla(\cdot)$ is a Laplace operator, which stands for a gradient operation followed by a divergence operation to a function.

3.4 Summary

In this chapter, a comprehensive summary involving the necessary theories to build the model is provided. This encompasses:

- The electrochemical theories necessary to describe the transfer of the electrons (Ohm's law) and charge carrier particles (Fick's law and Nernst-Planck equation), as well as the description of electrochemical reactions (Butler-Volmer equation).
- Some basic concepts related to the battery system are also introduced for a deep understanding of the literature in this field.
- Constitutive equations for materials, including linear and non-linear material models (creep), as well as key definitions and detailed derivations are provided in Section 3.2 since mechanical behaviour of the metal anode plays as the core role in our model.
- The derivations for the two most important governing equations, i.e., the Cahn-Hilliard type non-linear diffusion equation and the Allen-Cahn type relaxation equation, are also provided. They are employed to govern the behaviour of lithium occupancy and the phase field order parameter in our model, respectively.

Chapter 4

A Phase Field-Based Electro-Chemo-Mechanical Formulation for Interface Degradation Prediction in SSBs[1].

In this chapter, a multi-coupling framework that governs the interface degradation phenomenon within SSBs is developed. The primary objective of this investigation is the development and application of a phase field-based model that integrates electrochemical and mechanical mechanisms to predict the evolution of interface degradation under operational conditions. This formulation is expected to provide a deeper understanding of the dynamics at play during battery discharge and charge cycles, the nucleation and growth of voids, and the critical conditions of the emergence of dendrites.

4.1 Theory of the Model

During discharge, Li ions move from the Li anode to the cathode, and *stripping* takes place; metallic lithium undergoes anodic dissolution, and this leads to the nucleation and growth of voids in the Li metal anode at its interface with the solid electrolyte. As a result, local regions of high current density ('hot spots') emerge at the electrolyte in the vicinity of the junction with the Li anode and the void.

[1]Part of the work presented in this chapter has been published in: Y. Zhao, R. Wang, and E. Martínez-Pañeda. A phase field electro-chemo-mechanical formulation for predicting void evolution at the Li–electrolyte interface in all-solid-state batteries. *Journal of the Mechanics and Physics of Solids*, 167(June):104999, 10 2022. [115]

During charging, metallic lithium is deposited in a process termed *plating*, which results in a reduction of the voids' size and, occasionally, in the occlusion of voids formed on the previous stripping cycle (see Fig. 4.1). More importantly, Li plating is exacerbated at hot spots, leading to the nucleation and subsequent propagation of dendrites, needle-like structures between electrodes that short-circuit the battery cell. This process has been recently shown to be very sensitive to the plating and stripping currents [62]. A critical plating current density exists, above which dendrites nucleate, and voids form when the stripping current density exceeds the rate at which Li is replenished at the surface [62, 116]. There is a need to predict the evolution of voids during multiple plating/stripping cycles and map the conditions that lead to voiding, dendrite formation and cell death.

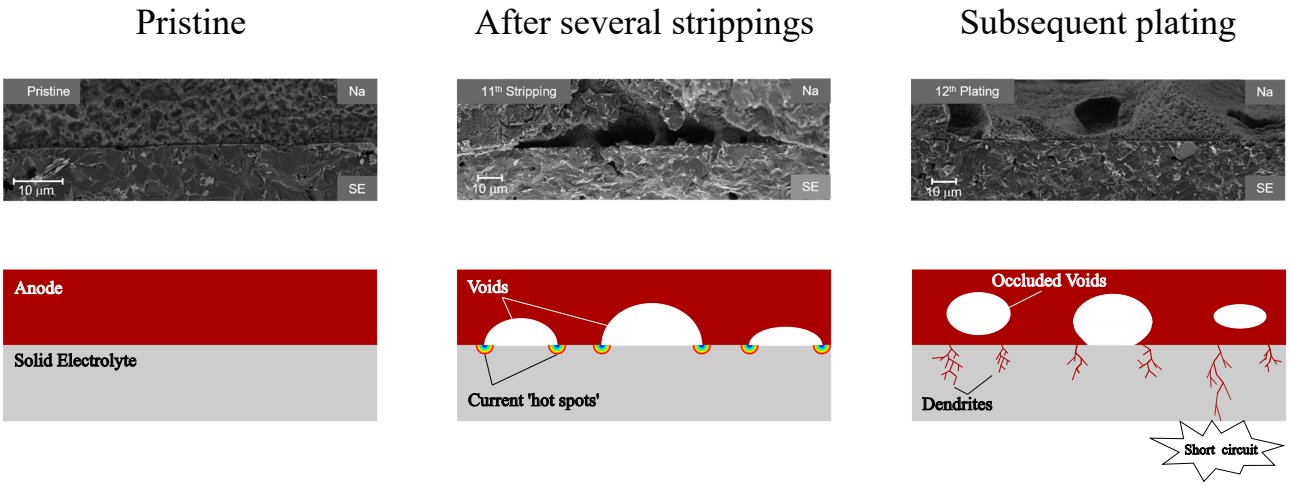


Figure 4.1: Interplay between voiding and dendrite formation: SEM images and sketches of the process of voiding and dendrite formation during plating and stripping cycles. The presence of voids generates local current 'hot spots' at the locations where the void meets the Li anode and the solid electrolyte. Li deposition will be exacerbated in these regions and lead to the nucleation of dendrites, which grow until causing the short circuit of the cell. The SEM images are based on the work by Spencer Jolly et al. [19] using Na anodes but are representative of what is observed in other all-solid-state battery systems, including Li-based.

4.1.1 Preliminaries

The theory aims at encapsulating the main physical mechanisms driving void nucleation and evolution during plating and stripping (see the work of Krauskopf et al. [73] for an example). The phenomena at play are sketched in Fig. 4.2.

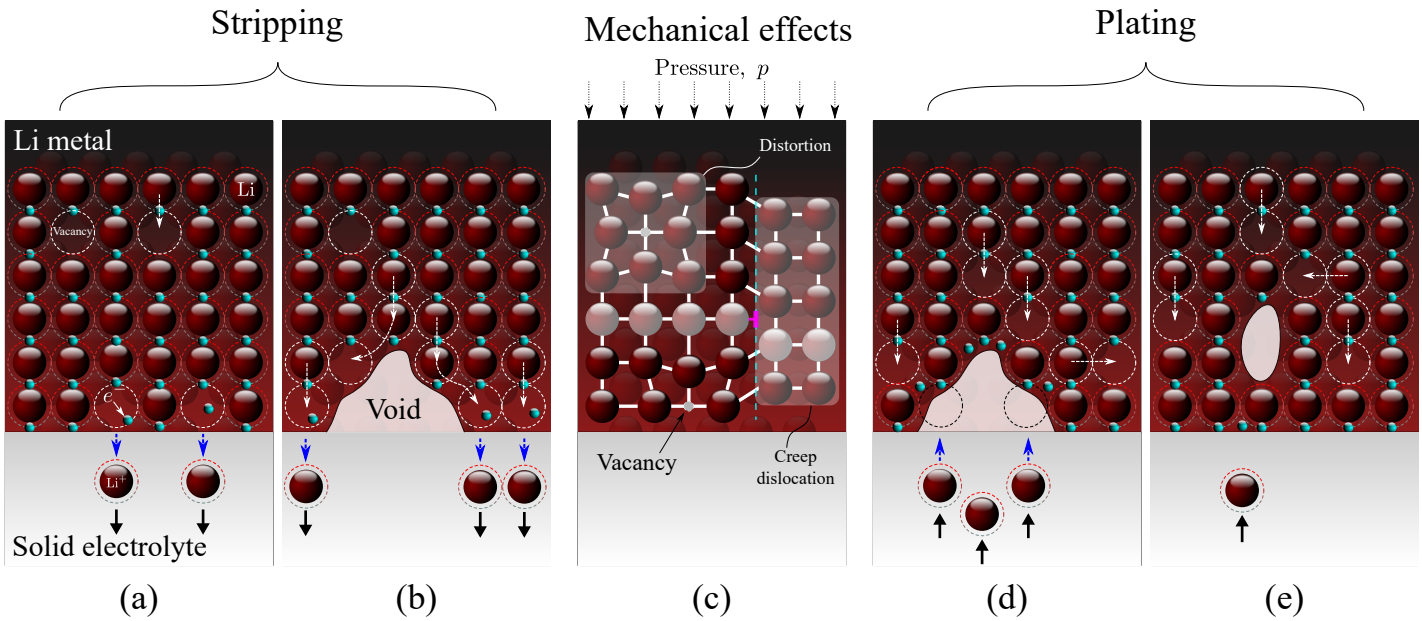


Figure 4.2: Schematic of the physical mechanisms governing voiding at the anode-electrolyte interface of all-solid-state batteries: (a) initial stripping stage, with vacancy diffusion and Li dissolution; (b) advanced stripping stage, with voiding, Li dissolution and both adatom and vacancy diffusion; (c) mechanical interactions relevant to both stripping and plating - vacancy diffusion distorts the lattice while creep due to an applied pressure closes the voids; (d) initial plating stage, with Li deposition reversing void growth; and (e) advanced plating stage, with void occlusion being observed due to further Li deposition.

Consider first the case of stripping. At the beginning of the process (Fig. 4.2a), two mechanisms are relevant: (i) substitutional diffusion within the bulk of the Li metal anode, where Li atoms diffuse to adjacent vacant sites, and (ii) dissolution of Li atoms at the anode-electrolyte interface, with Li ions moving to vacant or interstitial sites in the electrolyte and leaving behind in the anode an electron and a vacancy. If the current density is sufficiently large, the stripping rate of metal ions at the surface will exceed that of bulk vacancy diffusion, leading to void nucleation and contact loss (Fig. 4.2b). Specifically, voids form because vacancies condensate [117] or annihilate at available sinks such as dislocations, grain boundaries and free surfaces. Void growth is further enhanced by adatom diffusion, as the transport of atoms along the void surfaces is faster than bulk vacancy diffusion [118]. Voiding can be minimised by the application of mechanical pressure, as shown in Fig. 4.2c. Due to the viscoplastic nature of metallic lithium, plastic deformation and creep become relevant at sufficiently high pressures and act to close the voids and reduce contact loss. As depicted in Fig. 4.2c, another interaction with mechanics is the contraction and expansion of the Li atomic lattice in the anode as a result of vacancy diffusion. Finally, consider the plating process (Figs. 4.2d and 4.2e). Li ions move through the electrolyte into the anode, forming a Li atom in a surface site through vacancy nucleation and the interaction with an electron present in the anode. If the deposition current density is sufficiently high, void growth will be reversed, and surface contact will be improved, with voids often becoming

occluded from the interface.

Thus, voiding is governed by substitutional bulk and surface diffusion, lattice distortion, Li dissolution and deposition, nucleation and annihilation of vacancies, and creep deformation. These phenomena were captured by means of a coupled diffusion-deformation-phase field theory. The phase field paradigm is exploited to describe the evolution of the void-Li metal anode interface. Thus, the phase field order parameter (ξ) takes the values of 0 and 1 at the void and Li metal phases, respectively, and is defined to evolve as dictated by vacancy annihilation and nucleation. The diffusion problem takes as the primary kinematic variable the occupancy of Li sites in the anode (θ_m) and as boundary condition a current-dependent flux that incorporates the role of Li dissolution and deposition. Moreover, both bulk and surface diffusion are captured in its governing equation through the interaction with the mechanical and phase field problems. Finally, as appropriate for metallic lithium, the mechanical description is characterised by a viscoplastic constitutive response, capturing creep effects. Also, the role of lattice distortion is incorporated *via* chemical strains, and the balance of linear momentum is coupled to the phase field to account for the presence of voids. These elements of the theory are defined below in a thermodynamically-consistent manner. Moreover, the framework is extended to solve for the electric potential in the electrolyte, yielding a coupled electro-chemo-mechanical formulation able to predict the occurrence of local current hot-spots, which result from the voiding process and lead to the formation of dendrites.

4.1.2 Free Energy and Chemical Potential of the Lithium Metal Electrode

Consider a lithium metal electrode with a volume V, where the Li lattice sites can be annihilated into and nucleated from voids, as shown in Fig. 4.3. At some instant of time t, there are $N_{\mathrm{L}}^{\mathrm{m}}$ moles of lattice sites in the Li metal network, where $N_{\mathrm{Li}}^{\mathrm{m}}$ moles of Li atoms reside, leaving $N_{\mathrm{v}}^{\mathrm{m}}$ moles of lattice sites vacant. Throughout this manuscript, "m" is used as a superscript or a subscript to denote variables related to the metallic electrode.

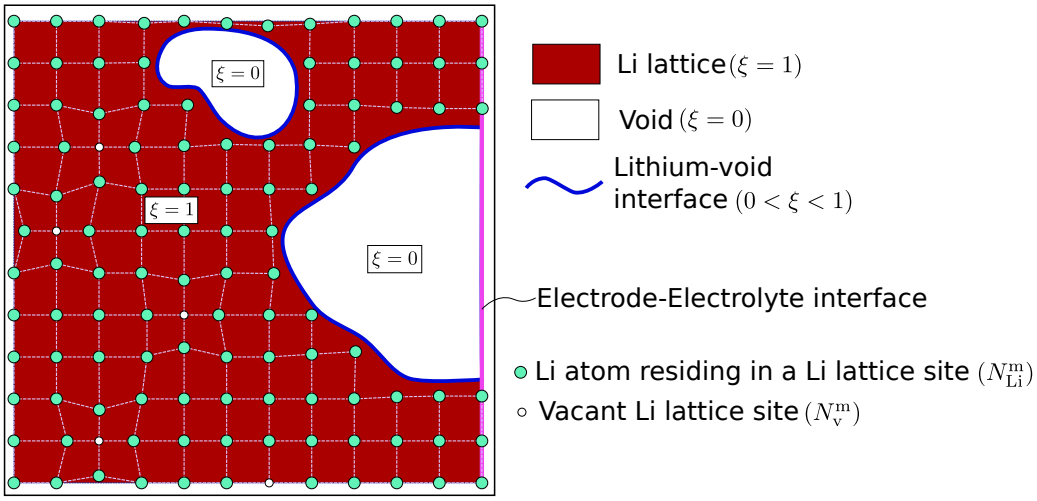


Figure 4.3: Illustration of the sites in a volume V of lithium metal. The shaded area denotes the network of lithium lattice sites and takes over a volume V^{m}. Thus, the voids occupy a volume of $V^{\mathrm{v}} = V - V^{\mathrm{m}}$. In V^{m}, there are $N_{\mathrm{Li}}^{\mathrm{m}}$ lattice sites occupied by lithium atoms, leaving $N_{\mathrm{v}}^{\mathrm{m}}$ lattice sites vacant.

Let Ω_{Li} and Ω_{v} respectively denote the molar volume of Li and vacant sites. Then, the total volume of the Li metal network equals

$$V^{\mathrm{m}} = N_{\mathrm{Li}}^{\mathrm{m}}\Omega_{\mathrm{Li}} + N_{\mathrm{v}}^{\mathrm{m}}\Omega_{\mathrm{v}}. \tag{4.1}$$

The remaining volume, denoted by V^{v}, corresponds to the voids. The total volume of the anode is thus $V = V^{\mathrm{m}} + V^{\mathrm{v}}$, and is kept constant. It is emphasised that voids refer to regions where vacancies have been condensated or annihilated; unlike vacancies, voids cannot store strain energy. In the absence of external loading, vacancies are in equilibrium with voids. Next step is to define the molar concentration of Li atoms $c_{\mathrm{Li}}^{\mathrm{m}}$, Li vacant sites $c_{\mathrm{v}}^{\mathrm{m}}$, and Li lattice sites $c_{\mathrm{L}}^{\mathrm{m}}$ as

$$c_{\mathrm{Li}}^{\mathrm{m}} = \lim_{\mathrm{d}V^{\mathrm{m}}\to 0} \frac{\mathrm{d}N_{\mathrm{Li}}^{\mathrm{m}}}{\mathrm{d}V^{\mathrm{m}}}, \quad c_{\mathrm{v}}^{\mathrm{m}} = \lim_{\mathrm{d}V^{\mathrm{m}}\to 0} \frac{\mathrm{d}N_{\mathrm{v}}^{\mathrm{m}}}{\mathrm{d}V^{\mathrm{m}}}, \quad c_{\mathrm{L}}^{\mathrm{m}} = \lim_{\mathrm{d}V^{\mathrm{m}}\to 0} \frac{\mathrm{d}N_{\mathrm{L}}^{\mathrm{m}}}{\mathrm{d}V^{\mathrm{m}}}. \tag{4.2}$$

Let $\theta_{\mathrm{m}} = c_{\mathrm{Li}}^{\mathrm{m}}/c_{\mathrm{L}}^{\mathrm{m}}$ denote the Li occupancy, while $\theta_{\mathrm{v}} = c_{\mathrm{v}}^{\mathrm{m}}/c_{\mathrm{L}}^{\mathrm{m}}$ gives the vacancy occupancy in the Li metal network. It follows that $\theta_{\mathrm{v}} = 1 - \theta_{\mathrm{m}}$. In the Li metal anode, Li is both the solute and the solvent, implying that there is no theoretical upper bound on the Li concentration when V_{m} reduces to 0 [102]. In such a scenario (e.g., stripping), the present phase field model will predict a transformation of the Li metal phase into the void phase, and all concentrations will automatically become equal to 0 (as elaborated below).

For a pressure p_{m} and a fixed electrode volume $V = V^{\mathrm{m}} + V^{\mathrm{v}}$, recall that the Helmholtz free energy

$\Psi = \mathcal{U} - T\mathcal{S} = \mathcal{G} - Vp_{\mathrm{m}}$; the Helmholtz free energy of the electrode reads [9]

$$Psi^{\mathrm{m}} = N_{\mathrm{Li}}^{\mathrm{m}}\mu_{\mathrm{m}}^{0} + N_{\mathrm{v}}^{\mathrm{m}}h_{\mathrm{v}} + N_{\mathrm{L}}^{\mathrm{m}}RT\left[\theta_{\mathrm{m}}\ln\theta_{\mathrm{m}} + (1-\theta_{\mathrm{m}})\ln(1-\theta_{\mathrm{m}})\right] + V^{\mathrm{m}}\psi_e, \tag{4.4}$$

where $\mathcal{U}$ is the internal energy, $\mathcal{S}$ is entropy, $\mathcal{G}$ is the Gibbs free energy, R is the gas constant, T is the absolute temperature, μ_{m}^{0} is the reference molar enthalpy of Li atoms at zero pressure, and h_{v} is the molar enthalpy of the formation of vacant sites in Li (≈ 50 kJ/mol [9]), ψ_e is the elastic strain energy density.

The chemical potentials of Li atoms and lattice sites can be respectively derived as

$$\mu_{\mathrm{Li}}^{\mathrm{m}} = \left.\frac{\delta\Psi^{\mathrm{m}}}{\delta N_{\mathrm{Li}}^{\mathrm{m}}}\right|_{N_{\mathrm{L}}^{\mathrm{m}}} = \left(\mu_{\mathrm{m}}^{0} - h_{\mathrm{v}}\right) + RT\ln\frac{\theta_{\mathrm{m}}}{1-\theta_{\mathrm{m}}} + \left(\Omega_{\mathrm{Li}} - \Omega_{\mathrm{v}}\right)\psi_e, \tag{4.5}$$

$$\mu_{\mathrm{L}}^{\mathrm{m}} = \left.\frac{\delta\Psi^{\mathrm{m}}}{\delta N_{\mathrm{L}}^{\mathrm{m}}}\right|_{N_{\mathrm{Li}}^{\mathrm{m}}} = h_{\mathrm{v}} + RT\ln(1-\theta_{\mathrm{m}}) + \Omega_{\mathrm{v}}\psi_e. \tag{4.6}$$

Note that the chemical potential of the vacancies can be calculated through $\mu_{\mathrm{v}}^{\mathrm{m}} = \left.\frac{\delta\Psi^{\mathrm{m}}}{\delta N_{\mathrm{v}}^{\mathrm{m}}}\right|_{N_{\mathrm{Li}}^{\mathrm{m}}}$, which equals $\mu_{\mathrm{L}}^{\mathrm{m}}$. In other words, the nucleation and annihilation of lattice sites are achieved by the addition and removal of vacancies.

The expression for equilibrium chemical potentials μ_{m}^{0} and h_{v} follows [9]. In equilibrium, diffusion of lithium atoms is precluded, and thus, the chemical potential is constant everywhere, viz. $\mu_{\mathrm{Li}}^{\mathrm{m}} = \mu_{\mathrm{L}}^{\mathrm{m}}$. Moreover, Li vacant sites are not annihilated or nucleated under equilibrium conditions, indicating that $\mu_{\mathrm{L}}^{\mathrm{m}}$ should vanish. Thus, $\mu_{\mathrm{Li}}^{\mathrm{m}} = \mu_{\mathrm{L}}^{\mathrm{m}} = 0$. If define θ_{m}^{0} as the equilibrium lithium occupancy in the absence of mechanical pressure and elastic straining, it naturally follows from Eqs. (4.5) and (4.6) that

$$h_{\mathrm{v}} + RT\ln\left(1-\theta_{\mathrm{m}}^{0}\right) = 0\,, \quad \text{and} \quad \mu_{\mathrm{m}}^{0} + RT\ln\theta_{\mathrm{m}}^{0} = 0\,. \tag{4.7}$$

Accordingly, θ_{m}^{0} can be calculated through h_{v} as [9]

$$\theta_{\mathrm{m}}^{0} = 1 - \exp\left(-\frac{h_{\mathrm{v}}}{RT}\right). \tag{4.8}$$

Substituting Eqs. (4.7) to Eq. (4.4) and rearrange yields

$$\Psi^{\mathrm{Bulk}} = N_{\mathrm{L}}^{\mathrm{m}}RT\left[\theta_{\mathrm{m}}\ln\frac{\theta_{\mathrm{m}}}{\theta_{\mathrm{m}}^{0}} + (1-\theta_{\mathrm{m}})\ln\frac{1-\theta_{\mathrm{m}}}{1-\theta_{\mathrm{m}}^{0}}\right] + V^{\mathrm{m}}\psi_e, \tag{4.9}$$

where the superscript "Bulk" is used instead of 'm' for the clarity of the derivations in the following sections with an emphasis on the absence of a Li metal-void interfacial energy term. Recalling Eq. (4.2), Eq. (4.9) can be reformulated as

$$\Psi^{\text{Bulk}} = \int_{V^{\text{m}}} \left\{ c_{\text{L}}^{\text{m}} RT \left[\theta_{\text{m}} \ln \frac{\theta_{\text{m}}}{\theta_{\text{m}}^{0}} + (1-\theta_{\text{m}}) \ln \frac{1-\theta_{\text{m}}}{1-\theta_{\text{m}}^{0}} \right] + \psi_e \right\} \mathrm{d}V. \tag{4.10}$$

4.1.3 Phase Field Formulation of the Helmholtz Free Energy of a Lithium Electrode with Voids

Let us now incorporate into the model the presence of an evolving void-anode interface. To achieve this, the phase field paradigm is exploited, which has been successfully applied to a wide range of interfacial problems, including corrosion [106, 119], microstructural evolution [120, 121], fracture [122, 123], and dendrite growth in liquid electrolytes [13, 124]. Thus, an order parameter $\xi = \xi(\mathbf{x}, t)$ is introduced, which is a time-dependent field variable defined in the volume V. As shown in Fig. 4.3, it bears the value of 1 in the lattice and 0 in the void, varying smoothly in-between. Further, the ξ-dependent variables are introduced: lattice concentration c_{L}^{ξ}, lithium occupancy θ_{m}^{ξ} and elastic strain energy density ψ_e^{ξ} as

$$c_{\text{L}}^{\xi} = c_{\text{L}}^{\text{m}}, \quad \theta_{\text{m}}^{\xi} = \theta_{\text{m}}, \quad \psi_e^{\xi} = \psi_e \qquad \text{in } V^{\text{m}}(\xi = 1), \text{ and} \tag{4.11}$$

$$c_{\text{L}}^{\xi} = 0, \quad \theta_{\text{m}}^{\xi} = \theta_{\text{m}}^{\text{const}}, \quad \psi_e^{\xi} = 0 \qquad \text{in } V^{\text{v}}(\xi = 0). \tag{4.12}$$

The lattice concentration c_{L}^{m} is taken as a constant, with the average molar volume of the lattice Ω_{L} as reciprocal. In the void, there are no lattice sites ($c_{\text{L}}^{\xi} = 0$), and thus, the model is, from a theoretical viewpoint, insensitive to the choice of θ_{m}^{ξ} in $V^{\text{v}}(\xi = 0)$. However, note that numerical convergence is facilitated by choices of $\theta_{\text{m}}^{\text{const}}$ that are close to the magnitude of the lithium occupancy in the lattice θ_{m}. Since $\theta_{\text{m}}^{\xi} \equiv \theta_{\text{m}}$ for $0 < \xi \leq 1$, the superscript ξ is dropped for the lithium occupancy. Contrarily, c_{L}^{ξ} and ψ_e^{ξ} are interpolated along the lithium-void interface by means of an interpolation function $h(\xi)$, such that

$$c_{\text{L}}^{\xi} = h(\xi) c_{\text{L}}^{\text{m}}, \qquad \text{and} \qquad \psi_e^{\xi} = h(\xi) \psi_e. \tag{4.13}$$

This interpolation function must satisfy $h(0) = 0$ and $h(1) = 1$, such that Eqs. (4.11) and (4.12) are naturally fulfilled when $\xi = 0$ and $\xi = 1$. Also, as discussed below, its first derivative must vanish

inside of the void $h'(0) = 0$. Accordingly, the following form is taken

$$h(\xi) = \xi^2 \left(\xi^2 - 3\xi + 3\right). \tag{4.14}$$

Recalling Eq. (4.2), the lithium concentration c_{Li}^{ξ} can be defined as

$$c_{\mathrm{Li}}^{\xi} = h(\xi) c_{\mathrm{L}}^{\mathrm{m}} \theta_{\mathrm{m}}. \tag{4.15}$$

Eq. (4.15) shows that, independently of the magnitude of θ_{m}, c_{Li}^{ξ} vanishes in the void.

Considering these ξ-dependent variables, the Helmholtz free energy (4.10) can be rewritten as

$$\Psi^{\mathrm{Bulk}} = \int_V \left\{ c_{\mathrm{L}}^{\xi} RT \left[\theta_{\mathrm{m}} \ln \frac{\theta_{\mathrm{m}}}{\theta_{\mathrm{m}}^0} + (1 - \theta_{\mathrm{m}}) \ln \frac{1 - \theta_{\mathrm{m}}}{1 - \theta_{\mathrm{m}}^0} \right] + \psi_e^{\xi} \right\} \mathrm{d}V. \tag{4.16}$$

An interfacial energy of the following form is introduced

$$\Psi^{\mathrm{Interface}} = \int_V \left(w g(\xi) + \frac{1}{2} \kappa |\boldsymbol{\nabla} \xi|^2 \right) \mathrm{d}V, \tag{4.17}$$

where κ is the gradient energy coefficient and the first term on the right-hand side of (4.17) is a double-well function with two minima at $\xi = 0$ and $\xi = 1$,

$$g(\xi) = \xi^2 (1 - \xi)^2, \tag{4.18}$$

where $w/16$ is the barrier height. The total free energy is then defined as the sum of the bulk and interfacial terms: $\Psi = \Psi^{\mathrm{Bulk}} + \Psi^{\mathrm{Interface}}$.

4.1.4 Kinematic and Constitutive Equations

The proposed deformation-diffusion-phase field model is described by three primal kinematic variables: the displacement field vector $\mathbf{u}(\mathbf{x}, t)$, the lithium occupancy $\theta_{\mathrm{m}}(\mathbf{x}, t)$, and the phase field order parameter $\xi(\mathbf{x}, t)$. These variables respectively characterise the mechanical response, lithium diffusion (vacancy and adatom diffusion), and the evolution of the void-anode interface, as dictated by site nucleation and annihilation. In this subsection, a description of the related kinematic and constitutive equations is provided.

Mechanical Relations

The deformation of the lithium metal electrode is characterised by a total strain rate $\dot{\boldsymbol{\varepsilon}}$, defined as

$$\dot{\boldsymbol{\varepsilon}} = \frac{1}{2}\left(\boldsymbol{\nabla}\dot{\mathbf{u}} + \boldsymbol{\nabla}\dot{\mathbf{u}}^{\mathrm{T}}\right), \tag{4.19}$$

where the superposed dot indicates differentiation with respect to time. The total strain rate can be additively decomposed into its elastic, viscoplastic and chemical components as follows

$$\dot{\boldsymbol{\varepsilon}} = \dot{\boldsymbol{\varepsilon}}_e + \dot{\boldsymbol{\varepsilon}}_v + \dot{\boldsymbol{\varepsilon}}_c. \tag{4.20}$$

The chemical strain rate is the strain variation induced by the transport of Li atoms within the electrode as, due to the different partial molar volumes of occupied and vacant lattice sites, lattice distortion takes place when Li atoms diffuse to occupy a vacancy. The chemical strain rate tensor is defined as

$$\dot{\boldsymbol{\varepsilon}}_c = \frac{1}{3}\frac{\partial(c^{\xi}_{\mathrm{Li}} - c^{\xi}_{\mathrm{ref}})}{\partial t}\left(\Omega_{\mathrm{Li}} - \Omega_{\mathrm{v}}\right)\mathbf{1}, \tag{4.21}$$

where $\mathbf{1}$ is the second-order unit tensor and c^{ξ}_{ref} is the stress-free concentration, which equals $c^{\xi}_{\mathrm{ref}} = h(\xi)c^{\mathrm{m}}_{\mathrm{L}}\theta^{0}_{\mathrm{m}}$. The term $(\Omega_{\mathrm{Li}} - \Omega_{\mathrm{v}})$ results from the consideration of the substitutional nature of Li diffusion. Recalling Eq. (4.15), and applying the chain rule to the concentration rate, which yields

$$\frac{\partial(c^{\xi}_{\mathrm{Li}} - c^{\xi}_{\mathrm{ref}})}{\partial t} = \dot{h}c^{\mathrm{m}}_{\mathrm{L}}(\theta_{\mathrm{m}} - \theta^{0}_{\mathrm{m}}) + hc^{\mathrm{m}}_{\mathrm{L}}\dot{\theta}_{\mathrm{m}}. \tag{4.22}$$

Inspection of Eq. (4.22) reveals that the rate of concentration has two contributions: site nucleation/annihilation ($\dot{h}$) and lithium diffusion in the lattice ($\dot{\theta}_{\mathrm{m}}$). Here, one should note that Li insertion or extraction is only allowed to take place at lattice sites (regions with $\xi > 0$), and accordingly, the chemical strain rate should vanish in the void. This is automatically satisfied in Eq. (4.22) because $h(\xi)$ is defined such that $h(0) = h'(0) = 0$, see Eq. (4.14).

The viscoplastic strain rate $\dot{\boldsymbol{\varepsilon}}_v$ is defined following Anand's model [105, 125], such that

$$\dot{\boldsymbol{\varepsilon}}_v = F_{\mathrm{cr}}\frac{3}{2}\frac{\boldsymbol{\sigma}^{\xi}_{\mathrm{dev}}}{\sigma^{\xi}_{e}}, \tag{4.23}$$

where $\boldsymbol{\sigma}^{\xi}_{\mathrm{dev}}$ and σ^{ξ}_{e} denote the deviatoric stress tensor and the von Mises effective stress, respectively.

They are defined as

$$\boldsymbol{\sigma}^{\xi}_{\text{dev}} = \boldsymbol{\sigma}^{\xi} - \frac{1}{3}\left(\text{tr}\boldsymbol{\sigma}^{\xi}\right)\mathbf{1}, \tag{4.24}$$

$$\sigma^{\xi}_{e} = \sqrt{\frac{3}{2}\boldsymbol{\sigma}^{\xi}_{\text{dev}} : \boldsymbol{\sigma}^{\xi}_{\text{dev}}}, \tag{4.25}$$

where $\text{tr}\boldsymbol{\sigma}^{\xi}$ is the trace of the stress tensor $\boldsymbol{\sigma}^{\xi}$. The equivalent plastic shear strain-rate F_{cr} is given by

$$F_{\text{cr}} = A\exp\left(-\frac{Q}{RT}\right)\left[\sinh\left(\frac{\sigma^{\xi}_{e}}{S_a}\right)\right]^{\frac{1}{m}}, \tag{4.26}$$

where A is a pre-exponential factor, Q is the activation energy, and m is the strain rate sensitivity exponent ($0 < m \leq 1$). The flow resistance rate $\dot{S}_a$ is defined as follows,

$$\dot{S}_a = H_0\left|1 - \frac{S_a}{S^*_a}\right|^a \text{sign}\left(1 - \frac{S_a}{S^*_a}\right)F_{\text{cr}}, \qquad \text{with} \qquad S^*_a = S_0\left(\frac{F_{\text{cr}}}{A\exp\left(-\frac{Q}{RT}\right)}\right)^n. \tag{4.27}$$

Here, H_0, a, n and S_0 are strain hardening parameters [105].

Regarding the elastic part, the elastic constants are degraded by the phase field to ensure that a zero stiffness response is attained in the void. Accordingly, the elastic moduli can be interpolated as

$$G^{\xi} = h(\xi)G\,, \quad \text{and} \quad K^{\xi} = h(\xi)K, \tag{4.28}$$

where G and K are the shear and bulk modulus of the lithium metal, respectively. Along the same lines, the elastic strain energy can be constructed as

$$\psi^{\xi}_{e} = G^{\xi}\boldsymbol{\varepsilon}_e : \boldsymbol{\varepsilon}_e + \frac{1}{2}\left(K^{\xi} - \frac{2}{3}G^{\xi}\right)\left(\text{tr}\boldsymbol{\varepsilon}_e\right)^2, \tag{4.29}$$

and the definition of the stress tensor $\boldsymbol{\sigma}^{\xi}$ readily follows as,

$$\boldsymbol{\sigma}^{\xi} = 2G^{\xi}\boldsymbol{\varepsilon}_e + \left(K^{\xi} - \frac{2}{3}G^{\xi}\right)\left(\text{tr}\boldsymbol{\varepsilon}_e\right)\mathbf{1}. \tag{4.30}$$

Combining Eqs. (4.24), (4.25) and (4.30), the deviatoric and effective von Mises stresses can be

defined, as required to calculate the viscoplastic strain, giving

$$\boldsymbol{\sigma}^{\xi}_{\mathrm{dev}} = 2G^{\xi}\boldsymbol{\varepsilon}_e - \frac{2}{3}G^{\xi}\left(\mathrm{tr}\boldsymbol{\varepsilon}_e\right)\mathbf{1}, \tag{4.31}$$

$$\sigma^{\xi}_{e} = \sqrt{\frac{3}{2}\boldsymbol{\sigma}^{\xi}_{\mathrm{dev}} : \boldsymbol{\sigma}^{\xi}_{\mathrm{dev}}} = G^{\xi}\sqrt{6\boldsymbol{\varepsilon}_e : \boldsymbol{\varepsilon}_e + 4\left(\mathrm{tr}\boldsymbol{\varepsilon}_e\right)^2}\,. \tag{4.32}$$

Chemical Potential for Lithium Diffusion

Next is to define the chemical potential for the diffusion of lithium atoms within the anode. The evolution of lithium per unit area is described by the time derivative of lithium concentration c^{ξ}_{Li}, as defined in Eq. (4.15). The work conjugate of c^{ξ}_{Li} is the chemical potential of lithium atoms, which can be derived as

$$\mu^{\xi}_{\mathrm{Li}} = \frac{1}{c^{\xi}_{\mathrm{L}}}\frac{\delta\Psi}{\delta\theta_{\mathrm{m}}} = -RT\ln\frac{\theta^0_{\mathrm{m}}}{1-\theta^0_{\mathrm{m}}} + RT\ln\frac{\theta_{\mathrm{m}}}{1-\theta_{\mathrm{m}}} - \left(\Omega_{\mathrm{Li}} - \Omega_{\mathrm{v}}\right)\sigma^{\xi}_{h}, \tag{4.33}$$

where σ^{ξ}_{h} is the hydrostatic stress, given by $\sigma^{\xi}_{h} = K^{\xi}\left(\mathrm{tr}\boldsymbol{\varepsilon}_e\right)$.

Chemical Potential for Lithium Lattice Sites

The evolution of lattice sites is characterised by the phase field order parameter ξ. The work conjugate of ξ, which acts as the driving force for the phase field evolution, can be derived as follows,

$$\mu_{\xi} = \frac{\delta\Psi}{\delta\xi} = RTc^{\mathrm{m}}_{\mathrm{L}}h'\ln\frac{1-\theta_{\mathrm{m}}}{1-\theta^0_{\mathrm{m}}} + \Omega_{\mathrm{v}}c^{\mathrm{m}}_{\mathrm{L}}h'\psi_e + wg' - \kappa\nabla^2\xi. \tag{4.34}$$

It can be seen that, if the interfacial and pressure terms are ignored, μ_{ξ} differs from the lattice site chemical potential (Eq. (4.6)) only by the factor $h'c^{\mathrm{m}}_{\mathrm{L}}$.

4.1.5 Governing Equations

Now, the governing equations can be derived. As shown in Fig. 4.4, the lithium electrode domain is enclosed by four boundaries Γ^l, Γ^r, Γ^u and Γ^b on the left, right, upper and lower edges, respectively. The current collector and the solid electrolyte lie on the left and right sides of the domain of interest, respectively. The upper and lower edges are electronically isolated, chemically impermeable and mechanically confined. The electrode area is further subdivided into two parts: the lithium metal V^{m} and the void V^{v}. Two more interfaces can then be identified: the one between the lithium metal and the void $\Gamma^{\mathrm{Interface}}$, and that between the void and the solid electrolyte Γ^{v}. Using the phase field

paradigm, $\Gamma^{\text{Interface}}$ has been replaced by a diffuse interface, characterised by the phase field order parameter ξ and its gradient. Following experimental observations, it can be assumed that voids can nucleate from the electrolyte side. Under this assumption, the solid electrolyte can be in contact with both the void and the lithium metal. The interface with the void can be denoted as Γ^{v} and the interface with lithium metal as Γ^f. Then, $\Gamma^{\text{v}} \cup \Gamma^f = \Gamma^r$. The lithium occupancy θ_{m}, displacements $\mathbf{u}$ and phase field order parameter ξ are chosen as independent field variables, which are defined in the complete domain V.

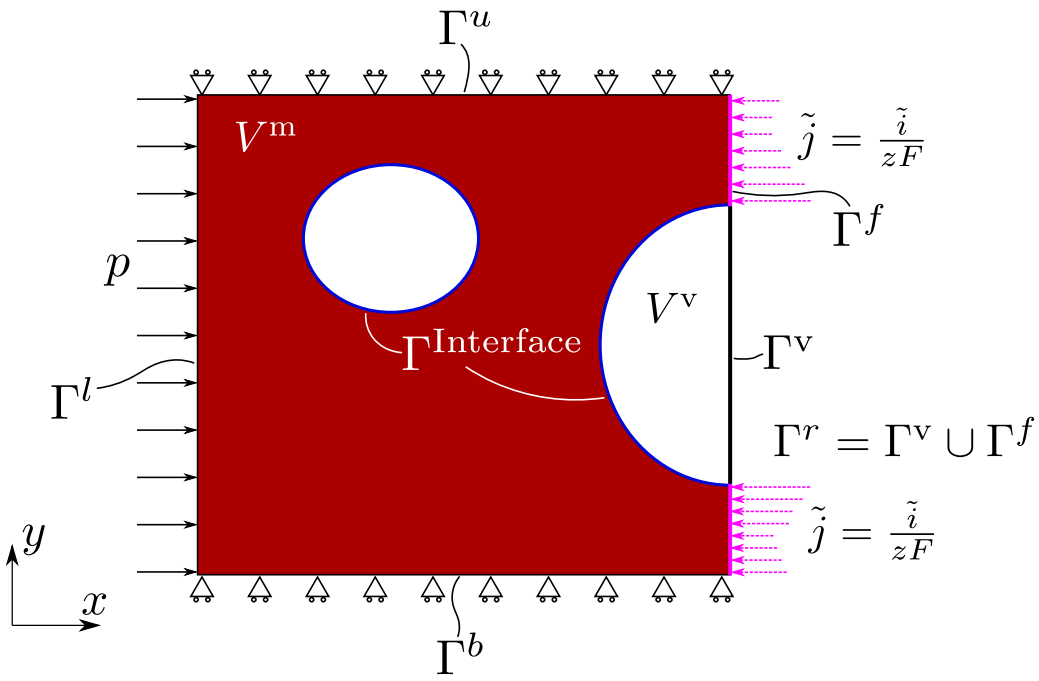


Figure 4.4: Illustration of different domains, boundaries and interfaces of the problem.

In order to capture the transport of Li atoms, the annihilation and creation of lithium lattice sites and the deformation of the Li metal, the following three sets of governing equations are derived.

Li Transport

The evolution of the Li concentration is governed by the following mass transfer equation

$$\frac{\partial c^{\xi}_{\text{Li}}}{\partial t} = -\boldsymbol{\nabla} \cdot \mathbf{j}^{\xi}_{\text{Li}}, \tag{4.35}$$

where $\mathbf{j}^{\xi}_{\text{Li}}$ is the lithium flux, which is defined as

$$\mathbf{j}^{\xi}_{\text{Li}} = -\frac{D_{\text{eff}} c^{\xi}_{\text{Li}}}{RT} \boldsymbol{\nabla} \mu^{\xi}_{\text{Li}}, \tag{4.36}$$

with D_{eff} being the effective diffusion coefficient. Combining Eqs. (4.33) and (4.36) yields

$$\mathbf{j}_{\text{Li}}^{\xi} = -\frac{D_{\text{eff}} h(\xi) c_{\text{L}}^{\text{m}}}{1-\theta_{\text{m}}} \boldsymbol{\nabla}\theta_{\text{m}} + \frac{D_{\text{eff}} h(\xi) c_{\text{L}}^{\text{m}} \theta_{\text{m}} (\Omega_{\text{Li}} - \Omega_{\text{v}})}{RT} \boldsymbol{\nabla}\sigma_h^{\xi}. \tag{4.37}$$

Hence, the lithium flux is driven by the gradients of lithium occupancy and hydrostatic stress. The flux must be zero inside of the void, and this is naturally captured in the formulation as $h(\xi = 0) = 0$. Also, the gradient terms vanish when $\xi = 0$, as the lithium occupancy is constant and the void carries no stress. Substituting Eqs. (4.15) and (4.37) into Eq. (4.35), the governing equation for mass diffusion becomes

$$h c_{\text{L}}^{\text{m}} \frac{\partial \theta_{\text{m}}}{\partial t} + c_{\text{L}}^{\text{m}} \theta_{\text{m}} h' \frac{\partial \xi}{\partial t} = \boldsymbol{\nabla} \cdot \frac{D_{\text{eff}} h c_{\text{L}}^{\text{m}}}{1-\theta_{\text{m}}} \boldsymbol{\nabla}\theta_{\text{m}} - \boldsymbol{\nabla} \cdot \frac{D_{\text{eff}} c_{\text{Li}}^{\xi} (\Omega_{\text{Li}} - \Omega_{\text{v}})}{RT} \boldsymbol{\nabla}\sigma_h^{\xi}. \tag{4.38}$$

Dividing by c_{L}^{m} on both sides and rearranging, the chemical balance can be formulated as,

$$h \frac{\partial \theta_{\text{m}}}{\partial t} + \theta_{\text{m}} h' \frac{\partial \xi}{\partial t} = \boldsymbol{\nabla} \cdot \frac{D_{\text{eff}} h}{1-\theta_{\text{m}}} \boldsymbol{\nabla}\theta_{\text{m}} - \boldsymbol{\nabla} \cdot \frac{D_{\text{eff}} h \theta_{\text{m}} (\Omega_{\text{Li}} - \Omega_{\text{v}})}{RT} \boldsymbol{\nabla}\sigma_h^{\xi}. \tag{4.39}$$

Inspection of Eq. (4.39) reveals that surface diffusion plays a dominant role, as σ_h^{ξ} varies significantly along the interface. This is in agreement with the terrace-ledge-kink model and the lower activation barriers reported for self-diffusion along surfaces [73]. Here, the surface diffusion is driven by both the chemical potential gradient and the curvature gradient. The driving force characterized by chemical potential gradient is explicitly reflected in the second term on the right-hand side of Eq. (4.39), which involves $\boldsymbol{\nabla}\sigma_h^{\xi}$. This term indicates that the gradient of hydrostatic stress along the interface facilitates the self-diffusion of Li there. On the other hand, the driving force as a result of the curvature gradient is captured implicitly through the process of minimizing the total free energy of the system, particularly the free energy of the interface as described by Eq. (4.17). A region at the interface with high curvature leads to a high gradient of the phase field order parameter and, consequently, an increased interface energy. According to the principle of energy minimization, the system should evolve in a direction that reduces its total energy, which involves the reduction of both the curvature and length of the interface. Therefore, the curvature-driven surface diffusion is inherently accounted for in the model through this energy minimization process. It is also worth emphasising the different nature of stress-assisted Li diffusion and creep, with the former being driven by the hydrostatic stress gradient (Eq. (4.39)) while the latter depends on the deviatoric stress (Eq. (4.23)).

Evolution of Lattice Sites

The nucleation and growth of voids are driven by the annihilation and creation of lattice sites, which are described here by a novel phase field formulation. The density of lattice sites is not a conserved quantity and their evolution is driven by the free energy of the system. Accordingly, the evolution for the phase field parameter ξ follows an Allen–Cahn-type equation

$$\frac{\partial \xi}{\partial t} = -L\mu_\xi = -\frac{LRTh'}{\Omega_\mathrm{L}} \ln \frac{1-\theta_\mathrm{m}}{1-\theta_\mathrm{m}^0} - \frac{L\Omega_\mathrm{v} h'}{\Omega_\mathrm{L}} \psi_e - Lwg' + L\kappa \nabla^2 \xi, \tag{4.40}$$

where L is the so-called phase field mobility or kinetic parameter.

Mechanical Deformation

In the absence of body forces and neglecting the role of inertia, the mechanical behaviour of the electrode is characterised by the balance of linear momentum:

$$\boldsymbol{\nabla} \cdot \boldsymbol{\sigma}^\xi = \mathbf{0}, \tag{4.41}$$

where the ξ-dependent stress tensor is used to capture the loss of stiffness associated with voided regions ($\xi = 0$).

4.2 Numerical Implementation

The theoretical framework described in Section 4.1 is numerically implemented using the finite element method. Specifically, the commercial finite element package COMSOL Multiphysics is used. Plane strain conditions are assumed, time integration is carried out using a backward Euler method, and quadratic quadrilateral elements are used for discretising the electrode and electrolyte domains. A mesh sensitivity analysis is conducted in all the computations, with the characteristic element length in the regions of void evolution being at least ten times smaller than the interface thickness ℓ, which is sufficient to ensure mesh-independent results [126]. As derived in Section 4.2.2, the interface length equals,

$$\ell = \sqrt{\frac{8\kappa}{w}}. \tag{4.42}$$

The number of degrees-of-freedom employed in the various boundary value problems examined ranges from 25 to 30 million. To achieve mesh-objective results, the finite element mesh has to be

sufficiently refined along the electrode-electrolyte and Li metal-void interfaces to resolve the gradients of the phase field order parameter and the local current.

4.2.1 Interface Velocity

Insights into the nature of the interface velocity were gained by simplifying the model presented in Section 4.1 and comparing its reduced form with the traditional surface diffusion model accounting for creep presented by Chuang et al. [127] and Needleman and Rice [128]. Following experimental observations [62] and the results obtained in Section 5.3.3, it can be assumed that bulk Li diffusion plays a secondary role in the evolution of the void-anode interface, i.e., variation of θ_{m} across the anode domain is negligible and insignificant compared to that of ξ. Consequently, it is reasonable to assume $\theta_{\mathrm{m}} = \theta_{\mathrm{m}}^{0}$ and simplify the mass transfer governing equation (4.39) to

$$\frac{\partial h}{\partial t} = -\frac{D_{\mathrm{eff}}(\Omega_{\mathrm{Li}} - \Omega_{\mathrm{v}})}{RT} \boldsymbol{\nabla} \cdot h \boldsymbol{\nabla} \sigma_h^{\xi}, \tag{4.43}$$

which can be re-arranged as,

$$\frac{\partial h}{\partial t} = -\frac{D_{\mathrm{eff}} h(\Omega_{\mathrm{Li}} - \Omega_{\mathrm{v}})}{RT} \boldsymbol{\nabla}^2 \sigma_h^{\xi} - \frac{D_{\mathrm{eff}}(\Omega_{\mathrm{Li}} - \Omega_{\mathrm{v}})}{RT} \boldsymbol{\nabla} h \cdot \boldsymbol{\nabla} \sigma_h^{\xi}. \tag{4.44}$$

It is anticipated that there are no sinks or sources of hydrostatic stresses in the Li metal anode (e.g. point loads or atom sinks), and lattice nucleation and annihilation only take place at the interface, leading to $\boldsymbol{\nabla}^2 \sigma_h^{\xi} = 0$ in the bulk ($h = 1$). Thus, by defining θ_{m} as constant, diffusion is constrained to the interface between the void and the lithium metal.

Denote s as the moving front displacement of the interface, whose direction is normal to the interface and can be expressed by $\boldsymbol{\nabla} h / |\boldsymbol{\nabla} h|$. The tangential direction is denoted by u. Recalling that

$$\frac{\partial (\cdot)}{\partial s} = \frac{\boldsymbol{\nabla} h}{|\boldsymbol{\nabla} h|} \cdot \boldsymbol{\nabla} (\cdot), \tag{4.45}$$

where $(\cdot)$ represents a field variable of interest, Eq. (4.44) can be expressed as

$$\frac{\partial s}{\partial t} = -\frac{h}{|\boldsymbol{\nabla} h|} \frac{D_{\mathrm{eff}}(\Omega_{\mathrm{Li}} - \Omega_{\mathrm{v}})}{RT} \left(\frac{\partial^2 \sigma_h^{\xi}}{\partial s^2} + \frac{\partial^2 \sigma_h^{\xi}}{\partial u^2} \right) - \frac{D_{\mathrm{eff}}(\Omega_{\mathrm{Li}} - \Omega_{\mathrm{v}})}{RT} \frac{\partial \sigma_h^{\xi}}{\partial s}. \tag{4.46}$$

In quasi-static problems, the pressure is equilibrated by surface tension, which means that both

$\partial\sigma_h^\xi/\partial s$ and $\partial^2\sigma_h^\xi/\partial s^2$ vanish in the surface. Thus, Eq. (4.46) can be further simplified to

$$\frac{\partial s}{\partial t} = -\frac{h}{|\boldsymbol{\nabla} h|}\frac{D_{\text{eff}}(\Omega_{\text{Li}} - \Omega_{\text{v}})}{RT}\frac{\partial^2\sigma_h^\xi}{\partial u^2}, \tag{4.47}$$

which has a similar form as the governing equation for surface diffusion; see, e.g., Chuang et al. [127] (equation (9)) and Needleman and Rice [128] (equation (28)). The regulation term $h/|\boldsymbol{\nabla} h|$ has a dimension of length, representing the width of the diffusion layer. The source of hydrostatic stress in the interface is the nucleation or annihilation of lattice sites, which is governed by the phase field equation (4.40). Note that Eq. (4.47) is a reduced form of the mass transfer governing equation (4.39) and serves as preliminary evidence of the validity of the full computational model developed in this study through qualitative comparison with existing frameworks. However, the correctness of the full model still requires further investigation, and will be discussed in detail in the following chapters through case studies.

Accordingly, Eq. (4.40) is simplified to

$$\frac{\partial \xi}{\partial t} = -L\Omega_{\text{v}} c_{\text{L}}^{\text{m}} h' \psi_e - L w g' + L\kappa\nabla^2\xi, \tag{4.48}$$

which clearly shows that when bulk diffusion is neglected, vacancy nucleation and annihilation can only take place in the interface ($0 < \xi < 1$).

4.2.2 Interfacial Energy and Thickness Based on the Phase Field Model

In the absence of mechanical and chemical contributions, the interfacial Helmholtz free energy density across the interface reads

$$\Psi^{\text{Interface}} = A^{\text{Interface}} \int_{-\infty}^{+\infty} w\xi^2 (1-\xi)^2 + \frac{1}{2}\kappa \left(\frac{\mathrm{d}\xi}{\mathrm{d}s}\right)^2 \mathrm{d}s, \tag{4.49}$$

where $A^{\text{Interface}}$ denotes the area of the interface, and s is in the direction normal to the interface. In equilibrium, $\delta\Psi^{\text{Interface}} = 0$, and the following Euler equation holds:

$$I - \left(\frac{\mathrm{d}\xi}{\mathrm{d}s}\right)\left[\frac{\partial I}{\partial\left(\mathrm{d}\xi/\mathrm{d}s\right)}\right] = \text{const.}, \tag{4.50}$$

where I is the integrand of Eq. (4.49). From Eqs. (4.50)-(4.49) one reaches

$$w\xi^2\left(1-\xi\right)^2-\frac{1}{2}\kappa\left(\frac{\mathrm{d}\xi}{\mathrm{d}s}\right)^2=\text{const.} \tag{4.51}$$

for all $s\in(-\infty,+\infty)$. It is assumed that $\xi=0$ in the limit of $s\to-\infty$ and $\xi=1$ in the limit of $s\to+\infty$. Then, it is clear that $\mathrm{d}\xi/\mathrm{d}s\geq 0$ and that Eq. (4.51) yields

$$\frac{\mathrm{d}\xi}{\mathrm{d}s}=\sqrt{\frac{2w}{\kappa}}\xi\left(1-\xi\right). \tag{4.52}$$

If the location of the interface is defined at $\xi=0.5$ ($s=s_0$), the solution for ξ reads

$$\xi=\frac{1}{\exp\left[-\sqrt{\frac{2w}{\kappa}}\left(s-s_0\right)\right]+1}. \tag{4.53}$$

The interfacial thickness ℓ and energy $\Psi^{\text{Interface}}/A^{\text{Interface}}$ are then respectively derived as

$$\ell=\left.\frac{1}{\mathrm{d}\xi/\mathrm{d}s}\right|_{s=s_0}=\sqrt{\frac{8\kappa}{w}}\quad\text{and} \tag{4.54}$$

$$\Psi^{\text{Interface}}/A^{\text{Interface}}=\int_0^1 2w\xi^2\left(1-\xi\right)^2\sqrt{\frac{\kappa}{2w}}\frac{1}{\xi\left(1-\xi\right)}\,\mathrm{d}\xi=\frac{\sqrt{2\kappa w}}{6}. \tag{4.55}$$

It is anticipated that the interfacial energy density (or surface tension) can be estimated based on Eqs. (4.54) and (4.55) as

$$\gamma=\frac{\Psi^{\text{Interface}}}{\ell A^{\text{Interface}}}=\frac{w}{12}. \tag{4.56}$$

The analytical estimate is now compared with the predictions from the finite element model. To achieve this, a single void boundary value problem depicted in Fig. 5.3 is simulated. No pressure or flux is applied, and the simulation is run until the equilibrium state is reached. The predicted ξ distribution for the choices of $\kappa=4.5\times10^{-7}\,\mathrm{N}$ and $w=3.5\times10^{6}\,\mathrm{N\,m^{-2}}$ is shown in Fig. 4.5, where the distance along the interface is shown normalised by the void radius (with R = 10 µm). Substituting the values of κ and w in Eq. (4.54) yields an interface thickness of $\ell=1$ µm $(0.1R)$, which is in excellent agreement with the simulation result shown in Fig. 5.3.

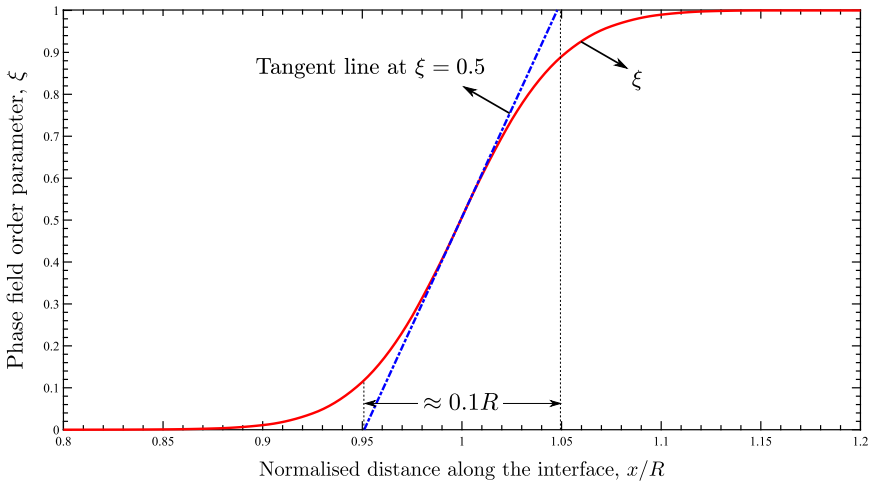


Figure 4.5: Phase field interface thickness: comparison between the theoretical estimate ($\ell = 1$ µm, for $\kappa = 4.5 \times 10^{-7}$ N and $w = 3.5 \times 10^{6}$ N m^{-2}) and the numerical prediction. The distance along the interface is normalised by the void radius (R = 10 µm). For consistency, the interface thickness is determined by drawing a line tangent to the ξ distribution predicted at $\xi = 0.5$.

4.3 Summary

In this chapter, a phase field-based electro-chemo-mechanical model that can predict the evolution of voids and current hot-spots as a function of material properties, applied current and mechanical pressure is presented. To capture the phenomena governing voiding and other interfacial instabilities in all-solid-state battery cells, the theory combines substitutional Li diffusion, a phase field description of vacancy nucleation and annihilation, and a viscoplastic constitutive model for Li metal.

The model established an energy landscape of a lithium-metal anode confined within a fixed volume, aiming to capture its state throughout different stages of the battery's operational cycle. Within this fixed volume of the anode, both the bulk Li metal and the voids are taken into account, characterizing the system's energy through mechanical, chemical potential, and metal-void interfacial contributions—the latter of which is elegantly represented by the phase-field variable.

Central to the analysis is the derivation of governing equations that address crucial physical phenomena within the anode volume. These phenomena include (i) the annihilation and nucleation of the Li lattice, depicted by the phase-field order parameter ξ and governed by Eq. 4.40; (ii) the evolution of the anode's capacity and substitutional diffusivity of Li atoms, represented by the occupancy variable θ_{m} and governed by Eq. 4.39; and (iii) the chemical stresses arising from the strain contributed by lattice vacancies, and viscoplastic responses to external loading, governed by the balance of linear momentum Eq. 4.41.

The robustness of the phase-field formulation is reinforced by the justification of the key phase-field parameters, including the interface length ℓ, gradient energy coefficient κ, and height of the double well potential w, as detailed in Section 4.2.

Chapter 5

Insights into Voiding at Li/SE Interface[1].

This chapter begins with a description of the configuration of the models, including the boundary conditions (Section 5.1.1), initial conditions (Section 5.1.2), and electric couplings with the SSE (Section 5.1.3) for practical problems. Section 5.2 described the choice of electrode-electrolyte system, presenting the phase field and material parameters and calibrating the viscoplastic constitutive behaviour of metallic lithium with the uniaxial tension tests conducted at various strain rates by LePage et al. [20]. Then, numerical experiments are conducted on a single void model (Section 5.3) to investigate: (i) the role of plating and stripping in driving void evolution (Section 5.3.1), (ii) the sensitivity to the applied current density and the phase field mobility parameter (Section 5.3.2), and (iii) the interplay between creep and vacancy diffusion (Section 5.3.3). Subsequently, a full-scale model is developed, which includes multiple voids and where several charge/discharge cycles are simulated to mimic realistic conditions (Section 5.4). This realistic model is used to gain insight into the important role of the applied pressure, and the results obtained are discussed in the context of experimental observations. In these boundary value problems, voids are introduced to mimic the non-ideal solid-solid contact between the Li anode and the ceramic electrolyte. Gaps along the anode-electrolyte interface can arise from multiple sources, including the pores that nucleate at impurities, volume change differences between charged and discharged electrodes [129], and the defects inherent to the manufacture of ceramic materials [85]. In the absence of initial defects (a perfect, void-free interface), the model predicts

[1]Part of the work presented in this chapter has been published in: Y. Zhao, R. Wang, and E. Martínez-Pañeda. A phase field electro-chemo-mechanical formulation for predicting void evolution at the Li–electrolyte interface in all-solid-state batteries. *Journal of the Mechanics and Physics of Solids*, 167(June):104999, 10 2022. [115]

uniform Li dissolution or deposition for stripping and plating, respectively. For the case of stripping, this leads to the formation of a layer where $\xi = 0$, due to the role of the stripping flux *via* Eq. (5.2) and vacancy annihilation. This layer soon stabilises at a thickness that scales with ℓ, capturing the arrest of the reaction (Eq. (5.1)) as a gap opens between the Li metal anode and the electrolyte.

5.1 Model Configuration

5.1.1 Boundary Conditions

Next, the boundary conditions for the coupled deformation-diffusion-phase field problem are discussed. For the sake of clarity, these are divided into three sets, as in the description of the local force balances.

Li Transport

As shown in Fig. 4.4, from the chemical viewpoint, there is only one relevant boundary; Γ^r, the one in contact with the electrolyte, through which lithium ions can penetrate *via* the following electrochemical reaction

$$\mathrm{Li}^+ + \mathrm{e}^- \rightleftharpoons \mathrm{Li}. \tag{5.1}$$

All other three boundaries are impermeable to lithium atoms. The arising current density $\tilde{i}$ can be obtained from a Butler–Volmer equation based on the above electrochemical reaction. It can also be prescribed as a distributed current density. As sketched in Fig. 4.4, no reactants are present in the void and consequently, the current must vanish along the void-electrolyte interface. In the remaining parts of the electrode-electrolyte interface, the flux should be proportional to the current density, such that the boundary condition is given by

$$-\mathbf{j}^{\xi}_{\mathrm{Li}} \cdot \mathbf{n} = \frac{\tilde{i}}{zF} \qquad \text{on} \quad \Gamma^r, \tag{5.2}$$

$$-\mathbf{j}^{\xi}_{\mathrm{Li}} \cdot \mathbf{n} = 0 \qquad \text{on} \quad \Gamma^l \cup \Gamma^u \cup \Gamma^b. \tag{5.3}$$

where F is the Faraday constant and z is the charge number of the ion, equal to 1 for Li. One should note that if Eq. (4.39) is used as the local force balance, both sides in Eq. (5.2) should be divided by

$c_{\mathrm{L}}^{\mathrm{m}}$. Since $c_{\mathrm{L}}^{\mathrm{m}}\Omega_{\mathrm{L}} = 1$, the boundary condition can be reformulated as

$$-\frac{\mathbf{j}_{\mathrm{Li}}^{\xi}}{c_{\mathrm{L}}^{\mathrm{m}}} \cdot \mathbf{n} = \frac{\tilde{i}\Omega_{\mathrm{L}}}{zF} \qquad \text{on} \quad \Gamma^{r}, \tag{5.4}$$

$$-\mathbf{j}_{\mathrm{Li}}^{\xi} \cdot \mathbf{n} = 0 \qquad \text{on} \quad \Gamma^{l} \cup \Gamma^{u} \cup \Gamma^{b}. \tag{5.5}$$

It is emphasised that the model comprises two classes of reactions: (i) Li dissolution/deposition, shown in Eq. 5.1) and captured through the interfacial flux and current density, see Eq. (5.2); and (ii) vacancy annihilation/nucleation, which is modelled through Eq. (4.40). Reaction (i) can only occur where the Li metal anode meets the solid electrolyte, where a vacancy can be generated (stripping) or consumed (plating) as a result, see Fig. 4.2. Reaction (ii) can occur anywhere inside the Li metal anode as long as the chemical potential allows for it. It may also occur along with Reaction (i). For instance, for a perfect Li-electrolyte interface without voids, Li atoms at the interface are oxidised and inserted into the electrolyte uniformly along the interface during stripping, leaving a layer of vacancies that may annihilate into a layer of voids; as a consequence, the lithium anode is peeled off from the electrolyte completely if no stack pressure is applied to maintain the contact.

Evolution of Lattice Sites

The boundary condition for the phase field order parameter ξ is a natural boundary condition for all sides, viz.

$$\boldsymbol{\nabla}\xi \cdot \mathbf{n} = 0 \qquad \text{on} \quad \Gamma^{l} \cup \Gamma^{u} \cup \Gamma^{b} \cup \Gamma^{r}. \tag{5.6}$$

Mechanical Deformation

Unlike the case of the diffusion problem, the only relevant boundary from a mechanical point of view is the left side of the electrode, Γ^{l}. It is assumed that all boundaries are traction-free in the tangential direction. In the normal direction to the boundary, pressure can be applied to minimise voiding and maximise the contact between the electrode and the electrolyte. Accordingly, the boundary conditions in the normal direction are defined as

$$\mathbf{n} \cdot \boldsymbol{\sigma}^{\xi} \cdot \mathbf{n} = -p_{\mathrm{applied}} \quad \text{or} \quad \mathbf{u} \cdot \mathbf{n} = \dot{u}_{\mathrm{applied}} t \qquad \text{on} \quad \Gamma^{l}, \tag{5.7}$$

$$\mathbf{u} \cdot \mathbf{n} = 0 \qquad \text{on} \quad \Gamma^{u} \cup \Gamma^{b} \cup \Gamma^{r}. \tag{5.8}$$

5.1.2 Initial Conditions

The initial conditions are defined as,

$$\xi = 1, \quad \theta_{\mathrm{m}} = \theta_m^0 \qquad \text{in} \quad V^{\mathrm{m}}, \tag{5.9}$$

$$\xi = 0, \quad \theta_{\mathrm{m}} = \theta_m^0 \qquad \text{in} \quad V^{\mathrm{v}}. \tag{5.10}$$

In all computations, the phase field distribution is allowed to equilibrate before applying any loading.

5.1.3 Coupling with the Electro-Mechanical Behaviour of the Solid Electrolyte

To enable the prediction of current hot spots, which act as dendrite nucleation sites, the electrode deformation-diffusion-phase field model is extended to capture the electro-mechanical behaviour of the electrolyte. As shown in Fig. 5.1, the electrolyte occupies a volume V^{el} and is in contact with the right-hand side of the electrode at the interface Γ^r. The additional governing equations and boundary conditions for the coupled problem are summarised here and in Fig. 5.1; the reader is referred to Zhao et al. [115] for a more comprehensive description of solid electrolyte behaviour.

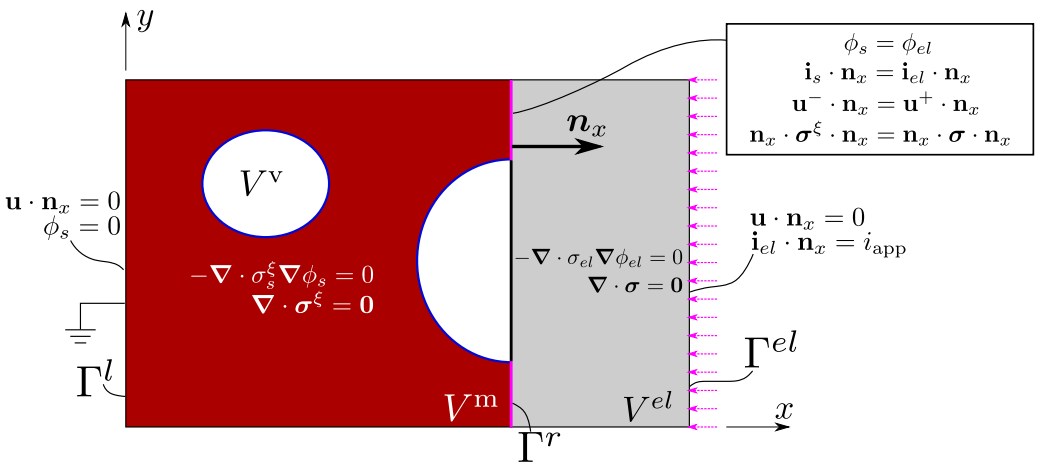


Figure 5.1: Complete electro-chemo-mechanical model, coupling the deformation-diffusion-phase field behaviour of the Li metal electrode with the electro-mechanical behaviour of the solid electrolyte.

The following assumptions underpin the model: (i) the electrolyte is a single ion conductor, where Li-ion is the only charge carrier, (ii) the concentration of Li-ion in the electrolyte remains constant in time, and (iii) the diffusion of Li ions within the interstitials of the electrolyte will not distort the electrolyte lattice. These assumptions exempt us from solving the lithium concentration field explicitly and allow us to focus on the electric and mechanical fields in the electrolyte. The current delivered by

Li^+ is dictated by Ohm's law and reads,

$$\mathbf{i}_{el} = -\sigma_{el}\boldsymbol{\nabla}\phi_{el}, \tag{5.11}$$

where $\mathbf{i}_{el}$ is the electric current and σ_{el} is the electric conductivity. Upon further assuming that no charge is present, one reaches

$$\boldsymbol{\nabla}\cdot\mathbf{i}_{el} = 0. \tag{5.12}$$

Mechanically, it is assumed that the electrolyte behaves in a linear elastic manner. Thus, the displacement $\mathbf{u}$ in the electrolyte is described by the Navier-Lamè equation

$$(\lambda + G)\,\boldsymbol{\nabla}\,(\boldsymbol{\nabla}\cdot\mathbf{u}) + G\boldsymbol{\nabla}^2\mathbf{u} = \mathbf{0}, \tag{5.13}$$

where λ and G are the Lamè constants of the electrolyte.

Let us now turn our attention to the governing equations in the electrode. The chemical and mechanical governing equations have been introduced in Section 4.1.5. The governing equation for the electric field can now be derived. The current in the Li metal electrode anode is conducted by electrons. Since the conductivity of the Li metal (σ_s) is several orders of magnitude greater than that of the electrolyte, a common assumption of a constant electric potential within the electrode can be adopted. However, the air in the void can act as an electron insulator with zero conductivity, influencing the distribution of electric potential in the electrode. Therefore, a phase field-dependent conductivity is defined and reads

$$\sigma_s^{\xi} = f(\xi)\sigma_s. \tag{5.14}$$

The choice of $f(\xi)$ must satisfy the following requirements: $f(0) = 0$, $f(1) = 1$, and $f'(0) = 0$. Here, the following higher-order form is adopted to achieve a steep conductivity change near the interface,

$$f(\xi) = \xi^{15}(\xi^4 - 3\xi^2 + 3). \tag{5.15}$$

The current density ($\mathbf{i}_s$) and electric potential (ϕ_s) in the electrode then read

$$\mathbf{i}_s = -\sigma_s^{\xi} \boldsymbol{\nabla} \phi_s, \tag{5.16}$$

$$\boldsymbol{\nabla} \cdot \mathbf{i}_s = 0. \tag{5.17}$$

Finally, the boundary and interface conditions are defined. As shown in Fig. 5.1, two boundaries are identified: the left side of the electrode domain (Γ^l) and the right side of the electrolyte (Γ^{el}). The electrode is in contact with the current collector on the left, which ensures that the electrode potential vanishes. The electrolyte is in contact with a counter electrode on the right, which supplies a uniformly distributed current density i_{app}. The interface impedance is disregarded at the electrode-electrolyte interface Γ^r, and thus, both current density and electric potential are continuous. Mechanically, all normal displacements on Γ^l and Γ^{el} are fixed. At the interface Γ^r, continuity conditions apply. Accordingly, the boundary and interface conditions read

$$\phi_s = 0, \qquad \mathbf{u} \cdot \mathbf{n}_x = 0, \qquad \text{on} \quad \Gamma^l, \tag{5.18}$$

$$\begin{aligned} &\phi_s = \phi_{el}, && \mathbf{u}^- \cdot \mathbf{n}_x = \mathbf{u}^+ \cdot \mathbf{n}_x, \\ &\mathbf{i}_s \cdot \mathbf{n}_x = \mathbf{i}_{el} \cdot \mathbf{n}_x, && \mathbf{n}_x \cdot \boldsymbol{\sigma}^{\xi} \cdot \mathbf{n}_x = \mathbf{n}_x \cdot \boldsymbol{\sigma} \cdot \mathbf{n}_x, \qquad \text{on} \quad \Gamma^r, \end{aligned} \tag{5.19}$$

$$\mathbf{i}_{el} \cdot \mathbf{n}_x = i_{\text{app}}, \qquad \mathbf{u} \cdot \mathbf{n}_x = 0, \qquad \text{on} \quad \Gamma^{el}, \tag{5.20}$$

where $\mathbf{n}_x$ is the normal vector along the x direction. Superscripts $^-$ and $^+$ denote the left and right side of the interface Γ^r, respectively.

Remark. In the presented formulation, four kinetic events that govern void evolution are encapsulated: (i) the rate of Li dissolution/deposition, (ii) Li diffusion, (iii) the nucleation/annihilation of vacancies, and (iv) creep. These phenomena are incorporated independently through boundary/interface conditions (for (i)), field governing equations (for (ii) and (iii)) and constitutive relations (for (iv)). As described in Section 4.2.1, in the absence of applied current and bulk diffusion, a simplified model can be derived and estimate the interface velocity. The resulting expression for the interface velocity highlights the importance of the lattice annihilation-induced pressure source term inside the interface and the similarities with traditional models of surface diffusion [127, 128].

5.2 Material Model Calibration and Parameter Selection

The numerical experiments are conducted in a cell composed of a metallic lithium anode and a $Li_7La_3Zr_2O_{12}$ (LLZO) solid electrolyte, arguably the most relevant electrode-electrolyte system. The garnet LLZO is a common choice in the experimental and theoretical literature, as it can be synthesized at high relative densities (>95%), exhibits high conductivity and stiffness, and is stable against metallic lithium [69, 130]. The phase field and material parameters used are shown in Table 5.1. The phase field interface kinetics coefficient, L, which controls the rate of the interface motion and the dynamic process of interface diffusion, is an empirical parameter chosen through an iterative process. The initial guess of this parameter should ensure that the Li metal-void interface remains still when subjected to no external load (including pressure and applied current density) within the simulation time of interest. Adjustments to L were carried out iteratively after typical external loads were introduced, such that if the interface moves too fast compared with experimental observations, its value should be reduced, and vice versa. An L value too large or too small should be avoided to mitigate stability and convergence issues.

Table 5.1: Phase field and material parameters for a Li anode - LLZO electrolyte system

Parameter	Magnitude	Ref
Effective diffusion coefficient, D_{eff} [$\text{m}^2\,\text{s}^{-1}$]	7.5×10^{-13}	Chen et al. [13]
Young's modulus of lithium metal, E_{Li} [GPa]	4.9	Shishvan et al. [12]
Young's modulus of LLZO, E_{LLZO} [GPa]	150	Yu et al. [131]
Poisson's ratio of lithium metal, ν_{Li} [-]	0.38	Shishvan et al. [12]
Poisson's ratio of LLZO, ν_{LLZO} [-]	0.257	Yu et al. [131]
Interface kinetics coefficient, L [$\text{m}^2\,\text{N}^{-1}\,\text{s}^{-1}$]	1×10^{-9}	
Height of the double well potential, w [$\text{N}\,\text{m}^{-2}$]	3.5×10^{6}	
Gradient energy coefficient, κ [N]	4.5×10^{-7}	
Gas constant, R [$\text{J}\,\text{mol}^{-1}\,\text{K}^{-1}$]	8.314	
Absolute temperature, T [K]	298	
Molar volume of lithium, Ω_{Li} [$\text{m}^3\,\text{mol}^{-1}$]	13.1×10^{-6}	Shishvan et al. [12]
Molar volume of vacancies, Ω_{v} [$\text{m}^3\,\text{mol}^{-1}$]	6×10^{-6}	Shishvan et al. [12]
Average molar volume of Li lattice sites, Ω_{L} [$\text{m}^3\,\text{mol}^{-1}$]	13.1×10^{-6}	Shishvan et al. [12]
Electric conductivity of lithium metal, σ_s [$\text{S}\,\text{m}^{-1}$]	1.1×10^{7}	Chen et al. [13]
Ionic conductivity of solid electrolyte (LLZO), σ_{el} [$\text{S}\,\text{m}^{-1}$]	5.5×10^{-6}	Buschmann et al. [132]

It remains to define the constitutive parameters of the viscoplastic formulation adopted to charac-

terise the mechanical behaviour of the Li metal anode. As described in Section 4.1.4, the viscoplastic and creep behaviour of metallic lithium is described using the model developed by Anand and Narayan [105]. The parameters of the model are calibrated against the experimental work by LePage et al. [20]. Accordingly, the activation energy is taken to be $Q = 37$ kJ/mol, and the hardening and strain rate sensitivity coefficients are determined by matching the uniaxial stress-strain curves reported by LePage et al. [20] at different strain rates and room temperature. The comparison between the experimental data and the numerical results of the model is given in Fig. 5.2. A good agreement with experiments is obtained for the parameters reported in Table 5.2, and thus, these values are adopted in the subsequent calculations.

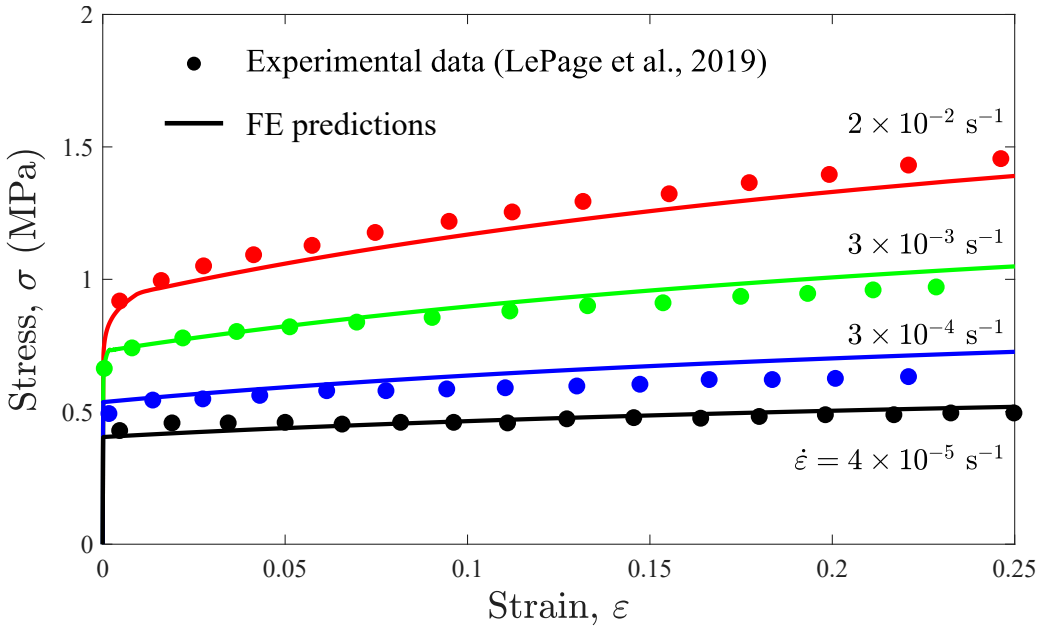


Figure 5.2: Uniaxial stress σ versus strain ε curves for lithium metal at $T = 298$ K and different strain rates ($\dot{\varepsilon}$). Comparison between the experiments by LePage et al. [20] (symbols) and numerical predictions of the model (lines) for the parameters listed in Table 5.2.

Table 5.2: Viscoplastic material parameters for lithium metal

Parameter	Magnitude
Pre-exponential factor, A [s^{-1}]	4.25×10^4
Activation energy, Q [$kJ\,mol^{-1}$]	37
Strain rate sensitivity exponent, m [-]	0.15
Deformation resistance saturation coefficient, S_0 [MPa]	2
Initial value of the flow resistance, $S_a(t = 0)$ [MPa]	1.1
Hardening constant, H_0 [MPa]	10
Hardening sensitivity, a [-]	2
Deformation resistance sensitivity, n [-]	0.05

5.3 Single Void Analysis

Insight is first gained by simulating the evolution of a single void lying at the interface between the Li metal anode and the electrolyte, see Fig. 5.3. The electrolyte and the electrode are assumed to have a rectangular shape and equal dimensions, with a height of H = 250 µm and width of W = 0.16H, such that the complete domain has dimensions of $250 \times 80\,\mu m^2$. The void has a perfect semi-circular shape with radius R = 0.04H = 10 µm initially.

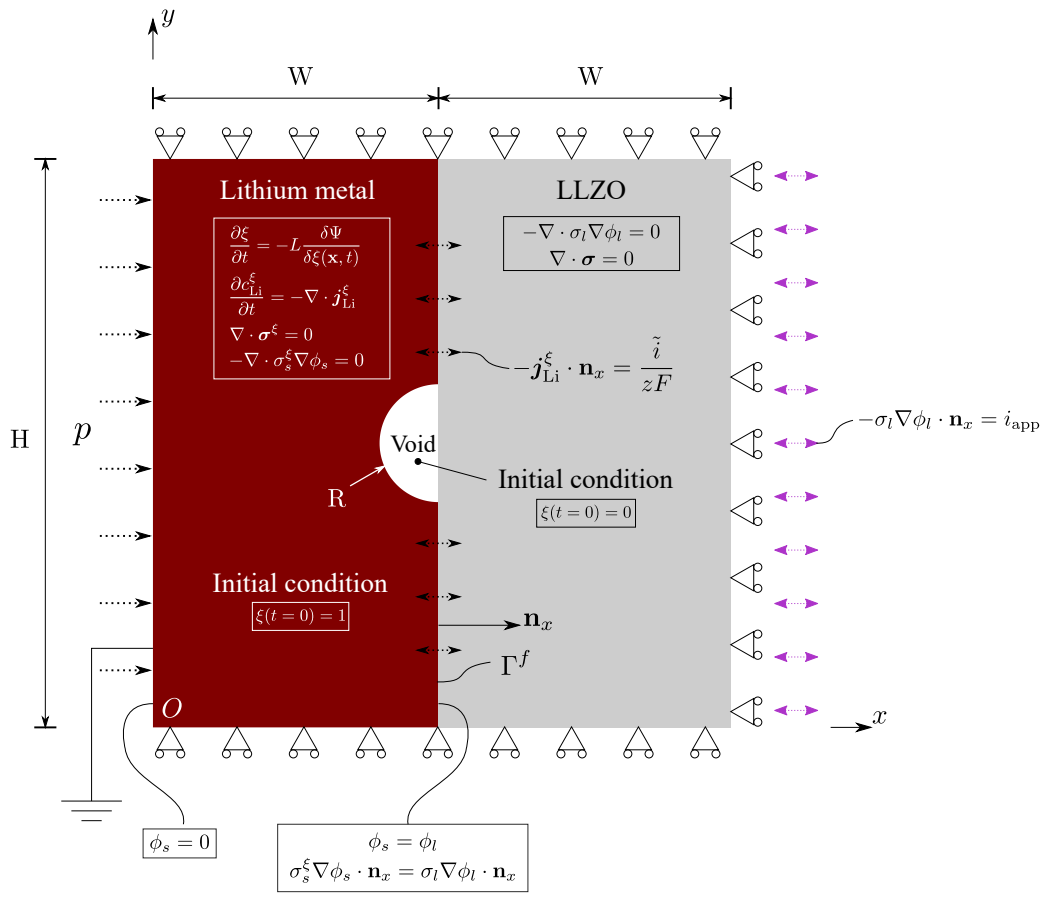


Figure 5.3: Single void boundary value problem: dimensions, configuration and boundary conditions. The initial conditions and governing equations for the electrolyte and electrode domain are also included.

All the edges of the Li metal anode are impermeable to Li flux except for Γ^f, the electrode-electrolyte interface. Regarding the electric problem, a uniformly distributed current density (i_{app}) is applied to the right edge of the electrolyte. This current is generally taken to be equal to $|i_{\mathrm{app}}| = 0.1$ mA cm^{-2}, but other magnitudes are also considered to investigate its influence. Mechanically, the vertical displacements of the bottom and top edges of the electrode and of the electrolyte are constrained. The horizontal displacement of the right edge of the electrolyte is also kept equal to zero. This reflects the assumption of composite cathodes, whose macroscopic volume change is negligible during operation compared to lithium anodes. Moreover, the cathode and electrolyte are both assumed to be much stiffer than lithium metal. As for the left edge, two scenarios are considered: (i) a pressure of p is applied at this boundary to study the influence of the applied pressure, or (ii) a fixed displacement is enforced in order to mimic the constraint of a solid shell that wraps the battery cell.

5.3.1 Void Evolution in the Electrode under Stripping and Plating

First, the model predictions of void evolution under stripping and plating conditions are presented. For the sake of clarity, no pressure is applied to the electrode, and simulations are presented for one continuous cycle of stripping or plating. Otherwise, the loading conditions correspond to those described above. Currents with the same magnitude (but different sign) are applied for plating and stripping; specifically, $i_{\text{app}} = 0.1\ \text{mA}\,\text{cm}^{-2}$ during plating and $i_{\text{app}} = -0.1\ \text{mA}\,\text{cm}^{-2}$ during stripping. The corresponding Li^+ flux $\boldsymbol{j}_{\text{Li}}^{\xi}$ flowing across the electrode-electrolyte interface is then calculated from the interfacial current density.

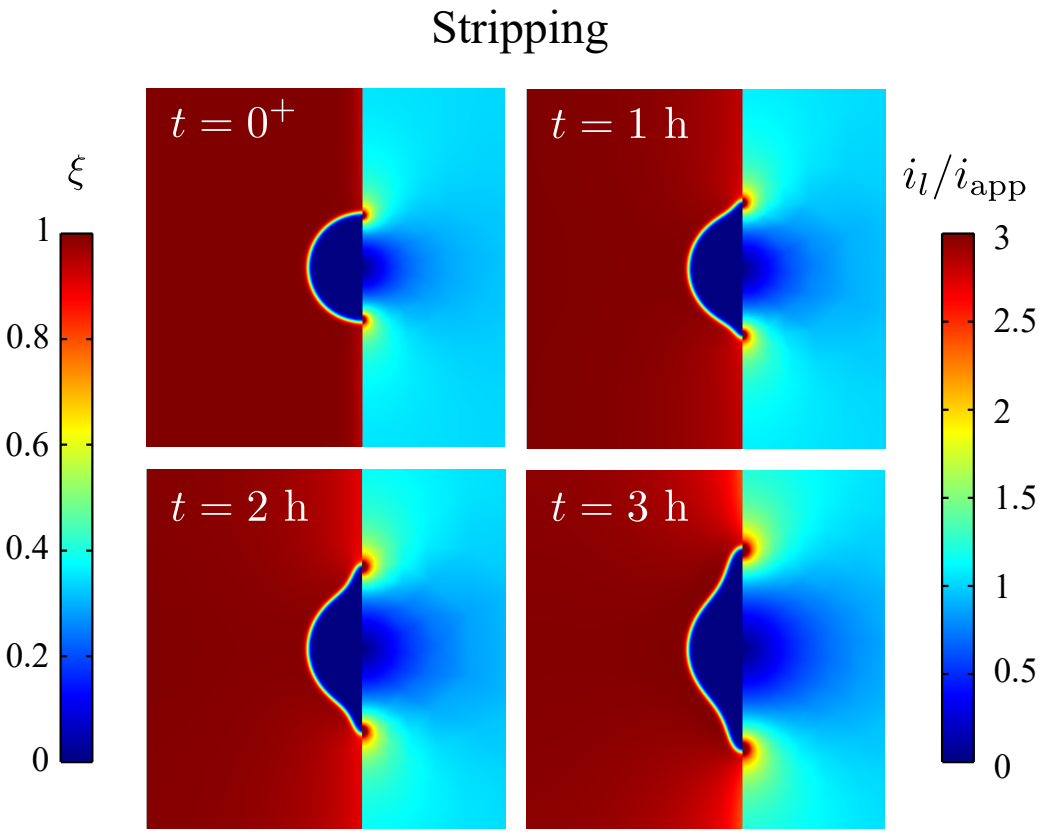


Figure 5.4: Numerical experiments on a single void model: voiding and local current hot spots under stripping, as characterised by the evolution of the phase field order parameter in the electrode and the current density distribution in the electrolyte.

The results of the stripping and plating processes are shown in Figs. 5.4 and 5.5, respectively. Void evolution is characterised by contours of the phase field order parameter (ξ) in the electrode, while the contours in the electrolyte describe the predicted normalised electrolyte current density (i_l/i_{app}). Consider first the results obtained for the stripping process, Fig. 5.4. The numerical predictions reveal that stripping causes the void to deviate from its original shape, widening along the electrode-electrolyte interface. This is in agreement with experimental observations (see Fig. 4.1) and occurs due to the

faster rate of Li dissolution at the interface relative to the rate at which Li is supplied from the bulk due to vacancy diffusion. The rate of Li dissolution is further exacerbated by the higher stripping flux in regions of high current density, as per Eq. (5.5). These current hot spots arise in the regions where the void, Li metal and solid electrolyte meet, and extend their size as the void grows with increasing stripping time. By accelerating void growth, these regions of high current intensity contribute to reducing the contact area between the electrode and the electrolyte, increasing cell resistance. Moreover, hot spots act as dendrite nucleation sites during the subsequent plating cycle [130]. The emergence of hot spots near the void edges is predicted as a result of the abrupt change in conductivity taking place along the void-Li metal interface, see Eqs. (5.14)-(5.17), with the conductivity going from being equal to the Li metal conductivity ($\sigma_s^\xi = \sigma_s$) in the Li phase ($\xi = 1$) to zero inside of the void ($\sigma_s^\xi = 0$ for $\xi = 0$).

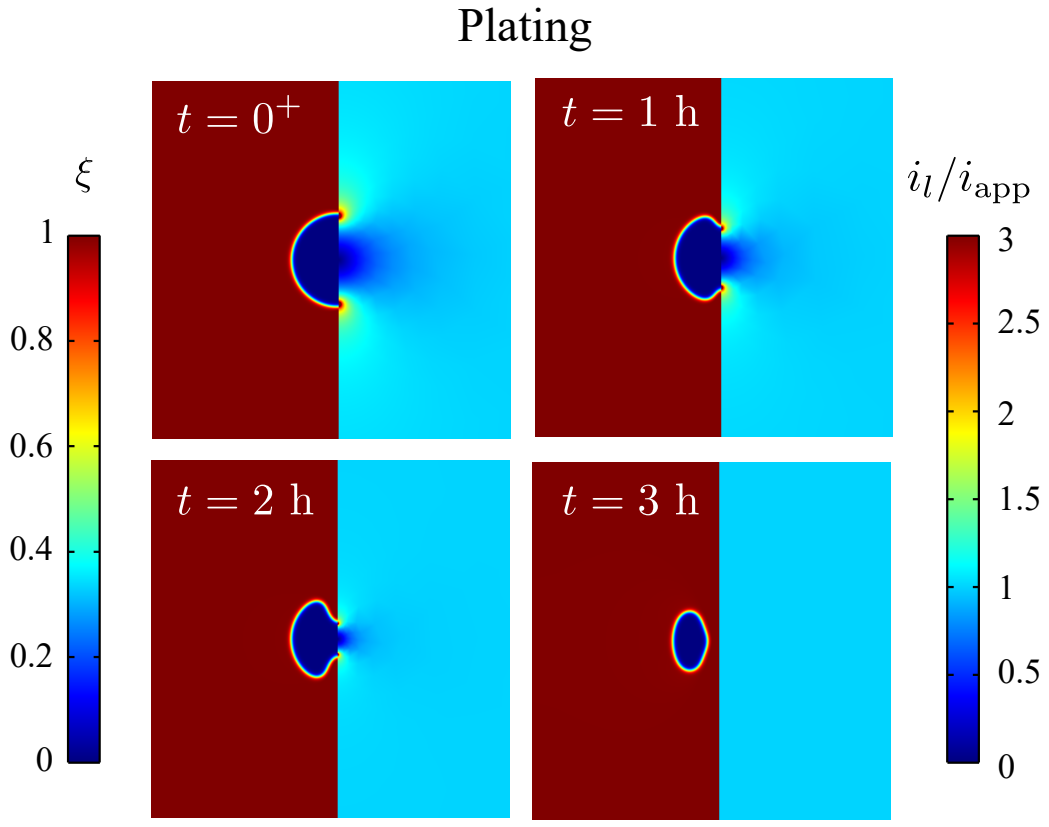


Figure 5.5: Numerical experiments on a single void model: voiding and local current hot spots under plating, as characterised by the evolution of the phase field order parameter in the electrode and the current density distribution in the electrolyte.

On the other hand, see Fig. 5.5, the results obtained for plating show the opposite trend. The opening of the void narrows at the electrode-electrolyte interface and eventually closes completely, isolating the void from the electrolyte. Thus, see Fig. 4.1, the model captures the two phenomena

that can be observed during plating: the reduction in void size and void occlusion. It is worth noting that the regions of high current reduce in size as the plating process evolves, and that these hot spots eventually disappear, recovering an intact electrode-electrolyte interface. The exact void shapes are reported as a function of time in Fig. 5.6, for both stripping and plating. Here, the void-electrode interface is taken to be described by the $\xi = 0.5$ iso-contour. It can be seen how the void changes shape mostly near the electrode-electrolyte interface, contracting during plating and expanding during stripping. At the end of the stripping cycle, the length of the region where the electrode and electrolyte are no longer in contact has almost duplicated.

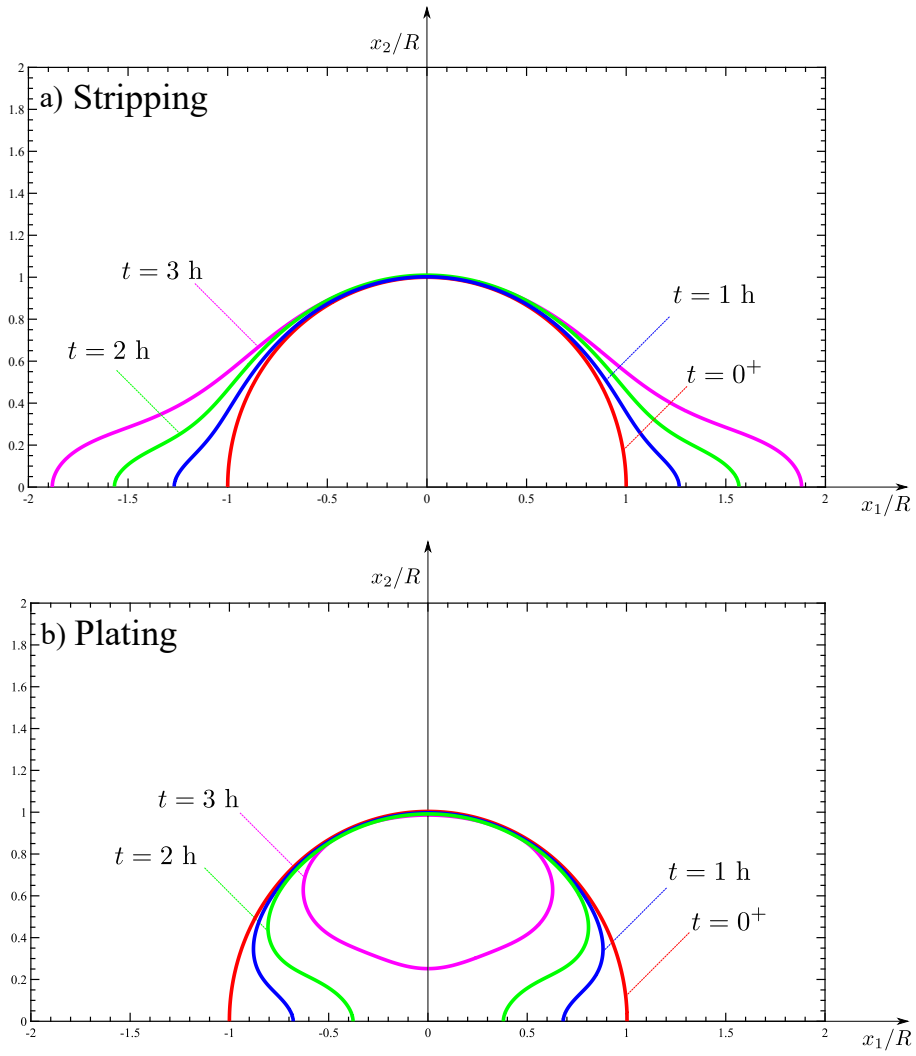


Figure 5.6: Numerical experiments on a single void model: quantifying changes in void shape for (a) stripping and (b) plating. The results are shown relative to a Cartesian coordinate system (x_1, x_2) whose origin is located in the centre of the circle containing the semi-circular void, with x_2 being perpendicular to the electrode-electrolyte interface.

5.3.2 Influence of the Applied Current and the Phase Field Kinetic Coefficient

A parametric analysis is conducted to investigate the influence of the applied current density i_{app} and the phase field kinetic parameter L. The aim is to investigate the competition between relevant kinetic phenomena. Thus, voiding is governed by four kinetic events: the rate of Li dissolution/deposition, bulk Li transport, the nucleation/annihilation of vacancies, and creep. Let us momentarily leave aside the role of creep, which is investigated below (Section 5.3.3). The first three events are governed by the applied current i_{app}, the effective diffusion coefficient D_{eff}, and the phase field mobility coefficient L, respectively. Since D_{eff} is known and can be independently measured, let us now focus our attention on the sensitivity to i_{app} and L. The boundary value problem corresponds to that considered in the previous section and depicted in Fig. 5.3. Again, no pressure is applied so as to isolate the effects. The outcome of the simulations is reported in terms of void shape evolution for selected values of i_{app} and L at a time of $t = 1$ h. As in Fig. 5.6, the results are shown in a normalised Cartesian coordinate system $(x_1/R, x_2/R)$ whose origin is located in the centre of the circle containing the semi-circular void, with x_2 being perpendicular to the electrode-electrolyte interface.

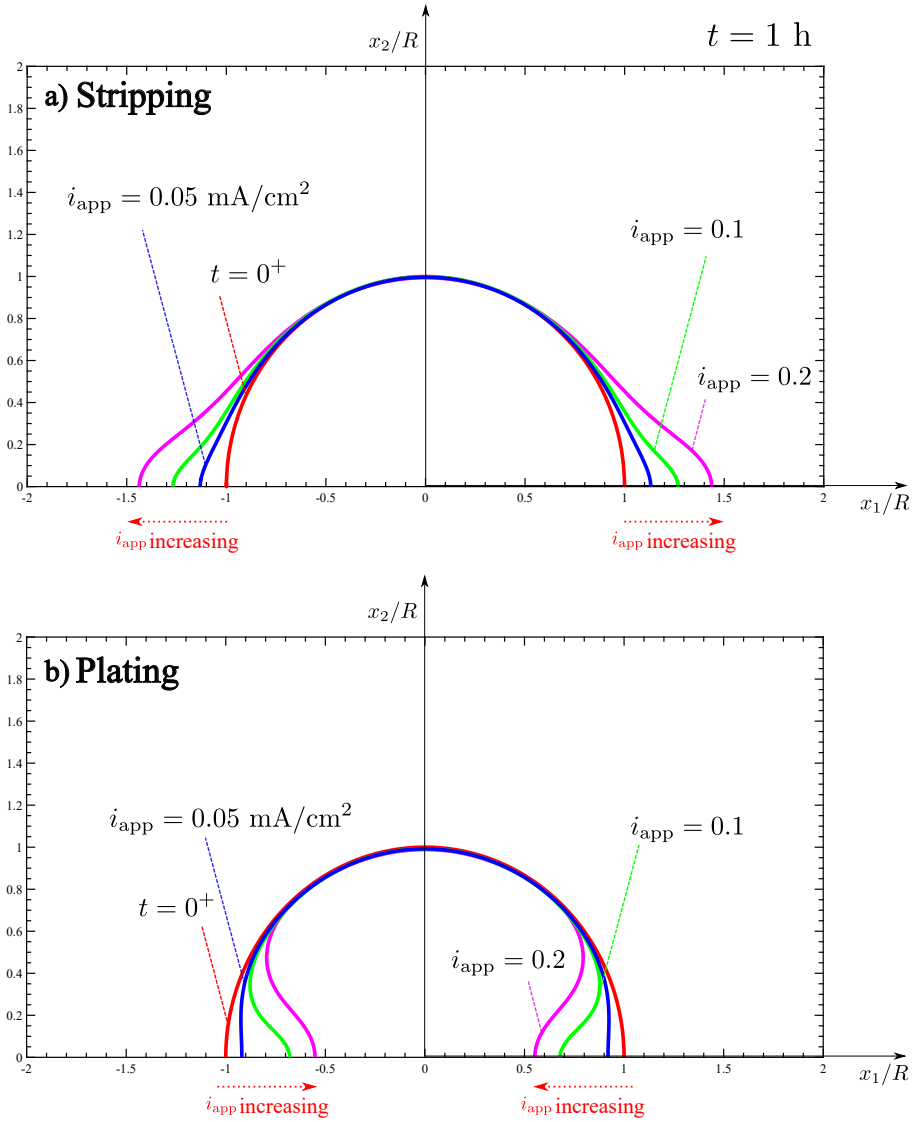


Figure 5.7: Numerical experiments on a single void model: quantifying the role of the applied current i_{app} for (a) stripping and (b) plating. Results are shown for a time of 1 h and relative to a Cartesian coordinate system (x_1, x_2) whose origin is located in the centre of the circle containing the semi-circular void, with x_2 being perpendicular to the electrode-electrolyte interface.

The results obtained for different values of the applied current density are given in Fig. 5.7. In agreement with expectations and experimental observations, the sensitivity of the void shape to plating and stripping increases with increasing i_{app}. By comparing with Fig. 5.6, it can be seen that the void evolution appears to be qualitatively very similar for all the choices of i_{app} considered, with the main effect being related to the rate at which these changes take place. Thus, the ratio of i_{app} to the charging cycle time is a key factor. For example, the generation of voids will be minimised if the stripping current is low relative to the duration of the stripping cycle. Moreover, voiding is very sensitive to the interplay between i_{app} and D_{eff}, as the formation of voids will be entirely suppressed if the stripping current removes Li from the interface more slowly than it can be replenished. For the

values of i_{app} considered, this is not observed in the stripping results reported in Fig. 5.7. However, simulations conducted with smaller values of i_{app} reveal that no noticeable void growth takes place after $t = 1\,\text{h}$ when the applied current is equal to 0.005 $\text{mA}\,\text{cm}^{-2}$ or smaller. Thus, the simulations are consistent with the existence of a critical current density, as inferred experimentally [62].

Let us now investigate the role of the phase field kinetic parameter L, also termed the phase field mobility coefficient. In this formulation, L characterises the ability of a material to nucleate or annihilate vacancy sites. The results obtained for selected values of L are shown in Fig. 5.8, for both stripping and plating processes. The stripping results reveal that low L values ($L \sim 10^{-11}$) result in a void that largely maintains its original shape. However, the change in shape is noticeable for values of L on the order of $\sim 10^{-10}$ or larger, for the $t = 1\,\text{h}$ of stripping considered. As in the previous stripping simulations, void growth is mostly enhanced near the interface, smearing the void and losing the initial semi-circumferential shape. During plating, the void shrinks inwards from all sides for small L values, while large L values enhance the closing of the void opening at the electrode-electrolyte interface. If L, i_{app} or the plating time is sufficiently large, then the void opening closes completely, and the void becomes occluded in the electrolyte (see Fig. 5.6b). These simulations suggest that L could be obtained from first principles calculations or inferred from experiments by applying inverse engineering. Further insight into the interface velocity is gained analytically in Section 4.2.1.

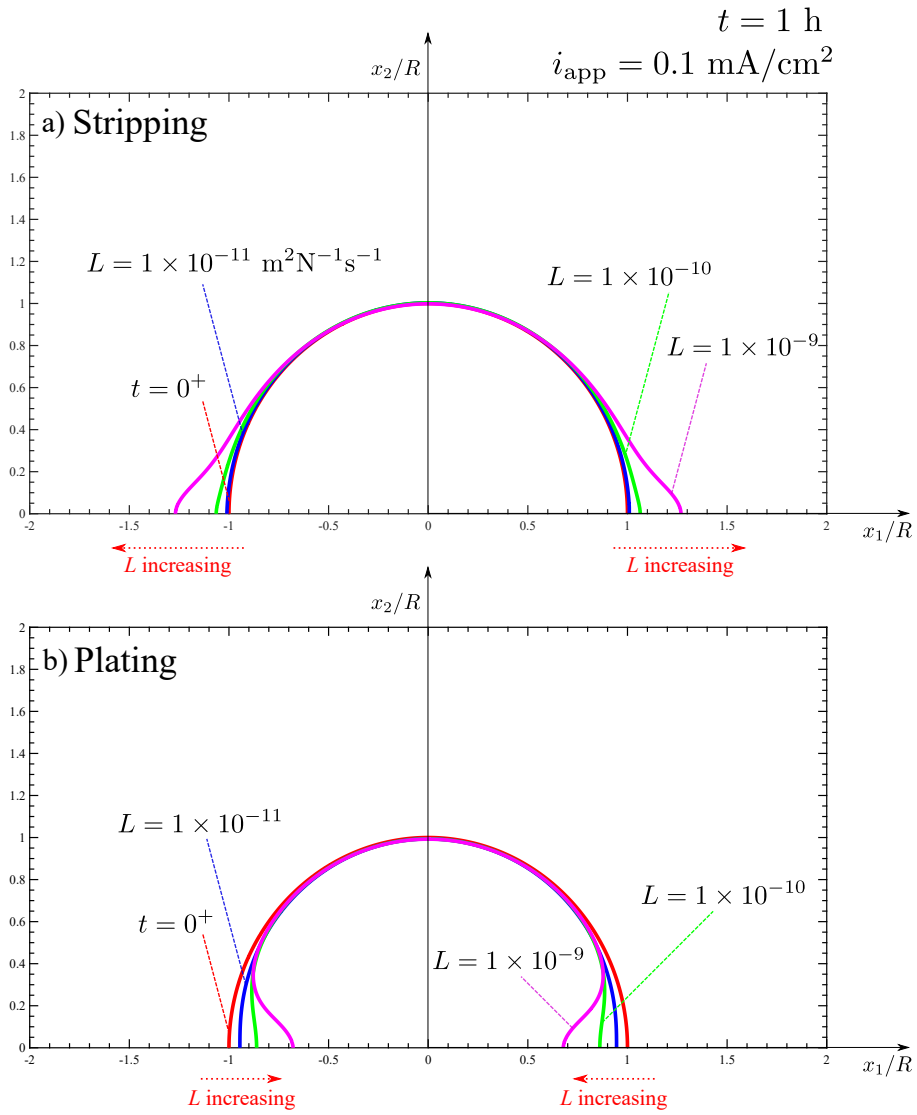


Figure 5.8: Numerical experiments on a single void model: quantifying the role of the phase field kinetic parameter L for (a) stripping and (b) plating. Results are shown for a time of 1 h and relative to a Cartesian coordinate system (x_1, x_2) whose origin is located in the centre of the circle containing the semi-circular void, with x_2 being perpendicular to the electrode-electrolyte interface.

The characteristic times are also investigated for a deeper insight behind the dis/charging, the bulk diffusion of Li, and the phase field interface dynamic processes. The dis/charging characteristic time $\tau_I = C_{\text{th}}^{\text{V}} \text{W}/i_{\text{app}}$, where C_{th}^{V} is the theoretical volumetric capacity of Li (see Eq. (3.58)), is found to be within the range of a magnitude of 10^{-2} s for applied current densities of $i_{\text{app}} = \{0.05,\ 0.1,\ 0.2\}$ mA cm^{-2}. In contrast, the characteristic time for the bulk diffusion of Li $\tau_d = \text{W}^2/D_{\text{eff}}$ has a much larger value with a magnitude of 10^3 s. Similarly, the characteristic time for the phase field interface dynamic process $\tau_L = 1/(Lw)$, which is obtained through dimensional analysis, possesses values from $10^2 \sim 10^4$ s for $L = \{1 \times 10^{-9},\ 1 \times 10^{-10},\ 1 \times 10^{-11}\}$ m^2 N^{-1} s^{-1}.

It can be seen that τ_d is approximately 100 000 times larger than τ_I, indicating a much faster

material transfer process induced by Li stripping/plating at the interface than diffusion of lithium from/into the bulk. This aligns with the experimental reports [62] and the theoretical predictions made in this study (see section 4.2.1) that diffusion does not play a dominant role in void evolution at the Li-SE interface. This also suggests that the diffusion in bulk Li constitutes a primary limiting factor in suppressing the void formation and dendrite growth as it is not fast enough to either replenish the lost Li during stripping or redistribute the excess Li during plating at the Li-SE interface, leading to void enlargement or nucleation of dendrite. On the other hand, The characteristic time for the phase field kinetic process τ_L, which can be regarded as a measurement of the time scale of the phase field interface to reach a new equilibrium state from its initial state, or an indicator of the responsiveness of the phase field interface with respect to its driving force, also exhibits a value much larger than τ_I; but can be larger or smaller than τ_d depending on the selection of L. This indicates that the phase field interface dynamic process is still much slower than the dis/charging process but can be faster than the bulk diffusion process if a large L is selected. This necessitates a comparison between the simulation outcomes with experimental observations for the determination of L.

5.3.3 Investigating the Competing Role of Creep Deformation and Li Diffusion

Finally, let us use the single void boundary value problem to gain insight into the competition between diffusion and creep. These effects can be isolated by assuming that no flux is applied on the electrode-electrolyte interface and by replacing the electrolyte and its mechanical constraint by a fixed displacement $u_x = 0$ at Γ^f. A pressure with magnitude $p = 0.6\,\mathrm{MPa}$ is applied on the left edge of the electrode. This pressure is applied instantaneously (time $t = 0^+$) and then held fixed for 7 h, such that creep strains significantly outweigh their elastic counterparts. The results obtained are shown in Fig. 5.9 for three scenarios. Consider first the void shape evolution results, Fig. 5.9a. Three curves are shown to characterise the contributions of Li diffusion and creep to void shape evolution: (i) the initial void shape before the pressure is applied (time $t = 0$); (ii) the void shape after 7 h if the undeformed shape is considered (i.e., the change in shape due to diffusion only); and (iii) the void shape after 7 h considering both diffusion and material deformation contributions. The results reveal that, in the absence of current, the void shrinks while maintaining a semi-circular shape — no localisation events are observed. It is also seen that the change in void shape due to diffusion appears to be a small contribution to the final void shape.

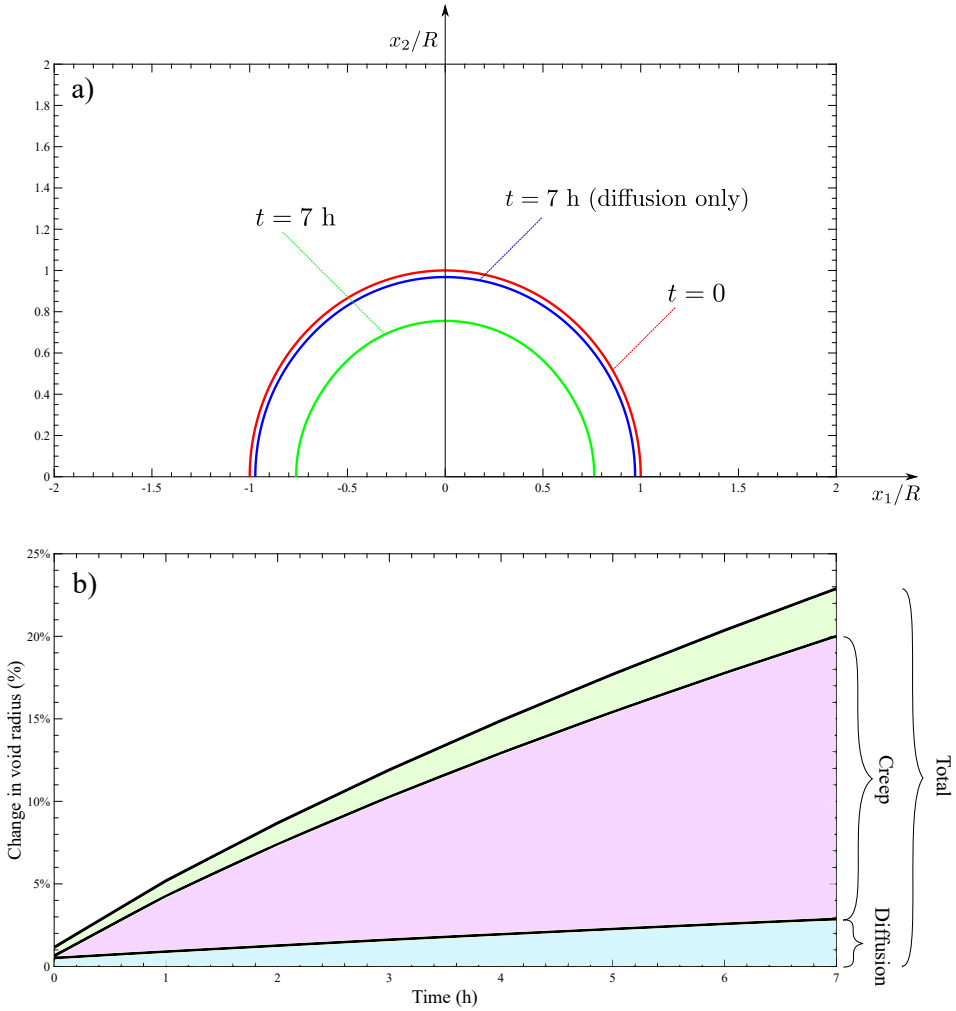


Figure 5.9: Numerical experiments on a single void model: quantifying the competition between Li diffusion and creep; (a) void shape evolution relative to a Cartesian coordinate system (x_1, x_2) whose origin is located in the centre of the circle containing the semi-circular void, with x_2 being perpendicular to the electrode-electrolyte interface, and (b) percentage change in void radius versus time.

Quantitative insight can be gained from Fig. 5.9b, where the contributions from creep and Li diffusion to void evolution are shown in terms of the relative change of the void radius. It can be seen that creep deformation dominates the voiding process, relative to the contribution from Li diffusion. This is in agreement with recent experimental measurements for various levels of applied pressure, which suggest that creep rather than diffusion dominates the rate at which Li is replenished at the interface [62]. The precise weighting of the contributions from diffusion and creep will depend on the total time and the material's ability to annihilate vacancies. The characteristic time for creep (evaluated through $\tau_{cr} = 1/F_{cr}$, see Eq. (4.26)), especially in stress concentration areas at the triple junction of the anode, void, and SE, is found to be within the range of the magnitude of $10^1 \sim 10^2$ s as they enter the secondary creep stage. This indicates that the creep process is faster than the bulk diffusion but still much slower than the dis/charging process compared with τ_I and τ_d. Consequently, when no

stripping or plating current is applied, and the anode is subject to pressure-induced deformation, the creep process dominates the void evolution process.

Remark. It is worth mentioning that the volume change due to lattice nucleation and annihilation, which is reflected in the chemical strain ε_c (see Eq. (4.21)) during both stripping and plating peaks at a magnitude of approximately 10^{-5}, which is at a relatively small level considering the typical threshold for yielding significant mechanical impact. Although local stress may arise due to these small strains, they do not significantly change the outcomes of the interface dynamics. Hence this strain can be considered negligible and its role in the results is considered insignificant. The results also show that the gradient of the hydrostatic stress is primarily present in the interface rather than the bulk, which aligns with the theoretical predictions made based on the mass transfer governing equation (4.39). This indicates that the gradient of the hydrostatic stress mainly serves as a driving force for lithium diffusion, leading to a redistribution of Li from local areas with high hydrostatic stresses to those experiencing low stresses.

5.4 Cyclic Charging of A Solid-State Cell with Multiple Interface Defects

Let us proceed now to predict the evolution of voids and hot-spots in an all-solid-state cell undergoing multiple plating and stripping cycles. The aim is two-fold: to gain new insight and to showcase the abilities of the model in delivering predictions under realistic conditions. The schematic of the boundary value problem is given in Fig. 5.10. The electrode-electrolyte system has dimensions of H = 250 µm and W = 0.16H. The current at the electrode-electrolyte interface is unevenly distributed because of the presence of defects and surface roughness. This is captured by defining six small voids that have different radii and are located in arbitrary positions along the anode-electrolyte interface. These voids, numbered from left to right in Fig. 5.10, have radii of $R_1 = 0.0132H$, $R_2 = 0.025H$, $R_3 = 0.0084H$, $R_4 = 0.02H$, $R_5 = 0.0168H$, and $R_6 = 0.0112H$. Their precise positions are provided in Fig. 5.10 through the relative location of the centre of the circles containing each of the semi-circular voids. The initial and boundary conditions of the problem are also given in Fig. 5.10; these aim at mimicking the operating conditions of solid-state cells. From the point of view of diffusion, a flux is defined at the electrode-electrolyte interface, whose magnitude is determined by the current density. Regarding the electrical problem, a uniform current density i_{app} is prescribed in the free surface of the LLZO electrolyte. Mechanically, a pressure p is applied to the free surface of the Li metal anode but also

evaluate its influence by considering the case of $p = 0$, where the normal displacement component is constrained.

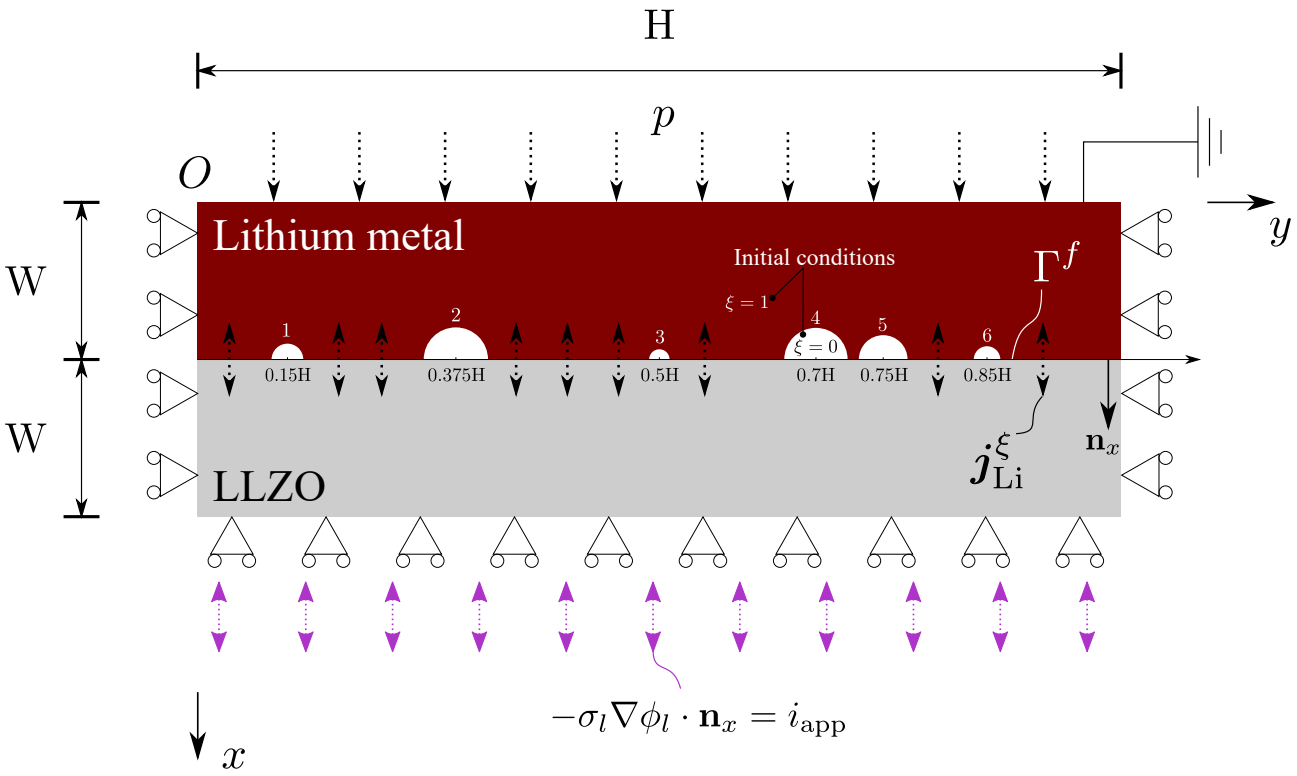


Figure 5.10: Solid-state cell with multiple interface defects: dimensions, configuration and boundary conditions. Initial and boundary conditions are also provided. Six voids of different radii are introduced to induce an uneven current distribution; as quantified in the schematic, these voids are placed at arbitrary locations along the electrode-electrolyte interface.

First, the evolution of the voids' morphology during multiple cycles of plating and stripping is investigated. Specifically, 5 charging cycles are simulated, each of which lasts for 2.5 h; stripping regimes of 1.25 h followed by plating periods of the same duration. The results obtained in the absence of an applied pressure ($p = 0$) are shown in Fig. 5.11. Several interesting features are observed. In the first stripping regime, it is found that all voids enlarge along the interface, with current hot spots appearing at their edges. The voids, initially semi-circular, widen and notably change their aspect ratio, going towards an elliptical shape. This effect is more pronounced for the smaller voids (voids 1, 3 and 6). If voids are close to each other (see voids 4 and 5), the symmetry of their shape is lost and coalescence is observed. After 1.25 h, the current is inverted and plating takes place. As observed for the single void analysis (see Fig. 5.5), the edges of each void become closer to each other. However, unlike the single void study, the void edges do not come into contact in the first plating cycle, as the initial state for plating is the stripped electrode.

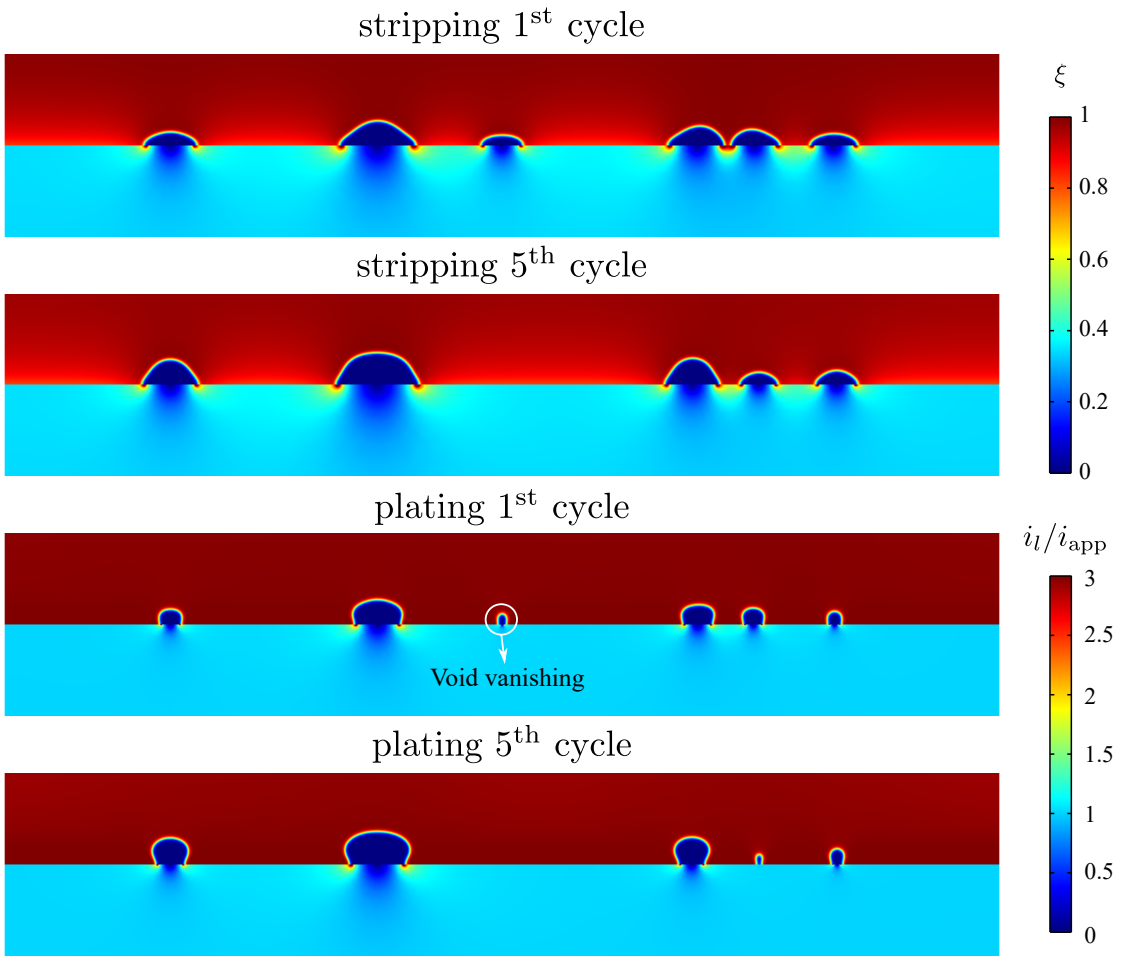


Figure 5.11: Numerical experiments on a Li metal anode - LLZO electrolyte system under realistic conditions: predictions of void evolution and current distribution for several stripping and plating cycles.

As the charging and discharging cycles proceed, the majority of the voids increase their size; see, e.g., the evolution of void 2 between the first and fifth plating cycles. However, the smallest void (void 3) vanishes during the fourth plating period and therefore, current hot-spots are not subsequently present in that region. It is also observed how the void shape changes with plating and stripping cycles, adopting aspect ratios closer to the initial one. Overall, a deterioration of the electrolyte-electrode interface can be seen, with voids increasing in size and a reduction in the electrolyte-electrode contact area.

It has been frequently argued that the most promising strategy to prevent the interfacial instabilities that result from voiding is the application of mechanical pressure [62, 70]. Small stripping currents can readily lead to rates of Li oxidation that are greater than the rate at which Li is replenished due to bulk Li diffusion. Hence, the aim is to apply a constant pressure to provide another source of Li to the interface *via* creep deformation. As shown in Section 5.3.3, creep plays a much more significant role in shrinking voids than Li diffusion and thus is key to minimising voiding and the emergence of current

hot spots. Let us proceed to apply a constant pressure during plating and stripping, and compare the outcome of the simulations with the predictions obtained for $p = 0$. The results obtained for selected values of the applied pressure ($p = 0$, 0.5 and 1 MPa) are shown in Fig. 5.12.

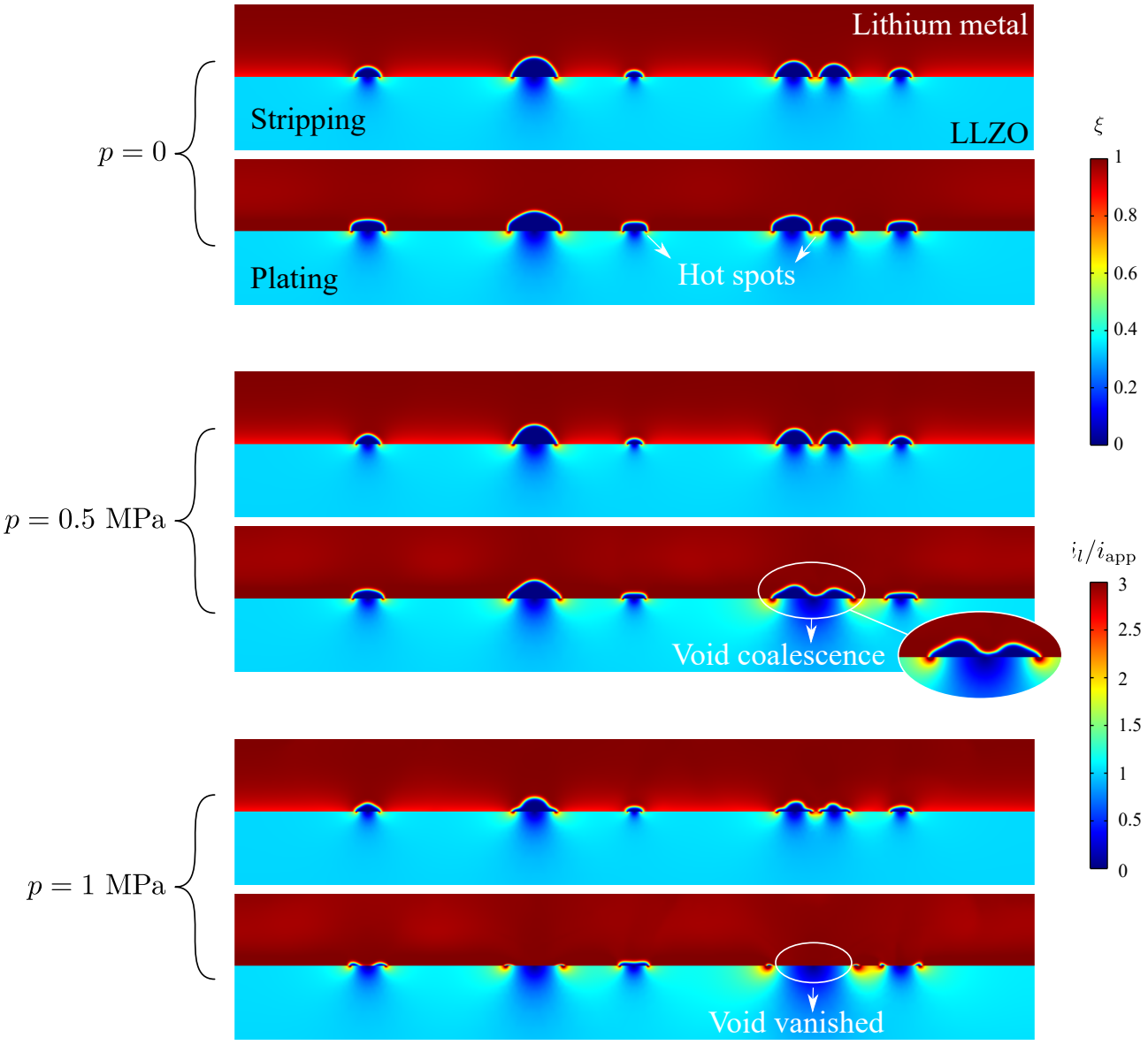


Figure 5.12: Numerical experiments on a Li metal anode - LLZO electrolyte system under realistic conditions: influence of the applied pressure p in the void evolution and current distribution. A complete charge-discharge cycle over 2.5 h is simulated, starting with a 1.25 h stripping half cycle. The figures display the results obtained after 30% of the stripping ($t = 22.5$ min.) and plating ($t = 97.5$ min.) half cycles.

It can be observed that the application of pressure is very effective in reducing the size of the voids. The cases with $p > 0$ show ellipsoidal voids that flatten with time, up to the point of vanishing for $p = 1$ MPa. This leads to the suppression of current hot spots that are otherwise present at the void ligaments (see the region between voids 4 and 5 for $p = 0$). Significant differences are observed with the case of no pressure, in terms of the electrode-electrolyte contact area. Phenomena such as void

coalescence can also be observed for intermediate pressures ($p = 0.5\,\mathrm{MPa}$). The sensitivity of void size to pressure is important, as smaller voids lead to a higher conductance of the battery cell. For the charging conditions ($i_{\mathrm{app}} = 0.2\ \mathrm{mA\,cm^{-2}}$) and materials ($D_{\mathrm{eff}} = 7.5 \times 10^{-13}\ \mathrm{m^2\,s^{-1}}$) considered here, a constant pressure of 1 MPa appears to be sufficient to reduce voiding significantly.

5.5 Summary

In this chapter, the framework presented in Chapter 4 is extended to predict deformation and current distribution in the electrolyte, accounting for electrode-electrolyte interactions and capturing the emergence of regions of high current near the void edges. Being able to predict the nucleation and intensity of these local current 'hot spots' is of utmost importance as they lead to the formation of dendrites and subsequent cell short-circuit. To deliver predictions over relevant time and space scales, the model is numerically implemented using the finite element method. Case studies involving stripping and plating cycles in electrode-electrolyte systems with one or multiple voids are carried out to showcase the predictive capabilities of the model and gain insight into interfacial stabilities in all-solid-state batteries. Calculations are conducted to investigate the competition and interplay between creep, bulk and surface Li diffusion, Li dissolution and deposition, and vacancy nucleation and annihilation. The main findings are:

- Void morphology is very sensitive to charging conditions. As observed experimentally, stripping currents lead to an expansion of the void along the interface, while plating translates into a contraction of the void edges, potentially leading to complete void occlusion. These phenomena are magnified with increasing applied current and in materials that can more readily annihilate vacancies (as characterised by the phase field kinetic parameter L).

- High magnitudes of current density are predicted near the void edges, with the region where the local current is high ($i_l/i_{\mathrm{app}} > 3$) increasing in size with the stripping time.

- The application of mechanical pressure on the free surface of the electrode notably reduces voiding and leads to much larger contact areas between the electrode and electrolyte. It is observed that smaller voids can eventually vanish under relevant conditions if the pressure is sufficiently large.

- Creep is found to play a much more significant role than bulk Li diffusion in governing the shape of the voids.

- Complex voiding phenomena such as void coalescence are found to govern interfacial instabilities when simulating realistic conditions (multiple voids and charging cycles).

The work in this chapter can be further enhanced by incorporating a dendrite nucleation criterion or explicitly simulating dendrite evolution. Thus, the theoretical and computational framework presented establishes the basis for the development of advanced prognosis tools that can accelerate future developments in battery technology.

Chapter 6

Understanding the Accelerated Short-Circuiting Mechanism of Anode-Free SSBs[1].

Anode-free SSBs represent a pioneering attempt in the quest for energy storage solutions that are both high in energy density and inherently safe. By forgoing the use of active anode material and instead relying on in situ lithium plating during the initial charge, these batteries have the potential to achieve remarkably high energy densities, approximately 1500 $\mathrm{Wh\,l^{-1}}$ (Fig. 6.1a). This innovative approach not only promises to increase energy storage efficiency significantly but also simplifies the manufacturing process by eliminating the need to handle air-sensitive lithium metal, potentially reducing costs and enhancing the practicality of SSBs [133, 134]. Despite the advantages, the successful implementation of anode-free SSBs faces considerable challenges [135, 136], primarily due to the complexities of achieving stable lithium plating and stripping cycles at the solid-state electrolyte interfaces, which are crucial for the battery's long-term cycling stability and safety. This chapter first reviews the efforts of my experimental collaborators and then presents the associated numerical simulations to delve into the reproduction of the critical phenomenon of accelerated short-circuiting in anode-free SSBs employing the phase-field-based framework of this study, uncovering the underlying mechanisms and offering insights into potential mitigation strategies.

[1]Part of the work presented in this chapter has been published in: J. A. Lewis, S. E. Sandoval, Y. Liu, D. L. Nelson, S. G. Yoon, R. Wang, Y. Zhao, M. Tian, P. Shevchenko, E. Martínez-Pañeda, and M. T. McDowell. Accelerated Short Circuiting in Anode-Free Solid-State Batteries Driven by Local Lithium Depletion. *Advanced Energy Materials*, 13(12):2204186, 2023. [21]

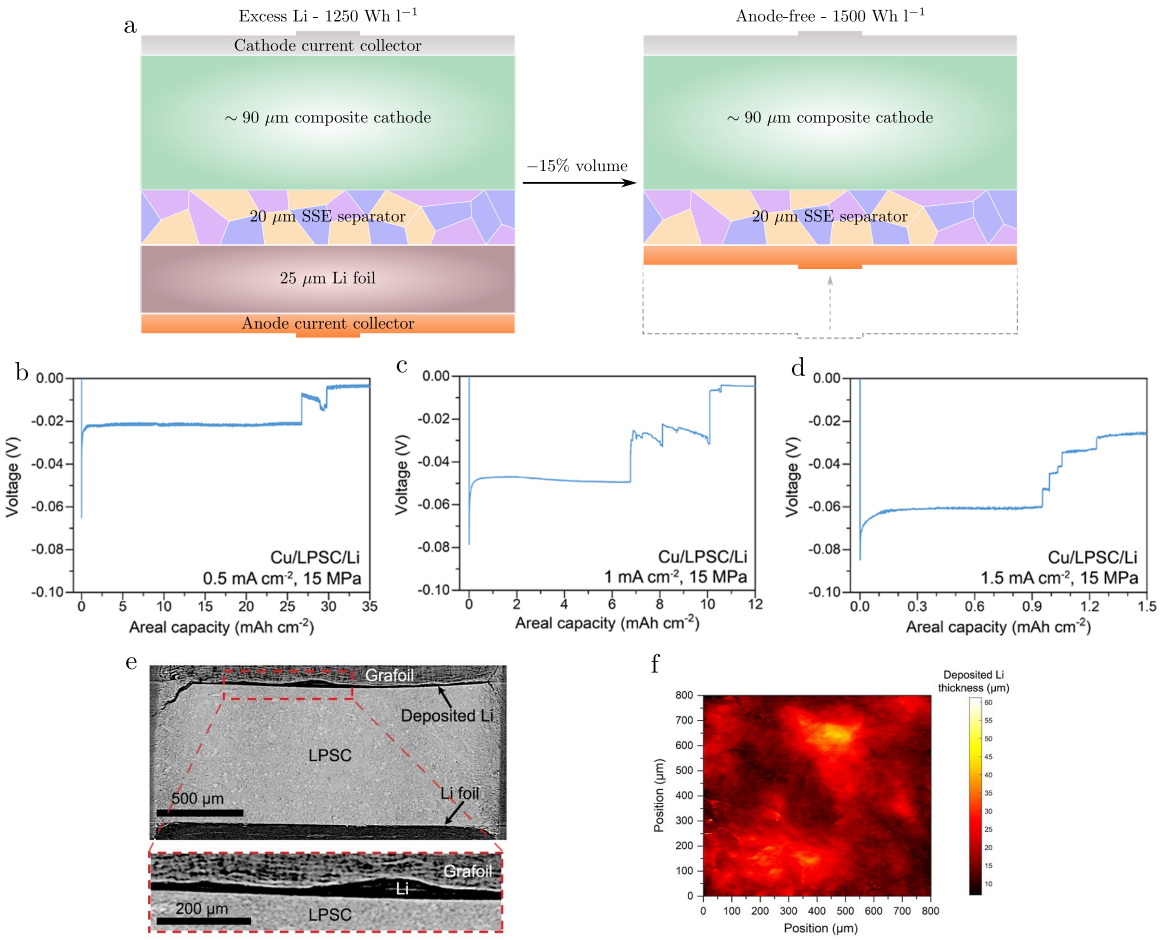


Figure 6.1: a) Cells forgoing the active anode material (right) could effectively reduce the stack volume by approximately 15% compared with Li-excess SSBs (left). b) to d) Illustrate the cell voltage fluctuations during Li deposition onto copper foil at current densities of 0.5, 1, and 1.5 mA cm^{-2}, under a stack pressure of 15 MPa. e) Presents a synchrotron X-ray tomography cross-section of the anode-free SSB after depositing 5.5 mAh cm^{-2} Li at 0.5 mA cm^{-2}, featuring a close-up to highlight thickness variations. f) Depicts a mapping of Li layer thickness over an area of 800 um by 800 um, where brighter colours signify thicker Li layers, as indicated by the legend bar on the right [21].

6.1 Experimental Insight

6.1.1 In Situ Li Deposition Behaviour at the Current Collector Surface

In advancing the comprehension of anode-free SSBs, my collaborative work began with a thorough investigation into initial lithium deposition behaviour involving a sulfide SSE Li_6PS_5Cl (LPSC). To this end, copper foils were employed as the anode current collector to construct Cu/LPSC/Li half-cells. The cell was constructed by cold pressing a 10 μm copper foil current collector against one side of a dense LPSC layer, with a stack pressure of about 15 MPa, and applying a thick lithium metal foil on the opposite side of LPSC as the lithium source. The investigation included tests at various deposition current densities — 0.5, 1, and 1.5 mA cm^{-2} — to elucidate the influence of current density

on the deposition process (as depicted in Figs. 6.1b to d). Notably, the voltage profiles at both the commencement and conclusion of electrodeposition showcased distinct steps. The initial surge in voltage is attributed to the nucleation overpotential, which drives the formation of the initial lithium metal layer [67, 136]. Subsequently, a voltage step following the plateau indicates the imminent risk of short-circuiting, essentially marking the capacity limit of the in-situ formed anode at the given current density. The results reveal that a lower current density enhances lithium deposition into the Cu/SSE interstice, depositing over 25 $\mathrm{mAh\,cm^{-2}}$ of lithium at 0.5 $\mathrm{mA\,cm^{-2}}$ before short-circuiting occurs, in stark contrast to just 1 $\mathrm{mAh\,cm^{-2}}$ at 1.5 $\mathrm{mA\,cm^{-2}}$. This finding aligns with established perceptions of lithium plating in SSBs, underscoring the criticality of the deposition current density.

By leveraging a variety of analytical techniques, such as optical and scanning electron microscopy (SEM) observations of cross-sectional slices, as well as X-ray tomography (XRT) imaging of the interface, it has been observed that the thickness of the lithium-metal layer formed in situ at the interface does not maintain uniformity, even when a constant current density is applied throughout the process. Synchrotron XRT scans of the cross-section of the anode-free SSB after Li deposition (Fig. 6.1e) distinctly reveal the presence of irregular lithium accumulations along the interface. A comprehensive mapping of the lithium layer's thickness across a square area of 800 µm by 800 µm (Fig. 6.1f) further illustrates these fluctuations. Notably, this inconsistency in thickness exacerbates as the current density escalates which has been confirmed in many other research [67, 85, 136]. A thorough elucidation of the mechanisms driving this phenomenon is still lacking, with existing literature predominantly offering superficial explanations that rely heavily on assumptions and conjecture.

The mechanism underlying these observations is undoubtedly complex. A pivotal factor is the influence of surface micro-defects and impurities at the interface between the CC and the SSE. Such anomalies contribute to the initial formation of lithium on a surface that lacks uniform smoothness and integrity, culminating in an uneven lithium layer. Despite numerous claims by researchers regarding the meticulous surface preparation of the CC and the SSE, it is imperative to acknowledge that current technological advances are yet inadequate for achieving atomic-level flatness on the surface, let alone the intrinsic grain and lattice structure of some SSEs with superior electrochemical properties, such as garnet LLZO, which makes achieving a perfect surface unattainable. Further complicating this issue, as highlighted in the work of Wang et al. [136], is the nature of the in-situ Li metal anode formation, which occurs from numerous nucleation sites and initially expands perpendicularly until meeting the resistance of the interface. Due to the low yield strength of lithium, this resistance redirects the growth laterally and ultimately forms a lithium layer. As a consequence, thickness inhomogeneity will be

an unavoidable limitation that is expected to persist into the foreseeable future. Acknowledging this limitation is essential for future endeavours aimed at addressing interface instability, serving as a fundamental consideration in labs and simulations.

6.1.2 Cycling Performance of the Anode-free SSBs

Cycling experiments were conducted to investigate the performance of these cells and for detailed effects of delithiation. Typical cycling behaviour at 0.5 mA cm^{-2} with anode-free half-cells showed that they would short-circuit prematurely, often by the third deposition cycle (as shown in Fig. 6.2a), indicating that repeated delithiation severely diminishes performance and exacerbates short-circuiting. Further insights were gained by comparing anode-free full cells and half-cells under identical conditions. Interestingly, full cells showed delayed short-circuiting, occurring at the ninth cycle compared to the third one in half-cells (Fig. 6.2b). This suggests that full cells have a slightly improved cycling performance, possibly due to their lower initial CE, which indicated more lithium retention on the anode post-discharge, contributing to a more resilient cycling process.

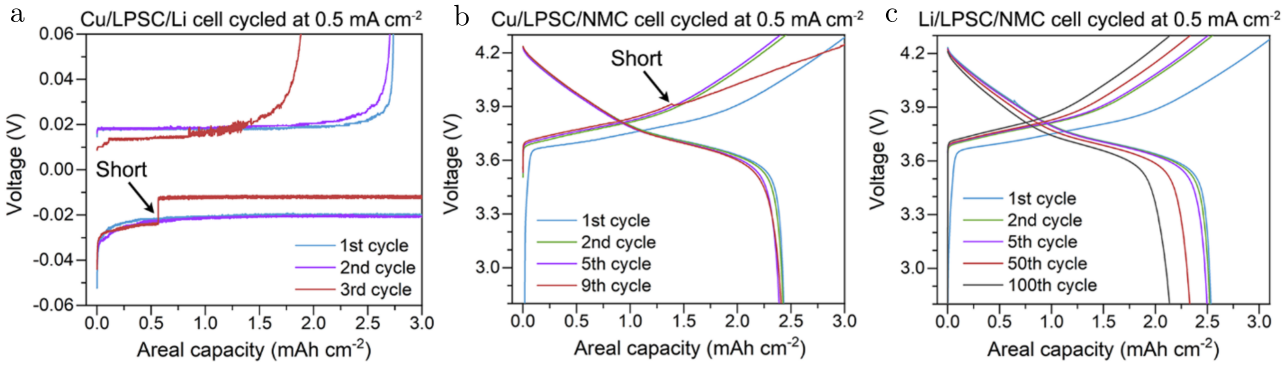


Figure 6.2: Cycling performance of anode-free SSBs: a) Demonstrates the Cu/LPSC/Li half-cell cycling at 0.5 mA cm^{-2}, featuring an in-situ deposited capacity of 3 mAh cm^{-2}. b) Showcases the Cu/LSPC/NMC full-cell cycling at the same current density, with the NMC cathode initially holding a capacity of 3 mAh cm^{-2}. c) Compares these results with a Li-excess full-cell (Li/LPSC/NMC) cycled under identical conditions, where the NMC cathode has a 3 mAh cm^{-2} capacity, supplemented by a pre-existing Li metal anode measuring 0.3 mm [21].

The reasons behind the loss of CE may be manifold. In this study, potential factors include the irreversible binding of Li atoms to the Cu substrate at room temperature, lithium loss due to non-reversible side reactions with the LSPC, and the creation of 'dead Li' from lithium isolated from the bulk through repeated dissolution and deposition cycles [67]. Generally, CE loss is detrimental to anode-free SSBs, leading to the irreversible depletion of electrochemically active lithium, which is essential for maintaining battery capacity and, consequently, a swift decline in battery performance.

Nonetheless, my colleagues' experiments highlight an unexpected benefit of this loss. The residual lithium increase at the interface, resulting from CE loss, compensates for the reduced electrochemically active material, thereby enhancing battery cycling stability by preserving interfacial contact. This suggests that maintaining good interfacial contact during cycling is particularly effective in preventing accelerated lithium dendrite short-circuiting in anode-free SSBs. This is further evidenced by the experiments performed in Fig. 6.2c. Building on the setup from Fig. 6.2b, a Li metal foil anode was introduced to create a Li-rich environment prior to initiating the first deposition half-cycle, ensuring consistent Li presence at the interface after each cycle. As can be seen, this modification significantly boosts the cell's cycling capability, enabling it to exceed 100 cycles without experiencing a short circuit.

In conclusion, the studies on lithium deposition and cycling behaviour in anode-free SSBs elucidate several critical insights for the subsequent work. A primary observation is that the formation of the initial in-situ lithium anode layer with uneven thickness is inevitable. Employing lower current densities and moderate pressures facilitates the deposition of a larger initial lithium capacity onto the electrode substrate. Although the specific impact of pressure is not the central focus of this paper, numerous studies have underscored the significance of applying judiciously calibrated pressure [7, 19, 62, 69–72]. Note that excessive pressure is unnecessary and harmful as it might lead to SSE fracturing and premature dendritic short circuits by forcing excess lithium into the SSE's cracks and defects [7]. Furthermore, the variability in the thickness of the Li anode layer can worsen over successive battery cycles. This variability may induce localized lithium depletion and sever ion-electron exchange pathways, resulting in local current constrictions, precipitating rapid growth of lithium dendrites and, consequently, swift battery failure. More importantly, retaining a consistent amount of lithium at the interface throughout the cell cycles and maintaining interface contact can effectively counteract this accelerated short-circuiting phenomenon.

6.1.3 Inferred Mechanisms for Accelerated Short-Circuit Phenomena

The experiments lead to a definitive conclusion that the cycling performance of Li-excess cells markedly surpasses those with just the right amount of deposited lithium. However, it's imperative to remember the primary objective behind developing anode-free SSBs is to achieve exceptionally high energy density. While supplementing the anode with excess lithium addresses early short-circuiting issues, it also detracts from its key advantage by introducing inactive mass that does not participate in the energy cycle, thereby diminishing the battery's overall market competitiveness. This underscores the critical need to comprehend the microdynamics at the solid-solid interface. A profound understanding of the

interactions and mechanisms at play is essential for cultivating the full potential of anode-free SSBs in practical applications, achievable through meticulous surface modification, material innovation, and structural design.

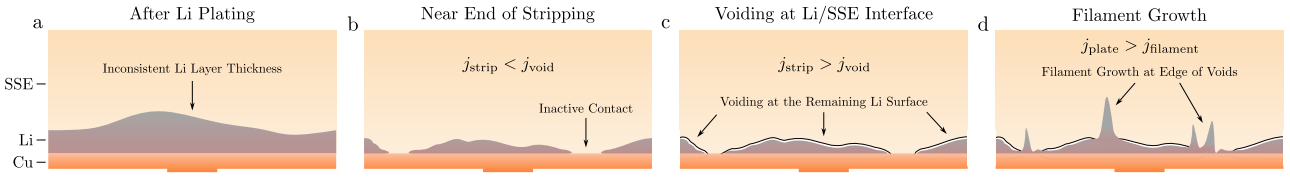


Figure 6.3: A diagram illustrating the material and morphological changes at the interface between the copper substrate and the SSE in an anode-free SSB: a) Initial state of the interface immediately following the first in-situ lithium deposition. b) Morphology of the interface approaching the completion of lithium stripping, with current constrictions present but not yet reaching the critical threshold for void formation. c) As stripping continues, current constrictions intensify, causing localized current densities to exceed the critical level for void formation, leading to the emergence of voids at the Li/SSE interface. d) During the plating half-cycle succeeding c), current constrictions elevate local current densities significantly above the overall current density, surpassing the critical threshold for lithium filament growth and facilitating its development.

A mechanism hypothesis is hereby proposed, seeking to elucidate the underlying processes governing the behaviour observed in preceding experiments. Contrary to the expected flat interface following the initial in-situ lithium deposition, an undulating interface with significant thickness variations is observed, as depicted in Fig. 6.3a. This uneven lithium layer thickness results in a non-uniform distribution of current density across the interface. According to Faraday's law of electrolysis, the current density in an electrochemical system dictates the rate of material flux, with regions of higher current density experiencing increased lithium deposition/dissolution.

At the onset of the stripping half-cycle, the irregularities in geometry and electrochemical reaction rates across the interface promote further non-ideal morphological changes, eventually leading to lithium depletion in certain areas and the formation of inactive contact zones devoid of substance exchange, as shown in Fig. 6.3b. Although current constriction occurs, local stripping current densities j_{strip} have not yet reached the critical level for void formation j_{void}. As stripping progresses, the severity of current constriction increases, pushing local current densities beyond the critical threshold for voiding. Consequently, voids start emerging at the Li/SSE interface, exacerbating the degradation of the remaining interface contact, as illustrated in Fig. 6.3c. This complicates the subsequent lithium plating process, creating conditions where local plating current densities j_{plate} surpass critical values for lithium filament nucleation and growth j_{filament}, as shown in Fig. 6.3d. Without intervention, the likelihood of cell short-circuiting becomes inevitable.

6.2 Phase-Field Decipher of the Impact of Local Li Depletion

To substantiate the hypothetical mechanism that is proposed in the previous section, some enhancements to the preceding model utilized in Chapter 4 and 5 are undertaken, specifically the boundary conditions at the electrode/SE interface, which will be elaborated in detail in the following content of this section. These modifications are intended to capture the interfacial material and morphological changes at play more precisely. However, interestingly, some of these adjustments also unexpectedly improved the convergence of the model.

6.2.1 Governing Equations

The governing equations that lay the foundation for the succeeding discussion, as summarized in Fig. 6.4, follow from the definition of the Gibbs and Helmholtz free energies of the electro-chemo-mechanical system depicted in Chapter 4.

Vacancy Diffusion/Substitutional Li Diffusion, incorporating both surface and bulk Li diffusion. This is achieved through the introduction of a Li occupancy variable, θ_{m}, representing the fraction of lattice sites occupied by lithium, as defined in Chapter 4. The evolution of θ_{m} is governed by a dynamic equation that integrates phase-field order parameters to capture the nuances of bulk and surface lithium diffusion:

$$h(\xi)\frac{\partial \theta_{\mathrm{m}}}{\partial t}+\theta_{\mathrm{m}} h'(\xi)\frac{\partial \xi}{\partial t}=\nabla \cdot \frac{D_{\mathrm{eff}} h(\xi)}{1-\theta_{\mathrm{m}}}\nabla \theta_{\mathrm{m}}-\nabla \cdot \frac{D_{\mathrm{eff}} h(\xi)\theta_{\mathrm{m}}\left(\Omega_{\mathrm{Li}}-\Omega_{\mathrm{v}}\right)}{RT}\nabla \sigma_h^{\xi}, \tag{6.1}$$

where ξ is the phase field variable, distinguishing between void ($\xi = 0$) and lithium metal ($\xi = 1$) phases. $h(\xi) = \xi^2(\xi^2 - 3\xi + 3)$ is an interpolation function. D_{eff} is the effective substitutional diffusion coefficient of Li. Ω_{Li} and Ω_{v} denote the molar volumes of occupied and vacant lattice sites, respectively. R is the gas constant, and T denotes absolute temperature. σ_h^{ξ} is the hydrostatic stress, with the superscript ξ indicating ξ-dependent variations across void-metal phases within the electrode domain.

Void Evolution due to vacancy nucleation/annihilation is captured through the phase field variable ξ, which evolves through the following Allen-Cahn-type equation:

$$\frac{\partial \xi}{\partial t}=-L\frac{RTh'(\xi)}{\Omega_{\mathrm{L}}}\ln\frac{1-\theta_{\mathrm{m}}}{1-\theta_{\mathrm{m}}^0}-L\frac{\Omega_{\mathrm{v}}h'(\xi)}{\Omega_{\mathrm{L}}}\psi_e-Lwg'(\xi)+L\kappa\nabla^2\xi, \tag{6.2}$$

where L is the so-called phase field mobility parameter, θ_{m}^0 is the equilibrium lithium occupancy, ψ_e is the elastic strain energy density, $g(\xi)$ is the double-well function (of height w) and κ is the gradient

energy coefficient.

Electrical Behaviour in the anode and electrolyte is captured by using Ohm's law:

$$-\nabla \cdot \left(\sigma_s^{\xi} \nabla \phi_s\right) = 0, \tag{6.3}$$

$$-\nabla \cdot (\sigma_l \nabla \phi_l) = 0, \tag{6.4}$$

where σ_s^{ξ} and σ_l respectively denote the electric conductivity of the anode and the ionic conductivity of the SSE, with the former being interpolated with ξ across void regions, enabling the appearance of localized current regions, and ϕ_s and ϕ_l being the electric potentials of the anode and the SSE, respectively.

Mechanical Deformation of the anode is captured by means of the balance of linear momentum:

$$\nabla \cdot \boldsymbol{\sigma}^{\xi} = 0, \tag{6.5}$$

with $\boldsymbol{\sigma}^{\xi}$ being the Cauchy stress tensor, which is interpolated with phase field variable ξ to capture the loss of stiffness associated with voided regions. Creep behaviour is captured employing Anand's viscoplastic model [105], by which viscous plastic strains are given by $\dot{\boldsymbol{\varepsilon}}_v = \left(\frac{3}{2}\right) F_{\mathrm{cr}} \boldsymbol{\sigma}_{\mathrm{dev}}^{\xi} / \sigma_e^{\xi}$, where F_{cr} is the equivalent plastic shear strain-rate, and $\boldsymbol{\sigma}_{\mathrm{dev}}$ and σ_e respectively denote the deviatoric stress tensor and the von Mises effective stress. The boundary conditions, aimed at capturing the role of the stack pressure in keeping the contact between the anode and the electrolyte, are discussed in the next section.

6.2.2 Boundary Conditions and Initial Conditions

Electrode kinetics boundary conditions of the transport problem enable capturing Li dissolution/deposition at the anode-electrolyte interface Γ_r (see Fig. 6.4) through changes in the arising current density $\widetilde{i}$ of the local interface:

$$-\mathbf{j}_{\mathrm{Li}}^{\xi} \cdot \mathbf{n} = \frac{\widetilde{i}}{zF}, \tag{6.6}$$

where $\mathbf{j}_{\mathrm{Li}}^{\xi}$ is the lithium flux, with the superscript ξ indicating that it is influenced by the phase field variable along the interface. z is the charge number, F is Faraday's constant and $\mathbf{n}$ is normal to the surface.

The local current density $\widetilde{i}$ at the interface exhibits variations that are closely linked to the phase field variables along the interface. It is understood that any loss of interfacial contact invariably leads

to an escalation in interfacial resistance, which is a phenomenon that was not adequately addressed in the modelling efforts described in earlier chapters. This section aims to delineate the fluctuations in current density and material exchange at the interface more accurately, in tandem with interface morphology changes, by incorporating the Butler-Volmer type's electrode kinetics. Given the small surface overpotential, the linearized form of the Butler-Volmer equation is utilized, which contributes to a robust analysis of the interface electrochemical processes when submitted to numerical calculations:

$$\widetilde{i} = i_0 \left[\frac{(\alpha_a + \alpha_c)\, F}{RT} \right] \eta, \tag{6.7}$$

where i_0 represents the exchange current density at the interface, α_a and α_c denote the apparent transfer coefficients for the anodic and cathodic processes, respectively, and η is used to signify the overpotential. By rearranging Eq. (6.7) and setting both α_a and α_c to a value of 0.5, the theoretical interface resistance can be derived as:

$$Z_0 = \frac{RT}{i_0 F}. \tag{6.8}$$

To accurately capture the evolving nature of interface resistance as the contact quality at the interface gradually deteriorates, a phase-field dependency to Z_0 with a reciprocal relationship, represented as $Z_0^{\xi} = Z_0/h(\xi)$, is introduced. The modification transforms the initial form of Eq. (6.7) to reflect the dynamic interplay between the interface morphology and its resistance characteristics through:

$$\widetilde{i} = \frac{\eta}{Z_0^{\xi}} = h(\xi)\frac{\eta}{Z_0}. \tag{6.9}$$

The overpotential η required for Eq. (6.9) is estimated as a function of the electric potentials and the equilibrium potential U as $\eta = \phi_s - \phi_l - U$. And $\mathbf{i}_s \cdot \mathbf{n} = -\mathbf{i}_l \cdot \mathbf{n} = \widetilde{i}$ for conservation of charge.

Electrically, a galvanostatic condition is assumed and ensured by constant electrolyte current density of $\mathbf{i}_{el} \cdot \mathbf{n} = i_{app}$ applied across Γ_r^{SSE}. It's important to note that this study deliberately omits the cathode to streamline computational resources and enhance efficiency, focusing attention on the anode's behaviour. The left boundary of the Li anode Γ_l is designated as grounded, establishing a zero potential reference point. The remaining boundaries of the anode (Γ_t, Γ_b) and the SSE (Γ_t^{SSE}, Γ_b^{SSE}) are treated as electrically insulated, preventing any unintended electrical flow across these interfaces and ensuring the electrical conditions are accurately represented.

Mechanically, the left boundary of the anode Γ_l is subjected to a uniformly applied velocity $-\mathbf{v} \cdot \mathbf{n} = v_n$ rather than a constant pressure. This is to mimic the role of a gradually increasing

pressure in enhancing interface contact between the anode and the SSE, meanwhile mitigating the potential convergence issues that may arise from the sudden application of substantial pressure at the simulation's onset, particularly when engaging with non-linear material models. It must be emphasised that, in the interest of achieving convergence and ensuring the generation of plausible results, the simulated pressure exerted on the lithium metal anode remains significantly lower, ranging from 0 to 0.3 MPa, compared to the 15 MPa employed in experimental settings.

This discrepancy in pressure levels could potentially explain the diminished efficacy in stripping the same amount of lithium capacity prior to the complete loss of interface contact in the simulation. To address this and justify the methodology, it's important to consider the scalability and applicability of the model under varying conditions. By systematically analyzing the impact of lower pressure levels on interface contact and lithium anode behaviour, insights can be derived into the material's mechanical properties and interface dynamics under less extreme conditions. Furthermore, extrapolating from these findings may allow for the prediction of behaviour at higher pressures, offering a pathway to reconcile the simulation results with experimental observations.

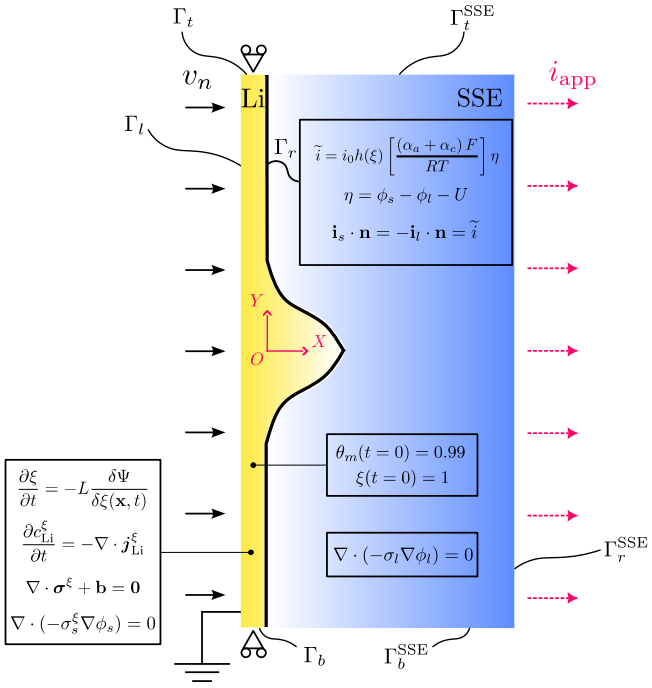


Figure 6.4: Sketch of the simulated domain, including the Li metal anode and the SSE, with the associated governing equations of the model. The initial and boundary conditions are also provided.

In addition, the role of the stack pressure in enhancing contact between the anode and the solid electrolyte is captured by combining two numerical treatments. One is an Arbitrary Lagrangian-Eulerian (ALE) formulation ("Deformed geometry" in COMSOL) that captures the depletion of

lithium and the associated rigid body motion of the anode. The second is a penalty approach that imposes a body force to prevent the Li metal from penetrating the solid electrolyte.

The parameters of the model are chosen to mimic the experimental conditions; a complete list is given in Table 6.1. The phase field mobility coefficient L is chosen according to its relationship with the applied current density (0.25 mA cm−2, see Cui et al. [82] for details). The effective diffusion coefficient for substitutional Li transport D_{eff} is taken from the experimental measurements of the work from Dologlou [137] and the ionic conductivity of LPSC is taken to be $\sigma_l = 0.18\ \text{S}\,\text{m}^{-1}$, as per the experiments. Finally, as in Chapter 5, the parameters of the viscoplastic model are calibrated against the uniaxial tension tests at different strain rates on pure Li by LePage et al. [20]. A rectangle Li anode domain of a height of 60 μm and a thickness of 3 μm and a bulge depth (6 μm) is chosen based on the experimentally observed Li deposition thicknesses and their variation due to uneven plating/stripping. The results in Fig. 6.5 are provided at three representative stages: $t = 0^+$, $t = 3300$ s and $t = 3800$ s.

Table 6.1: Reported material properties

Parameter	Magnitude	Ref
Mass density of Li, ρ_{Li} [kg m^{-3}]	534	
Young's modulus of Li, E_{Li} [GPa]	7.82	Masias et al. [138]
Poisson's ratio of Li, μ_{Li} [-]	0.381	Masias et al. [138]
Molar volume of Li, Ω_{Li} [cm^3 mol^{-1}]	[1]12.90 - 13.02	Hallstedt [139]
Effective diffusion coefficient of Li, D_{eff} [m^2 s^{-1}]	7.65×10^{-15}	Dologlou [137]
Gas constant, R [J mol^{-1} K]	8.314	
Faraday's constant, F [C mol^{-1}]	96485	
Temperature, T [K]	298	
Interface kinetics coefficient, L [m^2 N^{-1} s^{-1}]	2.417×10^{-9}	This work
Height of the double well potential, w [N m^{-2}]	3.5×10^{6}	This work
Gradient energy coefficient, κ [N]	4.5×10^{-8}	This work
Viscoplastic pre-exponential factor of Li, A [s^{-1}]	4.25×10^{4}	LePage et al. [20]
Viscoplastic activation energy, Q [kJ mol^{-1}]	37	LePage et al. [20]
Viscoplastic strain rate sensitivity exponent, m [-]	0.15	LePage et al. [20]
Deformation resistance saturation coefficient, S_0 [MPa]	2	LePage et al. [20]
Initial value of the flow resistance, $S_a(t = 0)$ [MPa]	1.1	LePage et al. [20]
Hardening constant, H_0 [MPa]	10	LePage et al. [20]
Hardening sensitivity, a [-]	2	LePage et al. [20]
Deformation resistance sensitivity, n [-]	0.05	LePage et al. [20]
Electric conductivity of Li, σ_{Li} [S m^{-1}]	1×10^{7}	Chen et al. [13]
Ionic conductivity of LPSC, σ_{LSPC} [S m^{-1}]	0.18	This work
[2]Exchange current density, i_0 [A m^{-2}]	50	Chen and Pao [124]
Surface energy of lithium, γ [N m^{-1}]	0.6538	Doll et al. [140]

[1]Measured at a temperature of 298.15 K.

[2]Exchange current density is reported to be on the order of 10 - 100 A m^{-2} under typical battery operating condition [124].

6.2.3 Results and Discussion

The FEM simulation results helped to reveal an in-depth understanding related to the lithium depletion mechanism. Fig. 6.5 shows the results of these simulations, with a lithium metal electrode with a non-uniform thickness (yellow) in contact with an SSE (blue). This figure shows simulation results at three different times as stripping commences. The normalized current i_l/i_{app} in the SSE is shown by the colour gradation scale on the right of Fig. 6.5. The phase field parameter ξ within the lithium, which represents the tendency for voiding (closer to zero represents voiding), is shown by the scale on the left of Fig. 5. At an early time shortly after stripping begins (Fig. 6.5a), the current distribution shown in the SSE phase is almost uniform with only slight alteration at the lithium bulge. As stripping proceeds (Fig. 6.5b), the current becomes somewhat localized at the bulge. When the surrounding flat lithium is completely stripped (Fig. 6.5c), however, the current becomes highly concentrated in the remaining lithium region, inducing obvious voiding at the interface (see inset). This current localization is observed after the loss of the surrounding active area, supporting the proposed mechanism.

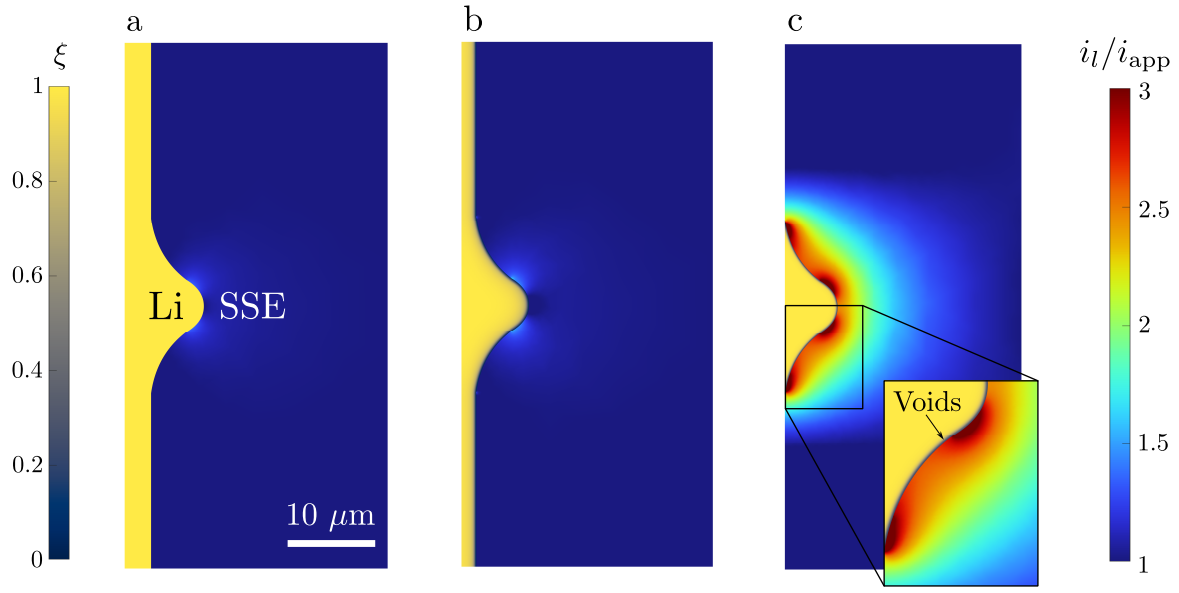


Figure 6.5: Mechanistic numerical predictions of stripping behaviour (as characterized by the phase field parameter ξ within the lithium metal) and normalized current in the SSE i_l/i_{app}, where i_{app} is the globally applied current of 0.25 mA cm^{-2}. a) Initial geometry and conditions shortly after stripping begins ($t = 0+$), with a small lithium bulge introduced to mimic the result of uneven plating/stripping. b) Later in the stripping process ($t = 3300$s), showing some voiding and current localization at the lithium bulge. c) Snapshot after the surrounding flat lithium area has been fully stripped ($t = 3800$s), revealing localized voiding and significant localization of current at the bulge.

6.3 Summary

These experimental and simulation results show that the plating/stripping mechanisms in anode-free SSBs are fundamentally different from excess-lithium SSBs. The tendency for local lithium depletion and isolated lithium formation during stripping in anode-free SSBs is likely unavoidable since neither deposition nor stripping will always occur with complete uniformity. Thus, the local current density j_{strip} will increase locally and ultimately exceed j_{void} at the remaining lithium regions due to the decrease in the active area, even for relatively low applied current densities. This differs from lithium-excess SSBs, where there is never local depletion of lithium (i.e., lithium remains present across the entire interface) because of the thick lithium present. Voids can form during stripping in lithium-excess SSBs, but only when the global current density is greater than the critical current density for void formation, j_{void}. These concepts explain the improved resistance to short-circuiting exhibited by excess-lithium cells (such as the full cell in Fig. 6.2c) compared to the anode-free full and half cells (Fig. 6.2a-b). The requirements for stable operation of anode-free SSBs are thus even more stringent than excess-lithium cells: in addition to preventing general physical contact loss and void formation, a key challenge for anode-free SSBs is to ensure that lithium is plated and stripped uniformly across the entire interface to minimize the localized depletion of lithium during stripping.

Chapter 7

Towards Quantitative SSB Predictions

Quantitative analysis was carried out to validate the utility of the model. Since the current model is not aimed at reproducing the nucleation and growth of dendrites, this chapter will focus on the stripping process of the electrode. Experiments have reported that a sustained stripping process will lead to a loss of interfacial contact and increased interfacial resistance, resulting in ohmic polarization. This polarization causes a significant deviation of the cell voltage from its OCV [21–23], which can serve as a critical reference for validating the accuracy of the model in quantitative prediction capabilities.

The model setup is similar to that used in Fig. 5.3 in Chapter 5 but incorporates the Butler-Volmer kinetics at the electrode/SE interface, as illustrated in Fig 7.1 below. The initial size of the void is set to $R = R_0 = 0.5$ um for a better representation of a relatively good interface contact between Li and SE, as achieved with an in-situ formed Li anode that was studied in the work of Lee et al. [22]. The bulk dimensions of the configuration are redefined as W = 10 R_0 and H = 2 W.

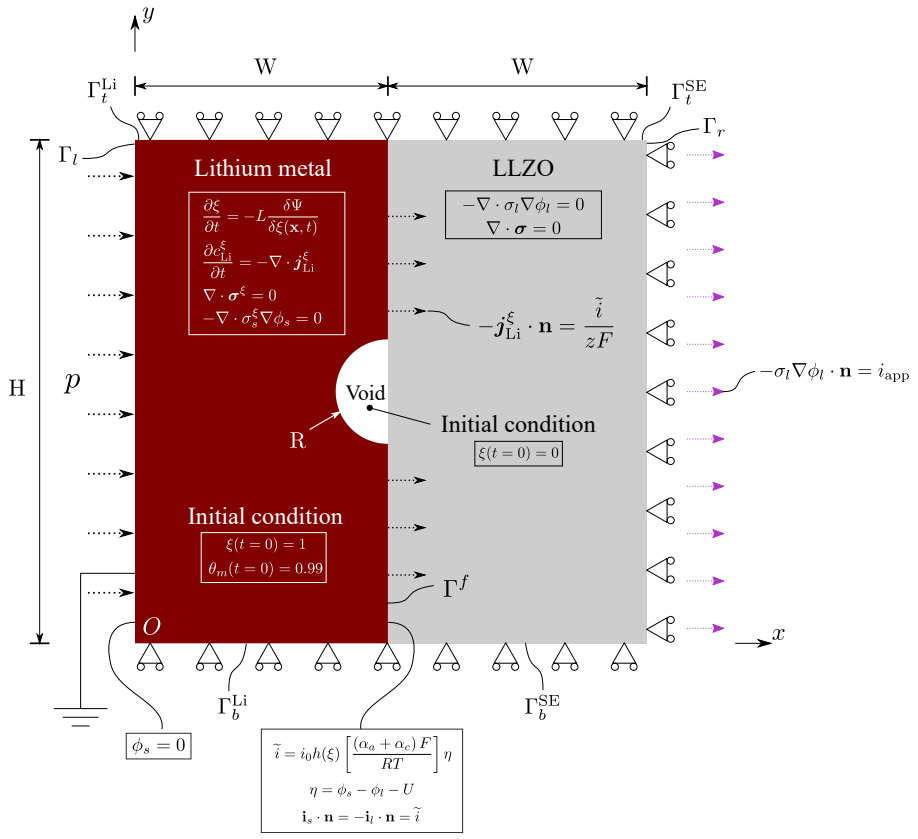


Figure 7.1: Model setup for quantitative studies.

The results of the analysis demonstrate that the model could offer insightful quantitative predictions to some extent. However, there are also evident limitations that should be acknowledged. Detailed discussions will be presented in the following sections.

7.1 Boundary Conditions and Initial Conditions

The boundary conditions and initial conditions are similar to those applied in Section 5.3 with several additional conditions at the Li/SE interface, which are summarized as follows:

Mechanically, a pressure p is applied to the Li anode while normal displacement in other outer boundaries is restrained, which renders

$$\mathbf{n} \cdot \boldsymbol{\sigma}^{\xi} \cdot \mathbf{n} = -p \qquad \text{on} \quad \Gamma_l, \tag{7.1}$$

$$\mathbf{u} \cdot \mathbf{n} = 0 \qquad \text{on} \quad \Gamma_t^{\mathrm{Li}} \cup \Gamma_t^{\mathrm{SE}},\ \Gamma_b^{\mathrm{Li}} \cup \Gamma_b^{\mathrm{SE}},\ \text{and}\ \Gamma_r. \tag{7.2}$$

Electrically, the left boundary of the Li anode is grounded while a constant current density i_{app} is applied to the right boundary of the SE for conduction of a galvanostatic simulation. Other outer boundaries of the Li anode and the SE are insulated. A linear Butler-Volmer relation dependent on

the phase field order parameter is introduced at the Li/SE interface. These conditions render

$$\phi_s = 0 \qquad \text{on} \quad \Gamma_l, \tag{7.3}$$

$$-\sigma_l \nabla \phi_l \cdot \mathbf{n} = i_{\text{app}} \qquad \text{on} \quad \Gamma_r, \tag{7.4}$$

$$-\mathbf{n} \cdot \mathbf{i}_s = 0 \qquad \text{on} \quad \Gamma_t^{\text{Li}} \text{ and } \Gamma_b^{\text{Li}}, \tag{7.5}$$

$$-\mathbf{n} \cdot \mathbf{i}_l = 0 \qquad \text{on} \quad \Gamma_t^{\text{SE}} \text{ and } \Gamma_b^{\text{SE}}, \tag{7.6}$$

and

$$\widetilde{i} = i_0 h(\xi) \left[\frac{(\alpha_a + \alpha_c) F}{RT} \right] \eta, \;\; \eta = \phi_s - \phi_l - U, \;\; \mathbf{i}_s \cdot \mathbf{n} = -\mathbf{i}_l \cdot \mathbf{n} \quad \text{on} \quad \Gamma^f. \tag{7.7}$$

For Li transport at the interface, the boundary condition renders

$$-\boldsymbol{j}_{\text{Li}}^{\xi} \cdot \mathbf{n} = \frac{\widetilde{i}}{zF} \qquad \text{on} \quad \Gamma^f, \tag{7.8}$$

$$-\boldsymbol{j}_{\text{Li}}^{\xi} \cdot \mathbf{n} = 0 \qquad \text{on} \quad \Gamma_t^{\text{Li}}, \Gamma_b^{\text{Li}}, \Gamma_l. \tag{7.9}$$

Specifically, considering the poor wettability between the Li metal and the ceramic SE, a larger contact angle $\omega = 150^\circ$ at the three-phase junction of air, Li and SE in the initial configuration is introduced [5], such that

$$\frac{\nabla \xi \cdot \mathbf{n}}{|\nabla \xi|} = \cos \frac{5}{6} \pi \qquad \text{on} \quad \Gamma^f, \tag{7.10}$$

and in the meantime

$$\nabla \xi \cdot \mathbf{n} = 0 \qquad \text{on} \quad \Gamma_t^{\text{Li}}, \Gamma_b^{\text{Li}}, \Gamma_l. \tag{7.11}$$

The initial conditions are the same as those defined in Eqs. (5.9) and (5.10).

Remark. For the studies carried out in this chapter, the thickness of the phase field interface ℓ is set to 0.1 um hence according to the derivations carried out in Section 4.2.2, the height of double well potential $w = 1.087 \times 10^8$ N m^{-2}, and the gradient energy coefficient $\kappa = 6.29 \times 10^{-8}$ N. Other parameters are identical to those listed in Tables 5.1 and 5.2.

7.2 Quantitative analysis of Interface Contact Loss During Stripping

7.2.1 Results Considering Creep Deformation of the Li Metal Anode

Galvanostatic stripping studies with varying applied current densities $i_{\text{app}} = \{0.05, 0.1, 0.2, 0.4, 0.6\}$ mA cm^{-2} under a constant pressure of $p = 0.005$ MPa were conducted. The simulation terminates when significant voltage polarization is observed and complete loss of interfacial contact occurs. Fig. 7.2 illustrates the morphology of the void and the interface contact state at the conclusion of the simulations for each applied stripping current density. Each simulation commenced with the same initial configuration, as shown in the first sub-figure with $t = 0^+$. The duration t_f required to achieve complete interfacial contact loss decreased with increasing current density, consistent with general experimental observations [22, 23].

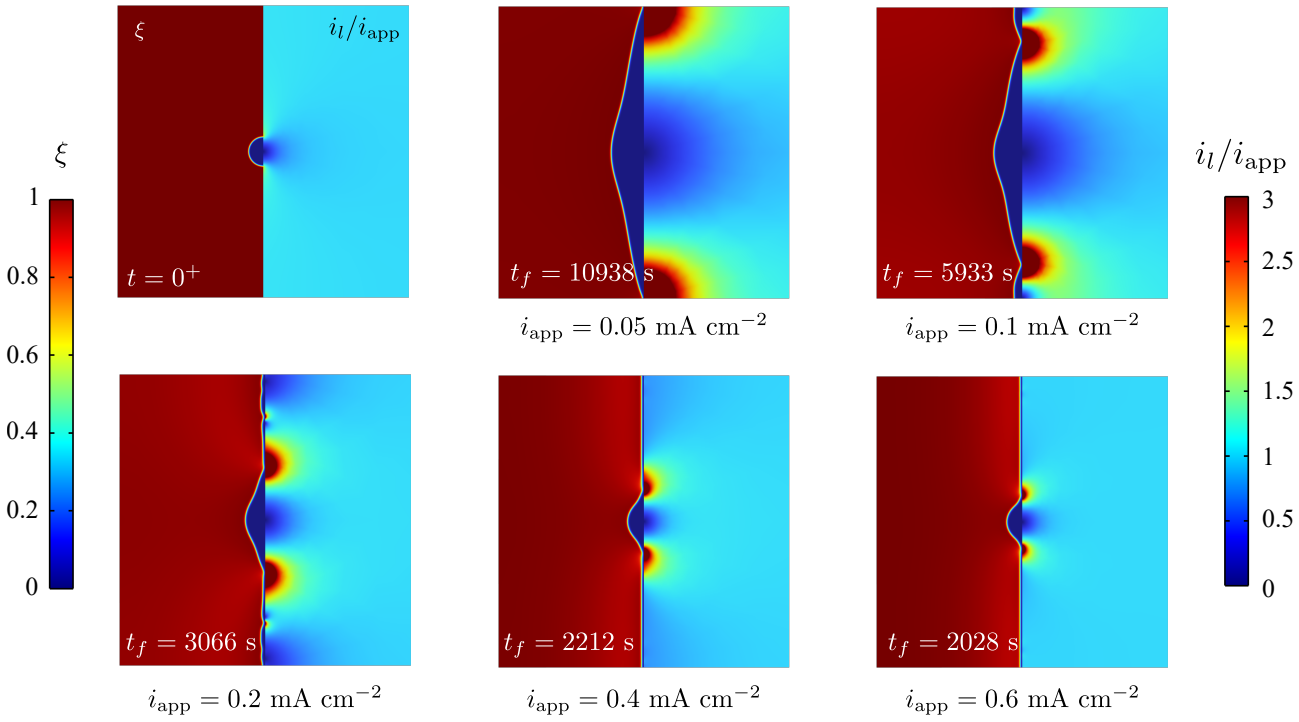


Figure 7.2: Numerical results of the final moment before complete interfacial contact loss happens under different stripping current densities and constant pressure of $p = 0.005$ MPa. The viscoplastic material model is adopted for the Li metal anode. $t = 0^+$ is the communal initial state for all current density cases.

Additionally, with increased stripping current density, the final volume of the pre-existing void at t_f diminished, as illustrated in Fig. 7.3 (a). This finding corroborates the experimental results reported by Lu et al. [23], where low current densities tend to generate larger and more dispersed voids, while higher current densities favour the formation of smaller but denser void distributions. The nature of the interfacial contact loss lies in the disruption of the lithium replenishment-loss equilibrium at the Li/SE

interface. Consequently, the most straightforward explanation for this observed phenomenon–where void size is affected by current density–is that higher current densities disrupt the lithium equilibrium not only in the current hot-spot regions near the void but also in the remaining regions, as depicted in Fig. 7.3 (b). As the interface contact deteriorates, the average current density in the remaining contact area is lifted to a much higher level, which leads to the nucleation of new voids in these areas.

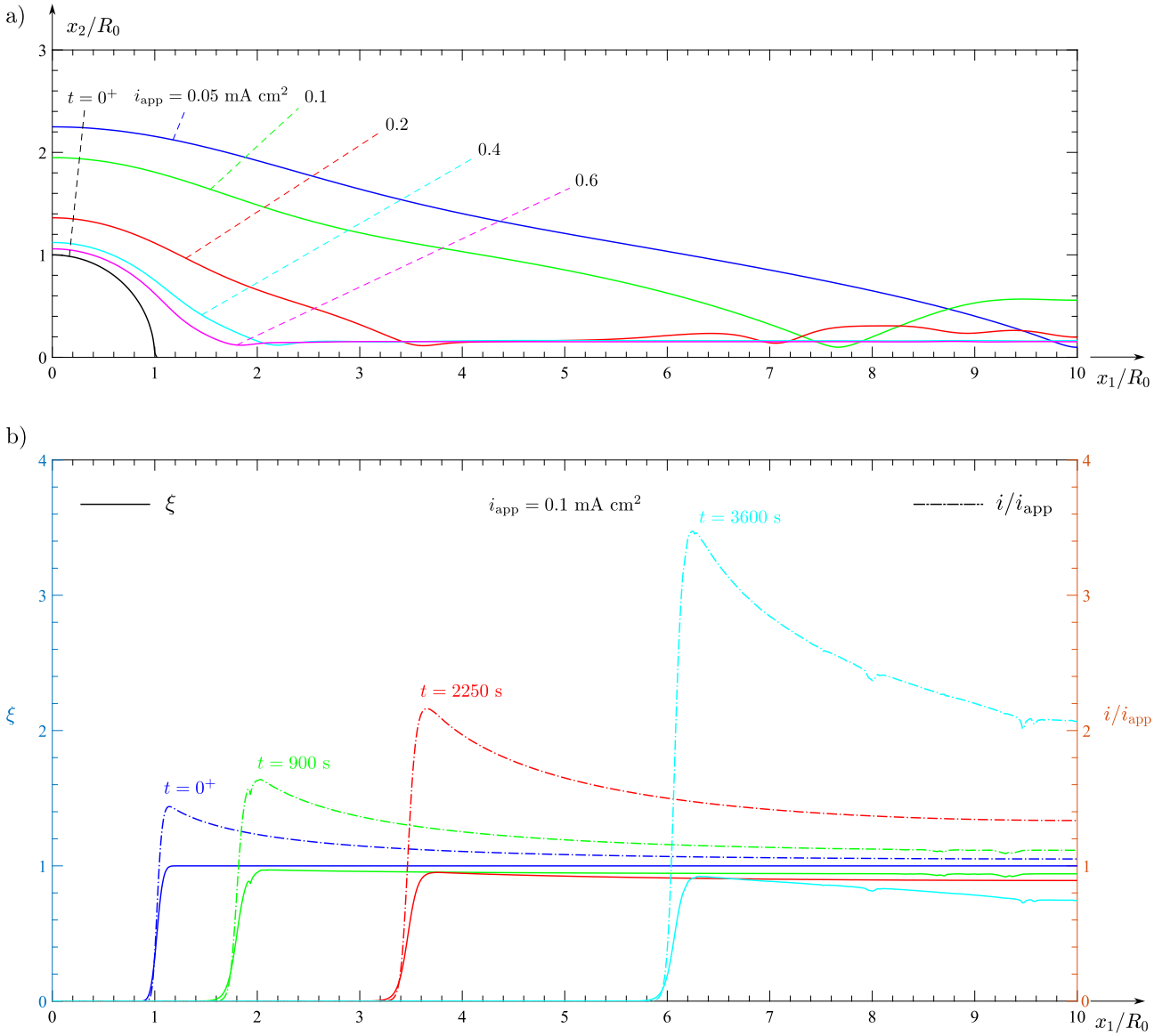


Figure 7.3: Results of the numerical experiments showing a) The precise locations of the void interface that is shown in Fig. 7.2 (represented by $\xi = 0.5$) for different applied current densities. (x_1, x_2) is a Cartesian coordinate system with its origin located at the centre of the void and x_2 in the perpendicular direction of the Li/SE interface. The coordinate system is normalized by the initial radius of the void R_0, and b) the magnitude of ξ and i/i_{app} along the Li/SE interface under $i_{app} = 0.1$ mA cm^{-2} at different stripping moment t.

The evolution of the cell voltage as a function of stripping time is then compared with those reported in the work of Lee et al. [22]. The outcome is illustrated in Fig. 7.4. The circles represent the experimental data, which were measured at different current densities under constant pressure of

$p = 5.6$ MPa [22]. The solid curves represent the FE predictions of the model. As previously stated, the pressure applied in the simulation is 0.005 MPa, which is significantly smaller than the pressure condition in the majority of experiments found in the existing literature (usually larger than 1 MPa [7, 19, 62, 69–72]). According to the critical pressure characterized by Wang et al. [69] to suppress contact loss, 0.005 MPa is far from sufficient to reverse the process of contact deterioration under the smallest current density of 0.05 mA cm^{-2}. Unfortunately, due to the nonlinearity of the viscoplastic material model and the complexity of the multi-physics coupling, applying a large pressure to the model leads to convergence issues and no effective solution has been found to address this challenge thus far. Nonetheless, insights can still be drawn from these numerical outputs.

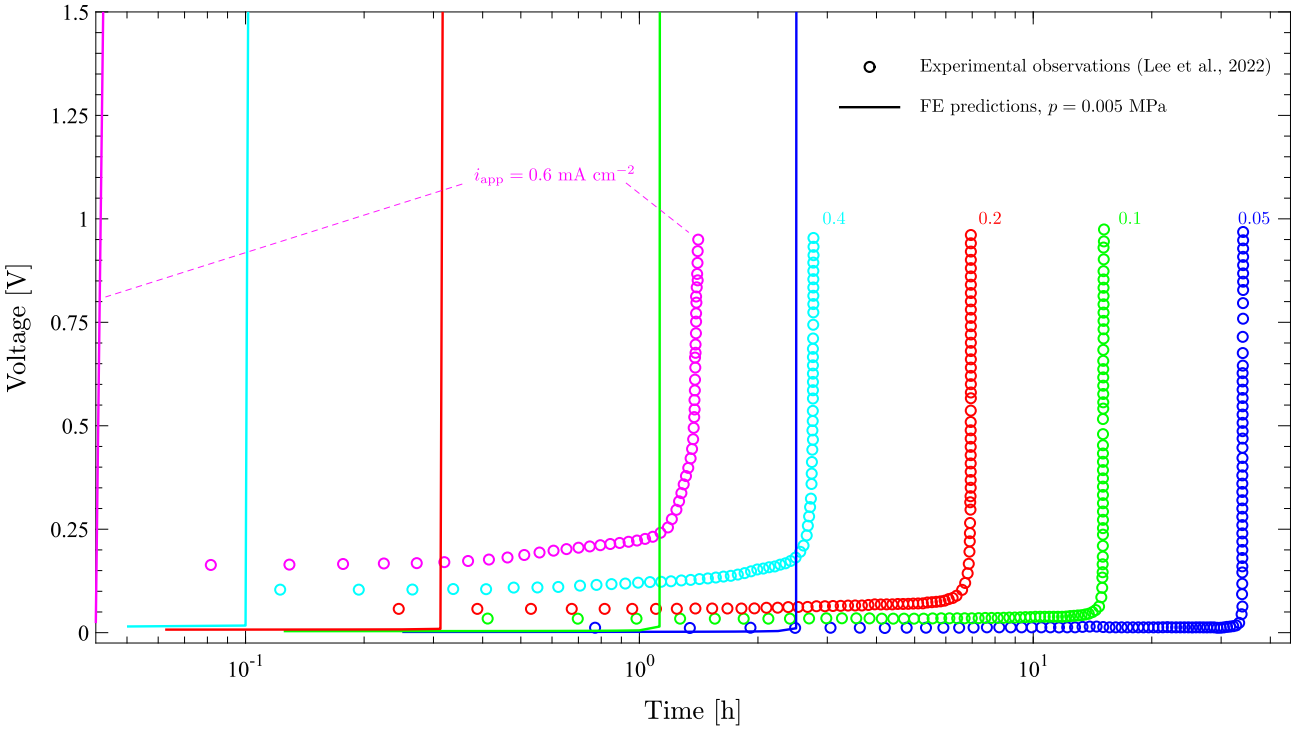


Figure 7.4: Evolution of the cell voltage versus time during stripping considering the creep deformation of the Li metal anode. The FE predictions are depicted by solid lines, with different stripping current densities represented by distinct colours. The circles represent experimental data reported by Lee et al. [22].

It is clearly seen from Fig. 7.4 that the moment t_f in the simulation at which the voltage evolution curve exhibits a sharp increase occurs significantly earlier compared to the experimental observations reported by Lee et al. [22]. The insufficient pressure applied in the model is primarily responsible for this discrepancy. This consolidates experimental findings, which conclude that applying higher pressure improves interfacial contact, refills interfacial voids, and delays the onset of cell failure. In addition, the simulation results show that the cell voltage during the stable phase (before the sharp voltage increase occurs) is lower than their experimental counterparts. This is because the model only

considers the interfacial charge transfer resistance while ignoring the interfacial film resistance (e.g., resistance induced by SEI) and the diffusion impedance controlled by ion concentration. Furthermore, due to the limited size of the model, only a small portion of the SE thickness is considered. This leads to a significantly smaller bulk resistance of the SE compared to the actual circumstances. Consequently, the cell's internal resistance in the simulation is smaller than in reality, resulting in a low voltage.

7.2.2 Results Considering Elastic Deformation of the Li Metal Anode

Given the unsolvable convergence issues that arise when assigning a viscoplastic material model to the lithium metal anode and applying the necessary pressure, a simplified model is employed in this section. Only the linear elastic component of the constitutive relations for lithium is retained and the same pressure (5.6 MPa) used in the experiments by Lee et al. [22] is applied.

An empirical relation is adopted between the phase field interface kinetics coefficient L and the applied stripping current density i_{app}. This relation is acquired through a power-law fit of different L values. For each stripping current density, there is an optimal L value such that the simulation result could best match the corresponding experimental data. The relation reads

$$L = L_0 \left(\frac{i_{\mathrm{app}}}{i_{\mathrm{r}}} \right)^{\Theta}, \tag{7.12}$$

where $L_0 = 2.7 \times 10^{-11}\ \mathrm{m^2\,N^{-1}\,s^{-1}}$ is a pre-factor, $i_{\mathrm{r}} = 0.05\ \mathrm{mA\,cm^{-2}}$ is a reference current density, and $\Theta = 0.87$ is the power-law exponent. A connection between the current density and the mobility coefficient has been exploited and rationalised in phase field models for corrosion [82, 141]. However, it is acknowledged that this relation is developed for a solid-liquid interface suitable for corrosion problems, its validity towards a typical solid-solid or solid-air interface in SSB simulations still requires further investigation.

Table 7.1 lists the selected L values that exhibit the best match to the experiment, and Fig. 7.5 illustrate the power-law fitting that defined the empirical relation in Eq. (7.12). In addition, the diffusion coefficient was taken to be $D_{\mathrm{eff}} = 1.53 \times 10^{-13}\ \mathrm{m^2\,s^{-1}}$, to improve the correlation.

Table 7.1: Selected values of the phase field interface kinetics coefficient L for different i_{app}

i_{app} [mA cm^{-2}]	L [m^2 N^{-1} s^{-1}]
0.05	3.2×10^{-11}
0.1	7×10^{-11}
0.2	9.35×10^{-11}
0.4	1.7×10^{-10}
0.6	2.78×10^{-10}

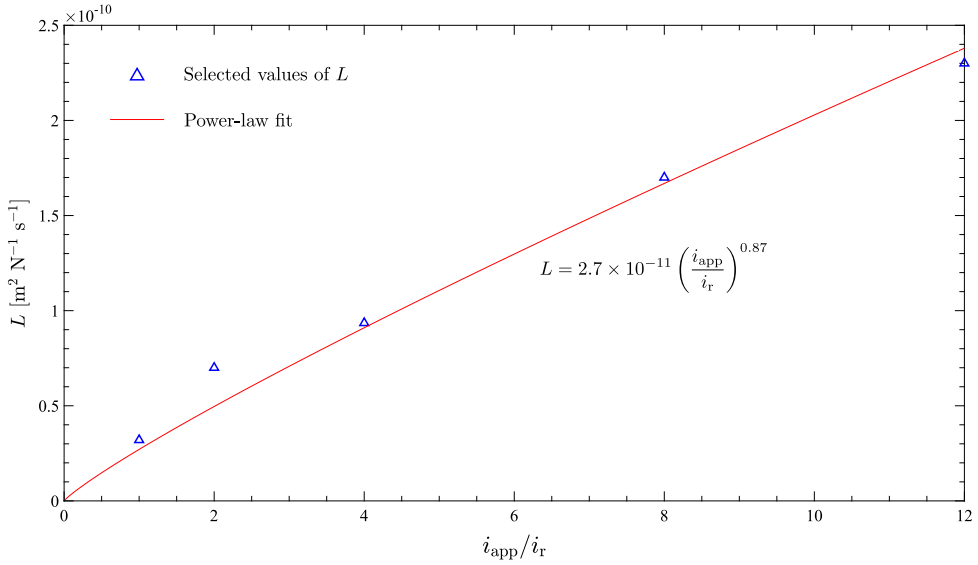


Figure 7.5: An illustration of the power-law fit between L and $i_{\text{app}}/i_{\text{r}}$.

A numerical technique to constrain the value of Li occupancy θ_{m} in the void area is enforced in the electrode domain such that

$$\theta_{\text{m}} = \begin{cases} \theta_{\text{m}}^0 & \text{if } \xi \leq 0.05, \\ \theta_{\text{m}} & \text{otherwise.} \end{cases} \tag{7.13}$$

Note that this technique introduced here is to improve the stability of the model. Recall Eq. (4.12) that $\theta_{\text{m}} = \text{const}$ in the void V^{v} and the fact that the observed variation of θ_{m} in the bulk is less significant than that of ξ (see Section 4.2.1), adopting this technique that forces θ_{m} in the newly formed void area to also be θ_{m}^0 could enhance the stability of the model while not affecting the qualitative results to a large extent, given the fact that the case study implemented in this section is experimental and exploratory in nature.

There are no convergence issues after treating the Li anode as pure elastic. Hence, a large pressure of 5.6 MPa can be applied to the model. Good consistency with the experiment can be acquired after

implementing the aforementioned choices of L, D_{eff} and θ_{m}. The outcome is illustrated in Fig. 7.6.

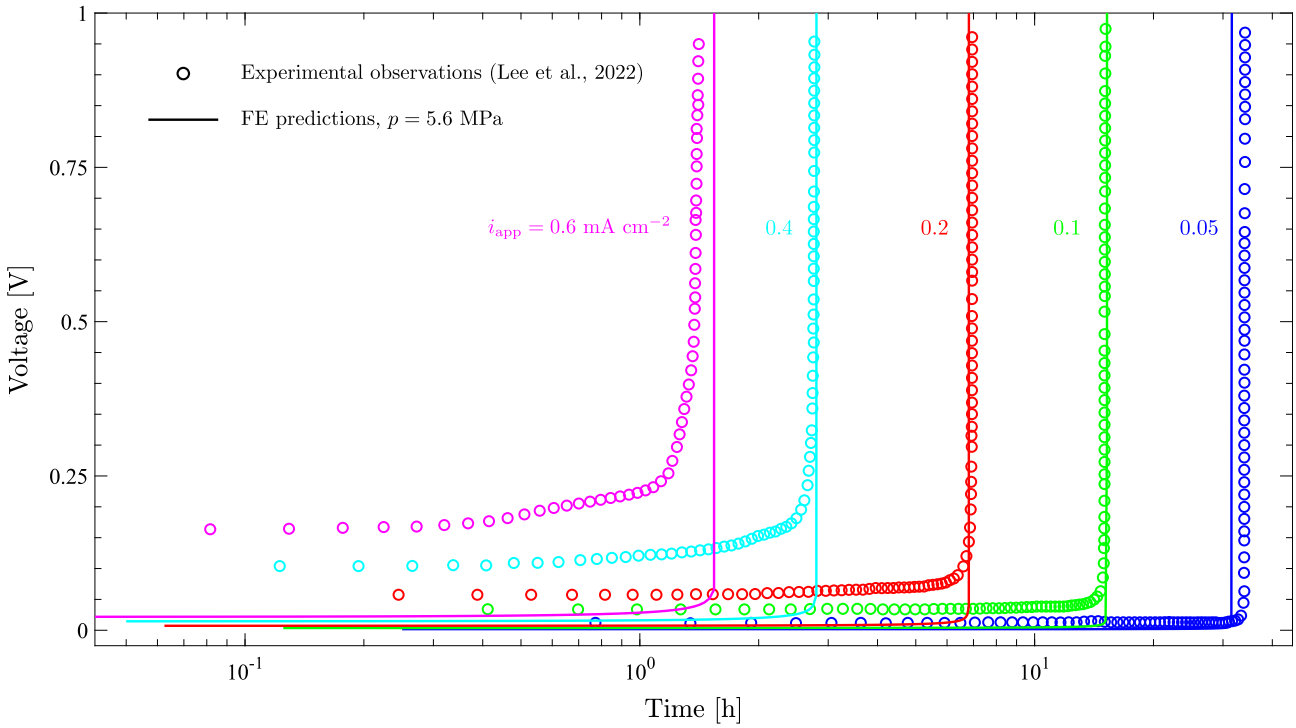


Figure 7.6: Evolution of the cell voltage versus time during stripping considering the elastic deformation of the Li metal anode. The FE predictions are depicted by solid lines, with different stripping current densities represented by distinct colours. The circles represent experimental data reported by Lee et al. [22].

The following Fig. 7.7a and b are the contour output of the final morphology of the void and their precise locations. Compared with the SEM images (Figs. 7.7c and d) reported by Lee et al. [22] of the Li anode after stripping at current densities of 0.1 and 0.4 mA cm^{-2}, it is noted that there is a clear difference. The experimental results of Lee et al. [22] showed that a higher stripping current density leads to a smaller final profile of the void, consistent with the conclusion drawn by Lu et al. [23]. However, the simulation results indicate the opposite, where a higher stripping current density resulted in a larger void after complete interface contact loss happens. A primary reason for this difference is that the elastic material model accommodates a much higher $\boldsymbol{\nabla}^2\sigma_h^{\xi}$ under a large applied pressure compared with those implemented with a creep material model and low pressure (Fig. 7.2), resulting in a boost to the driving force for the phase field interface evolution. The outcome indicates that a good agreement with the experiments at the macroscopic level (Fig. 7.6) does not necessarily imply good consistency at the microscopic level, and also highlights the importance of incorporating the creep deformation of Li for simulations of this kind.

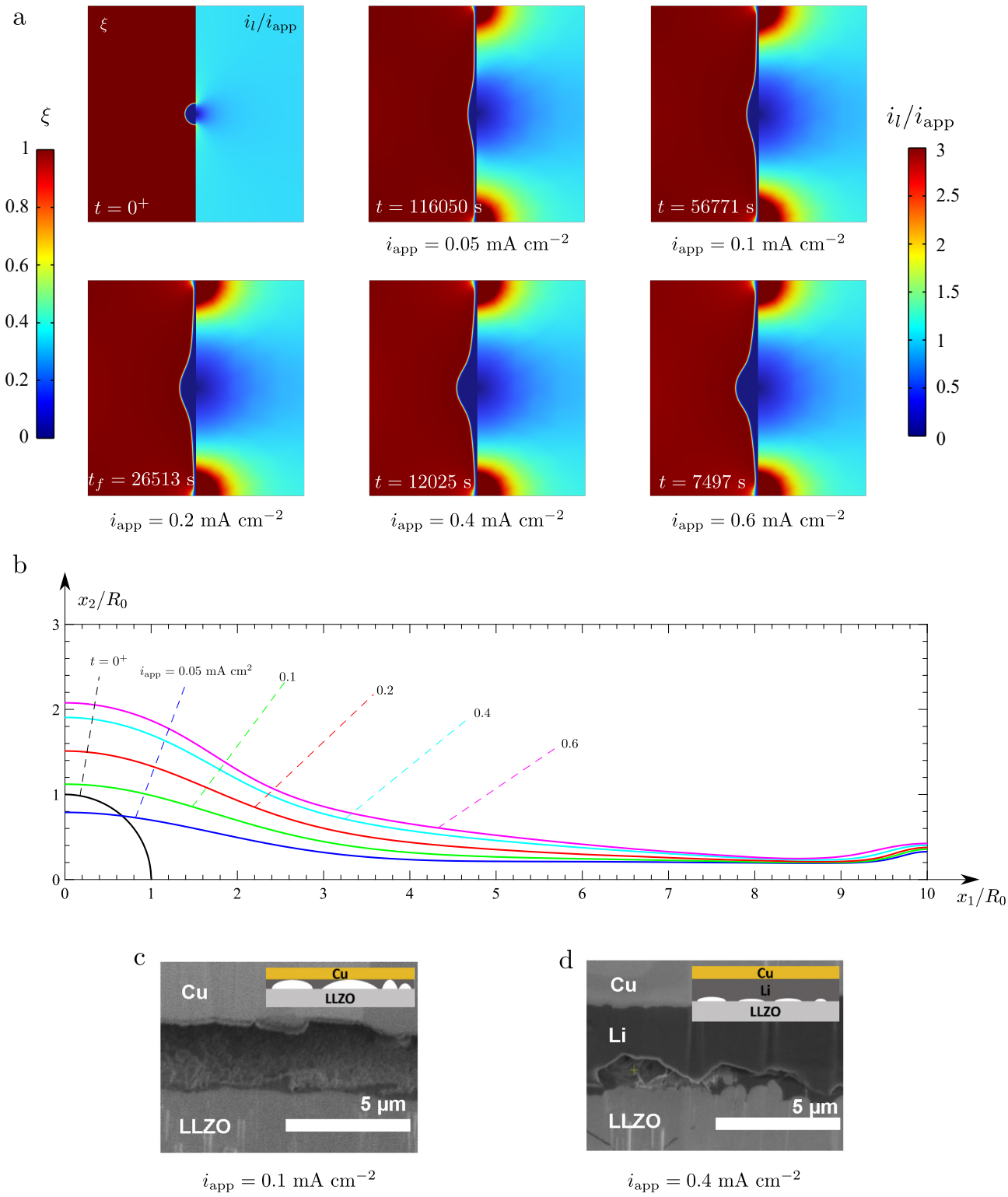


Figure 7.7: a) Numerical contours of the final moment before complete interfacial contact loss happen under different stripping current densities and constant pressure of $p = 5.6$ MPa. A linear elastic material model is adopted for the Li metal anode. $t = 0^+$ is the communal initial state for all current density cases. b) The precise locations of the void interface (represented by $\xi = 0.5$) for those shown in a). c) and d) SEM images and sketch (top right illustration) of the Cu substrate, Li anode, and the LLZO after stripping at current densities of 0.1 and 0.4 mA cm^{-2}, respectively [22].

Another validation effort was undertaken. Lu et al. [23] investigated the effect of different stripping

current densities on the nucleation and growth of voids at the Li/SE interface. They reported the reduction of the active area ratio for each current density as a measurement of interface contact loss, with the cell failing when it reaches zero. The data were extracted, and the model's conditions were aligned with those of the experiment and conducted calculations. The outcomes are illustrated in Fig. 7.8, and a good consistency is acquired.

A similar method to that used in deriving Eq. 7.12 is employed here, such that

$$L = L_0 \frac{i_{\text{app}}}{i_{\text{r}}}, \tag{7.14}$$

where $L_0 = 8 \times 10^{-11}\ \text{m}^2\,\text{N}^{-1}\,\text{s}^{-1}$, and $i_{\text{r}} = 2\ \text{mA}\,\text{cm}^{-2}$. Numerically, the active area in the simulation is defined as the regions with $\xi \geq 0.99$.

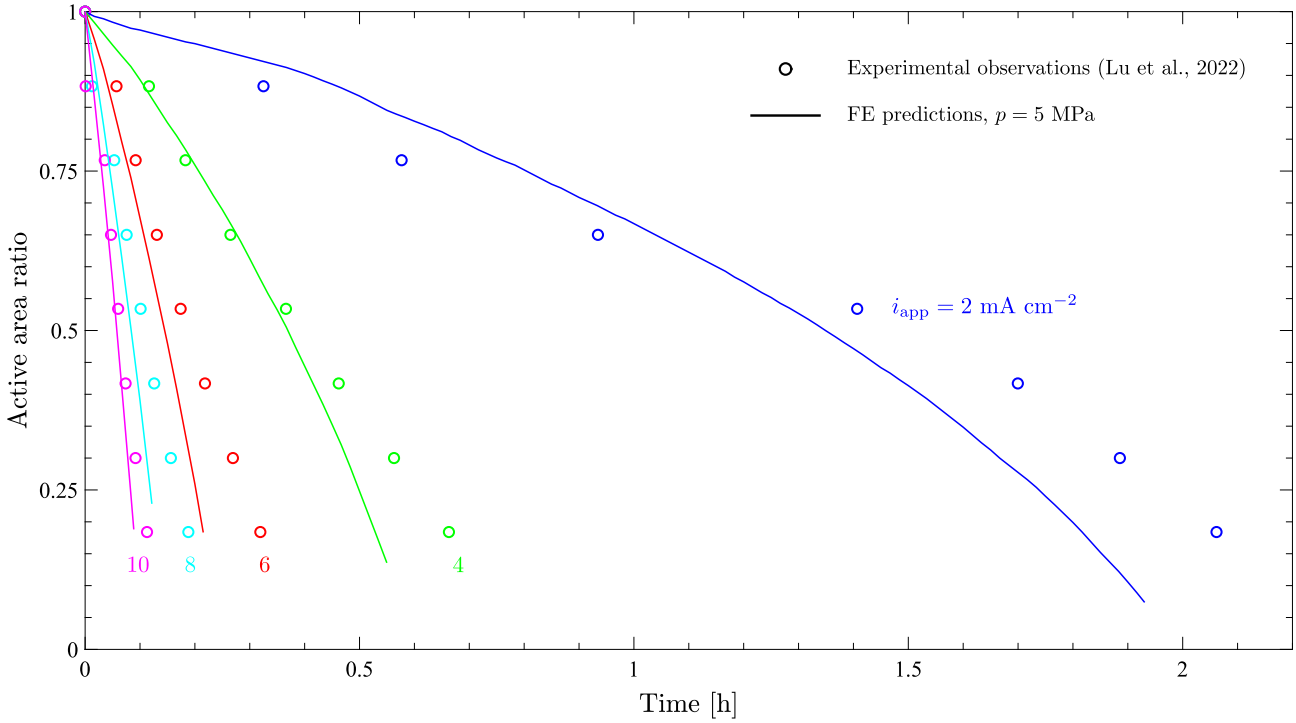


Figure 7.8: The reduction of the active area ratio of the interface as stripping proceeds for different current densities under an applied pressure of 5 MPa. The solid lines are the simulation outputs, and the circles are experimental data reported by Lu et al. [23].

7.3 Summary

In this chapter, numerical experiments were conducted focusing on the stripping process and interfacial contact loss to validate the model's capabilities for quantitative prediction. The simulation results were rigorously compared with experimental data, and detailed discussions of the outcomes were presented.

Unfortunately, it is concluded that the current model framework lacks precise quantitative analytical capabilities due primarily to its inability to resolve challenges associated with large stack pressures and significant deformations–obstacles that are hard to bypass for a constructive study.

Despite these limitations, the model successfully predicted the evolutionary trend of void size and distribution in response to variations in stripping current densities, thereby affirming its utility for qualitative analysis. On this basis, although the model is not yet capable of producing accurate absolute quantitative predictions, it demonstrates potential for making correct relative or indicative quantitative predictions focusing on changes at the interface within a very short period after the initiation of each cycle.

Chapter 8

Concluding Remarks and Future Works

This PhD thesis aimed at deepening our understanding of the sophisticated multi-coupling mechanisms behind the most challenging obstacles hindering the practicality of SSBs. To achieve commercially viable SSBs, numerous researchers have persistently tackled these tricky issues, resulting in promising progress at the laboratory level. However, even the best experimental results to date still fall short of what is required for SSB commercialization. Problems such as dendrite penetration, material degradation, and low ionic conductivity of SE materials remain unresolved. This is primarily due to the fact that the mechanisms of the coupled electrochemical-mechanical multiphysics processes occurring within SSBs are still not well understood. Modelling and mathematically describing these challenges would help deepen our understanding of these problems. However, modelling attempts to tackle the various issues SSBs face are still in their infancy, and a comprehensive theoretical framework has not yet been fully developed.

Chapter 2 of this work provides a comprehensive review and discussion of the experimental and modelling attempts made in recent years for SSBs. It is then identified that short-circuiting caused by dendrite penetration constitutes the most critical and pressing challenge hindering the practical implementation of SSBs. To deepen the understanding of this problem, a phase field-based, electrochemical-mechanical multi-coupling model is proposed in this study and applied for the first time to the simulation of the dynamic evolution of voids at the electrode/SE interface. The focus on the evolution of interfacial voids stems from the recognition that the primary causative factor for dendrite growth is the uneven distribution of interfacial current density. This uneven distribution results from inhomogeneous interfacial contact and the local accumulation or depletion of electrode-active materials during battery cycling. Understanding the evolution mechanism of interfacial contact loss, i.e., the

growth of interfacial voids, will aid in finding ways to suppress them, thereby curbing the formation of dendrites before they nucleate.

The model involves coupling between multiple physical fields, including mechanics, electrochemistry, and phase field methods. The fundamental theories related to these physics fields are summarized in detail in Chapter 3, which lays the foundation for the subsequent construction of the coupled multiphysics model. In Chapter 4, the model is constructed, and the derivation process is given. Compared with the models and numerical methods in the existing literature, the model built in this study introduces several innovative enhancements:

1. By introducing an auxiliary phase field order parameter, a continuous energy description in the electrode domain containing the electrode metal and the void is achieved. The phase field order parameter is assigned values of 1 and 0 within the metal and the void, respectively, and its evolution is defined as the annihilation and nucleation of the metal lattices. The main driving force of its evolution is the change in lithium occupancy controlled by the lithium flux at the Li/SE interface as a result of lithium deposition and dissolution reactions.

2. By introducing an auxiliary phase field order parameter, the dynamic evolution of voids within the metal anode and their resulting current density "hotspots" at the Li/SE interface can be readily tracked in real-time. Previous models in the literature have either neglected the transport of material inside the metal electrode, focusing solely on dendrite growth within the SE without considering the ongoing changes in material transport and interfacial current density distribution [13, 88, 88], or have only been capable of analyzing the effects of interface geometry on interfacial current density distribution and material transport at specific moments in time [12].

3. The Butler-Volmer electrode kinetic equation has been adapted to be coupled with the phase field order parameter, enabling dynamic adjustments to the interfacial charge transfer resistance based on the interfacial contact status.

4. A viscoplastic material model has been integrated into the framework to simulate the creep deformation of lithium metal. It is coupled with the phase field and lithium occupancy changes, enhancing the model's capacity to accurately replicate the mechanical behaviour of lithium metal during battery charging/discharging cycles and under external stack pressure.

After establishing the model framework, the model's qualitative prediction capabilities are verified through several case studies, as presented in Chapters 5 and 6. In Chapter 5, the cyclic processes

of stripping and plating of lithium in the presence of single and multiple voids at the interface are simulated. The observed outputs of the model, including the enlargement of the voids and their coalesces during the stripping, the occlusion of the voids during the plating, and the flattening of the voids under pressure, are consistent with the experimental results. These findings preliminarily validate the potential of the proposed framework to track morphology changes at the interface dynamically. In Chapter 6, in collaboration with experimental colleagues from GeorgiaTech, the model is employed to substantiate their proposed mechanism for accelerated short-circuit phenomena in anode-free SSBs. These case studies not only validated the effectiveness of the model but also yielded several insightful conclusions:

1. Expansion of voids during stripping is a self-enhancing process. The presence of voids leads to the formation of current density hotspots near the edges of the voids. The current densities in these hotspot regions are significantly higher than those far away, promoting a higher rate of local lithium dissolution and stimulating the expansion of the voids during stripping. This expansion exacerbates the current constriction, further accelerating the expansion of voids and leading to excess lithium deposition in hotspot regions in the subsequent plating cycle, which becomes the origin of dendrite nucleation and growth.

2. The severity of the current density constriction phenomenon is positively correlated with the size of the voids while the absolute magnitude of its peak is controlled by the applied current density. According to the theory of Kasemchainan et al. [62], void nucleation is related to the disruption of the dynamic equilibrium of electrode-active materials at the interface. When the replenishment rate at the interface is slower than the depletion rate, void nucleation and growth commence. Given the self-enhancing nature of void expansion, it can be inferred that without external intervention, cell failure is almost inevitable once the initial size of the voids at the interface or the applied current density exceeds a critical threshold.

3. Applying stack pressure can significantly inhibit the growth of voids, as experimental observations show that the loss of interfacial contact due to void growth can be reversed when the applied stack pressure is sufficiently high. In this process, the creep deformation of lithium under pressure plays a more important role than lithium self-diffusion in mitigating void growth.

4. Even in the absence of significant voids at the interface, interfacial undulations still lead to non-uniform lithium dissolution and deposition during cycling. This non-uniformity allows for

localized lithium depletion and the formation of isolated lithium in non-excessive Li-metal anodes, leading to rapid cell failure in subsequent cycles.

In Chapter 7, an attempt to validate the quantitative prediction capabilities of the model through calibration of the parameters and limited adjustment to the formulation, and reproduce the voltage jumps observed in stripping experiments is conducted. Success in this attempt would allow us to confidently extend the existing framework to encompass additional mechanisms and implement more comprehensive studies, targeting accurate predictions on interfacial morphological changes, contact loss and lithium dendrite growth. Ideally, the ultimate goal of this framework is to provide predictions for critical values such as critical stripping current densities that lead to void expansion, critical plating current densities conducive to dendrite growth, and the minimum stack pressure required to inhibit void growth and dendrite formation. Unfortunately, however, the framework developed in Chapters 4, 5, and 6 is not yet capable of providing quantitative agreement across all the regimes of interest. Owing to the complexity of the multi-coupling problem and the significant nonlinearity of the viscoplastic model, the framework struggles to achieve convergence under the necessary applied pressures which are required to ensure that the battery does not fail immediately after the commencement of the cycle in experiments. Consequently, the validity of the model's quantitative analysis remains an aspect of future work. Despite these challenges, the validity of the model's qualitative predictions has been verified, and the model's strong capacity for dynamically tracking changes in interfacial morphology, facilitated by the introduction of the phase field approach, is undeniable.

Future work could explore adjustments and modification strategies to the current modelling approach. One potential direction is to conceptualize lithium metal as an incompressible viscous fluid and assess the morphological changes and resulting stresses at the interface when subjected to compression, utilizing fluid-structure interaction (FSI) theory. For instance, Yan et al. [72] effectively explored the impact of pressure on pre-existing voids at the interface of lithium subjected to compressive creep using this methodology. However, their approach did not incorporate the phase field method, thus it did not possess the ability to capture or trace the dynamically changing morphology of the voids during cycling. The FSI theory involves the Arbitrary Lagrangian-Eulerian (ALE) method, which could provide enhanced flexibility in modelling lithium metal deformation that is akin to fluid flow under compressive conditions. Under this method, lithium metal domains would be treated as fluids, whereas ceramic solid electrolytes, with their higher Young's modulus, would be modelled as solids.

In conclusion, the modelling framework proposed in this study is groundbreaking in tracking

the dynamic changes in interface morphology during SSB cycling. Since such dynamic changes are difficult to observe in real-time in experiments, the model can play a critical role in deepening our understanding of the interface evolution mechanism. Nonetheless, it is acknowledged that the current model exhibits some critical limitations that require further optimization and improvement in future research endeavours.

References

[1] J.-M. Tarascon and M. Armand. Issues and challenges facing rechargeable lithium batteries. *Nature*, 414(6861):359–367, 11 2001.

[2] International Energy Agency. Global EV Outlook 2023. Technical report, International Energy Agency, Paris, 2023.

[3] R. Chen, Q. Li, X. Yu, L. Chen, and H. Li. Approaching Practically Accessible Solid-State Batteries: Stability Issues Related to Solid Electrolytes and Interfaces. *Chemical Reviews*, 120 (14):6820–6877, 7 2020.

[4] Z. Wan, D. Lei, W. Yang, C. Liu, K. Shi, X. Hao, L. Shen, W. Lv, B. Li, Q. Yang, F. Kang, and Y. He. Low Resistance–Integrated All-Solid-State Battery Achieved by Li 7 La 3 Zr 2 O 12 Nanowire Upgrading Polyethylene Oxide (PEO) Composite Electrolyte and PEO Cathode Binder. *Advanced Functional Materials*, 29(1):1–10, 1 2019.

[5] A. Sharafi, E. Kazyak, A. L. Davis, S. Yu, T. Thompson, D. J. Siegel, N. P. Dasgupta, and J. Sakamoto. Surface Chemistry Mechanism of Ultra-Low Interfacial Resistance in the Solid-State Electrolyte Li7La3Zr2O12. *Chemistry of Materials*, 29(18):7961–7968, 2017.

[6] A. Kato, A. Hayashi, and M. Tatsumisago. Enhancing utilization of lithium metal electrodes in all-solid-state batteries by interface modification with gold thin films. *Journal of Power Sources*, 309:27–32, 2016.

[7] J. Doux, H. Nguyen, D. H. S. Tan, A. Banerjee, X. Wang, E. A. Wu, C. Jo, H. Yang, and Y. S. Meng. Stack Pressure Considerations for Room-Temperature All-Solid-State Lithium Metal Batteries. *Advanced Energy Materials*, 10(1), 1 2020.

[8] C. Monroe and J. Newman. The Impact of Elastic Deformation on Deposition Kinetics at Lithium/Polymer Interfaces. *Journal of The Electrochemical Society*, 152(2):A396, 2005.

[9] S. Shishvan, N. Fleck, R. McMeeking, and V. Deshpande. Dendrites as climbing dislocations in ceramic electrolytes: Initiation of growth. *Journal of Power Sources*, 456(March):227989, 4 2020.

[10] W. Guo, F. Shen, J. Liu, Q. Zhang, H. Guo, Y. Yin, J. Gao, Z. Sun, X. Han, and Y. Hu. In-situ optical observation of Li growth in garnet-type solid state electrolyte. *Energy Storage Materials*, 41(March):791–797, 10 2021.

[11] Z. Ning, G. Li, D. L. R. Melvin, Y. Chen, J. Bu, D. Spencer-Jolly, J. Liu, B. Hu, X. Gao, J. Perera, C. Gong, S. D. Pu, S. Zhang, B. Liu, G. O. Hartley, A. J. Bodey, R. I. Todd, P. S. Grant, D. E. J. Armstrong, T. J. Marrow, C. W. Monroe, and P. G. Bruce. Dendrite initiation and propagation in lithium metal solid-state batteries. *Nature*, 618(7964):287–293, 6 2023.

[12] S. S. Shishvan, N. A. Fleck, and V. S. Deshpande. The initiation of void growth during stripping of Li electrodes in solid electrolyte cells. *Journal of Power Sources*, 488(December 2020):229437, 3 2021.

[13] L. Chen, H. W. Zhang, L. Y. Liang, Z. Liu, Y. Qi, P. Lu, J. Chen, and L.-Q. Chen. Modulation of dendritic patterns during electrodeposition: A nonlinear phase-field model. *Journal of Power Sources*, 300:376–385, 12 2015.

[14] C. Miehe, H. Dal, L. Schänzel, and A. Raina. A phase-field model for chemo-mechanical induced fracture in lithium-ion battery electrode particles. *International Journal for Numerical Methods in Engineering*, 106(9):683–711, 6 2016.

[15] C. Yuan, X. Gao, Y. Jia, W. Zhang, Q. Wu, and J. Xu. Coupled crack propagation and dendrite growth in solid electrolyte of all-solid-state battery. *Nano Energy*, 86(January):106057, 8 2021.

[16] D. Bistri and C. V. Di Leo. A continuum electro-chemo-mechanical gradient theory coupled with damage: Application to Li-metal filament growth in all-solid-state batteries. *Journal of the Mechanics and Physics of Solids*, 174(February):105252, 5 2023.

[17] P. Atkins, J. d. Paula, and J. Keeler. *Atkins' physical chemistry*. Oxford University Press, New York, 11th edition, 2018.

[18] I. Baccouche, S. Jemmali, B. Manai, N. Omar, and N. Amara. Improved OCV Model of a Li-Ion NMC Battery for Online SOC Estimation Using the Extended Kalman Filter. *Energies*, 10(6): 764, 5 2017.

[19] D. Spencer Jolly, Z. Ning, J. E. Darnbrough, J. Kasemchainan, G. O. Hartley, P. Adamson, D. E. J. Armstrong, J. Marrow, and P. G. Bruce. Sodium/Na β" Alumina Interface: Effect of Pressure on Voids. *ACS Applied Materials & Interfaces*, 12(1):678–685, 1 2020.

[20] W. S. LePage, Y. Chen, E. Kazyak, K.-H. Chen, A. J. Sanchez, A. Poli, E. M. Arruda, M. D. Thouless, and N. P. Dasgupta. Lithium Mechanics: Roles of Strain Rate and Temperature and Implications for Lithium Metal Batteries. *Journal of The Electrochemical Society*, 166(2): A89–A97, 1 2019.

[21] J. A. Lewis, S. E. Sandoval, Y. Liu, D. L. Nelson, S. G. Yoon, R. Wang, Y. Zhao, M. Tian, P. Shevchenko, E. Martínez-Pañeda, and M. T. McDowell. Accelerated Short Circuiting in Anode-Free Solid-State Batteries Driven by Local Lithium Depletion. *Advanced Energy Materials*, 13(12):2204186, 2023.

[22] K. Lee, E. Kazyak, M. J. Wang, N. P. Dasgupta, and J. Sakamoto. Analyzing void formation and rewetting of thin in situ-formed Li anodes on LLZO. *Joule*, 6(11):2547–2565, 11 2022.

[23] Y. Lu, C.-Z. Zhao, J.-K. Hu, S. Sun, H. Yuan, Z.-H. Fu, X. Chen, J.-Q. Huang, M. Ouyang, and Q. Zhang. The void formation behaviors in working solid-state Li metal batteries. *Science Advances*, 8(45):1–13, 11 2022.

[24] J. Janek and W. G. Zeier. A solid future for battery development. *Nature Energy*, 1(9):16141, 9 2016.

[25] M. V. Reddy, A. Mauger, C. M. Julien, A. Paolella, and K. Zaghib. Brief History of Early Lithium-Battery Development. *Materials*, 13(8):1884, 4 2020.

[26] M. Lazzari and B. Scrosati. A Cyclable Lithium Organic Electrolyte Cell Based on Two Intercalation Electrodes. *Journal of The Electrochemical Society*, 127(3):773–774, 3 1980.

[27] D. Murphy, F. Di Salvo, J. Carides, and J. Waszczak. Topochemical reactions of rutile related structures with lithium. *Materials Research Bulletin*, 13(12):1395–1402, 12 1978.

[28] M. Li, J. Lu, Z. Chen, and K. Amine. 30 Years of Lithium-Ion Batteries. *Advanced Materials*, 30 (33):1–24, 8 2018.

[29] J. Janek and W. G. Zeier. Challenges in speeding up solid-state battery development. *Nature Energy*, 8(3):230–240, 2 2023.

[30] S. Randau, D. A. Weber, O. Kötz, R. Koerver, P. Braun, A. Weber, E. Ivers-Tiffée, T. Adermann, J. Kulisch, W. G. Zeier, F. H. Richter, and J. Janek. Benchmarking the performance of all-solid-state lithium batteries. *Nature Energy*, 5(3):259–270, 3 2020.

[31] N. Kamaya, K. Homma, Y. Yamakawa, M. Hirayama, R. Kanno, M. Yonemura, T. Kamiyama, Y. Kato, S. Hama, K. Kawamoto, and A. Mitsui. A lithium superionic conductor. *Nature Materials*, 10(9):682–686, 9 2011.

[32] M. Pasta, D. Armstrong, Z. L. Brown, J. Bu, M. R. Castell, P. Chen, A. Cocks, S. A. Corr, E. J. Cussen, E. Darnbrough, V. Deshpande, C. Doerrer, M. S. Dyer, H. El-Shinawi, N. Fleck, P. Grant, G. L. Gregory, C. Grovenor, L. J. Hardwick, J. T. S. Irvine, H. J. Lee, G. Li, E. Liberti, I. McClelland, C. Monroe, P. D. Nellist, P. R. Shearing, E. Shoko, W. Song, D. S. Jolly, C. I. Thomas, S. J. Turrell, M. Vestli, C. K. Williams, Y. Zhou, and P. G. Bruce. 2020 roadmap on solid-state batteries. *Journal of Physics: Energy*, 2(3):032008, 7 2020.

[33] J. Betz, G. Bieker, P. Meister, T. Placke, M. Winter, and R. Schmuch. Theoretical versus Practical Energy: A Plea for More Transparency in the Energy Calculation of Different Rechargeable Battery Systems. *Advanced Energy Materials*, 9(6):1–18, 2019.

[34] L. Hu, J. Wang, K. Wang, Z. Gu, Z. Xi, H. Li, F. Chen, Y. Wang, Z. Li, and C. Ma. A cost-effective, ionically conductive and compressible oxychloride solid-state electrolyte for stable all-solid-state lithium-based batteries. *Nature Communications*, 14(1):3807, 6 2023.

[35] J. Goodenough, H.-P. Hong, and J. Kafalas. Fast Na+-ion transport in skeleton structures. *Materials Research Bulletin*, 11(2):203–220, 2 1976.

[36] P. G. Bruce and A. R. West. The A-C Conductivity of Polycrystalline LISICON, Li2 + 2x Zn1 - x GeO4, and a Model for Intergranular Constriction Resistances. *Journal of The Electrochemical Society*, 130(3):662–669, 3 1983.

[37] Y. Meesala, A. Jena, H. Chang, and R.-S. Liu. Recent Advancements in Li-Ion Conductors for All-Solid-State Li-Ion Batteries. *ACS Energy Letters*, 2(12):2734–2751, 12 2017.

[38] Y. Inaguma, C. Liquan, M. Itoh, T. Nakamura, T. Uchida, H. Ikuta, and M. Wakihara. High ionic conductivity in lithium lanthanum titanate. *Solid State Communications*, 86(10):689–693, 6 1993.

[39] R. Murugan, V. Thangadurai, and W. Weppner. Fast Lithium Ion Conduction in Garnet-Type Li 7 La 3 Zr 2 O 12. *Angewandte Chemie International Edition*, 46(41):7778–7781, 10 2007.

[40] Y. Kato, S. Hori, T. Saito, K. Suzuki, M. Hirayama, A. Mitsui, M. Yonemura, H. Iba, and R. Kanno. High-power all-solid-state batteries using sulfide superionic conductors. *Nature Energy*, 1(4):16030, 3 2016.

[41] M. A. Kraft, S. Ohno, T. Zinkevich, R. Koerver, S. P. Culver, T. Fuchs, A. Senyshyn, S. Indris, B. J. Morgan, and W. G. Zeier. Inducing High Ionic Conductivity in the Lithium Superionic Argyrodites Li 6+ x P 1– x Ge x S 5 I for All-Solid-State Batteries. *Journal of the American Chemical Society*, 140(47):16330–16339, 11 2018.

[42] S. Lou, F. Zhang, C. Fu, M. Chen, Y. Ma, G. Yin, and J. Wang. Interface Issues and Challenges in All-Solid-State Batteries: Lithium, Sodium, and Beyond. *Advanced Materials*, 33(6):1–29, 2 2021.

[43] T. Asano, A. Sakai, S. Ouchi, M. Sakaida, A. Miyazaki, and S. Hasegawa. Solid Halide Electrolytes with High Lithium-Ion Conductivity for Application in 4 V Class Bulk-Type All-Solid-State Batteries. *Advanced Materials*, 30(44):1–7, 2018.

[44] X. Li, J. Liang, J. Luo, M. Norouzi Banis, C. Wang, W. Li, S. Deng, C. Yu, F. Zhao, Y. Hu, T.-K. Sham, L. Zhang, S. Zhao, S. Lu, H. Huang, R. Li, K. R. Adair, and X. Sun. Air-stable Li 3 InCl 6 electrolyte with high voltage compatibility for all-solid-state batteries. *Energy & Environmental Science*, 12(9):2665–2671, 2019.

[45] X. Li, J. Liang, N. Chen, J. Luo, K. R. Adair, C. Wang, M. N. Banis, T. K. Sham, L. Zhang, S. Zhao, S. Lu, H. Huang, R. Li, and X. Sun. Water-Mediated Synthesis of a Superionic Halide Solid Electrolyte. *Angewandte Chemie - International Edition*, 58(46):16427–16432, 2019.

[46] N. Wu, P. Chien, Y. Qian, Y. Li, H. Xu, N. S. Grundish, B. Xu, H. Jin, Y. Hu, G. Yu, and J. B. Goodenough. Enhanced Surface Interactions Enable Fast Li + Conduction in Oxide/Polymer Composite Electrolyte. *Angewandte Chemie International Edition*, 59(10):4131–4137, 3 2020.

[47] R. Fang, B. Xu, N. S. Grundish, Y. Xia, Y. Li, C. Lu, Y. Liu, N. Wu, and J. B. Goodenough. Li2S6-Integrated PEO-Based Polymer Electrolytes for All-Solid-State Lithium-Metal Batteries. *Angewandte Chemie - International Edition*, 60(32):17701–17706, 2021.

[48] M. TACHEZ, J. MALUGANI, R. MERCIER, and G. ROBERT. Ionic conductivity of and phase transition in lithium thiophosphate Li3PS4. *Solid State Ionics*, 14(3):181–185, 11 1984.

[49] P. Albertus, S. Babinec, S. Litzelman, and A. Newman. Status and challenges in enabling the lithium metal electrode for high-energy and low-cost rechargeable batteries. *Nature Energy*, 3(1): 16–21, 12 2017.

[50] Z. Luo, X. Qiu, C. Liu, S. Li, C. Wang, G. Zou, H. Hou, and X. Ji. Interfacial challenges towards stable Li metal anode. *Nano Energy*, 79:105507, 1 2021.

[51] B. S. Vishnugopi, E. Kazyak, J. A. Lewis, J. Nanda, M. T. McDowell, N. P. Dasgupta, and P. P. Mukherjee. Challenges and Opportunities for Fast Charging of Solid-State Lithium Metal Batteries. *ACS Energy Letters*, 6(10):3734–3749, 10 2021.

[52] X. Zhu, K. Wang, Y. Xu, G. Zhang, S. Li, C. Li, X. Zhang, X. Sun, X. Ge, and Y. Ma. Strategies to Boost Ionic Conductivity and Interface Compatibility of Inorganic - Organic Solid Composite Electrolytes. *Energy Storage Materials*, 36(December 2020):291–308, 4 2021.

[53] X. Feng, H. Fang, N. Wu, P. Liu, P. Jena, J. Nanda, and D. Mitlin. Review of modification strategies in emerging inorganic solid-state electrolytes for lithium, sodium, and potassium batteries. *Joule*, 6(3):543–587, 3 2022.

[54] Y. Li, J. Cheng, J. Li, Z. Zeng, Y. Guo, H. Zhang, H. Liu, X. Xu, Y. Rao, D. Li, and L. Ci. Indium doped sulfide solid electrolyte with tamed lithium dendrite and improved ionic conductivity for all-solid-state battery applications. *Journal of Power Sources*, 542(April):231794, 9 2022.

[55] V. Thangadurai, S. Narayanan, and D. Pinzaru. Garnet-type solid-state fast Li ion conductors for Li batteries: critical review. *Chemical Society Reviews*, 43(13):4714, 2014.

[56] S. Skaarup, K. West, and B. Zachau-Christiansen. Mixed phase solid electrolytes. *Solid State Ionics*, 28-30(PART 2):975–978, 9 1988.

[57] S. Chen, D. Xie, G. Liu, J. P. Mwizerwa, Q. Zhang, Y. Zhao, X. Xu, and X. Yao. Sulfide solid electrolytes for all-solid-state lithium batteries: Structure, conductivity, stability and application. *Energy Storage Materials*, 14(December 2017):58–74, 9 2018.

[58] Z. D. Hood, H. Wang, Y. Li, A. S. Pandian, M. Parans Paranthaman, and C. Liang. The “filler

effect": A study of solid oxide fillers with β-Li3PS4 for lithium conducting electrolytes. *Solid State Ionics*, 283:75–80, 12 2015.

[59] L. Cheng, E. J. Crumlin, W. Chen, R. Qiao, H. Hou, S. Franz Lux, V. Zorba, R. Russo, R. Kostecki, Z. Liu, K. Persson, W. Yang, J. Cabana, T. Richardson, G. Chen, and M. Doeff. The origin of high electrolyte–electrode interfacial resistances in lithium cells containing garnet type solid electrolytes. *Phys. Chem. Chem. Phys.*, 16(34):18294–18300, 2014.

[60] J. A. Lewis, F. J. Q. Cortes, Y. Liu, J. C. Miers, A. Verma, B. S. Vishnugopi, J. Tippens, D. Prakash, T. S. Marchese, S. Y. Han, C. Lee, P. P. Shetty, H.-W. Lee, P. Shevchenko, F. De Carlo, C. Saldana, P. P. Mukherjee, and M. T. McDowell. Linking void and interphase evolution to electrochemistry in solid-state batteries using operando X-ray tomography. *Nature Materials*, 20(4):503–510, 4 2021.

[61] V. Raj, V. Venturi, V. R. Kankanallu, B. Kuiri, V. Viswanathan, and N. P. B. Aetukuri. Direct correlation between void formation and lithium dendrite growth in solid-state electrolytes with interlayers. *Nature Materials*, 21(9):1050–1056, 9 2022.

[62] J. Kasemchainan, S. Zekoll, D. Spencer Jolly, Z. Ning, G. O. Hartley, J. Marrow, and P. G. Bruce. Critical stripping current leads to dendrite formation on plating in lithium anode solid electrolyte cells. *Nature Materials*, 18(10):1105–1111, 10 2019.

[63] B. S. Vishnugopi, K. G. Naik, H. Kawakami, N. Ikeda, Y. Mizuno, R. Iwamura, T. Kotaka, K. Aotani, Y. Tabuchi, and P. P. Mukherjee. Asymmetric Contact Loss Dynamics during Plating and Stripping in Solid-State Batteries. *Advanced Energy Materials*, 13(8), 2 2023.

[64] C. T. Yang and Y. Qi. Maintaining a Flat Li Surface during the Li Stripping Process via Interface Design. *Chemistry of Materials*, 33(8):2814–2823, 2021.

[65] B. Kinzer, A. L. Davis, T. Krauskopf, H. Hartmann, W. S. LePage, E. Kazyak, J. Janek, N. P. Dasgupta, and J. Sakamoto. Operando analysis of the molten Li—LLZO interface: Understanding how the physical properties of Li affect the critical current density. *Matter*, 4(6):1947–1961, 2021.

[66] C.-L. Tsai, V. Roddatis, C. V. Chandran, Q. Ma, S. Uhlenbruck, M. Bram, P. Heitjans, and O. Guillon. Li 7 La 3 Zr 2 O 12 Interface Modification for Li Dendrite Prevention. *ACS Applied Materials & Interfaces*, 8(16):10617–10626, 4 2016.

[67] T. Krauskopf, R. Dippel, H. Hartmann, K. Peppler, B. Mogwitz, F. H. Richter, W. G. Zeier, and J. Janek. Lithium-Metal Growth Kinetics on LLZO Garnet-Type Solid Electrolytes. *Joule*, 3(8): 2030–2049, 8 2019.

[68] Y. Shao, H. Wang, Z. Gong, D. Wang, B. Zheng, J. Zhu, Y. Lu, Y.-S. Hu, X. Guo, H. Li, X. Huang, Y. Yang, C.-W. Nan, and L. Chen. Drawing a Soft Interface: An Effective Interfacial Modification Strategy for Garnet-Type Solid-State Li Batteries. *ACS Energy Letters*, 3(6): 1212–1218, 6 2018.

[69] M. J. Wang, R. Choudhury, and J. Sakamoto. Characterizing the Li-Solid-Electrolyte Interface Dynamics as a Function of Stack Pressure and Current Density. *Joule*, 3(9):2165–2178, 9 2019.

[70] J. Sakamoto. More pressure needed. *Nature Energy*, 4(10):827–828, 10 2019.

[71] X. Zhang, Q. J. Wang, K. L. Harrison, S. A. Roberts, and S. J. Harris. Pressure-Driven Interface Evolution in Solid-State Lithium Metal Batteries. *Cell Reports Physical Science*, 1(2):100012, 2020.

[72] H. Yan, K. Tantratian, K. Ellwood, E. T. Harrison, M. Nichols, X. Cui, and L. Chen. How Does the Creep Stress Regulate Void Formation at the Lithium-Solid Electrolyte Interface during Stripping? *Advanced Energy Materials*, 12(2):2102283, 1 2022.

[73] T. Krauskopf, H. Hartmann, W. G. Zeier, and J. Janek. Toward a Fundamental Understanding of the Lithium Metal Anode in Solid-State Batteries—An Electrochemo-Mechanical Study on the Garnet-Type Solid Electrolyte Li 6.25 Al 0.25 La 3 Zr 2 O 12. *ACS Applied Materials & Interfaces*, 11(15):14463–14477, 4 2019.

[74] D. K. Singh, T. Fuchs, C. Krempaszky, B. Mogwitz, S. Burkhardt, F. H. Richter, and J. Janek. Overcoming Anode Instability in Solid-State Batteries through Control of the Lithium Metal Microstructure. *Advanced Functional Materials*, 33(1):2211067, 1 2023.

[75] T. Fuchs, C. G. Haslam, A. C. Moy, C. Lerch, T. Krauskopf, J. Sakamoto, F. H. Richter, and J. Janek. Increasing the Pressure-Free Stripping Capacity of the Lithium Metal Anode in Solid-State-Batteries by Carbon Nanotubes. *Advanced Energy Materials*, 12(26), 7 2022.

[76] Y. Zhao, P. Stein, Y. Bai, M. Al-Siraj, Y. Yang, and B.-X. Xu. A review on modeling of electro-chemo-mechanics in lithium-ion batteries. *Journal of Power Sources*, 413(December 2018): 259–283, 2 2019.

[77] J. Tian, Z. Chen, and Y. Zhao. Review on Modeling for Chemo-mechanical Behavior at Interfaces of All-Solid-State Lithium-Ion Batteries and Beyond, 2022.

[78] C. Monroe and J. Newman. Dendrite Growth in Lithium/Polymer Systems. *Journal of The Electrochemical Society*, 150(10):A1377, 2003.

[79] C. Monroe and J. Newman. The Effect of Interfacial Deformation on Electrodeposition Kinetics. *Journal of The Electrochemical Society*, 151(6):A880, 2004.

[80] D. Bistri, A. Afshar, and C. V. Di Leo. Modeling the chemo-mechanical behavior of all-solid-state batteries: a review. *Meccanica*, 56(6):1523–1554, 6 2021.

[81] W. Mai, S. Soghrati, and R. G. Buchheit. A phase field model for simulating the pitting corrosion. *Corrosion Science*, 110:157–166, 9 2016.

[82] C. Cui, R. Ma, and E. Martínez-Pañeda. A generalised, multi-phase-field theory for dissolution-driven stress corrosion cracking and hydrogen embrittlement. *Journal of the Mechanics and Physics of Solids*, 166(May):104951, 9 2022.

[83] E. Martínez-Pañeda, A. Golahmar, and C. F. Niordson. A phase field formulation for hydrogen assisted cracking. *Computer Methods in Applied Mechanics and Engineering*, 342:742–761, 12 2018.

[84] Hirshikesh, S. Natarajan, R. K. Annabattula, and E. Martínez-Pañeda. Phase field modelling of crack propagation in functionally graded materials. *Composites Part B: Engineering*, 169 (March):239–248, 7 2019.

[85] L. Porz, T. Swamy, B. W. Sheldon, D. Rettenwander, T. Frömling, H. L. Thaman, S. Berendts, R. Uecker, W. C. Carter, and Y. Chiang. Mechanism of Lithium Metal Penetration through Inorganic Solid Electrolytes. *Advanced Energy Materials*, 7(20):1–12, 10 2017.

[86] S. Shishvan, N. Fleck, R. McMeeking, and V. Deshpande. Growth rate of lithium filaments in ceramic electrolytes. *Acta Materialia*, 196:444–455, 9 2020.

[87] Z. Ning, D. S. Jolly, G. Li, R. De Meyere, S. D. Pu, Y. Chen, J. Kasemchainan, J. Ihli, C. Gong, B. Liu, D. L. R. Melvin, A. Bonnin, O. Magdysyuk, P. Adamson, G. O. Hartley, C. W. Monroe, T. J. Marrow, and P. G. Bruce. Visualizing plating-induced cracking in lithium-anode solid-electrolyte cells. *Nature Materials*, 20(8):1121–1129, 8 2021.

[88] H.-K. Tian, Z. Liu, Y. Ji, L.-Q. Chen, and Y. Qi. Interfacial Electronic Properties Dictate Li Dendrite Growth in Solid Electrolytes. *Chemistry of Materials*, 31(18):7351–7359, 9 2019.

[89] F. Han, A. S. Westover, J. Yue, X. Fan, F. Wang, M. Chi, D. N. Leonard, N. J. Dudney, H. Wang, and C. Wang. High electronic conductivity as the origin of lithium dendrite formation within solid electrolytes. *Nature Energy*, 4(3):187–196, 1 2019.

[90] J. E. Guyer, W. J. Boettinger, J. A. Warren, and G. B. McFadden. Phase field modeling of electrochemistry. II. Kinetics. *Physical Review E*, 69(2):021604, 2 2004.

[91] V. Yurkiv, T. Foroozan, A. Ramasubramanian, R. Shahbazian-Yassar, and F. Mashayek. Phase-field modeling of solid electrolyte interface (SEI) influence on Li dendritic behavior. *Electrochimica Acta*, 265:609–619, 3 2018.

[92] J. Newman and N. P. Balsara. *Electrochemical System*. John Wiley & Sons, Inc., 4th edition, 2021.

[93] S. W. Boettcher, S. Z. Oener, M. C. Lonergan, Y. Surendranath, S. Ardo, C. Brozek, and P. A. Kempler. Potentially Confusing: Potentials in Electrochemistry. *ACS Energy Letters*, 6(1): 261–266, 1 2021.

[94] J. Newman and K. E. Thomas-Alyea. *Electrochemical Systems*. John Wiley & Sons, Incorporated, Hoboken, New Jersey, 3rd edition, 2012.

[95] H. Abdi, B. Mohammadi-ivatloo, S. Javadi, A. R. Khodaei, and E. Dehnavi. Energy Storage Systems. In *Distributed Generation Systems*, pages 333–368. Elsevier, 2017.

[96] N. Kularatna. Rechargeable battery technologies. In *Energy Storage Devices for Electronic Systems*, pages 29–61. Elsevier, 2015.

[97] W.-Y. Chang. The State of Charge Estimating Methods for Battery: A Review. *ISRN Applied Mathematics*, 2013(1):1–7, 7 2013.

[98] R. Zhang, B. Xia, B. Li, L. Cao, Y. Lai, W. Zheng, H. Wang, W. Wang, and M. Wang. A Study on the Open Circuit Voltage and State of Charge Characterization of High Capacity Lithium-Ion Battery Under Different Temperature. *Energies*, 11(9):2408, 9 2018.

[99] M. Coleman, Chi Kwan Lee, Chunbo Zhu, and W. Hurley. State-of-Charge Determination From EMF Voltage Estimation: Using Impedance, Terminal Voltage, and Current for Lead-Acid and Lithium-Ion Batteries. *IEEE Transactions on Industrial Electronics*, 54(5):2550–2557, 10 2007.

[100] C. Fang, X. Wang, and Y. S. Meng. Key Issues Hindering a Practical Lithium-Metal Anode. *Trends in Chemistry*, 1(2):152–158, 5 2019.

[101] D. Lu, Y. Shao, T. Lozano, W. D. Bennett, G. L. Graff, B. Polzin, J. Zhang, M. H. Engelhard, N. T. Saenz, W. A. Henderson, P. Bhattacharya, J. Liu, and J. Xiao. Failure Mechanism for Fast-Charged Lithium Metal Batteries with Liquid Electrolytes. *Advanced Energy Materials*, 5 (3):1–7, 2 2015.

[102] D. Lin, Y. Liu, and Y. Cui. Reviving the lithium metal anode for high-energy batteries. *Nature Nanotechnology*, 12(3):194–206, 3 2017.

[103] A. F. Bower. *Applied Mechanics of Solids*, volume 4. CRC Press, 10 2009.

[104] M. E. Gurtin, E. Fried, and L. Anand. *The Mechanics and Thermodynamics of Continua*. Cambridge University Press, 4 2010.

[105] L. Anand and S. Narayan. An Elastic-Viscoplastic Model for Lithium. *Journal of The Electrochemical Society*, 166(6):A1092–A1095, 4 2019.

[106] C. Cui, R. Ma, and E. Martínez-Pañeda. A phase field formulation for dissolution-driven stress corrosion cracking. *Journal of the Mechanics and Physics of Solids*, 147(September 2020):104254, 2 2021.

[107] W. Ai, B. Wu, and E. Martínez-Pañeda. A coupled phase field formulation for modelling fatigue cracking in lithium-ion battery electrode particles. *Journal of Power Sources*, 544(June):231805, 10 2022.

[108] S. Kovacevic, W. Ali, E. Martínez-Pañeda, and J. LLorca. Phase-field modeling of pitting and mechanically-assisted corrosion of Mg alloys for biomedical applications. *Acta Biomaterialia*, 164: 641–658, 7 2023.

[109] Y. U. Wang. Computer modeling and simulation of solid-state sintering: A phase field approach. *Acta Materialia*, 54(4):953–961, 2 2006.

[110] R. Termuhlen, X. Chatzistavrou, J. D. Nicholas, and H.-C. Yu. Three-dimensional phase field sintering simulations accounting for the rigid-body motion of individual grains. *Computational Materials Science*, 186(July 2020):109963, 1 2021.

[111] J. W. Cahn and J. E. Hilliard. Free Energy of a Nonuniform System. I. Interfacial Free Energy. *The Journal of Chemical Physics*, 28(2):258–267, 2 1958.

[112] J. W. Cahn. On spinodal decomposition. *Acta Metallurgica*, 9(9):795–801, 9 1961.

[113] S. Allen and J. Cahn. Ground state structures in ordered binary alloys with second neighbor interactions. *Acta Metallurgica*, 20(3):423–433, 3 1972.

[114] S. M. Allen and J. W. Cahn. A correction to the ground state of FCC binary ordered alloys with first and second neighbor pairwise interactions. *Scripta Metallurgica*, 7(12):1261–1264, 12 1973.

[115] Y. Zhao, R. Wang, and E. Martínez-Pañeda. A phase field electro-chemo-mechanical formulation for predicting void evolution at the Li–electrolyte interface in all-solid-state batteries. *Journal of the Mechanics and Physics of Solids*, 167(June):104999, 10 2022.

[116] Y. Lu, C. Zhao, H. Yuan, X. Cheng, J. Huang, and Q. Zhang. Critical Current Density in Solid-State Lithium Metal Batteries: Mechanism, Influences, and Strategies. *Advanced Functional Materials*, 31(18), 5 2021.

[117] A. Cuitiño and M. Ortiz. Ductile fracture by vacancy condensation in f.c.c. single crystals. *Acta Materialia*, 44(2):427–436, 2 1996.

[118] M. Jäckle, K. Helmbrecht, M. Smits, D. Stottmeister, and A. Groß. Self-diffusion barriers: Possible descriptors for dendrite growth in batteries? *Energy and Environmental Science*, 11(12): 3400–3407, 2018.

[119] T. Q. Ansari, H. Huang, and S.-Q. Shi. Phase field modeling for the morphological and microstructural evolution of metallic materials under environmental attack. *npj Computational Materials*, 7(1):143, 9 2021.

[120] J. Li, B. Ni, T. Zhang, and H. Gao. Phase field crystal modeling of grain boundary structures and growth in polycrystalline graphene. *Journal of the Mechanics and Physics of Solids*, 120: 36–48, 11 2018.

[121] A. Ask, S. Forest, B. Appolaire, K. Ammar, and O. U. Salman. A Cosserat crystal plasticity and phase field theory for grain boundary migration. *Journal of the Mechanics and Physics of Solids*, 115:167–194, 6 2018.

[122] B. Bourdin, G. Francfort, and J.-J. Marigo. Numerical experiments in revisited brittle fracture. *Journal of the Mechanics and Physics of Solids*, 48(4):797–826, 4 2000.

[123] P. K. Kristensen, C. F. Niordson, and E. Martínez-Pañeda. A phase field model for elastic-gradient-plastic solids undergoing hydrogen embrittlement. *Journal of the Mechanics and Physics of Solids*, 143:104093, 10 2020.

[124] C. H. Chen and C. W. Pao. Phase-field study of dendritic morphology in lithium metal batteries. *Journal of Power Sources*, 484(July 2020), 2021.

[125] S. Narayan and L. Anand. A large deformation elastic–viscoplastic model for lithium. *Extreme Mechanics Letters*, 24:21–29, 10 2018.

[126] P. K. Kristensen, C. F. Niordson, and E. Martínez-Pañeda. An assessment of phase field fracture: crack initiation and growth. *Philosophical Transactions of the Royal Society A: Mathematical, Physical and Engineering Sciences*, 379(2203):20210021, 8 2021.

[127] T.-J. Chuang, K. I. Kagawa, J. R. Rice, and L. B. Sills. Overview no. 2: Non-equilibrium models for diffusive cavitation of grain interfaces. *Acta Metallurgica*, 27(3):265–284, 3 1979.

[128] A. Needleman and J. Rice. PLASTIC CREEP FLOW EFFECTS IN THE DIFFUSIVE CAVITATION OF GRAIN BOUNDARIES. In *Perspectives in Creep Fracture*, pages 107–124. Elsevier, 10 1983.

[129] D. Devaux, K. J. Harry, D. Y. Parkinson, R. Yuan, D. T. Hallinan, A. A. MacDowell, and N. P. Balsara. Failure Mode of Lithium Metal Batteries with a Block Copolymer Electrolyte Analyzed by X-Ray Microtomography. *Journal of The Electrochemical Society*, 162(7):A1301–A1309, 2015.

[130] W. Manalastas, J. Rikarte, R. J. Chater, R. Brugge, A. Aguadero, L. Buannic, A. Llordés, F. Aguesse, and J. Kilner. Mechanical failure of garnet electrolytes during Li electrodeposition observed by in-operando microscopy. *Journal of Power Sources*, 412(October 2018):287–293, 2 2019.

[131] S. Yu, R. D. Schmidt, R. Garcia-Mendez, E. Herbert, N. J. Dudney, J. B. Wolfenstine, J. Sakamoto, and D. J. Siegel. Elastic Properties of the Solid Electrolyte Li 7 La 3 Zr 2 O 12 (LLZO). *Chemistry of Materials*, 28(1):197–206, 1 2016.

[132] H. Buschmann, S. Berendts, B. Mogwitz, and J. Janek. Lithium metal electrode kinetics and ionic conductivity of the solid lithium ion conductors "Li7La3Zr2O12" and Li7-La3Zr2-Ta O12 with garnet-type structure. *Journal of Power Sources*, 206:236–244, 5 2012.

[133] R. V. Salvatierra, W. Chen, and J. M. Tour. What Can be Expected from "Anode-Free" Lithium Metal Batteries? *Advanced Energy and Sustainability Research*, 2(5), 5 2021.

[134] C. Heubner, S. Maletti, H. Auer, J. Hüttl, K. Voigt, O. Lohrberg, K. Nikolowski, M. Partsch, and A. Michaelis. From Lithium-Metal toward Anode-Free Solid-State Batteries: Current Developments, Issues, and Challenges. *Advanced Functional Materials*, 31(51), 2021.

[135] Y.-G. Lee, S. Fujiki, C. Jung, N. Suzuki, N. Yashiro, R. Omoda, D.-S. Ko, T. Shiratsuchi, T. Sugimoto, S. Ryu, J. H. Ku, T. Watanabe, Y. Park, Y. Aihara, D. Im, and I. T. Han. High-energy long-cycling all-solid-state lithium metal batteries enabled by silver–carbon composite anodes. *Nature Energy*, 5(4):299–308, 3 2020.

[136] M. J. Wang, E. Carmona, A. Gupta, P. Albertus, and J. Sakamoto. Enabling "lithium-free" manufacturing of pure lithium metal solid-state batteries through in situ plating. *Nature Communications*, 11(1):5201, 10 2020.

[137] E. Dologlou. Self-diffusion in solid lithium. *Glass Physics and Chemistry*, 36(5):570–574, 10 2010.

[138] A. Masias, N. Felten, R. Garcia-Mendez, J. Wolfenstine, and J. Sakamoto. Elastic, plastic, and creep mechanical properties of lithium metal. *Journal of Materials Science*, 54(3):2585–2600, 2 2019.

[139] B. Hallstedt. Molar volumes of Al, Li, Mg and Si. *Calphad: Computer Coupling of Phase Diagrams and Thermochemistry*, 31(2):292–302, 2007.

[140] K. Doll, N. M. Harrison, and V. R. Saunders. A density functional study of lithium bulk and surfaces. *Journal of Physics: Condensed Matter*, 11(26):5007–5019, 7 1999.

[141] C. Cui, R. Ma, and E. Martínez-Pañeda. Electro-chemo-mechanical phase field modeling of

localized corrosion: theory and COMSOL implementation. *Engineering with Computers*, 39(6): 3877–3894, 12 2023.